



ADVANCED TOPICS IN SCIENCE AND TECHNOLOGY IN CHINA
国家科学技术学术著作出版基金资助出版

Guoqiang Li
Peijun Wang

Advanced Analysis and Design for Fire Safety of Steel Structures



ZHEJIANG UNIVERSITY PRESS
浙江大学出版社



Springer

ADVANCED TOPICS
IN SCIENCE AND TECHNOLOGY IN CHINA

ADVANCED TOPICS IN SCIENCE AND TECHNOLOGY IN CHINA

Zhejiang University is one of the leading universities in China. In *Advanced Topics in Science and Technology in China*, Zhejiang University Press and Springer jointly publish monographs by Chinese scholars and professors, as well as invited authors and editors from abroad who are outstanding experts and scholars in their fields. This series will be of interest to researchers, lecturers, and graduate students alike.

Advanced Topics in Science and Technology in China aims to present the latest and most cutting-edge theories, techniques, and methodologies in various research areas in China. It covers all disciplines in the fields of natural science and technology, including but not limited to, computer science, materials science, life sciences, engineering, environmental sciences, mathematics, and physics.

Guoqiang Li
Peijun Wang

Advanced Analysis and Design for Fire Safety of Steel Structures

With 254 figures



Authors

Prof. Guoqiang Li
College of Civil Engineering,
Tongji University,
Shanghai 200092, China
E-mail: gqli@tongji.edu.cn

Associate Prof. Peijun Wang
School of Civil Engineering,
Shandong University,
Jinan 250061, China
E-mail: pjwang@sdu.edu.cn

ISSN 1995-6819
Advanced Topics in Science and Technology in China

e-ISSN 1995-6827

ISBN 978-7-308-08267-9
Zhejiang University Press, Hangzhou

ISBN 978-3-642-34392-6
Springer Heidelberg New York Dordrecht London

ISBN 978-3-642-34393-3 (eBook)

Library of Congress Control Number: 2012949647

© Zhejiang University Press, Hangzhou and Springer-Verlag Berlin Heidelberg 2013

This work is subject to copyright. All rights are reserved by the Publishers, whether the whole or part of the material is concerned, specifically the rights of translation, reprinting, reuse of illustrations, recitation, broadcasting, reproduction on microfilms or in any other physical way, and transmission or information storage and retrieval, electronic adaptation, computer software, or by similar or dissimilar methodology now known or hereafter developed. Exempted from this legal reservation are brief excerpts in connection with reviews or scholarly analysis or material supplied specifically for the purpose of being entered and executed on a computer system, for exclusive use by the purchaser of the work. Duplication of this publication or parts thereof is permitted only under the provisions of the Copyright Law of the Publishers' locations, in its current version, and permission for use must always be obtained from Springer. Permissions for use may be obtained through RightsLink at the Copyright Clearance Center. Violations are liable to prosecution under the respective Copyright Law.

The use of general descriptive names, registered names, trademarks, service marks, etc. in this publication does not imply, even in the absence of a specific statement, that such names are exempt from the relevant protective laws and regulations and therefore free for general use.

While the advice and information in this book are believed to be true and accurate at the date of publication, neither the authors nor the editors nor the publishers can accept any legal responsibility for any errors or omissions that may be made. The publishers make no warranty, express or implied, with respect to the material contained herein.

Printed on acid-free paper

Springer is part of Springer Science+Business Media (www.springer.com)

Preface

Advanced Analysis and Design for Fire Safety of Steel Structures presents a systematic description of recent research achievements on behaviors of structural steel components in a fire, such as the catenary actions of restrained steel beams, the design methods of restrained steel columns and the membrane actions of concrete floor slabs with steel decks in a fire. Using a systematic description of structural fire safety engineering principles, the authors illustrate the important difference between behaviors of isolated structural elements and restrained components in a global structure under fire conditions. The book is also essential for structural engineers who wish to improve their understanding of steel buildings exposed to fires. It is also an ideal textbook for introductory courses in fire safety for a master degree programme in structural engineering and a vital reading material for final year undergraduate students in civil engineering and fire safety engineering. Furthermore, it successfully bridges the information gap between fire safety engineers, structural engineers and building inspectors, and will be of significant interest to architects, code officials, building designers and fire fighters. We sincerely hope and anticipate that this book will be useful to anyone interested or involved in this fascinating and technologically important research area.

Since 1991 we have been devoted to the study of structural behaviors and analysis of steel structures in a fire. It is unimaginable that the work could have been carried out, year-by-year, without financial support. Therefore we gratefully acknowledge the National Natural Science Foundation of China (Grant Nos. 59478038, 59778032, 51008181), the National Natural Science Foundation of China for Distinguished Young Scholar (Grant No. 50225825), the Foundation for Innovative Research Groups of the National Natural Science Foundation of China (Grant Nos. 50321803, 50621062), the State Key Program of National Natural Science of China (Grant No. 50738005), the Joint Research Fund for Overseas Natural Science of China (Grant No. 50728805) and the Open Research Fund of the State Key Laboratory of Disaster Reduction in Civil Engineering (Grant No. SLDRCE09-TS-02) for the financial support.

It is indeed a great pleasure to extend our “thank you” to all our colleagues and former research students for their dedication to our research projects. Especially,

the contributions to Chapter 2 from Dr. Yong Du, to Chapter 3 from Mr. Kai Chen and Dr. Guobiao Lou, to Chapter 7 from Dr. Shixiong Guo and Dr. Yinzhi Wang, to Chapter 8 from Dr. Weiyong Wang, to Chapter 9 from Dr. Shouchao Jiang and Ms. Nasi Zhang, to Chapter 10 from Dr. Shouchao Jiang and to Chapter 11 from Dr. Huangtin Zhou, Dr. Yong Du and Ms. Jueqian Huang. Their efforts are deeply appreciated and acknowledged. Finally, we would like to thank the editorial staff of Springer Verlag and Zhejiang University Press for their great assistance.

The authors
Shanghai, China
July, 2012

Contents

1	Introduction	1
1.1	Damage to Steel Structures Caused by Fire	1
1.1.1	Global Collapse of Steel Structures in Fire	1
1.1.2	Damage to Structural Components by Fire	1
1.2	Requirements for Fire Resistance of Steel Structures	2
1.2.1	Ultimate Limit State of Structures in a Fire	2
1.2.2	Load Bearing Capacity Criteria	5
1.2.3	Fire-Resistance Duration Demands	5
1.3	Approach for Determining Fire-Resistance of Steel Structures	6
1.3.1	Experimental Approach	6
1.3.2	Analytical Approach	7
	References	8
2	Fire in Buildings	11
2.1	Basic Concepts	11
2.1.1	Fire Load	11
2.1.2	Heat Released Rate	12
2.2	Compartment Fire	13
2.2.1	Development of Compartment Fire	13
2.2.2	Heat Release Model of Fire before Flashover	15
2.2.3	Conditions Necessary for Flashover	15
2.2.4	Heat Release Rate of the Fire after Flashover	16
2.2.5	Modeling of Compartment Fire	17
2.2.6	Empirical Modeling of Compartment Fire	18
2.3	Large Space Building Fire	22
2.3.1	Characteristics of Large Space Building	22
2.3.2	Characteristics of Large Space Building Fire	22
2.3.3	Simulation of Large Space Building Fire using Zone Model	23
2.3.4	Characteristics of Large Space Building Fire	27
2.4	Standard Fire and Equivalent Exposure Time	31
2.4.1	Standard Fire	31

2.4.2	Equivalent Exposure Time	32
References	34
3	Properties of Steel at Elevated Temperatures	37
3.1	Thermal Properties of Structural Steel at Elevated Temperatures . . .	37
3.1.1	Conductivity	37
3.1.2	Specific Heat	38
3.1.3	Density	39
3.2	Mechanical Properties of Structural Steel at High Temperature	40
3.2.1	Test Regimes	40
3.2.2	Definition of Yield Strength at High Temperature	41
3.2.3	Mechanical Properties of Structural Steel at High Temperatures	42
3.2.4	Yield Strength and Elastic Modulus of Fire-Resistant Steel at High Temperatures	43
3.2.5	Stress-Strain Relationship of Normal Strength Structural Steel and Fire-Resistant Steel at Elevated Temperatures	48
3.3	Mechanical Properties of High Strength Steel at High Temperatures	48
3.3.1	High Strength Bolt	48
3.3.2	High Strength Cable	50
3.4	Properties of Stainless Steel at High Temperatures	54
3.4.1	Thermal Properties of Stainless Steel	54
3.4.2	Mechanical Properties of Stainless Steel at High Temperatures	54
References	64
4	Temperature Elevations of Structural Steel Components Exposed to Fire	67
4.1	Laws of Heat Transfer	67
4.1.1	Heat Transfer in Structural Members	67
4.1.2	Heat Transfer between Hot Smoke and a Structural Member	68
4.2	Practical Calculation Method for Temperature Elevation of Structural Members	69
4.2.1	Calculating Model	69
4.2.2	Temperature Elevation of Structural Component with Uniformly Distributed Temperature	70
4.2.3	Temperature of Structural Component with Non-Uniformly Distributed Temperature	79
4.3	Practical Calculation Method for Temperature Evolution of Structural Members Exposed to a Large Space Building Fire	79
4.3.1	Effects of Flame Radiation on Temperature Elevation of Un-Protected Steel Structural Components	80
4.3.2	Parametric Study	86
4.3.3	Limit Value of Flame Radiation	88
4.4	Example	89
References	90

5	Fire-Resistance of Isolated Flexural Structural Components	93
5.1	Load-bearing Capacity of a Flexural Steel Component at High Temperatures	93
5.1.1	Strength of a Flexural Steel Component at High Temperatures	93
5.1.2	Lateral Torsional Buckling Strength of a Flexural Steel Component at High Temperatures	93
5.1.3	Critical Temperature of a Flexural Steel Component in Fire	95
5.1.4	Example	96
5.2	Fire-resistance of Flexural Steel-Concrete Composite Components	99
5.2.1	Material Properties and Temperature Calculation of a Composite Beam	99
5.2.2	Strength of a Composite Beam at High Temperature	100
5.2.3	Critical Temperature of a Composite Beam	101
5.2.4	Parametric Study	102
5.2.5	Simplified Approach for the Fire Resistance Design of Composite Beams	106
5.2.6	Example and Comparison	108
5.2.7	Experimental Validation	110
	References	113
6	Fire-Resistance of Isolated Compressed Steel Components	115
6.1	Fire Resistance of Axially Compressed Steel Components	115
6.1.1	Load Bearing Capacity of Axially Compressed Steel Components	115
6.1.2	Critical Temperature of an Axially Compressed Component	119
6.1.3	Example	119
6.2	Design Method for a Structural Component under the Combined Axial Force and Bending Moment	122
6.2.1	Stability of a Structural Component under the Combined Axial Force and Bending Moment	122
6.2.2	Cross-Sectional Strength of the Structural Component under the Combined Axial Force and Bending Moment at Elevated Temperatures	123
6.2.3	Critical Temperature of the Structural Component Subjected to the Combined Axial Force and Bending Moment	123
6.2.4	Example	125
	References	129
7	Fire-Resistance of Restrained Flexural Steel Components	131
7.1	Fire-Resistance of a Restrained Steel Beam	131
7.1.1	Fire Test of Restrained Steel Beams	132
7.1.2	Analysis and Design for Fire-Resistance of a Restrained Steel Beam	143

7.2	Fire Resistance of Steel-Concrete Composite Beams	159
7.2.1	Fire Test on Restrained Steel-Concrete Composite Beams . .	159
7.2.2	Analysis of Restrained Steel-Concrete Composite Beams . . .	169
7.2.3	Practical Design Method for a Restrained Steel-Concrete Composite Beam	176
7.2.4	Axial Force in the Composite Beam	178
	References	184
8	Fire-Resistance of Restrained Steel Columns	189
8.1	Fire Test on Restrained Steel Columns with Axial and Rotational Restraint	189
8.1.1	Test Set-Up and Test Specimen	190
8.1.2	Displacement and Temperature Acquisition	192
8.1.3	Test Schedule	193
8.1.4	Test Results	193
8.1.5	Numerical Simulation of the Fire Test	200
8.2	Parametric Study of Restrained Steel Columns in a Fire	202
8.2.1	Parameters	204
8.2.2	Parametric Study on a Restrained Steel Column under Axial Load Only in a Fire	206
8.2.3	Parametric Study of a Restrained Column under Combined Axial Load and Bending Moment in a Fire	207
8.3	Simplified Design Method for Restrained Steel Columns in a Fire . .	214
8.3.1	Design Method for Restrained Columns under Axial Load Only in a Fire	217
8.3.2	Design Methods for the Restrained Columns under Combined Axial Load and Bending Moment	222
8.4	Fire-Resistance of Restrained Columns with Non-Uniform Temperature Distribution	231
8.4.1	Test Arrangement and Instrumentation	232
8.4.2	Temperature Distribution	233
8.4.3	Continuum Model	234
8.4.4	Experiment Study	238
	References	241
9	Fire-Resistance of Composite Concrete Slabs	245
9.1	Fire-resistance Design Method for Composite Concrete Slabs Based on Small Deflection Theory	245
9.1.1	Studied Slabs	245
9.1.2	Parametric Studies	247
9.1.3	Simplified Design Method	250
9.1.4	Verification by the Fire Resistance Test	252
9.2	Fire Resistance Design Method for the Composite Slab Considering Membrane Action	252

9.2.1	Development of the Membrane Action of a Composite Slab in a Fire	252
9.2.2	Fire Test on the Composite Slab	256
9.2.3	Analysis of the Composite Slab in Consideration of the Membrane Action in a Fire	268
References	279
10	Analysis of Steel Moment-Resistant Frames Subjected to a Fire	281
10.1	Element for Analysis	282
10.1.1	Properties of the Elemental Cross-Section	282
10.1.2	Location of the Neutral Axis in an Elastic State	283
10.1.3	Equivalent Axial Stiffness	283
10.1.4	Equivalent Bending Stiffness in an Elastic State	284
10.1.5	Initial Yielding Moment	284
10.1.6	Location of the Neutral Axis in Total Plastic State	284
10.1.7	Plastic Moment	285
10.1.8	Stiffness of Element	285
10.2	Thermal Force of Element	287
10.3	Structural Analysis	287
10.4	Experimental and Theoretical Prediction	290
References	297
11	Analysis and Design of Large Space Steel Structure Buildings Subjected to a Fire	299
11.1	Practical Analysis Approach for Steel Portal Frames in a Fire	299
11.1.1	Finite Element Modeling and Assumptions	299
11.1.2	Parameters Influencing the Fire Resistance of a Steel Portal Frame	301
11.1.3	Estimation of the Critical Temperature of a Steel Portal Frame	305
11.1.4	Example	308
11.1.5	Fire Protection	309
11.2	Critical Temperature of a Square Pyramid Grid Structure in a Fire ..	309
11.2.1	Parameters of Grid Structures	309
11.2.2	Definition of Parameters	310
11.2.3	Critical Temperature of the Structural Component	312
11.2.4	Critical Temperature of the Grid Structure in Uniform Temperature Field	312
11.2.5	Critical Temperatures of the Grid Structure in a Non-Uniform Temperature Field	314
11.2.6	Conditions for a Grid Structure with no Need of Fire Protection	316
11.3	Continuous Approach for Cable-Net Structural Analysis in a Fire ..	316
11.3.1	Behavior of a Single Cable in a Fire	317
11.3.2	Behavior of the Cable-Net Structure in a Fire	323

XII Contents

11.3.3 Simplified Method for the Critical Temperature of a Cable-Net Structure	327
11.3.4 Critical Temperature of a Cable-Net Structure with Elliptical or Diamond Plan View	329
11.3.5 Critical Temperature of the Cable-Net Structure with Parabolic Plan View	329
References	331
Appendix A: Parameters for Calculating the Smoke Temperature in Large Space Building Fire	333
Appendix B: Stiffness Matrixes of Beam-Column Elements	341
Appendix C: Height of the Flame	343
Appendix D: Critical Temperatures of Composite Beams	345
Appendix E: Critical Temperatures of a Steel Column Subjected to Combined Axial Force and Bending Moment	349
Appendix F: Maximum Fire Power at Which a Grid Structure Does not Need Fire Protection	351
Index	355

Introduction

1.1 Damage to Steel Structures Caused by Fire

Steel is a non-combustion material, but its yield strength and Young's modulus degrade quickly at high temperature, which makes the steel structure have a low fire resistance. At the temperature of 600 °C^[1], the steel will lose most of its strength and stiffness. The fire in the building may cause global collapse to the steel structure or severe damage to structural components.

1.1.1 Global Collapse of Steel Structures in Fire

With the degrading of strength and stiffness of steel at elevated temperatures, structural components may lose their load bearing capacities, which lead to global collapse of the building. Fig. 1.1 illustrates a steel portal frame industrial building collapsed in a fire^[2]. And the collapse of The World Trade Center is another disaster caused by fire^[3].

1.1.2 Damage to Structural Components by Fire

In 1990, the Broadgate Street building had a fire during the construction phase and steel columns and steel beams were seriously damaged^[4]. Fig. 1.2 illustrates the buckled steel column caused by the fire. Redistribution of the load to less severely heated components of the building leads to improved fire resistance performance of the structure.

In 2001, a severe fire happened at the Taipei Oriental Science District Building^[2]. Though the overall structure of the building did not collapse, a large number of steel structural components were severely damaged. The damage to the steel structure included (a) fracture of the beam-to-column connection, (b) local buckling of the steel beam and (c) large deflection in the steel beam and the floor slab, as shown in Fig. 1.3.

1.2 Requirements for Fire Resistance of Steel Structures

Fire resistance is a measure of the ability of a building element to resist a fire. It is most often quantified as the time during which the element can meet certain criteria during exposure to a standard fire-resistance test. Structural fire resistance tests can also be quantified using the critical temperature or load bearing capacity of a structural element exposed to a fire.

1.2.1 Ultimate Limit State of Structures in a Fire

When a building is subjected to fire, the load bearing capacity of a structural component decreases with the elevation of the temperature. The ultimate limit state of the structure in the fire is reached when the load bearing capacity of the structural component equals the applied load.

Depending on whether the structure fails locally or globally, the ultimate limit states include failure of the structural component and failure of the complete structure.

Failure of the structural component^[2] is identified as

- the structural component loses its stability;
- the deformation rate of the structural component exceeds a certain limit;
- the deformation of the structural component is not suitable for the load bearing function, which can be formulated as

$$\delta \geq \frac{l}{20} \quad (1.1)$$

The fire resistance test shows that when the character deformation rate of a structural component exceeds



Fig. 1.1 Collapse of an industrial building caused by fire



Fig. 1.2 Buckling of the column in a fire



(a) Fracture of the beam-to-column connection



(b) Local buckling of the steel beam



(c) Large deflection in the steel beam



(d) Large deflection in the floor slab

Fig. 1.3 Damage to the Taipei Oriental Science District Building caused by fire

$$\frac{d\delta}{dt} \geq \frac{l^2}{15h_x} \quad (1.2)$$

the component will fail in a short time, where δ is the maximum deflection of the structural component in mm, as shown in Fig. 1.4.

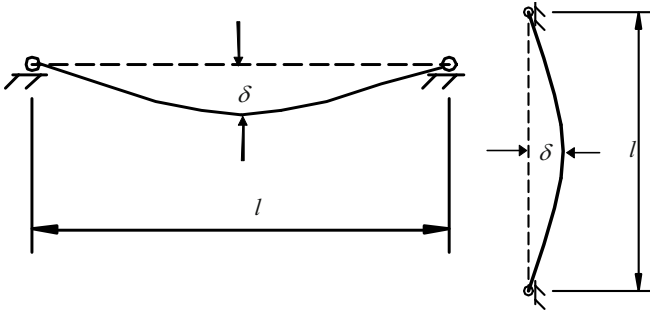


Fig. 1.4 Deformation of structural component in fire

Failure of the complete structure^[2] is identified as

- the structure loses its overall stability;
- the deformation of the structure is not suitable for load bearing function, as shown in Fig. 1.5, which is formulated as

$$\frac{\delta}{h} \geq \frac{1}{30} \quad (1.3)$$

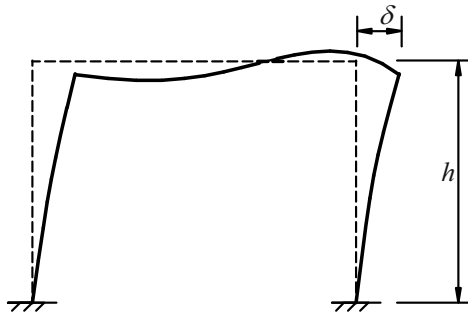


Fig. 1.5 Deformation of the structure in a fire

1.2.2 Load Bearing Capacity Criteria

The load bearing capacity criteria of the structural component or the overall structure in a fire is assessed on a calculation basis and can be expressed mathematically as follows using the limit state function, Z , which is defined as the algebraic difference between the structural capacity for fire-resistance and the corresponding demand. The load bearing capacity criteria can be expressed in one of the following three ways^[1]

- on a time basis

$$Z = t_{fi,d} - t_{fi,req} \geq 0 \quad (1.4)$$

- on a strength basis

$$Z = R_{fi,d} - E_{fi,d} \geq 0 \quad (1.5)$$

- on a temperature basis

$$Z = T_{cr,d} - T_d \geq 0 \quad (1.6)$$

1.2.3 Fire-Resistance Duration Demands

The China Design Code on Building Fire Protection and Prevention (GB50016-2006)^[5] gives the fire resistance duration demand for various structural components on a time basis, as listed in Table 1.1.

Table 1.1 Fire resistance of structural components

Type of structural component	Building grade for fire resistance (h)			
	Grade I	Grade II	Grade III	Grade IV
Fire resistance wall	3.00	3.00	3.00	3.00
Load bearing wall	3.00	2.50	2.00	0.50
Non-load bearing external wall	1.00	1.00	0.50	–
Stairway wall/ elevator wall	2.00	2.00	1.50	0.50
Partition wall between two residential cells	2.00	2.00	1.50	0.50
Partition wall along the evacuation route	1.00	1.00	0.50	0.25
Partition wall in a residential cell	0.75	0.50	0.50	0.25
Column	3.00	2.50	2.00	0.50
Beam	2.00	1.50	1.00	0.50
Slab	1.50	1.00	0.50	–
Roof load bearing structural component	1.50	1.00	–	–
Evacuation stair	1.50	1.00	0.50	–
Suspended ceiling (including the ceiling frame)	0.25	0.25	0.15	–

1.3 Approach for Determining Fire-Resistance of Steel Structures

The fire resistance of a steel structure can be obtained by experimental approach or analytical approach. Both of them have some advantages and disadvantages.

1.3.1 Experimental Approach

The standard fire resistance test is usually carried out to assign a fire resistance rating to a steel structure component to enable it to pass the regulatory fire resistance requirements. So far, numerous standard fire resistance tests for steel structural components have been carried out. In China it is GB/T 9978^[6] and in the United Kingdom it is the BS 476, Part 20^[7]. Other countries also have their own standards and all these standards are similar. For this reason, the fire exposure for the standard fire resistance test often uses an ISO standard^[8].

The standard test for fire resistance of a structural element is carried out in a furnace, either gas or oil fired. The average rise in furnace temperature may accord to the following temperature-time relationship provided by ISO 834^[8] as

$$T - T_0 = 345 \lg(8t + 1) \quad (1.7)$$

The fire resistance of a structural component can be assessed according to load bearing, insulation or integrity criteria^[9]. The load bearing criterion is concerned with the load resistant capacity of the specimen. The insulation criterion is concerned with the excessive temperature increase on the unexposed surface of the specimen. And the integrity criterion is associated with the fire spreading through gaps in the test specimen. For a framed steel or steel-concrete composite component, the load bearing criterion is usually the major concern.

Although the standard fire resistance test is a convenient way to grade the relative fire performance of different types of structural members, for a number of reasons it is not very effective in developing our understanding of realistic structural behavior in a fire.

The main deficiencies in the standard fire resistance test are as follows^[10]

- the standard fire exposure is only one of numerous types of realistic fire conditions;
- standard fire resistance tests are carried out on individual structural elements, not structural assemblies and the structural component interactions cannot be considered;
- standard fire resistance tests are carried out for very specific objectives and instrumentation is usually not adequate for thorough retrospective analysis;
- the boundary condition of the structural specimen under testing is usually simply supported, which is different from the condition of the element restrained in a real structure in most cases. However, any stiffness of this inevitable restraint could have a significant influence on the behavior of the element exposed to fire;
- the failure criteria usually do not adequately describe the intended usage of the building.

Despite all these shortcomings, the collective results of different standard fire resistance tests have made great contributions to our understanding of the behavior of steel structural elements in a fire. It is based on these results that fire safety design of steel structures has been made possible.

1.3.2 Analytical Approach

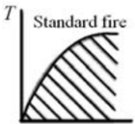
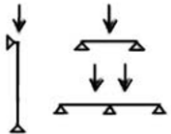
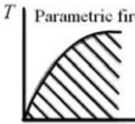
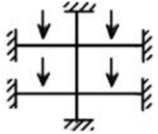
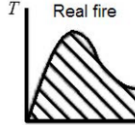
The fire resistance of a structure can also be obtained by analytical approach. The complexity of the fire resistance analytical model depends on complexities of heating models and structural models.

There are three heating models, as shown in Table 1.2^[2], which are (a) standard fire model (H_1), (b) equivalent fire model (H_2) and (c) real fire model (H_3), as shown in Table 1.2. The standard fire model (H_1) is simple, however it may be very different from the real fire. The equivalent fire model (H_2) uses the standard fire curve, but the duration of fire exposure is determined by the equivalent fire duration time related to actual fire characteristics of the compartment, such as the fire load, internal surface area of the compartment, the opening area of the compartment, thermal characteristics of compartment boundaries, etc. In lieu of a full calculation using such a model, it is permissible to use a parametric equation to represent the compartment fire^[11]. The real fire model (H_3) directly simulates fire development with consideration for the actual characteristics of the compartment.

Correspondingly, there are three structural models (Table 1.2^[2]), which are (a) element model (S_1), (b) sub-structural model (S_2) and (c) complete structural model (S_3). The element model (S_1) is very simple to accomplish. However, it is hard to consider the realistic boundary condition effects. The sub-structural model (S_2) can, nevertheless, simulate the boundary conditions of the specific element. The element model and sub-structural model can both be used to obtain the fire resistance of the structural component, while the complete structural model (S_3) can be used to obtain the fire resistance of the whole structure.

There are nine combinations for the fire resistance calculation of the structure, as shown in Table 1.2^[2]. For general buildings, the structural model S_1 or S_2 can be used and for important buildings the structural model S_3 should be used. For the compartment fire, the fire model H_1 or H_2 can be used and for important buildings and large space buildings, the fire model H_2 or H_3 should be used.

Table 1.2 Combination of the fire model and structural model for structural fire safety test and analysis

Fire exposure model	Structural model		
	S ₁ Structural component	S ₂ Sub-structure	S ₃ Complete structure
H ₁ Standard fire 	Calculation or test	Calculation or exceptional test	
H ₂ Parametric fire 			
H ₃ Real fire 	Calculation or exceptional test		

References

- [1] China Association for Engineering Construction Standardization. *Technical Code for Fire Safety of Steel Structures in Buildings (CECS200-2006)*. China Plan Press, 2006.
- [2] G. Q. Li, L. H. Han, G. B. Lou, and S. C. Jiang. *Steel and Steel-Concrete Composite Structures Fire Resistance Design*. China Architecture & Building Press, 2006.
- [3] Research 9.11. *Unthinkable Collapses*. <http://911research.wtc7.net/wtc/analysis/towers.html>, 2001.
- [4] The Steel Construction Institute. *The Behaviour of Steel Columns in Fire*. Number Report to the Department of the Environment, RT524. 1996.
- [5] Ministry of Housing and Urban-Rural Development of the People’s Republic of China. *Code of Design on Building Fire Protection and Prevention*. China Plan Press, 2006.
- [6] Standardization Administration of the People’s Republic of China. *Fire-Resistance Tests on Elements of Building Construction, Part 1: General Requirements*. China Standard Press, 2009.

- [7] British Standard Insititute. *Fire Tests on Building Materials and Structures, Part 20: Method for Determining the Fire Resistance of Elements of Construction*. British Standard Insititute, 2004.
- [8] International Organization for Standardization. *Fire-Resistance Tests, Elements of Building Construction, Part 1: General Requirements*. International Organization for Standardization, 1999.
- [9] A. H. Buchanan. *Structural Design for Fire Safety*. John Wiley & Sons, Ltd., 2001.
- [10] Y. Wang. *Steel and Composite Structures, Behavior and Design for Fire Safety*. John Wiley & Sons, Ltd., 2002.
- [11] European Committee for Standardisation. *Eurocode 1: Actions on Structures, Part 1-2: General Actions. Actions on Structures Exposed to Fire*. European Committee for Standardisation, 2009.

Fire in Buildings

2.1 Basic Concepts

2.1.1 Fire Load

Fire load is the calorific value of combustible materials per unit area in a building. The combustible material in a building may include

- wood, paper and combustible plastic for decoration;
- coal gas, natural gas and liquid petroleum gas for cooking;
- furniture, books, paper, bedding, curtain and carpet;
- wood, oil and alcohol stored in the room.

The net calorific value for a range of commonly used combustible materials is listed in Table 2.1 [1].

The fire load in a building can be obtained (1) by full calculation or (2) by empirical rating.

2.1.1.1 By Full Calculation

The fire load in a compartment is quantified as

$$q = \frac{1}{A_f} \sum M_V H_V \quad (2.1)$$

Usually, the material in a compartment does not combust completely. A factor μ is introduced to Eq.(2.1) as

$$q = \frac{1}{A_f} \mu \sum M_V H_V \quad (2.2)$$

where μ is a factor between 0 and 1.0, depending on the fire type.

In engineering practice, the fire load is usually expressed as the mass of equivalent wood given by

$$q = \frac{1}{A_f H_0} \mu \sum M_V H_V \quad (2.3)$$

where H_0 is the standard calorific value of wood and takes the value of 18.4 MJ/kg.

Table 2.1 Calorific value of combustible material (in MJ/kg)

Material	H_V	Material	H_V
Solids Anthracite	34	Liquids Gasoline	44
Asphalt	41	Diesel oil	41
Bitumen	42	Spirits	29
Cellulose	17	Acetylene	48
Charcoal	35	Hydrogen	120
Clothes	19	Methane	50
Coal	31	Ethanol	27
Cork	29	Petroleum	41
Cotton	18		
Grain	17		
Leather	19		
Foam rubber	37		
Epoxy	34		
Wool	23		
Wood	19		
Rubber tire	32		

2.1.1.2 Empirical Rating

Many authorities have provided empirical data for the calorific value in a given type of occupancy. CIB^[2] gives design values of 140 to 150, 102 to 124, 61 to 96, 116 and 67 MJ/m² for a dwelling, office, school, hospital and hotel respectively. The EC1^[3] gives five classes (I to V) with fire load ranging from 250 to 2000 MJ/m².

2.1.2 Heat Released Rate

For any fire, the heat release rate can be obtained if the amount of heat released in a certain time is known. The average heat release rate Q is give by

$$Q = \frac{E}{t} \quad (2.4)$$

BS7346^[4] provides design values for the heat release rate according to the type of occupancy, so that for retail areas with standard response sprinklers the heat release rate per unit area is 625 MW/m² and for retail areas with no sprinklers the heat release rate per unit area is 1200 MW/m².

2.2 Compartment Fire

Depending on whether there is a flashover, the fire in a building is divided into a compartment fire and a large space building fire. Usually there is a flashover in a compartment fire. A compartment refers to an enclosure where the volume is less than 100 m^3 and the ratio between length and width of the compartment is moderate. On the other hand, some enclosures are very high (higher than 4 m), or have a large floor area (greater than 500 m^2), such as an industrial workshop, theater, station, airport, exhibition center, shopping center. Fires in these kinds of buildings are called large space building fires. The large building fire will not usually experience flashover.

2.2.1 Development of Compartment Fire

The development of a compartment fire may roughly be divided into three stages as (1) fire growth, (2) steady burning and (3) decay, as shown in Fig. 2.1. The transition from fire growth to steady burning is called flashover^[5,6].

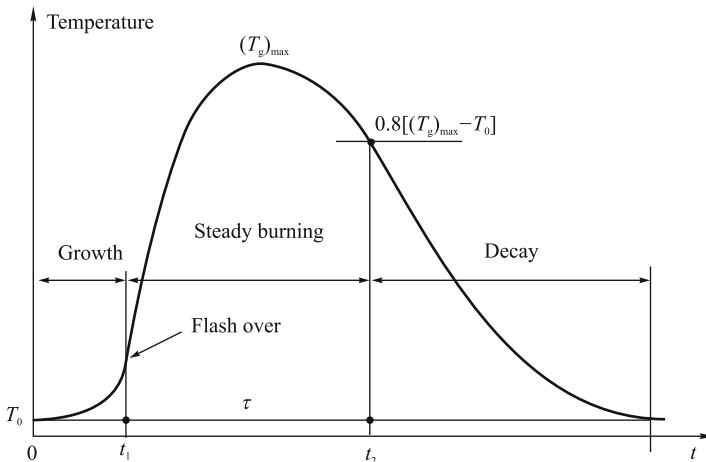


Fig. 2.1 Development of a compartment fire

2.2.1.1 Fire Growth

The fire is localized during the growth stage when the temperature distribution in the compartment is highly non-uniform. The main danger at this stage is the risk to life safety due to the production of large quantities of smoke and toxic gases by the fire. If the fire is promptly discovered and effective fire fighting is activated, it can be easily controlled and fire damage will be minimal. If the burning item is sufficiently

far away from other combustible material, the fire may die out due to the difficulty of igniting other combustible materials. Also, if there is an insufficient supply of oxygen the fire may appear to die down, but it may grow again if fresh air is supplied to the enclosure. In more dramatic situations, a sudden fresh air supply to an under-ventilated fire may lead to the so-called “back draught”, posing serious hazards for fire fighting. In structural fire engineering, it is assumed that fire spread will occur and that there is a sufficient supply of fresh air to aid fire growth.

With fire growth, hot gas is released and the fire plume will rise towards the ceiling due to buoyancy. In the meantime, fresh air is entrained and more hot smoke is released. On hitting the ceiling, the smoke will spread outwards until it hits the walls. Afterwards, a smoke layer will quickly form underneath the ceiling. The bottom of the smoke layer will descend as it becomes thicker. On reaching the top of any opening, e.g. an open doorway or window, smoke will flow out of the enclosure. To allow fresh air to enter, the smoke layer will stabilize at a height within the opening. At this stage, the enclosure fire environment may be approximately divided into two zones as (a) an upper zone of hot smoke and (b) a lower zone of cold air. The division between the upper and lower zones is the neutral plane, above which smoke flows out of the enclosure and below which fresh air is supplied to the enclosure.

As the volume of smoke stabilizes while more hot combustion gases are continuously supplied to the smoke layer, the smoke temperature increases. Owing to a lack of oxygen in the smoke layer, a large quantity of partially burnt fuel will also accumulate in the smoke layer. Meanwhile, the burning flame will become larger and penetrate the smoke layer. The flame spreads more quickly when it is aided by the partially burnt fuels in the smoke layer. The radiation from the burning flames and the high temperature smoke layer will accelerate the burning rate of the existing fire.

2.2.1.2 Flashover

The rapidly accelerating positive burning loop will lead to the flashover, when the radiation of the unburned combustible materials in the enclosure becomes so high that they become ignited at almost the same time. The onset of such an event is often referred to as “flashover”, as shown in Fig. 2.1. The fire growth stage before the onset of flashover is referred to as pre-flashover fire and that afterwards as post-flashover fire. After flashover, the fire temperature increases rapidly. It is not possible for flashover to occur in an open space.

2.2.1.3 Steady Stage

At the steady stage of the fire, the rate of burning may depend on the amount of fresh air that can be supplied, which is ventilation controlled fire. There are some occasions when the area covered by combustible materials in the fire enclosure is small. In these cases, the rate of burning depends on the surface area of burning fuels which is referred to as fuel controlled fire.

2.2.1.4 Decay

After a period of steady burning, most combustible material will be consumed and the burning rate starts to decrease. The fire will eventually die out when all combustible materials in the fire enclosure have been consumed.

2.2.2 Heat Release Model of Fire before Flashover

A simple way to describe the fire growth is to assume that the energy release rate increases as the square of time. By multiplying time squared by a factor α , various growth velocities can be simulated and the energy release rate as a function of time could be expressed as^[7]

$$Q = \alpha t^2 \quad (2.5)$$

where α is the fire growth factor in MW/s², which are 0.002931, 0.01127, 0.04689 and 0.1878 for the slow, medium, fast and ultra fast fire type respectively.

In many instances there is very scarce information available on the building contents. There is currently considerable ongoing activity internationally to give recommendations on such growth factors for various building types. As an example, Bukowski et al.^[8] give the growth rates according to occupancy types. For example, for a dwelling the fire growth rate is medium and for a hotel or nursing home the fire growth rate is fast.

The heat release rate will remain constant after it reaches a certain value Q_p till the burn up all combustible material in the fire room, as shown in Fig. 2.2^[9]. Assume the total calorific value of the combustible material is E , the fire duration time t_m is calculated through^[10]

$$t_m = \begin{cases} \left(\frac{3E}{\alpha}\right)^{1/3}, & E < E_1 \\ t_1 + \frac{E - E_1}{Q_p}, & E \geq E_1 \end{cases} \quad (2.6)$$

where

$$E_1 = t_1 Q_p / 3, \quad t_1 = \sqrt{\frac{Q_p}{\alpha}} \quad (2.7)$$

t_1 is the time when the heat release rate reaches maximum value Q_p .

2.2.3 Conditions Necessary for Flashover

There are certain pre-conditions necessary for flashover to occur, such as there must be sufficient fuel and ventilation for a growing fire to develop to a significant size, the ceiling must be able to trap hot gases and the geometry of the room must allow the radiant heat flux from the hot layer to reach critical ignition levels for the fuel items.

Drysdale^[6] gives a detailed discussion of these factors, with summaries of a number of compartment tests. In a typical room flashover occurs when the hot layer

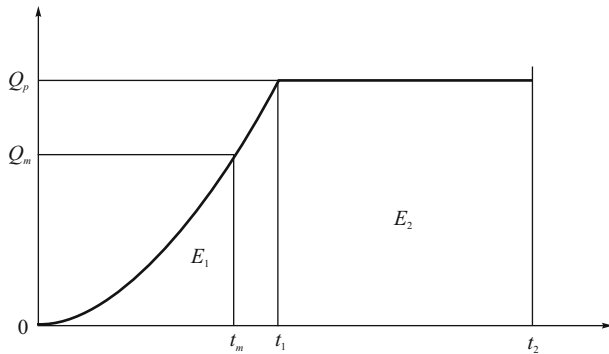


Fig. 2.2 Heat release rate at different burning time

temperature is about 600 °C resulting in a radiant heat flux of about 20 kW/m² at floor level.

From an analysis of a large number of experimental fires, it has been observed that flashover will only occur if the heat output from the fire reaches a certain critical value, related to the size of the ventilation openings. For a room with one window, the critical value of heat release is given by “Thomas’s flashover criterion”^[11] as

$$Q = 387A_v\sqrt{H_v} + 7.8A_t \quad (2.8)$$

where A_v is the area of window opening and calculated through

$$A_v = H_v B_b \quad (2.9)$$

2.2.4 Heat Release Rate of the Fire after Flashover

After flashover, the combustion will consume a large amount of oxygen. Hence, the ventilation will affect the heat release rate. The fire can be divided into a ventilation controlled fire and fuel controlled fire. Usually, the large space building fire is a fuel controlled fire.

For the compartment fire, if

$$\frac{A_v\sqrt{H_v}}{A_f} \geq 0.07 \quad (2.10)$$

the fire is a fuel controlled fire; otherwise it is a ventilation controlled fire^[12].

2.2.4.1 Heat Release Rate of Ventilation Controlled Fire

The heat release rate of a ventilation controlled fire depends on the dimension of the opening. Usually, it is supposed that all glass windows and glass doors will be

broken in a fire. The hot air goes out of the fire compartment and the cold air goes into the fire compartment.

The fire test shows that the wood burning rate in a compartment with one opening^[13,14] is

$$\dot{m} = 0.18A_v \sqrt{\frac{H_v W}{D}} (1 - e^{-0.036\Omega}) \quad (2.11)$$

and

$$\Omega = \frac{A_t - A_v}{A_v \sqrt{H_v}} \quad (2.12)$$

After obtaining \dot{m} , the heat release rate of a ventilation controlled fire is

$$Q_{vent} = \dot{m}\Delta H_c \quad (2.13)$$

2.2.4.2 Heat Release Rate of Fuel Controlled Fire

If the compartment is well ventilated, the compartment fire is a fuel controlled fire. The heat release rate depends on the fire area.

For a residential compartment, the fire duration is usually 1200 s^[15], hence the heat release rate can be calculated by

$$Q_{fuel} = E/1200 \quad (2.14)$$

However, in other kinds of compartments, the fire duration is not available. Drysdale^[6] brings forward the following equation to predicate the heat release rate

$$Q_{fuel} = \dot{q}_i A_f \Delta H_c / L_v \quad (2.15)$$

where \dot{q}_i takes the value of 0.07 MW/m². L_v takes a value of between 1.7 MJ/kg and 5.9 MJ/kg for wood and a value of between 1.2 MJ/kg and 3.7 MJ/kg for plastic.

2.2.5 Modeling of Compartment Fire

There are mainly two models for performing the simulation of an enclosure fire, which are the zone model and field model.

2.2.5.1 Zone Model

In the two zones model, a fire enclosure is divided into (a) an upper zone of hot smoke and (b) a lower zone of cold air^[16,17]. In the multi-zone model, the fire enclosure is divided into more than two zones. Each zone is assumed to have uniform properties, e.g. temperature and smoke concentration. Zone models are suited to most engineering applications where the geometry of the enclosure is not complicated and there is already a good qualitative understanding of the fire behavior. For post-flashover fire modeling which is of particular interest to structural fire engineering, the entire fire enclosure may be considered as one zone with the same temperature.

The controlling equation is formulated on the energy balance and mass balance in the fire enclosure, as shown in Fig. 2.3.

(a) Mass balance for the lower layer

$$m_L + m_{in} + m_p = 0 \quad (2.16)$$

(b) Conservation of energy for the hot layer yields

$$\dot{Q}_u = \dot{Q}_{in} - \dot{Q}_{loss} + m_p c_p T_a \quad (2.17)$$

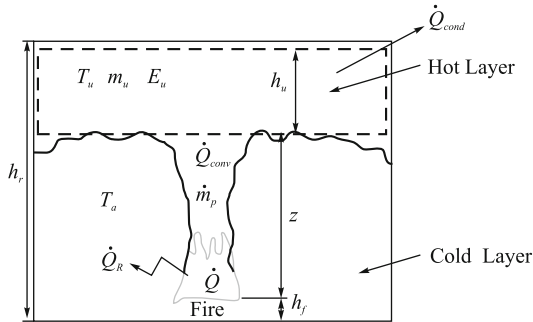


Fig. 2.3 Heat balance in a zone model

2.2.5.2 Field Model

Due to the complexity of the fire, zone models are suitable in only a few limited cases. For more precise fire modeling, Computational Fluid Dynamics (CFD) modeling can be used. In CFD modeling, the fire enclosure is divided into a large number of volumes. Partial differential equations of mass, momentum and energy transfer and conservation of species are written for each volume based on fundamental equations of fluid dynamics, thermodynamics, chemical reactions and mechanics. They are then numerically assembled for the entire fire enclosure. Appropriate initial boundary conditions are then applied to find numerical solutions to these equations. Clearly, CFD modeling is versatile and has the potential to give the most accurate and detailed results for a wide range of problems. Inevitably, CFD modeling requires specialist knowledge of fire modeling and has so far been mainly used for predicting the production and movement of smoke and toxic gases in pre-flashover fires at a given rate of heat release of the fire. Recently, CFD modeling has been extended to simulate flame spread and ignition^[18].

2.2.6 Empirical Modeling of Compartment Fire

The estimation of temperature in a compartment fire is an essential part of structural design for fire safety. The temperature in a fire enclosure at any time depends on the

balance between the heat released by the burning and the heat loss through opening by radiation and convection, and by conduction in the walls, floor and ceiling.

2.2.6.1 Dr. Zhong-Cheng Ma's model

Based on statistic analysis of the fire test results, Dr. Ma^[19] proposed an equation to calculate temperature in post-flashover fires

$$\frac{T_g - T_g(0)}{T_{gm} - T_g(0)} = \left[\frac{t}{t_m} e^{1-t/t_m} \right]^b \quad (2.18)$$

where b is a parameter. If $t \leq t_m$ then $b=0.8$, otherwise $b=1.6$.

The maximum temperature T_{gm} and the time t_m at which the temperature reaches its maximum value depends on the fire type.

(a) For a ventilation controlled fire

$$T_{gm} = 1240 - 13.37/\eta \quad (2.19)$$

and

$$t_m = \frac{0.11025G_0}{A_v\sqrt{H_v}} \quad (2.20)$$

where η is the opening factor and obtained through

$$\eta = \frac{A_v\sqrt{H_v}}{A_t} \quad (2.21)$$

(b) For the fuel controlled fire

$$\frac{T_{gm}}{T_{gmcr}} = \left(\frac{\eta_{cr}}{\eta} \right)^{1/2} \quad (2.22)$$

and

$$t_m = 1.5876 \frac{G_0}{A_f} \quad (2.23)$$

where

$$\eta_{cr} = 0.0697 \frac{A_f}{A_t} \quad (2.24)$$

$$T_{gmcr} = 1240 - 13.37/\eta_{cr} \quad (2.25)$$

The main parameters that affect the post-flashover fire enclosure temperature are all included in Dr. Ma's model. It can be accomplished by hand and is suitable for engineering practice. The comparison between test and simulation results is shown in Fig. 2.4. It can be seen that they agree very well with each other.

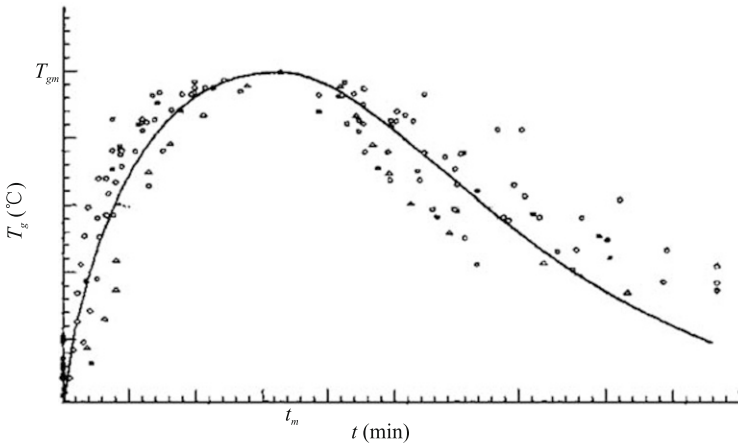


Fig. 2.4 Comparison of test and simulation results

2.2.6.2 ASCE Model

Based on the statistic analysis of fire test results and theoretical fire dynamic analysis, the ASCE^[20] gives an equation for ventilation controlled fire as

(a) The heating phase ($t < \tau$):

$$T_g = 250(10\eta)^{0.1/\eta^{0.3}} e^{-\eta^{t/30}} [3(1 - e^{-0.01t}) - (1 - e^{-0.05t}) + 4(1 - e^{-0.2t})] + C\left(\frac{600}{\eta}\right)^{0.5} \tag{2.26}$$

(b) The cooling phase ($t \geq \tau$):

$$T_g = T_\tau - 600\left(\frac{t}{\tau} - 1\right) \tag{2.27}$$

If the density of the lining material $\rho=1600 \text{ kg/m}^3$, $C=0.0$; and if $\rho < 1600 \text{ kg/m}^3$, $C=1.0$. τ is determined by

$$\tau = 0.18182 \frac{G_0}{A_v \sqrt{H_v}} \tag{2.28}$$

T_τ is calculated through Eq.(2.26) and η is calculated through Eq.(2.21).

ASCE fire model^[20] mainly deals with a ventilation controlled fire. Compared with Dr. Ma’s model^[19], the ASCE model considers effects of properties of the lining material and the time for the fire to reach its maximum temperature is longer when based on the ASCE model than on Dr. Ma’s model.

2.2.6.3 Swedish Curves

The most widely referenced time-temperature curves for real fire exposure are those of Magnusson and Thelandersson^[21]. These are often referred to as the “Swedish”

fire curves. They are derived from heat balance calculations, using Kawagoe's equation^[22] for the burning rate of ventilation controlled fires. Each group of curves is for a different ventilation factor, with fuel load as marked. Note that the unit of the fuel load is MJ per square meter of total surface area (not MJ per square meter of floor area, which is more often used in design calculations).

2.2.6.4 Eurocode Parametric Fires

The EC1^[3] gives an equation for a parametric fire, allowing a time-temperature relationship to be produced for any amount of fuel load, ventilation openings, wall lining materials, etc. The Eurocode parametric curves have been derived to give a good approximation to the burning period of the Swedish curves.

The Eurocode equation to determine fire temperature T_g for burning period ($t^* \leq t_h^*$) is

$$T_g = 1325 \left[1 - 0.324e^{-12t^*} - 0.204e^{-102t^*} - 0.472e^{-1140t^*} \right] \quad (2.29)$$

and for the decay period ($t^* > t_h^*$)

$$T_g = \begin{cases} T_{gm} - 10.417(t^* - t_h^*), & t_h^* < 30 \text{ min} \\ T_{gm} - 4.167(3 - t_h^*/60)(t^* - t_h^*), & 30 \text{ min} \leq t_h^* < 120 \text{ min} \\ T_{gm} - 4.167(t^* - t_h^*), & t_h^* > 120 \text{ min} \end{cases} \quad (2.30)$$

where t^* is a fictional time given by

$$t^* = \Gamma * t \quad (2.31)$$

t is the fire duration time and obtained through

$$\Gamma = \left(\frac{\eta / \sqrt{\lambda \rho c}}{0.04 / 1160} \right)^2 \quad (2.32)$$

$\sqrt{\lambda \rho c}$ is the thermal inertia in $\text{J}/(\text{m}^2 \cdot \text{s}^{1/2} \cdot \text{K})$. t_h^* is the duration of the burning phase given by

$$t_h^* = 7.8 \times 10^{-3} \left(\frac{A_f}{A_t} q \right) \Gamma / \eta \quad (2.33)$$

The most suitable condition for Eq.(2.29) is $0.02 \leq \eta \leq 0.2$ and $1000 \leq \sqrt{\lambda \rho c} \leq 2000$.

2.2.6.5 Comparison of Fire Enclosure Temperature-time Curves

Fig. 2.5 compares the temperature-time curves based on the above models. Dr. Ma's model gives a more rapid growth rate and decay rate of the fire than other models.

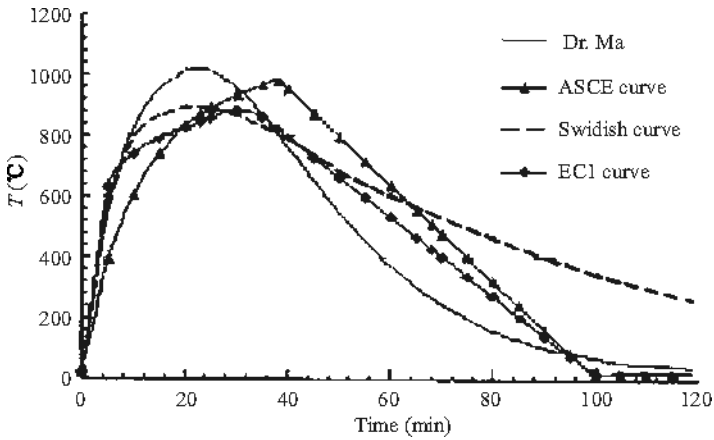


Fig. 2.5 Comparison of fire enclosure temperature-time curves with $\eta=0.06 \text{ m}^{1/2}$, $\sqrt{\lambda \rho c}=1500 \text{ J}/(\text{m}^2 \cdot \text{s}^{1/2} \cdot \text{K})$, $A_f=16 \text{ m}^2$, $A_r=64 \text{ m}^2$, $q=50 \text{ kg}/\text{m}^2$ and $\rho=2000 \text{ kg}/\text{m}^3$

2.3 Large Space Building Fire

2.3.1 Characteristics of Large Space Building

According to the building function, there are three kinds of large space buildings:

- with a very large floor area but low height, such as supermarket, industrial workshop. The floor area can be from several to tens of thousands of square meters and the ceiling height is usually lower than 6 m;
- with both a large floor area and height, such as an auditorium, exhibition hall, theater, gymnasium and warehouse. The floor area is usually from several to tens of hundreds of square meters and the ceiling height is usually from ten to twenty meters;
- with a small floor area but very great height, such as an atrium. The floor area is usually only several hundred square meters but the height can be tens of meters.

On account of restrictions of the building function, the large space building cannot be divided into several fire compartments. The total quantity of combustible material is large in these buildings and the rise of the fire plume and air entrainment into the fire plume is without any restriction.

2.3.2 Characteristics of Large Space Building Fire

The characteristics of a large space building fire are very different from the compartment fire in the following aspects

- the fire is hard to detect by an automatic fire detection system. The automatic fire detection system includes the smoke detection system and temperature detection

system, which are usually installed on the ceiling. However, for the large space building fire, the density and temperature of smoke are diluted and reduced a lot before reaching the ceiling, which cannot activate the detector;

- the sprinkler system is unable to work. For the large space building with a ceiling higher than 20 m, the smoke temperature cannot activate the sprinkler and, on the other hand, the water sprayed by a sprinkler installed on the ceiling cannot reach the fire from such a long distance;
- it is difficult to evacuate. The public large space building contains a large number of people and these people are not well organized, such as in a theater or gymnasium. When a fire happens, it is very difficult to evacuate;
- the damage to the structure can cause great damage. In a large space building, collapse and damage to the structure can cause great loss of life and property.

2.3.3 Simulation of Large Space Building Fire using Zone Model

2.3.3.1 Theoretical Formulations

The fire in a large space building is localized and there is usually no flashover in a large space building fire. Hence, the fire can be simulated by the zone model, as shown in Fig. 2.6.

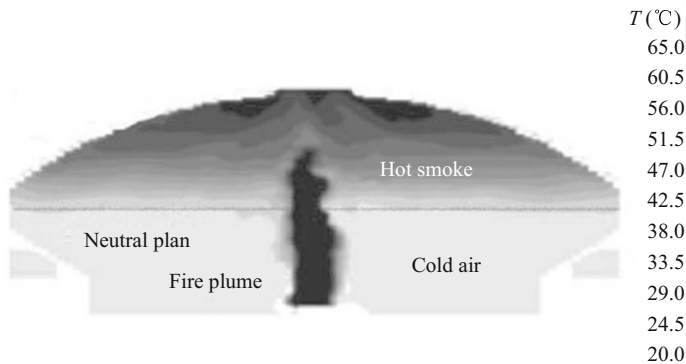


Fig. 2.6 Simulation of large space building fire using zone model

In the zone model, the space in the building is divided into two uniform layers^[23]. For the upper layer, the energy conservation equation is governed by

$$\frac{d(Z_u A \rho_u T_u C_p)}{dt} = Q_c + m C_p T_0 \quad (2.34)$$

and we assume the hot smoke layer is ideal gas, which gives

$$\rho_u T_u = \rho_0 T_0 \quad (2.35)$$

Notice that

$$\frac{dZ_u}{dt} = -\frac{dZ}{dt} \quad (2.36)$$

so Eq.(2.34) can be reformulated as

$$-(A\rho_0 C_p T_0) \frac{dZ}{dt} = Q_c + mC_p T_0 \quad (2.37)$$

where ρ_0 is the density of the air at ambient temperature and takes the value of 1.2 kg/m³, C_p is the specific heat of the smoke and takes the value of 1.004 kJ/(kg·°C), Q_c is the convection heat and $Q_c = 0.7Q$.

According to the fire test of Zukoski^[23] on an axis-symmetric plume fire, when the fire heat release rate is constant $Q=Q_0$, the height Z of the bottom of the smoke layer the above floor is determined by

$$Z = \left[0.12 \left(\frac{gQ_0}{\rho_0 C_p T_0 A^3} \right)^{1/3} t + H^{-2/3} \right]^{-3/2} \quad (2.38)$$

When the fire heat release rate is increased by t square, Eq.(2.37) can be reformulated as

$$Z = \left[0.075 \left(\frac{g\alpha}{\rho_0 C_p T_0 A^3} \right)^{1/3} t^{5/3} + H^{-2/3} \right]^{-3/2} \quad (2.39)$$

Based on the test result^[11], the mass release rate for persistent flame, intermittent flame and buoyant plume is calculated by

$$m = \begin{cases} 0.011Q_c \left(\frac{Z}{Q_c^{0.4}} \right)^{0.566}, & 0 \leq \frac{Z}{Q_c^{0.4}} < 0.08 \\ 0.026Q_c \left(\frac{Z}{Q_c^{0.4}} \right)^{0.909}, & 0.08 \leq \frac{Z}{Q_c^{0.4}} < 0.2 \\ 0.124Q_c \left(\frac{Z}{Q_c^{0.4}} \right)^{1.895}, & 0.2 \leq \frac{Z}{Q_c^{0.4}} \end{cases} \quad (2.40)$$

If the heat transfer between the hot smoke and the wall is not considered, the temperature of the fire plume can be obtained by the first law of thermodynamics as

$$T_p = T_\alpha + \frac{Q_c}{m.C_p} \quad (2.41)$$

The temperature of the upper smoke layer will heat the load bearing structural component of the building. It is the most important parameter for the structural fire safety engineer. The smoke temperature can be obtained by

$$T_s = -273 + \frac{(T_{s0} + 273)M_{s0} + (T_p + 273)m\Delta t}{M_s} \quad (2.42)$$

and

$$M_s = M_{s0} + m\Delta t \quad (2.43)$$

Using Eq.(2.40) and Eq.(2.41), the temperature-time relationship of a large space building fire can be calculated by Eq.(2.42) through incremental approach.

2.3.3.2 Simulation Results

Fig. 2.7 and Fig. 2.8 illustrate the smoke temperature and smoke layer height of large space building fires simulated using the zone model and field model, respectively. The floor area of the building is 1000 m^2 , the ceiling height is 6 m, the heat release rate of the fire is 25 MW and the fire growth factor $\alpha=0.04689 \text{ kW/s}^2$.

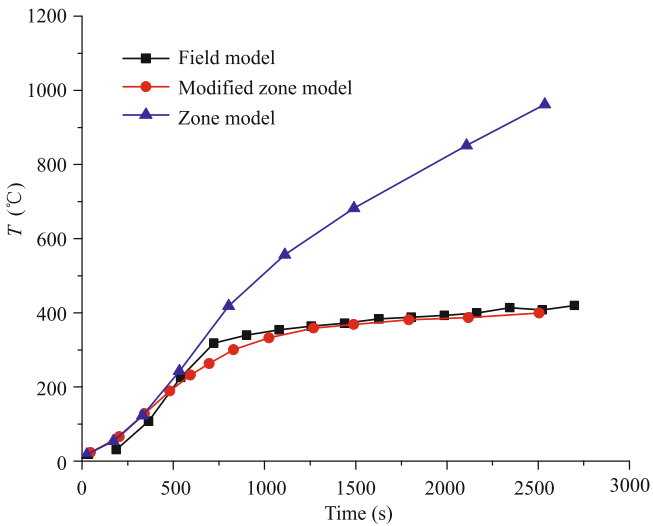


Fig. 2.7 Temperature of upper smoke layer

From Fig. 2.7, it can be seen that the smoke temperature based on the zone model agrees well with that of the field model at the growth phase. However, when the clearance height below the smoke layer is lower than $0.2H$, the smoke temperature calculated by the zone model is much higher than the field model. That means when 80% of the building space is filled by hot smoke, the equation for the zone model is not applicable, and the temperature based on the zone model is not precise. Hence, for a large space building fire, the zone model should be modified for calculating the smoke temperature^[24].

2.3.3.3 Modification of the Zone Model

Temperatures based on the zone model and field model for buildings with different dimensions and heat release rates are compared. Parameters of the fire condition for comparison are

- fire growth factor α is 0.04689 kW/s^2 ;
- simulation time is 45 min and
- heat release rates Q are 2000 kW, 5000 kW and 25000 kW, respectively.

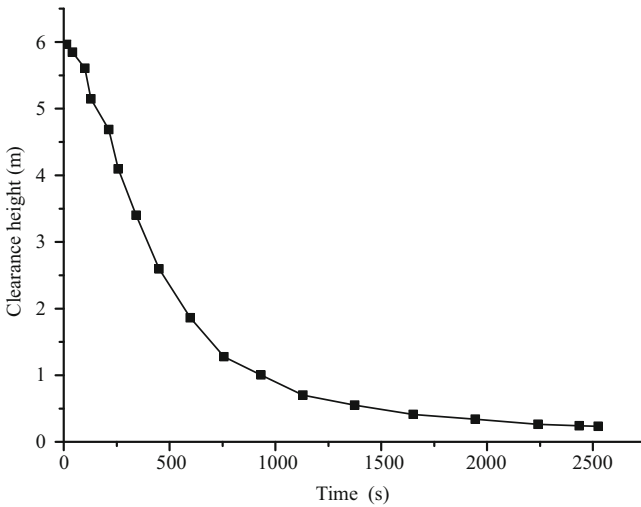


Fig. 2.8 Clearance height below the smoke layer

The temperature of the fire plume is calculated^[23] by

$$T_p = T_\alpha + T_Q = T_\alpha + \frac{Q_c}{mc_p} \tag{2.44}$$

where T_Q is the temperature difference between the fire plume and the surrounding temperature.

In order to account for the heat loss of the fire plume before entering the smoke layer, the fire plume temperature should be modified by

$$T'_{Q(n)} = T_{Q(n)} / (k_0 + \frac{k_1 n \Delta t}{10}) \tag{2.45}$$

where k_0 and k_1 are fire power dependent parameters and calculated by^[25]

(1) For the fire with power Q of 2 MW^[23]:

$$\begin{aligned} k_0 &= (2.0809 + 0.02974H^{1.5} - 0.2477\ln A)^{-1} \\ k_1 &= -0.0079 + 0.2331H^{-1} + 28.185A^{-1} - 0.7508H^{-2} \\ &\quad - 9618.2A^{-2} + 9.0767(HA)^{-1} \end{aligned} \tag{2.46}$$

(2) For the fire with power Q of 5 MW^[23]:

$$\begin{aligned} k_0 &= \exp(-4.1396 - 15.215H^{-0.5} + 32.205 \frac{\ln H}{H} + 0.0248A^{0.5}) \\ k_1 &= -0.0071 + 0.015\ln H + 19.947A^{-1} - 0.00336(\ln H)^2 \end{aligned} \tag{2.47}$$

(3) For the fire with power Q of 25 MW^[23]:

$$\begin{aligned}
 k_0 &= \exp\left(0.9719 + 27.287 \frac{H}{\ln H} - 78.753H^{0.5} \right. \\
 &\quad \left. + 55.421 \ln H + 0.0018 \frac{A}{\ln A} \right) \\
 k_1 &= \exp\left(-3.716 + 362.37H^{-1.5} - 354.9 \frac{\ln H}{H^2} \right. \\
 &\quad \left. - 223.1H^{-2} + 0.0086A^{0.5} \ln A - 0.1A^{0.5} \right)
 \end{aligned} \tag{2.48}$$

and the applicable range of the above equations for k_0 and k_1 are

- the floor area A is from 500 to 6000 m² and
- building height H is from 4 to 20 m.

The growth factor of the fire α only affects the fire growth rate and has little influence on the fire temperature. So equations for the fire with $\alpha=0.04689$ kW/s² can be used for other fires.

The smoke temperature calculated by the modified zone model is shown in Fig. 2.7. It can be seen that it agrees very well with the temperature obtained by the field model.

2.3.4 Characteristics of Large Space Building Fire

2.3.4.1 Simplification of Temperature Field of Large Space Building Fire

To investigate characteristics of a large space building fire, the field model may be employed. Obviously, the temperature distribution may be assumed to be asymmetric around the fire origin in a large space building fire. So the temperature field $T_{(x,y,z,t)}$ can be simplified by $T_{(x,r,t)}$ (Fig. 2.9), where r is the distance between the point studied and the fire origin.

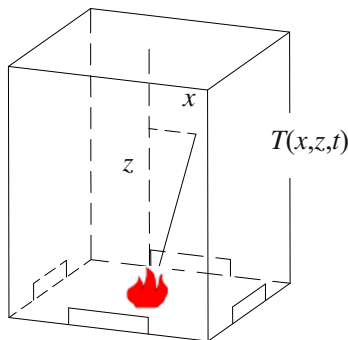


Fig. 2.9 Simplified field model

2.3.4.2 Smoke Temperature of Large Space Building Fire

The smoke temperature is expressed by

$$T = \alpha(1 - be^{-\lambda t}) \text{ and } a < 0, b > 0, \lambda > 0 \quad (2.49)$$

The first derivative of Eq.(2.49) is

$$\frac{dT}{dt} = ab\lambda e^{-\lambda t} \quad (2.50)$$

The smoke temperature $T(t)$ will be constant when $t \rightarrow \infty$ is

$$\lim_{t \rightarrow \infty} T = a \quad (2.51)$$

2.3.4.3 Parameters that affect the Large Space Building Fire

Parameters that may affect the large space building fire are (a) maximum heat release rate, (b) floor area, (c) building height and (d) distance to the fire origin.

Fig. 2.10 to Fig. 2.13 show effects of heat release rate, floor area, building height and distance to the fire origin on the smoke temperature of a large space building fire^[26]. It can be seen that

- (a) with the increase in the power of fire, the maximum smoke temperature in a steady state is higher;
- (b) with the increase in the floor area, the maximum smoke temperature in a steady state is lower;
- (c) with the increase in the building height, the maximum smoke temperature in a steady state is lower and
- (d) with the increase in the horizontal distance to the fire origin, the maximum smoke temperature in a steady state is lower.

2.3.4.4 Practical Calculation Method for Smoke Temperature of Large Space Building fire

Through curve fitting of 120 simulation results, for a large space building fire with different fire power, floor area, building height, and horizontal distance to fire origin, a formula to calculate the smoke temperature of a large space building fire is proposed^[27]:

$$T_{(x,r,t)} - T_{g(0)} = T_z(1 - 0.8e^{-\beta t} - 0.2e^{-0.1\beta t}) \left[\eta + (1 + \eta)e^{-\frac{x-b}{\mu}} \right] \quad (2.52)$$

where T_z is the smoke temperature at height z above the fire origin (see Appendix A), β is a parameter for accounting the effect of the fire power and fire growth type (see Appendix A), η is the reduction factor of the smoke temperature at a distance x horizontally (see Appendix A), b is the distance from the fire origin to the fire boundary and if $x < b$, then $\eta = 1$ and μ is a parameter (see Appendix A).

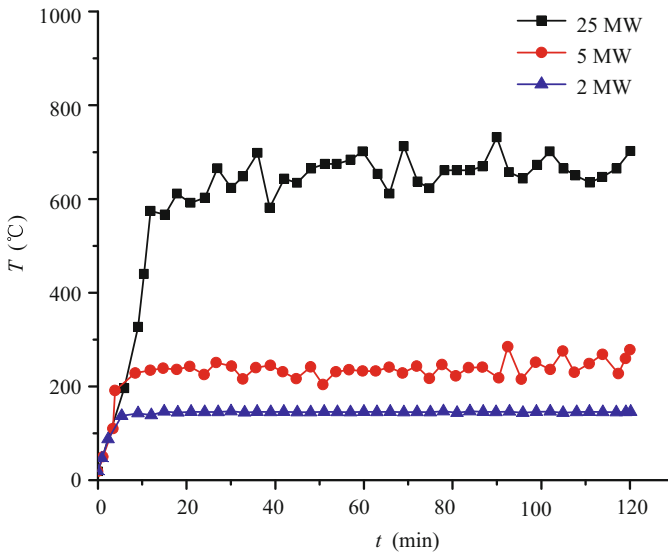


Fig. 2.10 Smoke temperature for a large space building fire with fires of different intensities

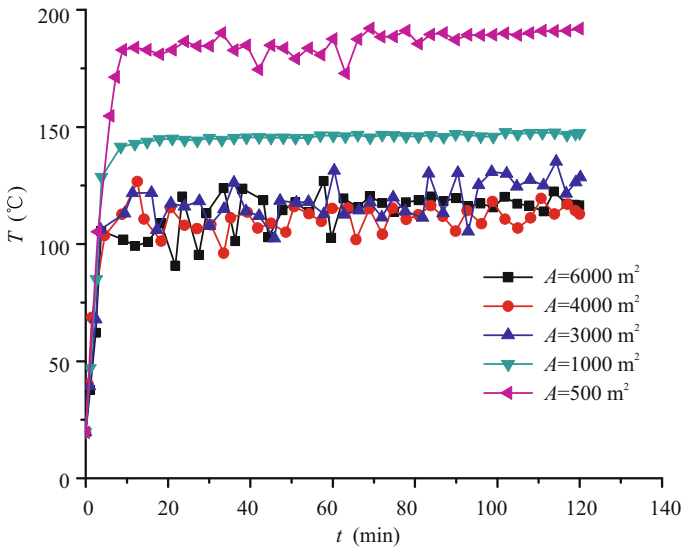


Fig. 2.11 Smoke temperature for a large space building fire with different floor areas

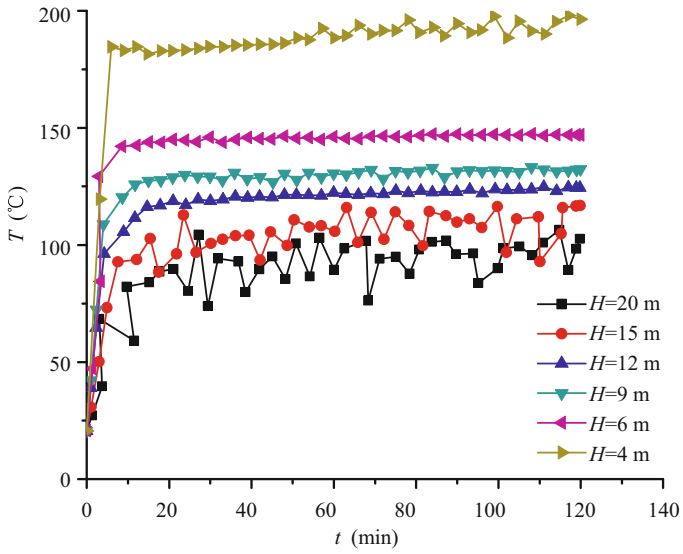


Fig. 2.12 Smoke temperature for a large space building fire with different building heights

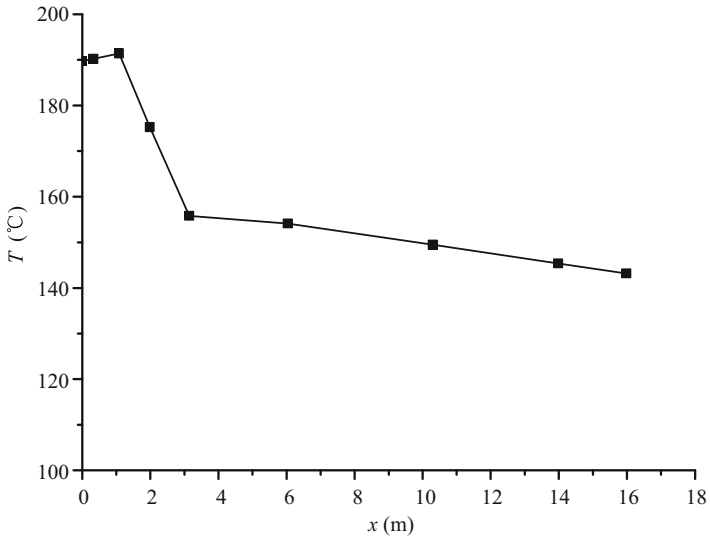


Fig. 2.13 Smoke temperature for a large space building fire with different horizontal distances to the fire origin

The fire power can be calculated by

$$Q = q_s A \quad (2.53)$$

where q_s is the fire power per square meter determined by Table 2.2.

Table 2.2 Fire power per square meter

Occupancy	q_s (kW/m ²)
Exhibition hall	100
Office building	250
Shopping center	500

The fire power Q can also be determined through Table 2.3 or Table 2.4^[4].

Table 2.3 Fire power in different buildings (MW)

Occupancy type	Fire power Q
Shopping center with sprinkler	5
Office building and hotel bedroom with sprinkler	1.5
Public building with sprinkler	2.5
Car park with sprinkler	1.5
Supermarket and Warehouse with sprinkler	4
Atrium with sprinkler	1
Office building and hotel bedroom without sprinkler	6
Car park without sprinkler	3
Atrium without sprinkler	4
Supermarket and Warehouse without sprinkler	20

2.4 Standard Fire and Equivalent Exposure Time

2.4.1 Standard Fire

In order to make the test results compatible, the structural component should be tested under the same fire conditions. Many countries published standard time-

Table 2.4 Fire power with different fire power grade (MW)

Fire power grade	Fire power Q
Small	< 3.5
Medium	3.5 – 15
Large	> 15

temperature curves for fire testing and structural fire resistance rating. The ISO834 standard time-temperature curve^[28] is used in China, which is determined using the following equation as

(a) In the heating phase ($t \leq t_h$)

$$T_g - T_g(0) = 3451g(8t + 1) \quad (2.54)$$

(b) In the cooling phase ($t > t_h$)

$$\frac{dT_g}{dt} = \begin{cases} -10.417, & t_h < 30 \text{ min} \\ -4.167(3 - t_h/60), & 30 \text{ min} \leq t_h < 120 \text{ min} \\ -4.167, & t_h \geq 120 \text{ min} \end{cases} \quad (2.55)$$

where t_h is the duration of the heating phase given by

$$t_h = 7.8 \times 10^{-3} (q \frac{A_f}{A_r}) / \eta \quad (2.56)$$

In the United States and Canada the ASTM-E119 standard time-temperature curve^[20] is used. The fire temperature is calculated by

$$T_g - T_g(0) = 1166 - 532e^{-0.01t} + 186e^{-0.05t} - 820e^{-0.2t} \quad (2.57)$$

Harmathy^[29] found that the ASTM-E119^[20] standard fire results in greater damage than the ISO834 standard fire^[28].

2.4.2 Equivalent Exposure Time

Despite having many limitations using the standard fire exposure, it also has some advantages over using realistic fire exposure

- The standard fire exposure concept has a long history and is familiar to those concerned with fire safety. The fact that building structures rarely fail in fires as a result of adequate specification of the standard fire resistance indicates that it is safe to use the standard fire curve.
- A large body of knowledge has been obtained from many years of standard fire resistance tests but little data exists for realistic fires.

- The standard fire curve has only one temperature-time relationship. In design calculations, it is much easier to deal with only one standard fire curve than with an infinite number of real fire curves.

Recently, attempts have been made to link realistic fires to the standard fire through the use of equivalent time. The equivalent time for a realistic fire is the time of exposing a construction element to the standard fire that would give the same effect as the realistic fire. It is important to select the appropriate “effect” to be compared.

Using the temperature rise in a construction element as an example, the equivalent time concept is illustrated in Fig. 2.14.

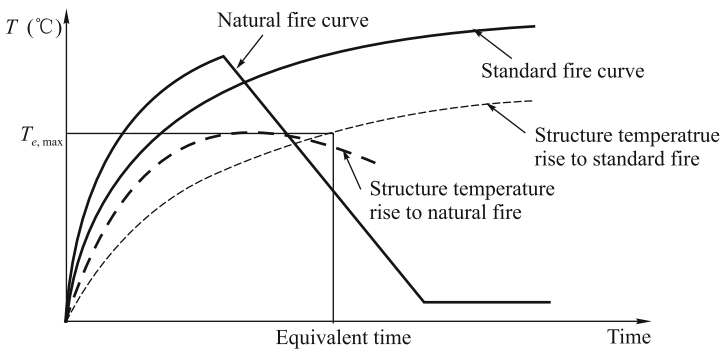


Fig. 2.14 Equivalent time concept

Harmathy^[30] and Eurocode 1^[3] also contain an equation for the equivalent time. Law’s equation^[14] was developed based on temperatures attained in insulated steel work. It is given by

$$t_{eqv} = K' \frac{L_f}{\sqrt{A_v A_T}} \tag{2.58}$$

where L_f is the total fire load in kg wood and K' is a constant whose value is close to unity. The equivalent time t_{eqv} is given in minutes.

In Eurocode 1^[3], the equivalent time is given by

$$t_{eqv} = q_{f,d} k_b w_f k_c \tag{2.59}$$

where $q_{f,d}$ is the design fire load density per floor area, w_f is the ventilation factor. In small compartments without horizontal opening, w_f is given by

$$w_f = \frac{A_f}{A_r} \frac{1}{\sqrt{O}} \tag{2.60}$$

O is the ventilation factor defined as

$$O = \frac{A_v \sqrt{h_v}}{A_t} \quad (2.61)$$

k_c is a modification factor intended to account for different types of construction. For the protected steelwork $k_c=1.0$ and for unprotected steelwork $k_c=13.70$. k_b is a conversion factor to account for the influence of fire enclosure linings and determined through Table 2.5^[3].

Table 2.5 Values of k_b for calculating the equivalent time

$b = \sqrt{k\rho C}$ (J/(m ² · s ^{1/2} · K))	k_b (min · m ² /MJ)
$b > 2500$	0.04
$720 \leq b \leq 2500$	0.055
$b < 720$	0.07

Due to simplicity, the concept of equivalent time is an attractive proposal, being easy to use and able to reflect the main effects of realistic fires. However, due to fundamental shortcomings in the approach, its limits of application should be clearly understood and the equivalent time equations should be used with extreme caution.

References

- [1] G. Q. Li, L. H. Han, G. B. Lou, and S. C. Jiang. *Steel and Steel-Concrete Composite Structures Fire Resistance Design*. China Architecture & Building Press, 2006.
- [2] CIB W14 Workshop. Design guide structural fire safety. *Fire Safety Journal*, 10(2):75–137, 1986.
- [3] European Committee for Standardisation. *Eurocode 1: Actions on Structures C Part 1-2: General Actions on Structures Exposed to Fire*. European Committee for Standardisation, 2009.
- [4] British Standard Institute. *Components for Smoke and Heat Control Systems. Functional Recommendations and Calculation Methods for Smoke and Heat Exhaust Ventilation Systems, Employing Steady-State Design Fires*. British Standard Institute, 2003.
- [5] B. Karlsson and J. G. Quintiere. *Enclosure Fire Dynamics*. CRC Press, 2000.
- [6] D. Drysdale. *An Introduction to Fire Dynamics, Second Edition*. John Wiley and Sons, 2007.
- [7] National Fire Protection Association. *Guide for Smoke and Heat Venting*. National Fire Protection Association, 1985.
- [8] R. W. Bukowski, F. B. Clarke III, J. R. Hall Jr, and S. W. Steifel. *Risk Assessment Method: Description of Methodology*. National Fire Protection Association, 1990.

- [9] A. H. Buchanan. *Structural Design for Fire Safety*. John Wiley & Sons, Ltd., 2001.
- [10] V. Babrauskas. Specimen heat fluxes for bench scale heat release rate testing. *Fire and Materials*, 19(2):243–252, 1995.
- [11] W. D. Walton and P. H. Thomas. *Estimating Temperatures in Compartment Fires*. SFPE Handbook of Fire Protection Engineering, Society of Fire Protection Engineers, USA, 1995.
- [12] T. Tanaka, M. Sato, and T. Wakamatsu. Simple formula for ventilation controlled fire temperatures. *Fire Science and Technology*, 17(1):15–27, 1997.
- [13] P. H. Thomas and A. J. M. Heselden. *Fully Developed Fires in Single Compartments*. A Co-operative Research Programme of the Conseil International du Batiment, Fire Research Note 923/1972, Joint Fire Research Organization, 1972.
- [14] M. Law. A basis for the design of fire protection of building structures. *Structural Engineer*, 61(1):25–33, 1983.
- [15] A. H. Buchanan. Modelling post-flashover fires with fast lite. *Journal of Fire Protection Engineering*, 9(3):1–11, 1997.
- [16] J. F. Cadorin and J. M. Franssen. A tool to design steel elements submitted to compartment fires—ozone v2-part 1: pre and post flashover compartment fire model. *Fire Safety Journal*, 36(5):395–427, 2003.
- [17] J. F. Cadorin, D. Pintea, J. C. Dotreppe, and J. M. Franssen. A tool to design steel elements submitted to compartment fires—ozone v2. part 2: Methodology and application. *Fire Safety Journal*, 36(5):429–451, 2003.
- [18] Z. Yan and G. Holmstedt. Cfd and experimental studies of room fire growth on wall lining materials. *Fire Safety Journal*, 27(3):201–238, 1996.
- [19] Z. C. Ma, B. Wu, and J. P. Ou. Fully developed compartment fire model. *Journal of Harbin University of Civil Engineering and Architecture*, 32(1):16–24, 1998.
- [20] Amer Society of Civil Engineers. *Structural Fire Protection (Asce Manual and Reports on Engineering Practice) (No. 78)*. Amer Society of Civil Engineers, 1992.
- [21] S. E. Magnusson and S. Thelandersson. *Temperature-Time Curves of Complete Process of Fire Development*. Acta Polytechnica Scandinavica, Civil Engineering and Building Construction Series, No. 65, Stockholm, 1970.
- [22] K. Kawagoe. *Fire Behavior in Rooms*. Report No. 27, Building Research Institute, Japan, 1958.
- [23] Y. Du. *A Practical Approach for Fire Resistance Design of Large Space Building Grid Structures*. PhD thesis, Tongji University, 2007.
- [24] Y. Du, G. Q. Li, and J. Q. Huang. Comparison of calculation models for smoke temperature in fire of large space building. *Journal of Natural Disasters*, 6, 2007.
- [25] J. Q. Huang, G. Q. Li, and Y. Du. The revision of two-zone fire model calculating the air temperature in large space buildings. *Fire Science and Technology*, 3, 2005.

- [26] G. Q. Li and Y. Du. Analyses the parameters of fire temperature elevation at the top of large space buildings. *Fire Science and Technology*, 1, 2005.
- [27] G. Q. Li and Y. Du. Utility temperature elevation empirical formula in large space fire. *Fire Science and Technology*, 3, 2005.
- [28] International Organization for Standardization. *Fire-Resistance Tests – Elements of Building Construction, Part 1: General Requirements*. International Organization for Standardization, 1999.
- [29] T. Z. Harmathy and M. A. Sultan. Correlation between severities of the ASTM E119 and ISO 834 fire exposure. *Fire Safety Journal*, 13, 1988.
- [30] T. Z. Harmathy and J. R. Mehaffey. The normalized heat load concept and its use. *Fire Safety Journal*, 12, 1987.

Properties of Steel at Elevated Temperatures

For structural fire engineering, two sets of data are very important which are

- the material thermal properties for thermal analysis of structural components, including the thermal conductivity, specific heat, density;
- the material mechanical properties for structural analysis, including the yield strength, Young's modulus, stress-strain relationship and the expansion coefficient.

This chapter describes the thermal and mechanical properties of structural steel, fire-resistant steel, high-strength steel and stainless steel at high temperature.

3.1 Thermal Properties of Structural Steel at Elevated Temperatures

3.1.1 Conductivity

The conductivity in $W/(m \cdot ^\circ C)$ or $W/(m \cdot K)$ is the property of a material representing its ability to conduct heat. EC3^[1] and EC4^[2] give the following equation for λ_s

(a) For $20^\circ C \leq T \leq 800^\circ C$

$$\lambda_s = 54 - 3.33 \times 10^{-2} T_s \quad (3.1)$$

(b) For $800^\circ C < T \leq 1200^\circ C$

$$\lambda_s = 27.3 \quad (3.2)$$

BS5950 Part 8^[3] gives the following temperature independent equation for λ_s as

$$\lambda_s = 37.5 \quad (3.3)$$

The temperature dependent thermal conductivity described by BS5950^[3] is

$$\lambda_s = 52.57 - 1.541 \times 10^{-2}T_s - 2.155 \times 10^{-5}T_s^2 \quad (3.4)$$

The Japan Building Synthetic Fire Prevention Design^[4] gives the following equation

$$\lambda_s = 52.08 - 5.05 \times 10^{-5}T_s^2 \quad (3.5)$$

The China Technical Code for Fire Safety of Steel Structures in Buildings^[5] also gives a temperature independent thermal conductivity of steel is

$$\lambda_s = 45.0 \quad (3.6)$$

The comparison of above equations by Li et al.^[6] is shown in Fig. 3.1. In the temperature range of 0 °C through 600 °C, the average value of λ_s is very close to 45 W/(m·°C), and in the temperature range of 200 °C to 800 °C, the average value of λ_s is very close to 37.5 W/(m·°C). Usually, the critical temperature of the structural component is in the temperature range of 300 °C to 600 °C, hence the thermal conductivity taking a value of 45 W/(m·°C) is reasonable.

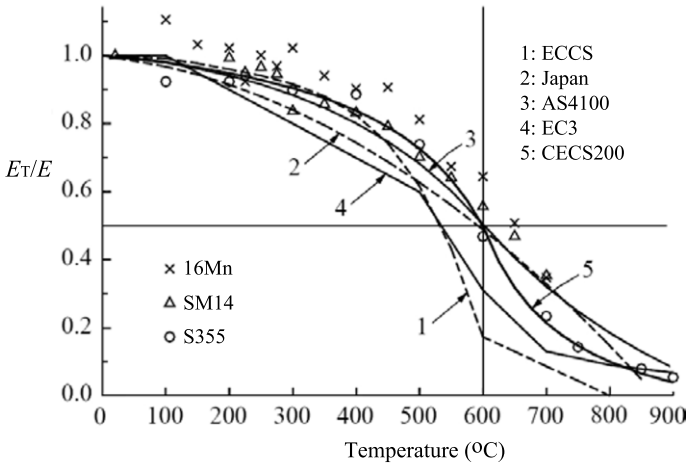


Fig. 3.1 Conductivity of steel proposed by different design codes

3.1.2 Specific Heat

Specific heat C_s in J/(kg·°C) or J/(kg·K) is the heat required or released to increase or decrease by 1 °C by a unit quantity of material.

EC3^[1] and EC4^[2] suggested that the specific heat of steel is taken as

(a) For $20\text{ °C} \leq T \leq 600\text{ °C}$

$$C_s = 425 + 7.73 \times 10^{-1}T_s - 1.69 \times 10^{-3}T_s^2 + 2.22 \times 10^{-6}T_s^3 \quad (3.7)$$

(b) For $600\text{ }^{\circ}\text{C} \leq T \leq 735\text{ }^{\circ}\text{C}$

$$C_s = 666 - \frac{13302}{T_s - 738} \quad (3.8)$$

(c) For $735\text{ }^{\circ}\text{C} \leq T \leq 900\text{ }^{\circ}\text{C}$

$$C_s = 545 + \frac{17820}{T_s - 731} \quad (3.9)$$

(d) For $900\text{ }^{\circ}\text{C} \leq T \leq 1200\text{ }^{\circ}\text{C}$

$$C_s = 650 \quad (3.10)$$

For simplifying the calculation, the specific heat of steel can take a constant value as

$$C_s = 600 \quad (3.11)$$

BS5950^[3] gives the following value for the specific heat as

$$C_s = 520 \quad (3.12)$$

The Annex of ECCS^[7] gives the following temperature dependent equation for the specific heat as

$$C_s = 470 + 20 \times 10^{-2} T_s + 38 \times 10^{-5} T_s^2 \quad (3.13)$$

The Japan Building Synthetic Fire Prevention Design^[4] gives the following equation for the specific heat as

$$C_s = 483 + 8.02 \times 10^{-4} T_s^2 \quad (3.14)$$

The China Technical code for fire safety of steel structures in buildings^[5] gives the temperature independent thermal conductivity as

$$C_s = 600 \quad (3.15)$$

Specific heats calculated by above equations^[6] are shown in Fig. 3.2. It can be seen that the specific heat of steel changes greatly with the elevation in temperature. In the temperature range of $0\text{ }^{\circ}\text{C}$ to $600\text{ }^{\circ}\text{C}$, the average value of specific heat is about $600\text{ J}/(\text{kg}\cdot^{\circ}\text{C})$. Taking the specific heat as a temperature independent value does not agree with the facts. However, it can greatly simplify the calculation and can be easily used by the engineer.

3.1.3 Density

The density of steel may be taken as its ambient value of $7850\text{ kg}/\text{m}^3$ over the normally experienced temperature range in a building fire.

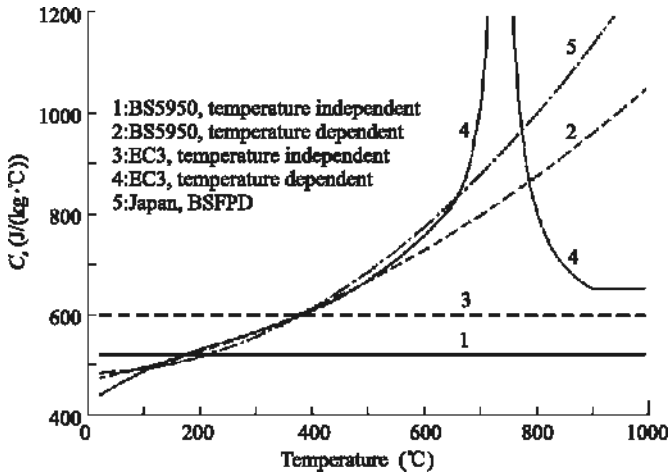


Fig. 3.2 Conductivity of steel proposed by different design codes

3.2 Mechanical Properties of Structural Steel at High Temperature

In order to determine the structural response subjected to fire, it is necessary to formulate constitutive laws for steel at elevated temperatures. A complete formulation is required only where a full analysis is undertaken.

3.2.1 Test Regimes

The mechanical property test is usually carried out by using a steady-state testing regime and the structural component fire test is usually carried out by using a transient-state testing regime.

3.2.1.1 Steady State Test

In the steady state test, the specimen is heated to a pre-determined temperature before the test and kept constant during the test. The stress-strain relationship of steel at a specific temperature can be obtained directly. Usually, in a building fire the temperature keeps changing. The steady state test is not representative of the actual fire scenario.

3.2.1.2 Transient State Test

In the transient state test, the specimen is loaded to a pre-determined stress level before test, then it is heated to failure at a specific heating rate. Usually, the heating rate is in a range of 5–50 °C/min^[8]. The thermal expansion should be obtained first

and subtracted from the total strain to determine the strain caused by stress. The transient state test represents the real situation of a structure in a fire. However, the test result includes the creep strain and relaxation of steel.

Kirby and Preston^[9] compared steady state test results and transient state test results and found that strength of steel obtained by the steady state test was higher than the transient state test.

3.2.2 Definition of Yield Strength at High Temperature

Owing to large strains exhibited at elevated temperatures in fire affected members, it is more usual to quote the 1.0% or 2.0% proof stress rather than the conventional ambient value of 0.2% proof stress. Some proposals are as follows:

- ECCS^[7] suggests that when the temperature is higher than 400 °C, the 0.5% proof stress is used to determine the yield strength; when the temperature is lower than 400 °C, the proof stress is interpolated linearly between 0.2% (20 °C) and 0.5% (400 °C). The fire test of a steel beam and steel column showed that the 0.5% proof stress is too conservative.
- BS5950 Part 8^[3] provides three proof stress levels for different structural components as (a) 2% proof stress for the flexural steel composite members with fire protection, (b) 1.5% proof stress for the flexural steel members and (c) 0.5% proof stress for the others.
- EC3^[1] and EC4^[2] use the 2% proof stress to determine the yield strength.
- Kirby and Preston^[9] suggest that the 1% proof stress should be used to determine the yield strength. The definition of yield stress is shown in Fig. 3.3.

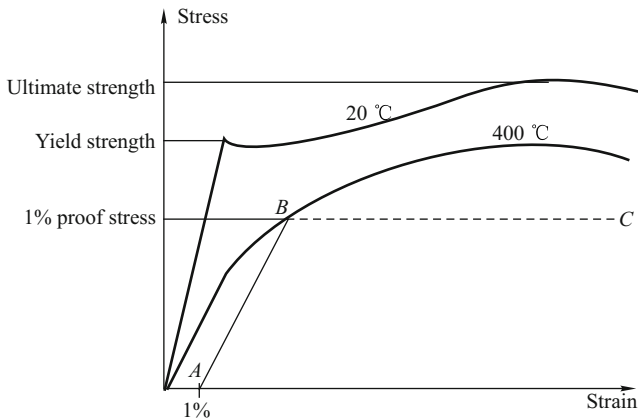


Fig. 3.3 Definition of yield stress

3.2.3 Mechanical Properties of Structural Steel at High Temperatures

3.2.3.1 ECCS Model

The European Committee of Constructional Steel (ECCS)^[7] provides the following equations for calculating the yield strength of steel at high temperatures

(a) For $0\text{ }^{\circ}\text{C} \leq T_s \leq 600\text{ }^{\circ}\text{C}$

$$\eta = \frac{f_{yT}}{f_y} = 1 + \frac{T_s}{767 \ln \frac{T_s}{1750}} \quad (3.16)$$

(b) For $600\text{ }^{\circ}\text{C} \leq T_s \leq 1000\text{ }^{\circ}\text{C}$

$$\frac{f_{yT}}{f_y} = \frac{108(1 - T_s/1000)}{T_s - 440} \quad (3.17)$$

The Young's modulus of steel at high temperature is calculated by

(a) For $0\text{ }^{\circ}\text{C} \leq T_s \leq 600\text{ }^{\circ}\text{C}$

$$\frac{E_T}{E} = 1 + 15.9 \times 10^{-5} T_s - 34.5 \times 10^{-7} T_s^2 + 11.8 \times 10^{-9} T_s^3 - 17.2 \times 10^{-12} T_s^4 \quad (3.18)$$

(b) For $600\text{ }^{\circ}\text{C} \leq T_s \leq 800\text{ }^{\circ}\text{C}$

$$\frac{E_T}{E} = 8.66 \times 10^{-4} (800 - T_s) \quad (3.19)$$

3.2.3.2 AS4100 Model

Australia standard AS4100^[10] gives the following equations for the yield strength of steel at elevated temperatures as

(a) For $0\text{ }^{\circ}\text{C} \leq T_s \leq 215\text{ }^{\circ}\text{C}$

$$\frac{f_{yT}}{f_y} = 1.0 \quad (3.20)$$

(b) For $215\text{ }^{\circ}\text{C} \leq T_s \leq 905\text{ }^{\circ}\text{C}$

$$\frac{f_{yT}}{f_y} = (905 - T_s)/690 \quad (3.21)$$

The Young's modulus at high temperature is determined by

(a) For $0\text{ }^{\circ}\text{C} \leq T_s \leq 600\text{ }^{\circ}\text{C}$

$$\frac{E_T}{E} = 1.0 + \frac{T_s}{2000 \ln(T_s/1000)} \quad (3.22)$$

(b) For $600\text{ }^{\circ}\text{C} \leq T_s \leq 1000\text{ }^{\circ}\text{C}$

$$\frac{E_T}{E} = \frac{690 - 0.69T_s}{T_s - 53.5} \quad (3.23)$$

3.2.3.3 EC3 and BS5950 Model

EC3^[1] and BS5950^[3] provide tables to define the reduction factor of yield strength and Young's modulus of steel at elevated temperatures. For more information you may consult Table 3.1 in EN1993-1-2^[1] and Table 1 in BS5950 Part 8^[3].

3.2.3.4 CECS200 Model

The China Technical code for Fire Safety of Steel Structures in Buildings^[5] gives the following equations for strength reduction factors of steel at elevated temperatures

(a) For $0\text{ }^{\circ}\text{C} \leq T_s \leq 300\text{ }^{\circ}\text{C}$

$$\frac{f_{yT}}{f_y} = 1.0 \quad (3.24)$$

(b) For $300\text{ }^{\circ}\text{C} \leq T_s \leq 800\text{ }^{\circ}\text{C}$

$$\frac{f_{yT}}{f_y} = -0.2168 + 9.228 \times 10^{-3}T_s - 2.096 \times 10^{-5}T_s^2 + 1.24 \times 10^{-8}T_s^3 \quad (3.25)$$

(c) For $800\text{ }^{\circ}\text{C} \leq T_s \leq 1000\text{ }^{\circ}\text{C}$

$$\frac{f_{yT}}{f_y} = 0.5 - T_s/2000 \quad (3.26)$$

The reduction factor for Young's modulus of steel at high temperature is calculated as

(a) For $0\text{ }^{\circ}\text{C} \leq T_s \leq 600\text{ }^{\circ}\text{C}$

$$\frac{E_T}{E} = \frac{7T_s - 4780}{6T_s - 4760} \quad (3.27)$$

(b) For $600\text{ }^{\circ}\text{C} \leq T_s \leq 1000\text{ }^{\circ}\text{C}$

$$\frac{E_T}{E} = \frac{1000 - T_s}{6T_s - 2800} \quad (3.28)$$

The yield strength and Young's modulus of structural steel at high temperatures obtained with the above equations are compared in Fig. 3.4 and Fig. 3.5^[6]. It can be seen that there are some differences in the yield strength and Young's modulus for structural steel proposed by different codes.

3.2.4 Yield Strength and Elastic Modulus of Fire-Resistant Steel at High Temperatures

The fire resistant steel produced by the Nippon Steel Corporation^[11] are SM490-FR, SM400-FR and F11T-FR, which have the ultimate strength f_u of 490 N/mm², 400 N/mm² and 1100 N/mm² respectively, and corresponds to the SM490, SM400 and

F11T of carbon steel. Jiang et al.^[11] carried out a series of high temperature tests on fire-resistant steel. Test results are listed in Table 3.1 and Table 3.2. The comparison of reduction factors for yield strength, ultimate strength and original elastic modulus of fire-resistant steel to normal steel is shown in Fig. 3.6, Fig. 3.7 and Fig. 3.8. Test results on the fire resistant steel produced by China Ma-An-Shan Steel Corporation (Ma Steel) and China Wuhan Steel Corporation (Wu Steel) are also presented^[12,13].

When the temperature of steel is not higher than 600 °C, the yield strength of fire-resistant steel is much higher than that of structural steel at the same temperature. For example, at the temperature of 600 °C, the yield strength reduction factor is still about 2/3 and the elastic modulus reduction factor is about 3/4.

A simplified equation for calculating the reduction factor of the yield strength and elastic modulus is proposed. For the structural use of fire-resistant steel the reduction factor of the yield strength and elastic modulus can be calculated by

(a) For $20\text{ °C} \leq T_s \leq 700\text{ °C}$

$$\frac{f_{yT}}{f_y} = \frac{6 T_s - 768}{5 T_s - 918} \quad (3.29)$$

(b) For $700\text{ °C} < T_s \leq 1000\text{ °C}$

$$\frac{f_{yT}}{f_y} = \frac{1}{8} \frac{1000 - T_s}{T_s - 600} \quad (3.30)$$

The reduction factor of Young's modulus can be calculated by

(a) For $20\text{ °C} \leq T_s \leq 650\text{ °C}$

$$\frac{E_T}{E} = 1 - \frac{T_s - 20}{2520} \quad (3.31)$$

(b) For $650\text{ °C} < T_s \leq 900\text{ °C}$

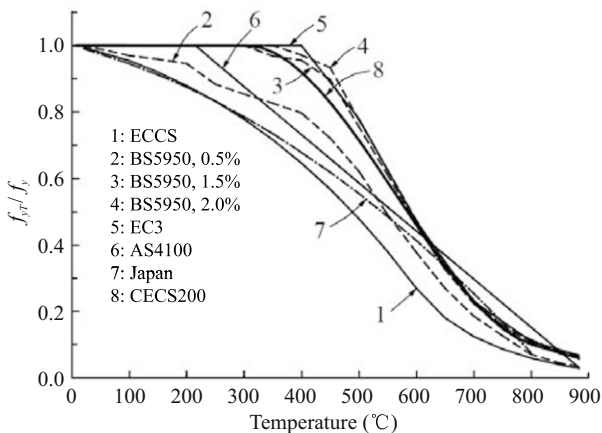


Fig. 3.4 Yield strength of structural steel at elevated temperatures

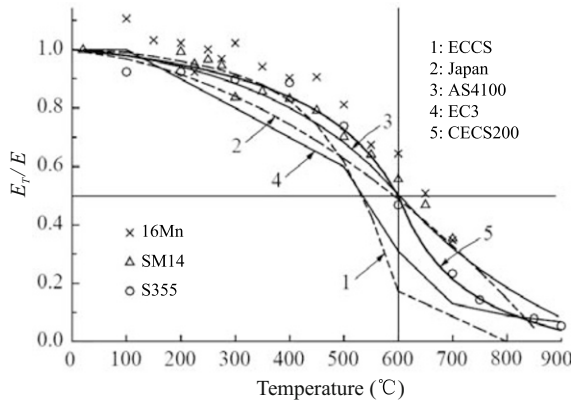


Fig. 3.5 Young's modulus of structural steel at high temperatures

Table 3.1 Yield strength reduction factor of fire resistant steel at high temperatures

	Ma Steel Q345		Wu Steel -10 mm plate		Nippon Steel SM490-FR		Nippon Steel SM400-FR	
At ambient	$f_y=378$	$f_u=693$	$f_y=468$	$f_u=615$	$f_y=358$	$f_u=554$	$f_y=326$	$f_u=476$
Temp.	f_yT/f_y	f_uT/f_u	f_yT/f_y	f_uT/f_u	f_yT/f_y	f_uT/f_u	f_yT/f_y	f_uT/f_u
20 °C	1.000	1.000	1.000	1.000	1.000	1.000	1.000	1.000
100 °C	1.113	0.953	0.920	0.923	0.993	0.950	0.963	0.947
200 °C	1.093	0.953	0.877	0.911	0.970	0.937	0.887	1.029
250 °C	1.179	0.978	0.850	0.890	-	-	-	-
300 °C	1.139	0.993	-	-	0.926	1.018	0.770	1.040
350 °C	1.033	0.986	-	-	0.926	0.989	-	-
400 °C	1.079	0.931	0.802	0.894	0.864	0.947	0.724	0.956
500 °C	0.974	0.780	0.759	0.833	0.837	0.823	0.724	0.788
550 °C	-	-	-	-	0.795	0.744	0.699	0.6930
600 °C	0.808	0.534	0.722	0.675	0.698	0.598	0.574	0.576
650 °C	-	-	-	-	0.510	0.451	0.469	0.435
700 °C	0.412	0.252	0.433	0.504	0.330	0.310	0.337	0.298
750 °C	-	-	-	-	0.229	0.199	0.190	0.172
800 °C	0.200	0.120	-	-	0.139	0.129	0.101	0.113

Table 3.2 Original elastic modulus reduction factor of fire resistant steel at high temperatures

Temp. (°C)	3Ma Steel Q345	Nippon Steel SM490-FR	Nippon Steel SM490	Nippon Steel SM400-FR
20	1.000	1.000	1.000	1.000
100	0.991	0.983	0.983	0.981
200	0.967	0.954	0.952	0.935
250	-	0.938	0.936	0.913
300	0.934	0.922	0.919	0.893
350	-	0.907	0.900	0.873
400	0.887	0.886	0.880	0.851
450	-	0.867	0.859	0.836
500	0.835	0.845	0.837	0.816
550	-	0.823	0.812	0.797
600	0.764	0.797	0.799	0.779
650	-	0.769	0.525	0.757
700	0.689	0.754	0.348	0.609
750	0.670	0.673	-	-
800	0.665	0.381	-	0.332
900	0.066	-	-	-

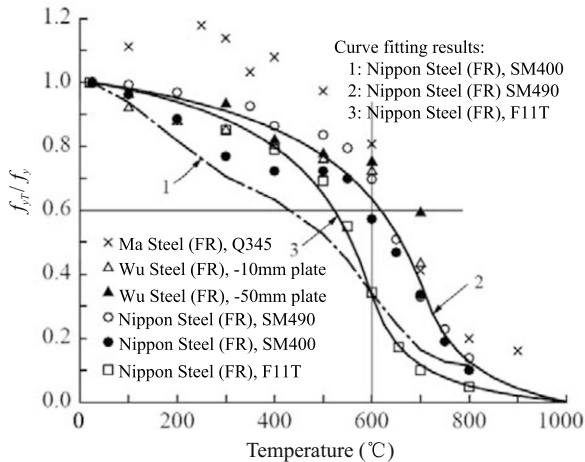


Fig. 3.6 Yield strength reduction factor of fire resistant steel (with permission from ASCE)

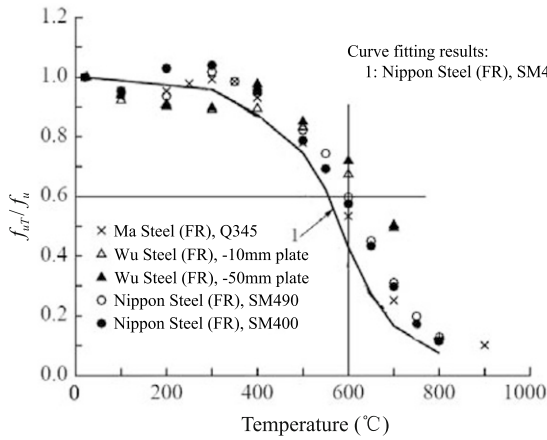


Fig. 3.7 Ultimate strength reduction factor of fire resistant steel (with permission from ASCE)

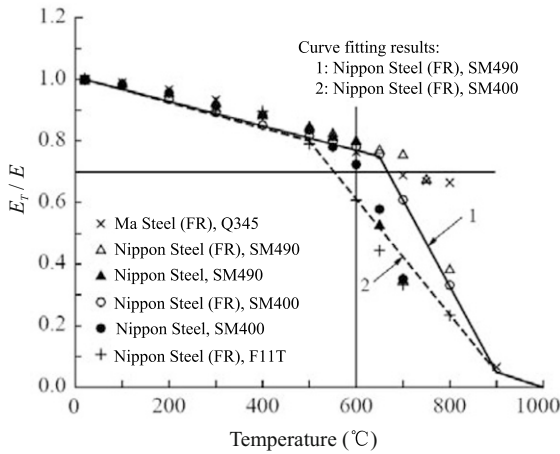


Fig. 3.8 Original elastic modulus reduction factor of fire resistant steel (with permission from ASCE)

$$\frac{E_T}{E} = 0.75 - \frac{7(T_s - 650)}{2500} \tag{3.32}$$

(c) For $900\text{ }^\circ\text{C} < T_s \leq 1000\text{ }^\circ\text{C}$

$$\frac{E_T}{E} = 0.5 - \frac{5T_s}{10000} \tag{3.33}$$

3.2.5 Stress-Strain Relationship of Normal Strength Structural Steel and Fire-Resistant Steel at Elevated Temperatures

CECS200^[5] simply assumes that the steel at high temperature is still elastic perfectly plastic. Hence, by using the degraded yield strength and Young's modulus of steel at high temperature, the stress-strain relationship is obtained.

EC3^[1] gives a non-linear stress-strain relationship of steel at high temperature (See Fig. 3.1 in EN1993-1-2).

3.3 Mechanical Properties of High Strength Steel at High Temperatures

3.3.1 High Strength Bolt

Because of the treatment of quenching and tempering, the mechanical properties of high strength bolt steel are different from those of structural steel (see Fig. 3.9). BS5950 part 8^[3] suggests that the yield strength of a Grade 8.8 high strength bolt at elevated temperatures is reduced 20% more than that of normal strength steel at the same temperature on the base of 0.5% proof strain.

Kirby^[14] and Theodorou^[15] carried out a series of tests on a Grade 8.8 high strength bolt at high temperatures. Test results are summarized as

- at all the pre-defined temperatures, there is no yield plateau in the stress-strain curve.
- at temperatures lower than 300 °C, the yield strength of high strength bolt steel reduces very little and there is not blue brittleness phenomena, which is very different from structural steel.
- in the temperature range of 300 °C through 400 °C, the yield strength of high strength bolt steel reduces quickly and the plastic deformation increases.
- in the temperature range of 400 °C through 600 °C, the ultimate strength of high strength bolt steel reduces to 65% that at ambient temperature, the plastic deformation is nearly the same as that of structural steel and
- when the temperature reaches 700 °C through 800 °C, the ultimate strength of high strength bolt steel reduces to 10% of that at ambient temperature.

Li et al.^[16,17] have carried out tests on high strength 20MnTiB and SM41 steel. The strength of high strength bolts are listed in Table 3.3. It can be seen that the different level of proof strain gives a different yield strength and the reduction factor in the ultimate strength of high strength steel is smaller than that of the yield strength.

Based on test results at 0.5% proof stress, Kirby^[14] proposed following equations for the yield strength reduction factor of high strength steel at elevated temperatures as

(a) For $T_s \leq 300$ °C

$$\frac{f_{yT}}{f_y} = 1.0 \quad (3.34)$$

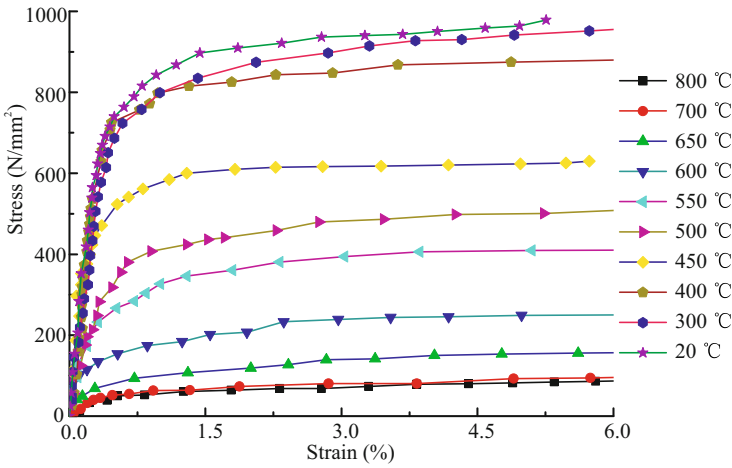


Fig. 3.9 Stress-strain curves and failure model of Grade 8.8 high strength steel

(b) For $300\text{ }^{\circ}\text{C} < T_s \leq 680\text{ }^{\circ}\text{C}$

$$\frac{f_{yT}}{f_y} = 1.0 - 2.128 \times 10^{-3}(T_s - 300) \quad (3.35)$$

(c) For $680\text{ }^{\circ}\text{C} < T_s \leq 1000\text{ }^{\circ}\text{C}$

$$\frac{f_{yT}}{f_y} = 0.17 - 5.312 \times 10^{-3}(T_s - 680) \quad (3.36)$$

Based on test results, Li et al. ^[16,17] adopt the 0.2% proof stress as the yield strength of high strength bolt steel at high temperatures in a fire and the following equation is proposed as

(a) For $20\text{ }^{\circ}\text{C} < T_s \leq 400\text{ }^{\circ}\text{C}$

$$\frac{f_{yT}}{f_y} = 1.011 - 5.5 \times 10^{-4}T_s \quad (3.37)$$

(b) For $400\text{ }^{\circ}\text{C} < T_s \leq 700\text{ }^{\circ}\text{C}$

$$\frac{f_{yT}}{f_y} = -0.501 + 1.125 \times 10^{-2}T_s - 2.826 \times 10^{-5}T_s^2 + 1.909 \times 10^{-8}T_s^3 \quad (3.38)$$

(c) For $700\text{ }^{\circ}\text{C} < T_s \leq 1000\text{ }^{\circ}\text{C}$

$$\frac{f_{yT}}{f_y} = 0.25 - \frac{0.25T_s}{1000} \quad (3.39)$$

Comparison of the yield strength reduction factor between structural steel and high strength bolt steel is shown in Fig. 3.10.

Table 3.3 Strength reduction factors of high strength steel at elevated temperatures

References	Test results							Proposed by	
	Kirby	Theodorou Li et al.		Sakmoto			Kirby	Li et al.	
Grade	G8.8	G8.8	20MnTiB		F10T	F11T			
Strength	η_{yT}	η_{uT}	η_{yT}	η_{uT}	η_{yT}	η_{yT}	η_{uT}	η_{yT}	η_{yT}
Proof strain	0.5%		0.2%		0.2%	0.2%			
$f_y(\text{N/mm}^2)$	628		1130	1176	987				
20 °C	1.000	1.000	1.000	1.000	1.000	1.000	1.000	1.000	1.000
100 °C	0.910	-	-	-	-	-	-	1.000	0.956
150 °C	0.875	-	-	-	-	-	-	1.000	0.929
200 °C	0.855	1.000	0.890	1.000	-	-	-	1.000	0.901
250 °C	0.845	-	-	-	0.88	-	-	1.000	0.874
300 °C	0.825	0.983	0.836	0.938	0.87	0.865	0.947	1.000	0.846
350 °C	0.785	-	0.767	0.837	0.780	-	-	0.894	0.794
400 °C	0.720	0.904	0.697	0.742	0.76	0.735	0.804	0.787	0.700
450 °C	0.625	0.668	0.572	0.598	0.64	-	-	0.681	0.579
500 °C	0.465	0.504	0.412	0.438	0.42	0.395	0.505	0.574	0.446
550 °C	0.270	0.437	0.295	0.315	-	-	-	0.468	0.314
600 °C	0.150	0.265	0.199	0.213	-	0.135	0.263	0.362	0.199
650 °C	0.085	0.168	-	-	-	0.073	0.168	0.255	0.115
700 °C	0.055	0.102	0.079	0.091	-	0.043	0.112	0.159	0.075
750 °C	0.045	-	-	-	-	-	-	0.133	0.0625
800 °C	0.040	0.093	-	-	-	0.032	0.074	0.106	0.050
1000 °C	-	-	-	-	-	-	-	0.000	0.000

3.3.2 High Strength Cable

Zhou^[18] carried out a series of high temperature tests on the high strength cable. The test specimen was made by seven high strength steel wires of Grade 1860 with character diameter of 15.24 mm. The effective area is 140 mm². The tested stress-strain relationship of the steel cable at different temperatures is shown in Fig. 3.11.

It can be seen that, with the elevation of temperatures, the strength of the steel cable degrades. The reduction factor of the ultimate strength, yield strength and elastic modulus of high strength steel cable are shown in Fig. 3.12.

It can be seen that, for a temperature lower than 200 °C, the strength and elastic modulus of high strength steel cable changes very little with the elevation of temperature. When the temperature is higher than 200 °C, the strength and elastic modulus of steel cable degrades quickly. At a temperature of 700 °C, the ultimate strength, yield strength and elastic modulus is only about 5% that at ambient temperature.

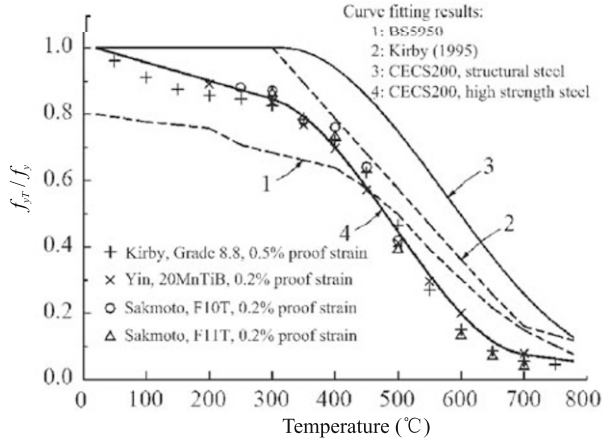


Fig. 3.10 Yield strength reduction factor of high strength bolt steel and structural steel at elevated temperatures

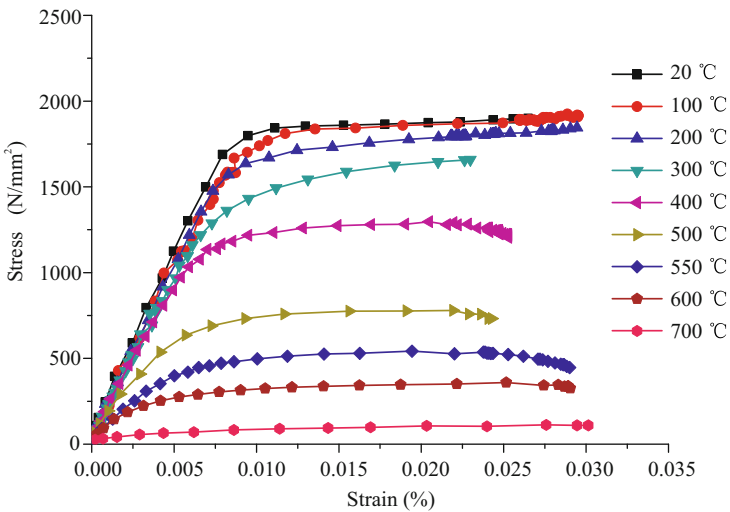


Fig. 3.11 Stress-strain relationship of high strength steel cable at high temperatures

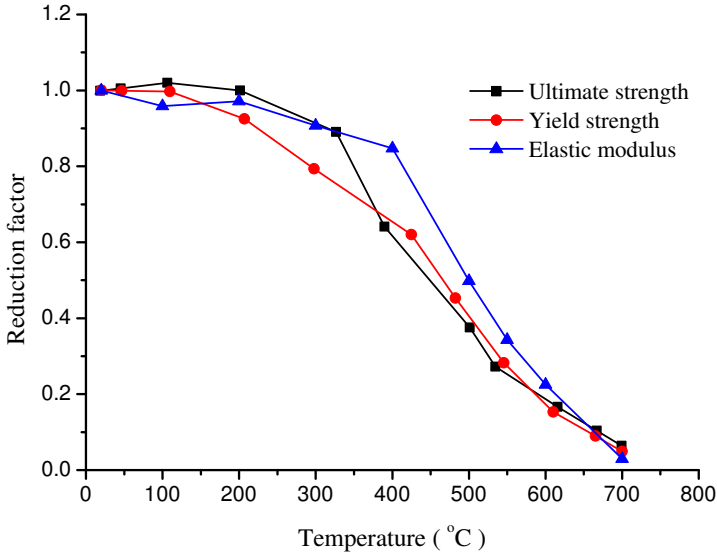


Fig. 3.12 Ultimate strength reduction factor of high strength steel cable at high temperatures

As a result of curve fitting, the yield strength of the high strength steel cable at high temperatures can be calculated by

$$\sigma_{yT} = \chi_T \sigma_{y0} \tag{3.40}$$

where χ_T is the reduction factor calculated by

$$\chi_T = \begin{cases} 1, & 20 \text{ }^\circ\text{C} \leq T \leq 200 \text{ }^\circ\text{C} \\ 1.41 - \frac{0.82T}{400}, & 200 \text{ }^\circ\text{C} < T \leq 600 \text{ }^\circ\text{C} \end{cases} \tag{3.41}$$

The elastic modulus of high strength steel cable at elevated temperatures is calculated by

$$E_y = \eta_T E_0 \tag{3.42}$$

where η_T is the reduction factor. When $20 \text{ }^\circ\text{C} \leq T \leq 600 \text{ }^\circ\text{C}$, η_T is obtained through

$$\eta_T = 0.9817 + 7.9229 \times 10^{-4} T - 3.1937 \times 10^{-6} T^2 \tag{3.43}$$

The comparison of yield strength reduction factors for high strength steel cable measured from tests and based on Eq.(3.40) and for normal steel recommended by CECS200^[5] and EC3^[1] are plotted in Fig. 3.13.

From Fig. 3.13, it can be seen that (a) the proposed equation for the yield strength reduction factor of the high strength steel cable agrees well with test results and (b) the yield strength of the high strength steel cable degrades faster at high temperatures than that of the carbon steel.

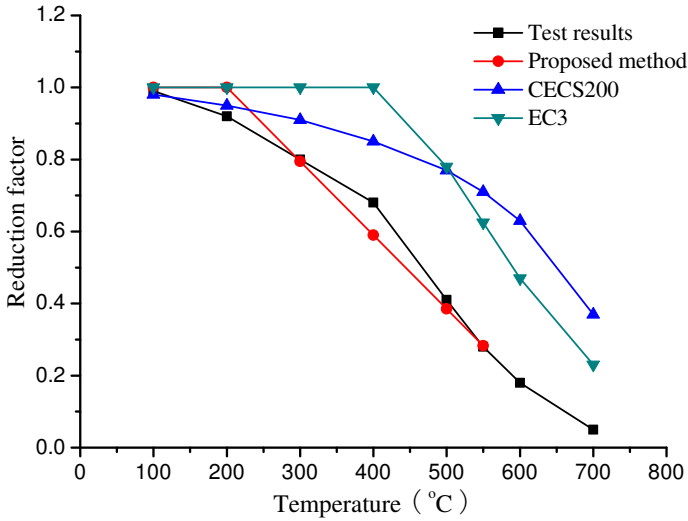


Fig. 3.13 Comparison of the yield strength reduction factor

The comparison of the elastic modulus reduction factor of the high strength steel cable measured from tests, based on Eq.(3.42) and that of normal strength steel used in EC3 is shown in Fig. 3.14.

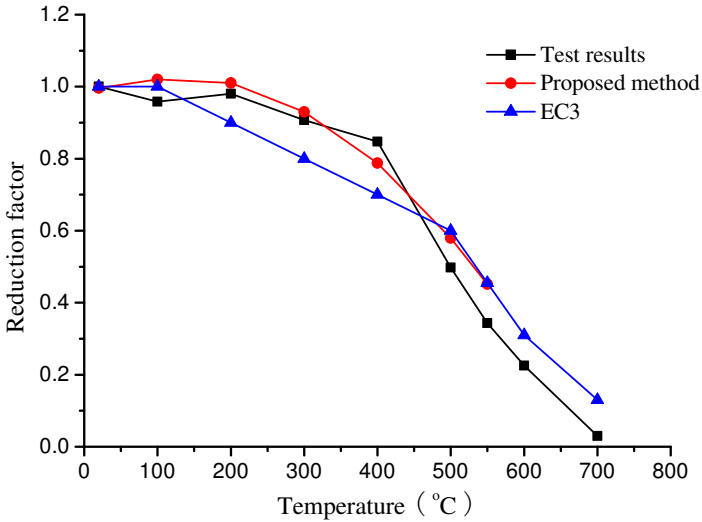


Fig. 3.14 Comparison of the yield strength reduction factor

From Fig. 3.14, it can be seen that the elastic modulus reduction factor given by the proposed equation agrees well with test results and that the elastic modulus reduction factor of high strength steel cable is little different to that of normal steel.

3.4 Properties of Stainless Steel at High Temperatures

Owing to good durability, aesthetic appeal and corrosion resistance, the use of stainless steel in construction is continuously increasing. Material properties of the stainless steel are significantly different from those of the carbon steel. For carbon and low-alloy steels, the proportional limit is assumed to be at least 70% of the yield point, but for stainless steel the proportional limit ranges from approximately 36% to 60% of the yield strength.

3.4.1 *Thermal Properties of Stainless Steel*

Stainless steel used in structures is mainly austenitic stainless steel containing alloy Ni, and Cr of 8%–11% and 18%–20% respectively. The alloy Ni and Cr are all high temperature resistant and stainless steel performs better than the carbon steel at very high temperature ($>600\text{ }^{\circ}\text{C}$). At room temperature, the thermal expansion coefficient of austenitic stainless steel is about 1.3 times that of carbon steel and the thermal conductivity is about 1/3 that of carbon steel.

Table 3.4 lists the thermal expansion coefficient, conductivity, specific heat of stainless steel at different temperatures described in UK and Japanese standards (Sakumoto^[11], Sandersin^[19]). It can be seen that (a) the thermal expansion of stainless steel increases with the increase in temperature, which is the same as that of normal steel, (b) the thermal conductivity of stainless steel increases with the increase in temperature, which is the opposite to that of carbon steel and (c) the increase in specific heat of stainless steel is insignificant with the increase in temperature, which is very different from that of carbon steel.

3.4.2 *Mechanical Properties of Stainless Steel at High Temperatures*

The stress-strain relationship of stainless steel has no yield platform even at ambient temperature, as shown in Fig. 3.15^[6]. There is a great strain hardening after the elastic limit. The ratio between yield strength and ultimate strength is about 0.36 to 0.40, which is lower than that of carbon steel. For stainless steel, the yield strength usually takes 0.2% proof stress. The tangent elastic modulus is about 1/15 of the original elastic modulus.

The Steel Construction Institute carried out a test on grade 1.4301 austenitic stainless steel^[20]. Strength reduction factors at elevated temperatures were developed from test results. A comparison between the behavior of carbon steel and stainless steel at elevated temperatures concludes that the stainless steel grade 1.4301

Table 3.4 Thermal properties of austenitic stainless steel

Temp. (°C)	Thermal expansion ($\times 10^{-5}$ °C)		Conductivity (W/(m·°C))		Specific heat (J/(kg·°C))		Poisson ratio	
	UK	Japan	UK	Japan	UK	Japan	UK	Japan
	316S31	SUS304	316S31	SUS304	316S31	SUS304	316S31	SUS304
20	-	1.73	14.3	14.3	-	-		
100	1.60	1.75	15.5	16.4	499	504		
200	1.66	1.78	17	-	510	-		
300	1.72	1.80	18.4	-	522	-		
400	1.77	1.82	20	20.6	533	-	0.31	0.3
500	1.83	1.85	21.5	21.8	544	-		
600	1.87	1.87	23	23.5	553	575		
700	1.91	1.89	24.5	-	560	-		
800	1.93	1.92	26	-	563	-		

(reproduced from Journal of Structural Engineering, ASCE, with permission from ASCE)

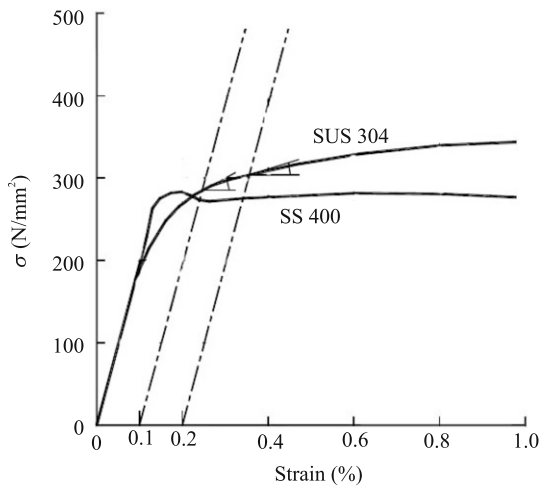


Fig. 3.15 Stress-strain relationship of stainless steel at ambient temperature

retains higher strength than carbon steel at temperatures above 500 °C and significantly higher values of Young’s Modulus^[21].

The strength reduction factor and Young’s modulus reduction factor for stainless steel^[20,21,22,23] are shown in Fig. 3.16 and Fig. 3.17 respectively. And strength reduction factors at different proof stress are listed in Table 3.5.

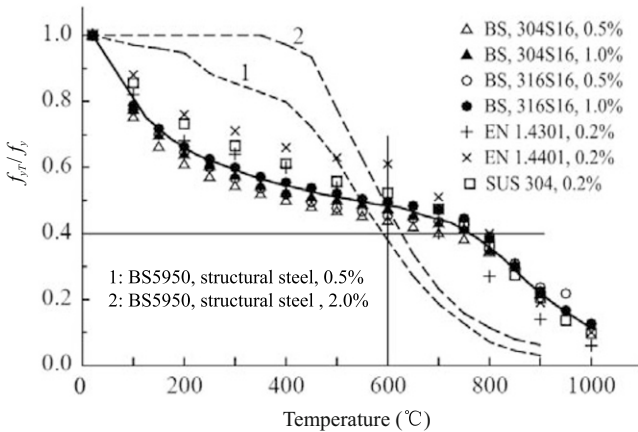


Fig. 3.16 Strength reduction factor of stainless steel at elevated temperatures

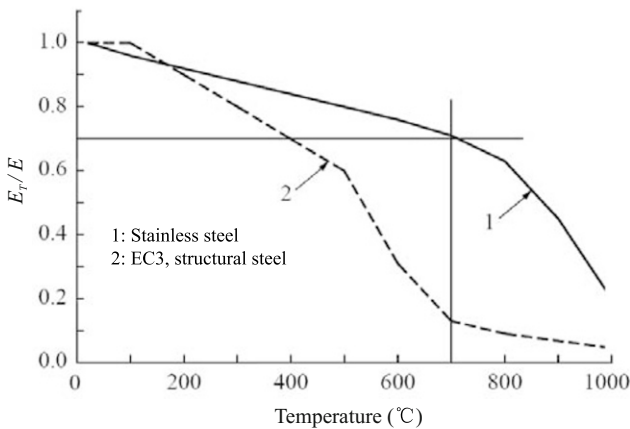


Fig. 3.17 Young’s modulus reduction factor of stainless steel at elevated temperatures

Table 3.5 Reduction factors of yield strength and Young’s modulus of stainless steel with different proof stresses

Temp. (°C)	304S16		316S16		SUS304		EN1.4301		EN1.4401		EN1.4301		EN1.4401	
	η_y		η_y		η_y	η_u	η_y	η_u	η_y	η_u	η_E	η_{Et}	η_E	η_{Et}
	0.5%	1.0%	0.5%	1.0%	0.2%		0.2%		0.2%					
20	1.0	1.0	1.0	1.0	1.0	1.0	1.00	1.0	1.0	1.0	1.11	1.0	0.05	
100	0.752	0.774	0.773	0.787	0.855	0.772	0.82	0.87	0.88	0.93	0.96	0.05	0.96	0.049
150	0.662	0.696	0.700	0.717	–	–	–	–	–	–	–	–	–	–
200	0.609	0.639	0.645	0.662	0.731	0.694	0.68	0.77	0.76	0.87	0.92	0.02	0.92	0.047
250	0.571	0.604	0.600	0.625	–	–	–	–	–	–	–	–	–	–
300	0.543	0.574	0.567	0.599	0.665	0.694	0.64	0.73	0.71	0.84	0.88	0.02	0.88	0.045
350	0.519	0.543	0.536	0.571	–	–	–	–	–	–	–	–	–	–
400	0.500	0.522	0.518	0.554	0.610	0.685	0.60	0.72	0.66	0.83	0.84	0.02	0.84	0.03
450	0.481	0.509	0.495	0.537	–	–	–	–	–	–	–	–	–	–
500	0.467	0.500	0.477	0.521	0.558	0.642	0.54	0.67	0.63	0.79	0.80	0.02	0.80	0.025
550	0.452	0.487	0.467	0.504	–	–	–	–	–	–	–	–	–	–
600	0.438	0.474	0.454	0.496	0.522	0.544	0.49	0.58	0.61	0.72	0.76	0.02	0.76	0.02
650	0.419	0.452	0.445	0.483	0.497	0.476	–	–	–	–	–	–	–	–
700	0.400	0.430	0.436	0.471	0.474	0.391	0.40	0.43	0.51	0.55	0.71	0.02	0.71	0.02
750	0.381	0.413	0.427	0.446	0.425	0.306	–	–	–	–	–	–	–	–
800	0.343	0.348	0.391	0.383	0.360	0.238	0.27	0.27	0.40	0.34	0.63	0.02	0.63	0.02
850	0.305	0.304	0.309	0.300	0.273	0.180	–	–	–	–	–	–	–	–
900	0.214	0.217	0.236	0.225	0.205	0.137	0.14	0.15	0.19	0.18	0.45	0.02	0.45	0.02
950	–	–	0.218	0.167	0.136	0.096	–	–	–	–	–	–	–	–
1000	–	–	0.127	0.125	0.097	0.073	0.06	0.07	0.10	0.09	0.20	0.02	0.20	0.02

Based on the curve shown in Fig. 3.18, a stress-stain relationship considering the strain hardening of stainless steel is proposed^[20]. The detailed equation is listed in Table 3.6.

An equation is proposed for the reduction factor of 0.2% proof stress. The unified equation for the reduction factor at elevated temperatures for stainless steel is as follows

$$\eta_T = a = \frac{(T - b)^n}{c} \tag{3.44}$$

Coefficients *a*, *b*, *c* and *n* of the equation are calibrated with all stainless steel test results, and the coefficients are presented in Table 3.7.

The reduction factor of 0.2% proof stress obtained from tests was compared with the proposed equation and also compared with test results conducted by Ala-Outinen^[24], Sakumoto et al.^[22] and Ala-Outinen et al.^[25], as shown in Fig. 3.19.

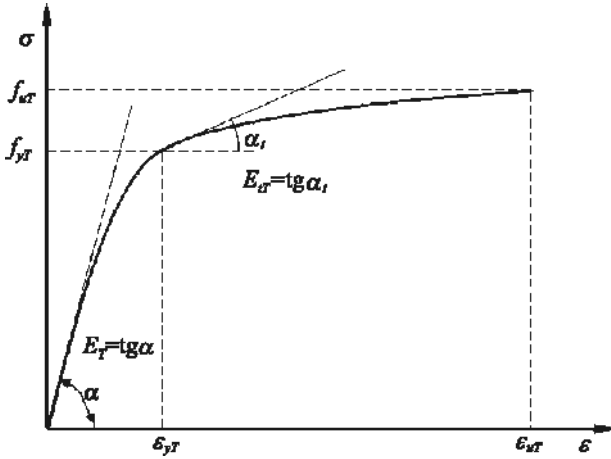


Fig. 3.18 Stress-strain relationship of stainless steel including work hardening

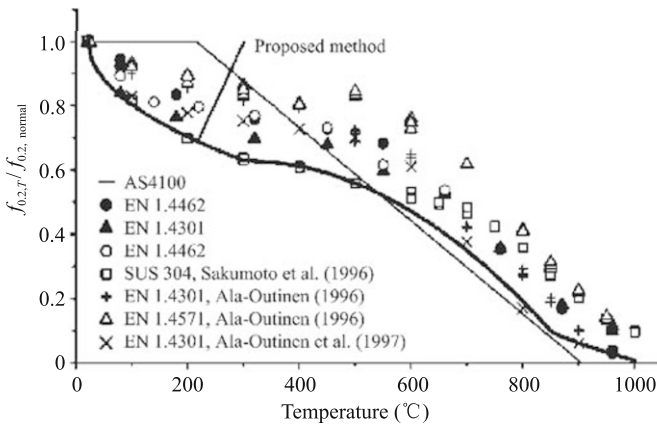
Table 3.6 Stress-strain relationship of stainless steel at elevated temperatures

Strain range	Stress	Tangent modulus
$\epsilon \leq \epsilon_{yT}$	$\frac{\epsilon E_T}{1 + m\epsilon^n}$	$\frac{E_T(1 + m\epsilon^e - mn\epsilon^n)}{(1 + m\epsilon^n)^2}$
$\epsilon_{yT} \leq \epsilon_u$	$f_{yT,0.2} - c + \frac{b}{a} \sqrt{a^2 - (\epsilon_u - \epsilon)^2}$	$\frac{b(\epsilon_u - \epsilon)}{a\sqrt{a^2 - (\epsilon_u - \epsilon)^2}}$
$\epsilon_{yT} = 0.002 + f_{yT,0.2}/E_T$ $m = \frac{E_T \epsilon_{yT} - f_{yT,0.2}}{f_{yT,0.2} \epsilon_{yT}^n}$ $n = \frac{E_T \epsilon_{yT} (1 - E_{T'} \epsilon_{yT} / f_{yT,0.2})}{f_{yT,0.2} (E_T \epsilon_{yT} / f_{yT,0.2} - 1)}$ $a = \sqrt{(\epsilon_{yT} - \epsilon_{pT})(\epsilon_{yT} - \epsilon_{pT} + c/E_T)}$ $b = \sqrt{c(\epsilon_{yT} - \epsilon_{pT})E_T + c^2}$ $c = \frac{(f_{yT} - f_{pT})^2}{(\epsilon_{yT} - \epsilon_{pT})E_T - 2(f_{yT} - f_{pT})}$		

$f_{yT,0.2}$ is 0.2% proof stress at temperature T ; E_T is original Young's modulus at temperature T ; ϵ_{yT} is the strain corresponding to stress $y_{yT,0.2}$; ϵ_{uT} is ultimate strain at temperature T

Table 3.7 Coefficients of the proposed equation for yield strength of stainless steel types EN1.4462 and EN 1.4301

Temperature	$22\text{ }^{\circ}\text{C} \leq T \leq 300\text{ }^{\circ}\text{C}$	$300\text{ }^{\circ}\text{C} < T \leq 850\text{ }^{\circ}\text{C}$	$850\text{ }^{\circ}\text{C} < T \leq 1000\text{ }^{\circ}\text{C}$
<i>a</i>	1.0	0.63	0.1
<i>b</i>	22	300	850
<i>c</i>	45	5.7×10^5	600
<i>n</i>	0.5	2	0.8

**Fig. 3.19** Comparison of reduction factor of 0.2% yield strength used in AS4100 and proposed equation with test results (Reprinted from Chen and Young (2006), with permission from Elsevier)

The proposed equation provides a conservative prediction for test results of stainless steel types EN 1.4462, EN 1.4301 and EN 1.4571.

The unified equation Eq.(3.44) that is used in this study for stainless steel can be used for the prediction of the elastic modulus for cold-formed carbon steel at elevated temperatures. Coefficients *a*, *b*, *c* and *n* of the equation are calibrated with all of stainless steel test results and coefficients are presented in Table 3.8.

The reduction factor of the elastic modulus obtained from tests are also compared with test results conducted by Ala-Outinen^[24], Sakumoto et al.^[22] and Ala-Outinen et al.^[25], as shown in Fig. 3.20. It can be seen that results are significantly different from each other. It is shown that the prediction of the reduction factor of the elastic modulus using Eq.(3.44) is generally conservative compared with test results obtained from this study for stainless steel types EN 1.4462 and EN 1.4301 and test results obtained by other researchers.

For the prediction of ultimate strength, coefficients *a*, *b*, *c* and *n* in Eq.(3.44) take the value listed in Table 3.9. It is shown that the prediction of the reduction factor of

Table 3.8 Coefficients of the proposed equation for yield strength of stainless steel types EN1.4462 and EN 1.4301

Temperature	$22\text{ }^{\circ}\text{C} \leq T \leq 922\text{ }^{\circ}\text{C}$
<i>a</i>	1.0
<i>b</i>	22
<i>c</i>	900
<i>n</i>	1

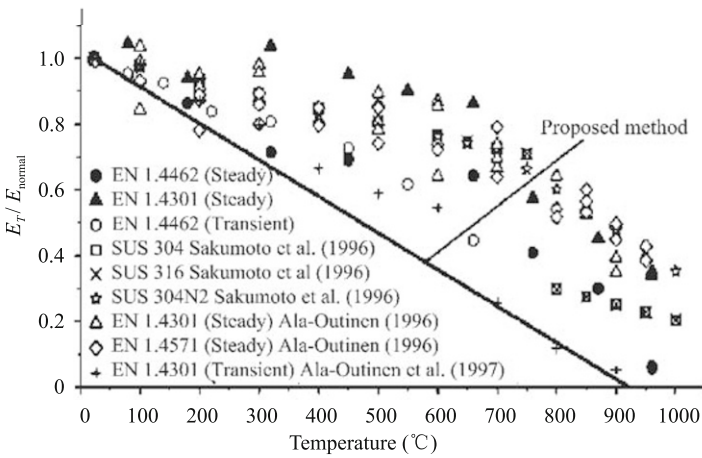


Fig. 3.20 Comparison of elastic modulus obtained using the proposed equation with test results (Reprinted from Chen and Young (2006), with permission from Elsevier)

the ultimate strength using Eq.(3.44) agrees well with test results obtained from this study for stainless steel types EN 1.4462 and EN 1.4301, as shown in Fig. 3.21.

For calculating the ultimate strain, coefficients *a*, *b*, *c* and *n* of the equation are calibrated with stainless steel test results in this study and coefficients are presented in Table 3.10. It is shown that the prediction of the reduction factor of ultimate strain using Eq.(3.44) generally agrees with test results obtained from this study for stainless steel types EN 1.4462 and EN 1.4301, as shown in Fig. 3.22.

The proposed stress-strain curve model is as follows

$$\epsilon_T = \begin{cases} \frac{f_T}{E_T} + 0.002 \left(\frac{f_T}{f_{yT}} \right)^{nr}, & f_T \leq f_{yT} \\ \frac{f_T - f_{yT}}{E_{yT}} + \epsilon_{uT} \left(\frac{f_T - f_{yT}}{f_{uT} - f_{yT}} \right)^{mT}, & f_T > f_{yT} \end{cases} \quad (3.45)$$

and

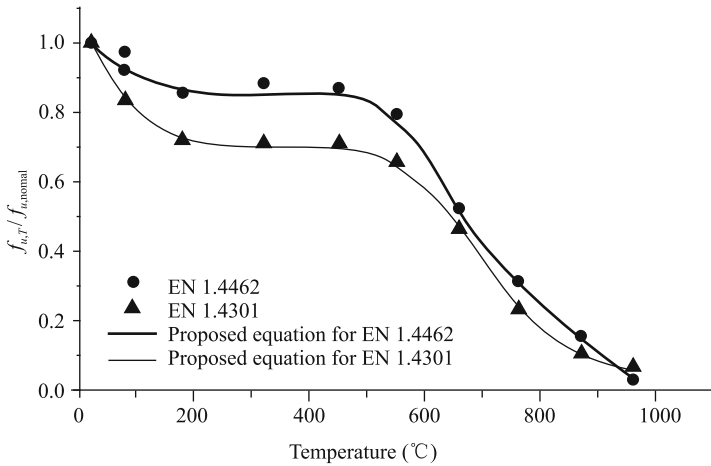


Fig. 3.21 Comparison of ultimate strength obtained using the proposed equation with test results (Reprinted from Chen and Young (2006), with permission from Elsevier)

Table 3.9 Coefficients of the proposed equation for ultimate strength

Temperature	$22\text{ }^{\circ}\text{C} < T \leq 450\text{ }^{\circ}\text{C}$	$450\text{ }^{\circ}\text{C} < T \leq 660\text{ }^{\circ}\text{C}$	$660\text{ }^{\circ}\text{C} < T \leq 960\text{ }^{\circ}\text{C}$	
EN1.4462	a	0.85	0.85	0.51
	b	450	450	660
	c	9.6×10^{13}	1.3×10^5	200
	n	5	2	0.8
EN1.4301	a	0.7	0.7	0.06
	b	450	450	960
	c	4.8×10^{13}	1.92×10^5	-2.2×10^5
	n	5	2	2

$$E_{yT} = \frac{E_T}{1 + 0.002n_T \frac{E_T}{f_{yT}}} \tag{3.46}$$

$$n_T = 6 + 0.2\sqrt{T} \tag{3.47}$$

$$m_T = \begin{cases} 5.6 - \frac{T}{200}, & \text{for EN1.4462} \\ 2.3 - \frac{T}{1000}, & \text{for EN1.4301} \end{cases} \tag{3.48}$$

The comparison of stress-strain curves obtained using Eq.(3.44) with test results for stainless steel types EN1.4462 and EN1.4301 at different temperatures are shown in Fig. 3.23 and Fig. 3.24, respectively. Generally, the proposed stress-strain curve

Table 3.10 Coefficients of the proposed equation for ultimate strain

Temperature	$22\text{ }^{\circ}\text{C} < T \leq 180\text{ }^{\circ}\text{C}$	$180\text{ }^{\circ}\text{C} < T \leq 560\text{ }^{\circ}\text{C}$	$560\text{ }^{\circ}\text{C} < T \leq 960\text{ }^{\circ}\text{C}$	
EN1.4462	<i>a</i>	1.0	0.67	0.15
	<i>b</i>	22	180	660
	<i>c</i>	480	5.42×10^{21}	5000
	<i>n</i>	1	8	1
EN1.4301	<i>a</i>	1.0	0.36	0.16
	<i>b</i>	22	180	660
	<i>c</i>	247	6.1×10^{16}	2000
	<i>n</i>	1	6	1

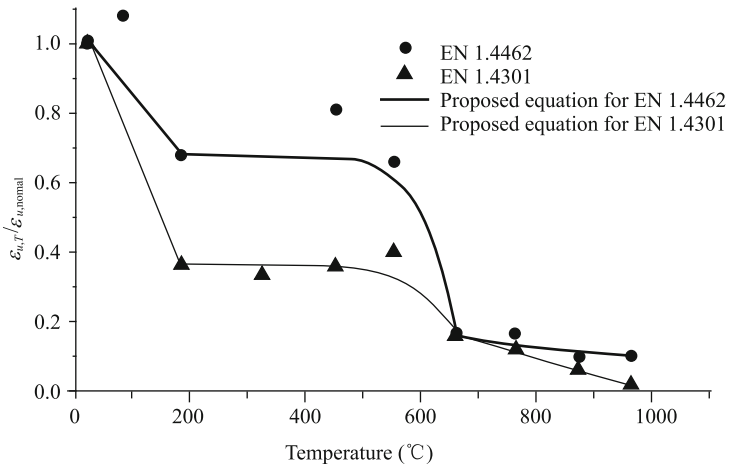


Fig. 3.22 Comparison of ultimate strain obtained using the proposed equation with test results (Reprinted from Chen and Young (2006), with permission from Elsevier)

model accurately predicted the stainless steel type EN1.4462 and conservatively predicted the stainless type EN1.4301 for the temperature range from 20 °C to 960 °C.

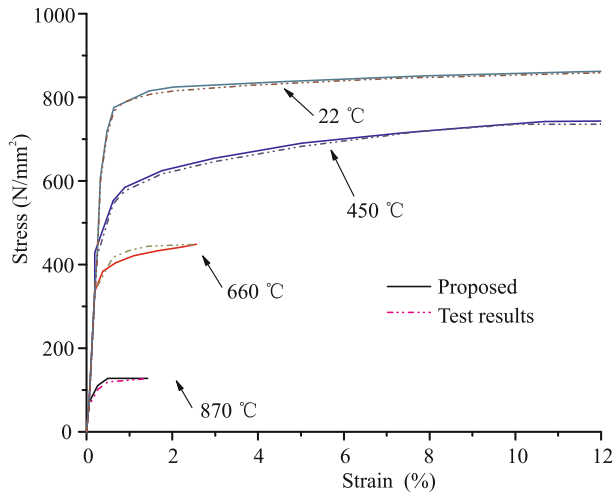


Fig. 3.23 Comparison of stress-strain curves based on the proposed model with test results for stainless steel type EN1.4462 (Reprinted from Chen and Young (2006), with permission from Elsevier)

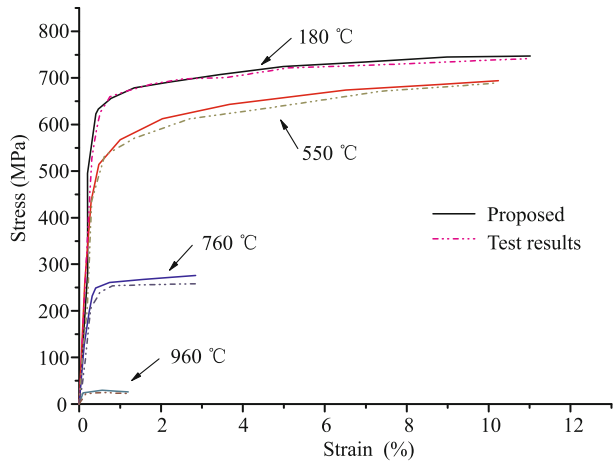


Fig. 3.24 Comparison of stress-strain curves based on the proposed model with test results for stainless steel type EN1.4301 (Reprinted from Chen and Young (2006), with permission from Elsevier)

References

- [1] European Committee for Standardization. *EN1993-1-2. Eurocode 3: Design of Steel Structures, Part 1.2, General Rules, Structural Fire Design*. European Committee for Standardization, 2005.
- [2] European Committee for Standardization. *EN1994-1-2. Eurocode 4: Design of Composite Steel and Concrete Structures, Part 1-2: General Rules, Structural Fire Design*. European Committee for Standardization, 2005.
- [3] British Standard Institution. *British Standard BS 5950, Part 8, Code of Practice for Fire Resistance Design*. British Standard Institution, 2000.
- [4] Japan Construction Department. *The Building Synthetic Fire Prevention Design*. Japan Construction Department, 1994.
- [5] China Association for Engineering Construction Standardization. *Technical Code for Fire Safety of Steel Structures in Buildings (CECS200-2006)*. China Plan Press, 2006.
- [6] G. Q. Li, L. H. Han, G. B. Lou, and S. C. Jiang. *Steel and Steel-Concrete Composite Structures Fire Resistance Design*. China Architecture & Building Press, 2006.
- [7] European Convention for Construction Steelwork. *Calculation for Fire Resistance of Composite Structures*. Technical Note No. 55, ECCS Technical Committee 3, 1989.
- [8] International Organization for Standardization. *Fire-Resistance Tests, Elements of Building Construction, Part 1: General Requirements*. International Organization for Standardization, 1999.
- [9] T. R. Kay, B. R. Kirby, and R. R. Preston. Calculation of the heating rate of an unprotected steel member in a standard fire resistance test. *Fire Safety Journal*, 26(4):327–350, 1996.
- [10] Australian Standard. *Steel Structures, Standards Australia (AS4100)*. Australian Standard, 1990.
- [11] Y. Sakumoto, T. Yamaguchi, M. Ohashi, and H. Saito. High-temperature properties of fire-resistant steel for buildings. *Journal of Structural Engineering*, 118(2):392–407, 1992.
- [12] S. C. Jiang, L. X. Lu, G. Q. Li, J. C. Shen, B. Q. Wu, and J. C. Wu. An experimental study on high-temperature properties of fire-resistant steel made by ma steel. *China Civil Engineering Journal*, 39(8):72–75, 2006.
- [13] L. X. Lu, G. Q. Li, S. C. Jiang, J. C. Shen, B. Q. Wu, and J. C. Wu. Fire-resistant experiments and theoretical calculations of fire-resistant steel columns. *Progress in Steel Building Structures*, 8(4):12–16, 2006.
- [14] B. R. Kirby. The behaviour of high-strength grade 8.8 bolts in fire. *Journal of Constructional Steel Research*, 33(1-2):3–38, 1995.
- [15] Y. Theodorou. *Mechanical Properties of Grade 8.8 Bolts at Elevated Temperatures*. MSc dissertation, University of Sheffield, 2001.
- [16] G. Q. Li, M. F. Li, Y. Z. Yin, and Shou C. J. Experimental studies on the behavior of high-strength bolts made of 20mntib steel at elevated temperatures. *China Civil Engineering Journal*, 34(5):100–104, 2001.

- [17] G. Q. Li, X. J. Zhang, S. C. Jiang, and Y. Z. Yin. Experimental studies of the material properties of SM41 steel at elevated temperatures. *Industry Construction*, 31(6):57–60, 2001.
- [18] H. T. Zhou. *Fire resistance of cable net structures*. PhD dissertation, Tongji University, 2006.
- [19] G. P. Sandersin and D. T. Llewellyn. Mechanical properties of austenitic stainless steels in the temperature range - 196 °C to 800 °C. *Journal of the Iron and Steel Institute*, 1969.
- [20] N. R. Baddoo and B. A. Burgan. Fire resistant design of austenitic structural stainless steel. *Journal of Constructional Steel Research*, 46(1-3):458–459, 1998.
- [21] B. A. Burgan, N. R. Baddoo, and K. A. Gilsenan. Structural design of stainless steel members - comparison between eurocode 3, part 1.4 and test results. *Journal of Constructional Steel Research*, 54(1):51–73, 2000.
- [22] Y. Sakumoto, T. Nakazato, and A. Matsuzaki. High-temperature properties of stainless steel for building structures. *Journal of Structural Engineering, ASCE*, 122(4):399–406, 1996.
- [23] B. Zhao. Stress-strain relationships of stainless steel at elevated temperatures. In *Proc. of the International Seminar on Steel Structures in Fire*, pages 134–149, Shanghai, P. R. China, 2001.
- [24] T. Ala-Outinen. Fire resistance of austenitic stainless steels polarit 725 (EN 1.4301) and polarit 761 (EN 1.4571). *VTT research notes 1760. Espoo, Finland*, 1996.
- [25] T. Ala-Outinen and T. Oksanen. Stainless steel compression members exposed to fire. *VTT research notes 1864. Espoo, Finland*, 1997.

Temperature Elevations of Structural Steel Components Exposed to Fire

This chapter will introduce heat transfer from a fire to structural steel components and its modeling in the context of structural engineering for fire safety. There are three basic mechanisms of heat transfer (a) conduction, (b) convection and (c) radiation. In conduction, energy is exchanged in solids on a molecular scale but without any movement of macroscopic portions of matter relative to one another. Convection refers to heat transfer at the interface between a fluid and a solid surface. Radiation is the exchange of energy by electromagnetic waves which can be absorbed, transmitted or reflected at a surface. Unlike conduction and convection, heat transfer by radiation does not require any intervening medium between the heat source and the receiver.

4.1 Laws of Heat Transfer

The analysis of temperature response in a structural component can be subdivided into two parts. One is heat transfer across the boundary from the fire into the surface of a structural member, which is through the combination of convection and radiation and is usually treated as a boundary condition. The other is heat transfer within the structural member, which is through conduction and treated as a governing equation expressed by the Fourier equation of heat transfer^[1].

4.1.1 Heat Transfer in Structural Members

Usually heat transfer along the length of a structural member can be neglected. The heat transfer in a structural member can be simplified to a 2D heat transfer problem. The equation describing this heat transfer^[1] is shown in Fig. 4.1 and is expressed as

$$\rho c \frac{\partial T}{\partial t} = \frac{\partial}{\partial x} \left(\lambda \frac{\partial T}{\partial x} \right) + \frac{\partial}{\partial y} \left(\lambda \frac{\partial T}{\partial y} \right) \quad (4.1)$$

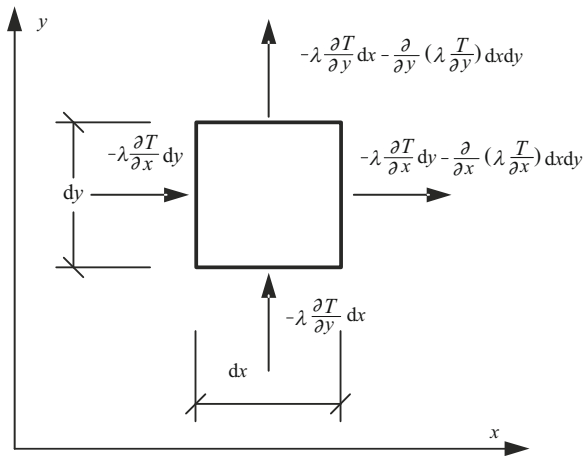


Fig. 4.1 Heat balance in a differential element

4.1.2 Heat Transfer between Hot Smoke and a Structural Member

The heat transfer between hot smoke and the surface of a structural member is by radiation and convection^[1], as shown in Fig.4.2.

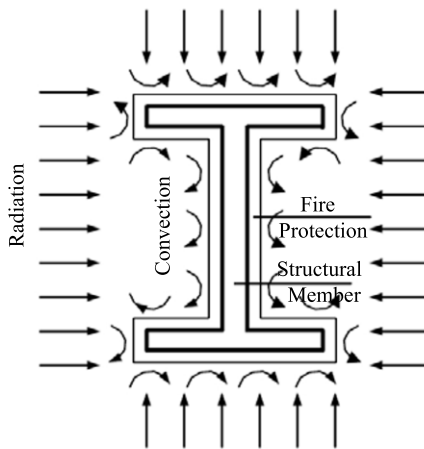


Fig. 4.2 Heat transfer between hot smoke and the structural member

4.1.2.1 Radiation

The heat transferred through radiation depends on the temperature difference between the hot air and the surface temperature of a structural member^[1], which is given by

$$q_r = \varphi \varepsilon_r \sigma [(T_g + 273)^4 - (T_b + 273)^4] \quad (4.2)$$

where ε_r is comprehensive radiation factor obtained through

$$\varepsilon_r = \varepsilon_f \varepsilon_m \quad (4.3)$$

ε_f is the radiation factor related to the fire compartment and usually takes the value of 0.8, ε_m is the radiation factor related to the surface character of a structural member and usually takes the value of 0.625, φ is the view factor and usually takes the value of 1.0, σ is the Stefan-Boltzmann constant and $\sigma=5.67 \times 10^{-8} \text{ W}/(\text{m}^2 \cdot \text{K}^4)$.

4.1.2.2 Convection

The energy transferred through convection^[1] is

$$q_c = \alpha_c (T_g - T_b) \quad (4.4)$$

where α_c is the heat convection factor. $\alpha_c=25 \text{ W}/(\text{m}^2 \cdot ^\circ\text{C})$ for the fiber material fire and $\alpha_c=50 \text{ W}/(\text{m}^2 \cdot ^\circ\text{C})$ for the hydrocarbon material fire. q_c is the heat transferred through convection in W/m^2 .

4.2 Practical Calculation Method for Temperature Elevation of Structural Members

The temperature elevation of structural components exposed to a fire can be obtained through solving the Eq.(4.1). However, it is not very easy to find an analytical solution. Numerical methods may be used instead.

4.2.1 Calculating Model

The structural component is divided into light section component and heavy section component according to the section factor F/V . The former one has a large section factor. The temperature over the cross section of a light section component exposed to fire can be assumed to be uniform.

The coating to protect a structural steel component is divided into lightweight fire protection and heavyweight fire protection. For lightweight fire protection, the heat absorbed by the fire protection material can be ignored. Otherwise, for heavyweight fire protection, the heat absorbed by the fire protection material cannot be ignored. The heat transfer and temperature distribution across the component section have different types^[2], as shown in Fig. 4.3 and Fig. 4.4.

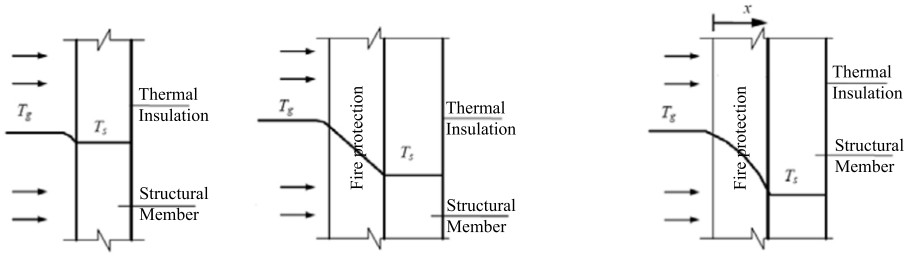


Fig. 4.3 Uniform temperature distribution across the light section with fire protection methods (a) unprotected, (b) protected with lightweight fire protection and (c) protected with heavyweight fire protection

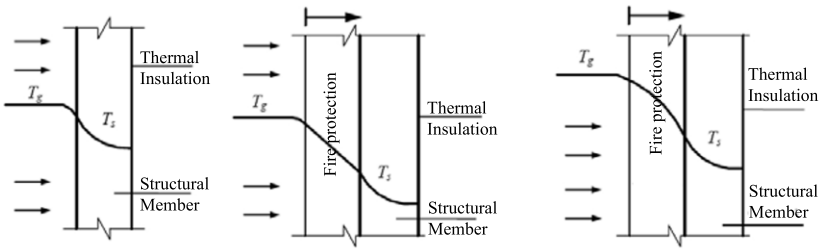


Fig. 4.4 Non-uniform temperature distribution across the heavy section with fire protection methods (a) unprotected, (b) protected with lightweight fire protection and (c) protected with heavyweight fire protection

4.2.2 Temperature Elevation of Structural Component with Uniformly Distributed Temperature

4.2.2.1 Unprotected Structural Component

For the component with uniform cross-sectional temperature distribution, the Fourier's law^[2] of heat conduction can be simplified to

$$q = \rho_s c_s V \frac{dT_s}{dt} \quad (4.5)$$

The energy transferred to the structural component can be expressed by

$$q = q_r + q_c \quad (4.6)$$

The radiation energy is calculated by

$$q_r = \alpha_r F (T_g - T_s) \quad (4.7)$$

Let $\phi = 1.0$ and Eq.(4.2) is reformulated as

$$q_r = \frac{5.67 \times 10^{-8} \epsilon_r}{T_g - T_s} [(T_g + 273)^4 - (T_s + 273)^4] \quad (4.8)$$

and Eq.(4.4) can be reformulated as

$$q_c = \alpha_c F (T_g - T_s) \tag{4.9}$$

Substituting Eq.(4.6), Eq.(4.7) and Eq.(4.9) into Eq.(4.5), we can get

$$\alpha (T_g - T_s) = \frac{\rho_s c_s V}{F} \frac{dT_s}{dt} \tag{4.10}$$

where α is the comprehensive heat transfer coefficient given by

$$\alpha = \alpha_r + \alpha_c \tag{4.11}$$

The increment format of Eq.(4.10)

$$\Delta T_s = \alpha \frac{1}{\rho_s c_s} \frac{F}{V} (T_g - T_s) \Delta T \tag{4.12}$$

where the time increment ΔT is suggested to be less than 5 s for obtaining satisfactorily precise results. The temperature dependent material properties can be included when using Eq.(4.12).

The expression of section factor (F/V) for various sections is listed in Table 4.1 by employing Eq.(4.12). The temperature elevation of an unprotected steel component subjected to ISO834^[3] standard fire is obtained and tabulated in Table 4.2^[2].

Table 4.1 Section factor of unprotected structural component

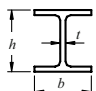
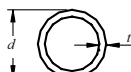
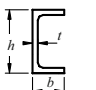
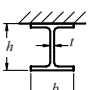
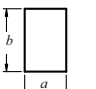
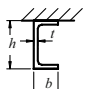
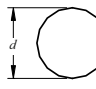
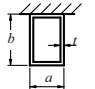
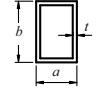
Section type	F/V	Section type	F/V
	$\frac{2h + 4b - 2t}{A}$		$\frac{d}{t(d-t)}$
	$\frac{2h + 4b - 2t}{A}$		$\frac{2h + 3b - 2t}{A}$
	$\frac{2(a+b)}{ab}$		$\frac{2h + 3b - 2t}{A}$
	$\frac{d}{4}$		$\frac{b + a/2}{t(a + b - 2t)}$
	$\frac{a + b}{t(a + b - 2t)}$		

Table 4.2 Temperature elevation of unprotected structural component

Time (min)	T_g (°C)	Section factor F/V (m^{-1})									
		10	20	30	40	50	100	150	200	250	300
0	20	20	20	20	20	20	20	20	20	20	20
5	576	32	44	56	67	78	133	183	229	271	309
10	678	54	86	118	148	178	311	416	496	552	590
15	739	81	138	193	246	295	491	609	669	697	711
20	781	112	197	277	350	416	638	724	752	763	767
25	815	146	261	365	456	533	737	786	798	802	805
30	842	182	327	453	556	636	799	824	830	833	834
35	865	221	396	538	646	721	838	852	856	858	859
40	885	261	464	618	723	787	866	874	877	879	880
45	902	302	531	690	785	835	888	893	896	897	898
50	918	345	595	752	834	871	906	911	913	914	915
55	932	388	655	805	871	898	922	926	928	929	929
60	945	432	711	848	900	919	936	940	941	942	943
65	957	475	762	883	923	936	949	952	954	954	955
70	968	518	807	911	941	951	961	964	965	966	966
75	979	561	846	933	956	963	972	974	976	976	977
80	988	603	880	952	969	975	982	984	986	986	987
85	997	643	908	968	981	985	992	994	995	995	996
90	1006	683	933	981	991	995	1001	1003	1004	1004	1004

Note: (1) if $F/V < 10$, the temperature distribution across the structural component section is non-uniform;
(2) if $F/V > 300$, the temperature of structural component can be assumed as the air temperature

4.2.2.2 Structural Component with Lightweight Fire Protection Material

Thermal properties of the lightweight fire protection satisfy

$$c_s \rho_s V \geq 2c_i \rho_i d_i F_i \quad (4.13)$$

From Eq.(4.2) and Eq.(4.4), the heat transfer between the hot air and the fire protection material is

$$q = \alpha F_i' (T_g - T_b) \quad (4.14)$$

where T_b is the surface temperature of the fire protection material and F_i' is the outer surface area of the fire protection per unit length.

The heat transfer between the fire protection and the structural component is

$$q = \frac{\lambda_i}{d} F_i' (T_b - T_s) \quad (4.15)$$

The conductivity, density and specific heat of commonly used fire protection materials are listed in Table 4.3^[2].

Eq.(4.7) and Eq.(4.8) can be rewritten as

$$q = \alpha F_i (T_g - T_s) \quad (4.16)$$

Table 4.3 Thermal properties of fire protection material

Material	ρ_i (kg/m ³)	λ_i (W/(m·°C))	c_i (kJ/(kg·°C))
Thin fire protection coat	600–1000	-	-
Thick fire protection coat	250–500	0.09–0.12	-
Plasterboard	800	0.20	1.7
Silica acid calcium board	500–1000	0.10–0.25	-
linen	80–250	0.10–0.20	-
Clay brick, ash sand brick	1000–2000	0.40–1.20	1.0
autoclaved aerated concrete	400–800	0.20–0.40	1.0–1.20
Light aggregate concrete	800–1800	0.30–0.90	1.0–1.20
concrete	2200–2400	1.30–1.70	1.20

where α is the comprehensive heat transfer coefficient calculated by

$$\alpha = \frac{1}{\frac{1}{\alpha_r + \alpha_c} + \frac{d_i F_i'}{\lambda_i F_i}} \approx \frac{1}{\frac{1}{\alpha_r + \alpha_c} + \frac{d_i}{\lambda_i}} \quad (4.17)$$

Generally, $\alpha_r + \alpha_c$ is far greater than λ_i/d_i . α is approximately expressed by

$$\alpha = \frac{\lambda_i}{d_i} \quad (4.18)$$

Substituting Eq.(4.16) into Eq.(4.5) gives

$$\frac{dT_s}{dt} = \frac{\lambda_i}{d_i} \frac{1}{\rho_s c_s} \frac{F_i}{V} (T_g - T_s) \quad (4.19)$$

The solution to Eq.(4.19) as

$$T_s(t) = \int_0^t T_g(\tau) e^{-A(t-\tau)} d\tau + T_g(0) e^{-At} \quad (4.20)$$

where $T_g(0)$ is the ambient temperature and A is a parameter given by

$$A = \frac{F_i \lambda_i}{V} \frac{1}{d_i \rho_s c_s} = \frac{F_i}{Q_s R} \quad (4.21)$$

Q_s is the heat capacity of structural component per unit length obtained by

$$Q_s = c_s \rho_s V \quad (4.22)$$

R is the heat resistance of the fire protection as

$$R = \frac{d_i}{\lambda_i} \quad (4.23)$$

The increment format of Eq.(4.20) is

$$\Delta T_s = \frac{\lambda_i}{d_i} \frac{1}{\rho_s c_s} \frac{F_i}{V} (T_g - T_s) \Delta t \quad (4.24)$$

The time increment Δt in Eq.(4.24) is suggested to be less than 30 s. The expression equation for the section factor of various protected structural components F_i/V is listed in Table 4.4.

In the commonly encountered temperature range ($T_s \leq 600$ °C), the temperature elevation of a protected structural component subjected to ISO834 standard fire can be obtained through the simplification of Eq.(4.20) as

$$T_s = (\sqrt{0.044 + 5 \times 10^{-5} B - 0.2})t + T_g(0) \quad (4.25)$$

and

$$B = \frac{\lambda_i F_i}{d_i V} \quad (4.26)$$

4.2.2.3 Structural Component with Heavyweight Fire Protection

If the properties of fire protection material do not satisfy Eq.(4.13), this is called heavyweight fire protection. The heat absorbed by fire protection material should be considered in calculating the structural component temperature when protected by heavyweight fire protection.

The energy balance of fire protection gives

$$\lambda_i \frac{\partial T_i^2}{\partial x^2} - \rho_i c_i \frac{\partial T_i}{\partial t} = 0 \quad (4.27)$$

The boundary conditions are

(a) at the interface between hot air and fire protection

$$T_i(x, 0) = T_0 \quad (4.28)$$

(b) at the interface between hot air and fire protection

$$F_i \lambda_i \frac{\partial T_i}{\partial x} + Q_s \frac{\partial T_s}{\partial t} = 0 \quad (4.29)$$

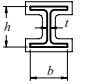
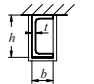
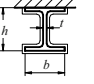
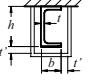
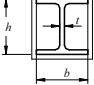
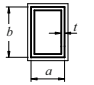
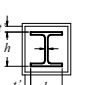
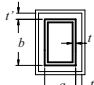

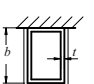
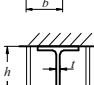
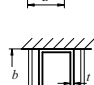
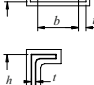
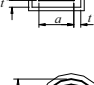
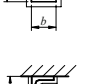

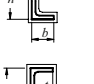

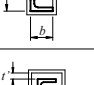
where T_i is the temperature of fire protection at a distance of x from the surface, T_s is the smoke temperature, d_i is the thickness of fire protection.

The solution to Eq.(4.27) can be expressed by a series as

$$\frac{T_i(x, t)}{T_0} = \sum_{n=1}^{\infty} K_n e^{-\beta_n t} \sin(\alpha_n x) \quad (4.30)$$

Substituting Eq.(4.30) into Eq.(4.27) gives $\beta_n = a \alpha_n^2$. And Eq.(4.30) can then be rewritten as

Table 4.4 Section factor of unprotected structural component

Section type	F_i/V	Section type	F_i/V
	$\frac{2h + 4b - 2t}{A}$		$\frac{2h + b}{A}$
	$\frac{2h + 3b - 2t}{A}$		$\frac{2h + b}{A}, t \leq h/4$
	$\frac{2(h + b)}{A}$		$\frac{a + b}{t(a + b - 2t)}$
	$\frac{2(h + b)}{A}, t \leq h/4$		$\frac{a + b}{t(a + b - 2t)}, t \leq h/4$
	$\frac{2h + b}{A}$		$\frac{a + b/2}{t(a + b - 2t)}$
	$\frac{2h + b}{A}, t \leq h/t$		$\frac{a + b/2}{t(a + b - 2t)}, t \leq b/4$
	$\frac{2h + 4b - 2t}{A}$		$\frac{d}{t(d - t)}$
	$\frac{2h + 3b - 2t}{A}$		$\frac{t}{t(d - t)}, t \leq d/4$
	$\frac{2(h + b)}{A}$		$\frac{d}{t(d - t)}$
	$\frac{2(h + b)}{A}, t \leq h/4$		

$$\frac{T_i(x,t)}{T_0} = \lim_{n=1}^{\infty} K_n e^{-a\alpha_n^2 t} \sin(\alpha_n x) \quad (4.31)$$

where α is the thermal diffusion rate in m^2/s . It is calculated by

$$a = \frac{\lambda_i}{\rho_i c_i} \quad (4.32)$$

Substituting Eq.(4.32) into Eq.(4.31) gives

$$\frac{\alpha_n d_i}{\text{ctg}(\alpha_n d_i)} = \mu \quad (4.33)$$

and

$$\mu = \frac{Q_i}{Q_s} \quad (4.34)$$

where Q_i is the heat capacity of fire protection per unit length obtained by

$$Q_i = F_i c_i \rho_i d_i \quad (4.35)$$

α_n is a parameter determined with Eq.(4.33). The parameter K_n in Eq.(4.31) is obtained by using the boundary condition governed by Eq.(4.28) as

$$K_n = \frac{2[(\alpha_n d_i)^2 + \mu^2]}{(\alpha_n d_i)[(\alpha_n d_i)^2 + \mu + \mu^2]} \quad (4.36)$$

The interior surface temperature of fire protection can be calculated by Eq.(4.31) as

$$T_s(t) = T_i(d_i, t) = T_0 \sum_{n=1}^{\infty} K_n \exp\left[-\frac{(\alpha_n d_i)^2}{RQ_i/F_i} t\right] \sin(\alpha_n d_i) \quad (4.37)$$

Eq.(4.37) can also be simplified as

$$\frac{T_s(t)}{T_0} = \begin{cases} 1.0, & t \leq \bar{t} \\ \exp\left(-\frac{t-\bar{t}}{\tau}\right), & t > \bar{t} \end{cases} \quad (4.38)$$

where

$$\tau = R \frac{Q_s + Q_i/3}{F_i} \quad (4.39)$$

\bar{t} is the time need for the temperature wave pass through the fire protection and determined by

$$\bar{t} = \frac{1}{8} \mu \tau \quad (4.40)$$

The temperature of a structural component can be obtained by Eq.(4.31) as

$$T_s(t) = \int_0^t (t - \xi) \Phi_n(\xi) d\xi \quad (4.41)$$

where $\Phi_n(t)$ is the first order derivative of $\Phi(t)$ and $\Phi(t)$ is the time needed for the temperature of a structural component to change by 1 °C given by

$$\Phi(t) = 1 - \frac{T_s(t)}{T_0(t)} \tag{4.42}$$

Reformulate the ISO834 standard fire curve in series format^[4] as

$$T_g(t) = \sum_{j=0}^3 B_j e^{-\beta_j t} \tag{4.43}$$

B_j and β_j are parameters given in Table 4.5.

Table 4.5 Average moisture in fire protection material

j	0	1	2	3
B_j (°C)	1325	-430	-270	-625
β_j (s ⁻¹)	0	5.56×10^{-5}	4.27×10^{-4}	5.28×10^{-3}

Considering Eq.(4.41), Eq.(4.42) and Eq.(4.43), the temperature of a protected structural component subjected to ISO834^[3] fire is obtained by

$$T_s(t) = \sum_{n=1}^{\infty} \sum_{j=0}^3 \frac{B_j K_n \sin(\alpha_n d_i)}{1 - \frac{\beta_j Q_i R / F_i}{(\alpha_n d_i)^2}} \left[\exp(-\beta_j t) - \exp\left(-\frac{(\alpha_n d_i)^2}{R Q_i / F_i} t\right) \right] \tag{4.44}$$

and correspondingly, from Eq.(4.38) the temperature of a protected structural component subjected to ISO834^[3] fire can be approximately obtained by

$$T_s = \sum_{j=0}^3 \frac{B_j}{1 - \beta_j \tau} \left\{ \exp[-\beta_j(t - \bar{t})] - \exp\left(-\frac{t - \bar{t}}{\tau}\right) \right\} \tag{4.45}$$

It is not very convenient to use Eq.(4.45) in engineering practice. For simplicity, ECCS^[5] provides the following increment formulation to calculate the temperature of a structural component with heavyweight fire protection as

$$\Delta T_s = \frac{\lambda_i}{d_i} \frac{1}{\rho_s c_s} \frac{F_i}{V} \frac{1}{1 + \mu/2} (T_g - T_s) \Delta t - \frac{\Delta T_g}{1 + \mu/2} \tag{4.46}$$

where ΔT_g is the increase of smoke temperature at every time step and

$$\mu = \frac{Q_i}{Q_s} = \frac{\rho_i c_i d_i F_i}{\rho_s c_s V} \tag{4.47}$$

The EC3^[6] gives the following equation for calculating the temperature of a protected structural component as

$$\Delta T_s = \frac{\lambda_i}{d_i} \frac{1}{\rho_s c_s} \frac{F_i}{V} \frac{1}{1 + \mu/3} (T_g - T_s) \Delta t - (e^{\mu/10} - 1) \Delta T_g \quad (4.48)$$

and ΔT_s should be greater than 0.

For the structural component subjected to ISO834 fire, the temperature of a structural component with heavyweight fire protection can be obtained with a simplified method. In this method, half of the heat capacity of fire protection $Q_i/2$ is added to the structural component and then the calculation procedure for a structural component with lightweight fire protection is employed. The increment format is

$$\Delta T_s = \frac{\lambda_i}{d_i} \frac{1}{\rho_s c_s} \left(\frac{F_i}{V}\right)_{\text{mod}} (T_g - T_s) \Delta t \quad (4.49)$$

where $\left(\frac{F_i}{V}\right)_{\text{mod}}$ is the modified section factor and

$$\left(\frac{F_i}{V}\right)_{\text{mod}} = \frac{1}{1 + \mu/2} \frac{F_i}{V} \quad (4.50)$$

4.2.2.4 Effects of Moisture in Fire Protection on Temperature Elevation of Structural Component

Usually there is some water in the fire protection. When the fire protection is subjected to fire, the water evaporation causes a delay in the temperature elevation of the protected structural component^[2]. The time is called delay time, as shown in Fig. 4.5. The design value for the delay time t_v is calculated by

$$t_v = \frac{p \rho_i d_i^2}{5 \lambda_i} \quad (4.51)$$

where p is the moisture content of the fire protection. The average moisture content of some fire protection material is listed in Table 4.6.

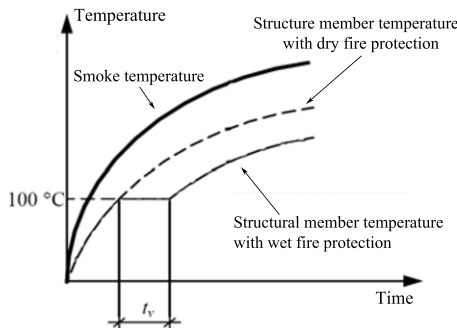
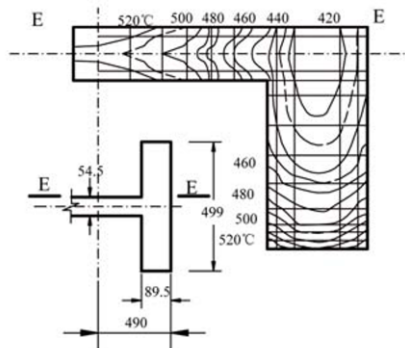


Fig. 4.5 Time delay of the structural component with wet fire protection

Table 4.6 Values of B_j and β_j

Material	ρ_i (kg/m ³)	Average moisture p (%)
Sprayed fibrous mineral	250–350	1.0
Plasterboard	800	20.0
Silica acid calcium board	500–1000	3.0–5.0
Linen	80–250	2.0
Clay brick, ash sand brick	1000–2000	0.2
Perlite and vermiculite board	300–800	15.0
Autoclaved aerated concrete	400–800	2.5
Lightweight aggregate concrete	800–1800	2.5
Concrete	2200–2400	1.5

**Fig. 4.6** Temperature distribution across the section of a heavy section structural component

4.2.3 Temperature of Structural Component with Non-Uniformly Distributed Temperature

For a structural component with a heavy section ($F/V < 10 \text{ m}^{-1}$), the temperature distribution across the section is not uniform. Fig. 4.6 shows the temperature distribution of a structural component with a heavy section subjected to ISO834 fire for 30 min. The maximum temperature difference over the section is nearly $100 \text{ }^\circ\text{C}$ ^[7]. The non-uniformly distributed temperature will cause additional stress in the section and greatly affects the behavior of a structural member in a fire. In this situation, the finite element method is the most feasible solution^[8].

4.3 Practical Calculation Method for Temperature Evolution of Structural Members Exposed to a Large Space Building Fire

The fire in a large space building is usually a fuel controlled fire. The temperature field can be divided into three zones (a) the upper hot smoke zone, (b) the flame

zone and (c) the lower cool air zone. The temperature of the smoke zone is usually lower than that in an enclosure compartment fire. Effects of flame radiation on the temperature elevation of steel structural components in a large space building need to be considered, as shown in Fig. 4.7.

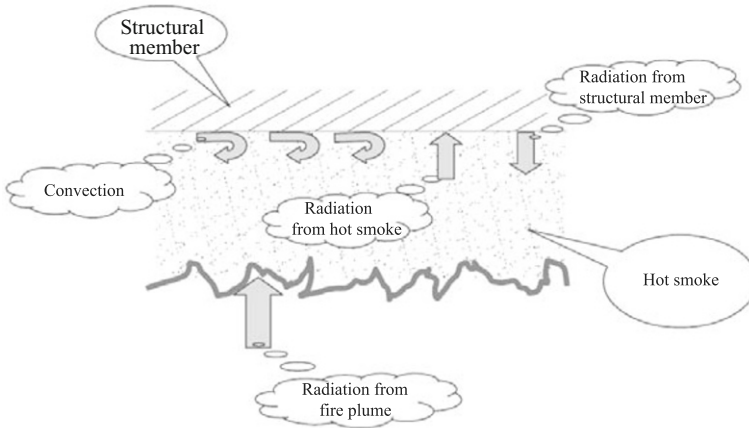


Fig. 4.7 Heat exchange between the structural component and the atmosphere

The heat transfer between the hot smoke and the steel structural member is the same as that in an enclosed compartment fire. And the temperature elevation of a protected or un-protected structural member due to radiation and convection from the hot smoke can be calculated according to the method described hereinbefore.

The heat transfer between the flame and the structural component is mainly by radiation, which depends on the distance and relative position between the flame and the structural component. When the structural component is far away from the flame, the radiation effect can be ignored^[9,10].

4.3.1 Effects of Flame Radiation on Temperature Elevation of Un-Protected Steel Structural Components

4.3.1.1 Temperature Elevation of Steel Structural Component

For the steel structural component with a lightweight section, the temperature distribution across the section is uniform. The temperature elevation can be obtained by lumped differential formulation as

$$Q_s = V_s \rho_s c_s \frac{dT_s}{dt} \quad (4.52)$$

To simplify the calculation of heat transferred to the structural component, make the following assumptions:

- Q_s only included the heat from the flame and the hot smoke;
- the temperature of smoke takes its maximum value;
- only a unit length along the longitudinal direction of the structural component is considered;
- the view factor between the flame and the structural component studied is the same.

The total heat transferred to the structural component is

$$Q_s = Q_{gr} + Q_{fr} + Q_{gc} \quad (4.53)$$

The value of Q_{gr} , Q_{fr} and Q_{gc} are determined as follows:

(a) Heat transferred from the smoke to the structural component through radiation^[11] is

$$Q_{gr} = \varepsilon_g \varepsilon_s \sigma F_s [(T_g + 273)^4 - (T_s + 273)^4] \quad (4.54)$$

(b) Heat transferred from the flame to the structural component through radiation^[11] is

$$Q_{fr} = \varepsilon_f \varepsilon_s \sum_{i=1}^n \phi_{sf}^i F_{sr}^i (1 - \varepsilon_g) \sigma [(T_f + 273)^4 - (T_g + 273)^4] \quad (4.55)$$

where F_{sr}^i is the exposure area per unit length on the i -th plate as listed in Table 4.7.

Assume that

$$\phi_{sf} F_{sr} = \sum_{i=1}^n \phi_{sf}^i F_{sr}^i \quad (4.56)$$

Through substituting Eq.(4.56) into Eq.(4.55), Q_{fr} is rewritten as

$$Q_{fr} = \varepsilon_f \varepsilon_s \phi_{sf} \xi F_s (1 - \varepsilon_g) \sigma [(T_f + 273)^4 - (T_g + 273)^4] \quad (4.57)$$

where ξ is the ratio between the surface area of the structural component and the area exposed to the flame given by

$$\xi = \frac{F_{sr}}{F_s} \quad (4.58)$$

(c) Heat transferred from the smoke to the structural component through convection is

$$Q_{sc} = F_s \alpha_c (T_g - T_s) \quad (4.59)$$

In summary, the temperature elevation of the structural component in a large space building fire can be calculated by

$$\frac{\Delta T_s}{\Delta t} = \{ F_s \alpha_c (T_g - T_s) + \varepsilon_g \varepsilon_s \sigma F_s [(T_g + 273)^4 - (T_s + 273)^4] + \varepsilon_f \varepsilon_s \phi_{sf} \xi F_s \sigma [(T_f + 273)^4 - (T_g + 273)^4] \} / (V_s \rho_s c_s) \quad (4.60)$$

With the incremental strategy, the temperature of the structural component at the time step $j + 1$ can be calculated through the results at the time step j as

$$T_s^{j+1} = T_s^j + \Delta T_s \quad (4.61)$$

Table 4.7 Values of B_j and β_j

Section type	Exposure area

Note: the dotted line stands for the radiation exposure area

4.3.1.2 Calculation of the View Factor

The view factor ϕ_{fs} is the portion of heat received by a structural component to the total heat emitted by the fire flame. There are two possible relative positions between the structural component surface and the fire flame, which are

(a) the structural component surface parallel to the fire flame surface^[12], as shown in Fig.4.8(a). The view factor is calculated through

$$\phi_{sf}^A = \frac{1}{2\pi} \left(\frac{\frac{X}{\sqrt{1+X^2}}}{\tan\left(\frac{Y}{\sqrt{1+X^2}}\right)} + \frac{\frac{Y}{\sqrt{1+Y^2}}}{\tan\left(\frac{X}{\sqrt{1+Y^2}}\right)} \right) \tag{4.62}$$

(b) the structural component surface perpendicular to the fire flame surface^[12], as shown in Fig.4.8(b). The view factor is calculated through

$$\phi_{sf}^B = \frac{1}{2\pi} \left(\frac{1}{\tan(Y)} - \frac{\frac{1}{\sqrt{1+X^2}}}{\tan\left(\frac{Y}{\sqrt{1+X^2}}\right)} \right) \tag{4.63}$$

where $X=A/C$ and $C=H - H_f$. H is the height of the structural component above the surface of the fire flame. H_f is the height of flame.

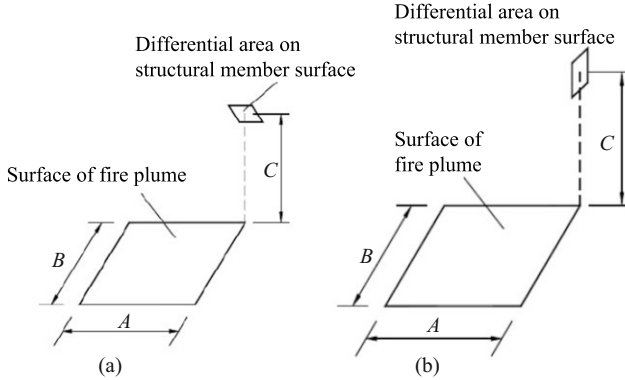


Fig. 4.8 Relative position of structural component surface to the fire plume surface

According to the relative position of a differential area on the i -th plate to the flame plane at the engineering practice, the view factor ϕ_{sf}^i is calculated through the following four equations:

(a) If the differential area parallel to the fire flame surface, as: shown in Fig.4.9(a), ϕ_{sf}^i is obtained by

$$\phi_{sf}^{ia} = 4\phi_{sf}^A \tag{4.64}$$

(b) If the differential area perpendicular to the fire flame surface, as shown in Fig.4.9(b), ϕ_{sf}^i is calculated by

$$\phi_{sf}^{ib} = 4\phi_{sf}^B \tag{4.65}$$

(c) If the differential area parallel to the fire flame surface and beyond the projection of the fire flame, as shown in Fig.4.9(c), ϕ_{sf}^i is calculated by

$$\phi_{sf}^{ic} = \phi_{(s+I+II+III)}^A - \phi_{(II+III)}^A - \phi_{(I+III)}^A + \phi_{III}^A \tag{4.66}$$

where X and Y are listed in Table 4.8. $\phi_{(s+I+II+III)}^A$, $\phi_{(II+III)}^A$, $\phi_{(I+III)}^A$ and ϕ_{III}^A are calculated through Eq.(4.62).

(d) The differential area perpendicular to the fire flame surface and beyond the projection of the fire flame, as shown in Fig.4.9(d), ϕ_{sf}^i is predicated by

$$\phi_{sf}^{id} = \phi_{(s+I+II+III)}^B - \phi_{(II+III)}^B - \phi_{(I+III)}^B + \phi_{III}^B \tag{4.67}$$

where X and Y are listed in Table 4.9. $\phi_{(s+I+II+III)}^B$, $\phi_{(II+III)}^B$, $\phi_{(I+III)}^B$ and ϕ_{III}^B are calculated through Eq.(4.63).

Table 4.8 Values of X and Y

View factor	X	Y
$\phi_{(s+I+II+III)}^A$	$(A + a)/C$	$(B + b)/C$
$\phi_{(II+III)}^A$	a/C	$(B + b)/b$
$\phi_{(I+III)}^A$	$(A + a)/C$	b/C
ϕ_{III}^A	a/C	b/C

4.3.1.3 Parameters Affecting the View Factor

Parameters that affect values of the view factor include the surface of a fire flame, the radiation area of the flame, the flame diameter and the flame height.

(a) Surface of a fire flame

The surface of a fire flame is treated as a square for calculating the view factor and the flame height H_f is assumed as the height of the square^[13].

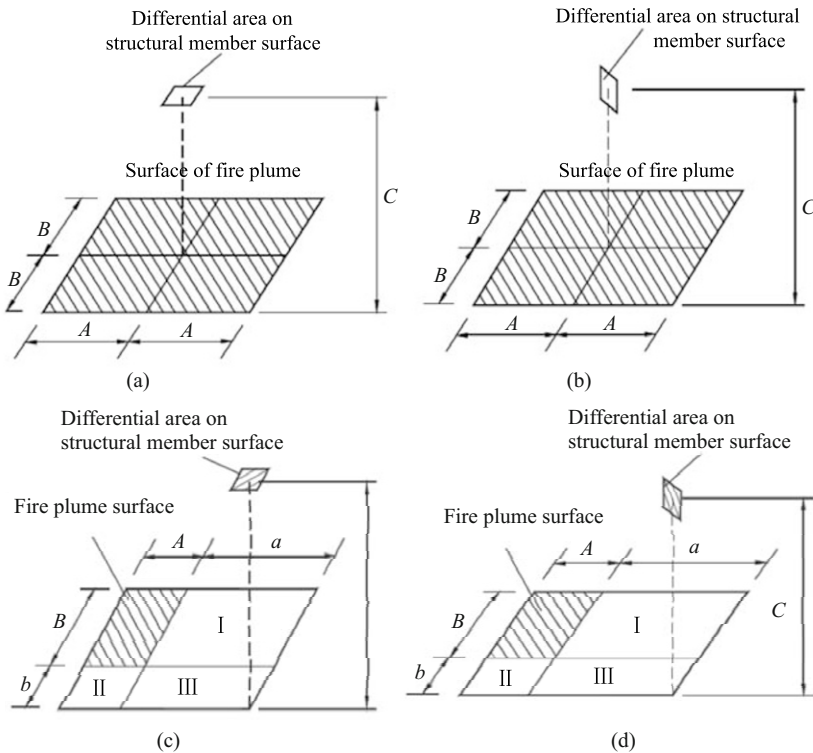


Fig. 4.9 Positions of the differential area of a structural component exposed to a fire

Table 4.9 Values of X and Y

View factor	X	Y
$\phi_{(s+I+II+III)}^B$	$(A+a)/C$	$(B+b)/C$
$\phi_{(II+III)}^B$	a/C	$(B+b)/b$
$\phi_{(I+III)}^B$	$(A+a)/C$	b/C
ϕ_{III}^B	a/C	b/C

(b) Radiation area of the flame

The radiation area of the flame is determined by the fire power Q and the heat release rate q_e as

$$F_f = \frac{Q}{q_e} \quad (4.68)$$

usually $q_e \leq 500 \text{ kW/m}^2$.

(c) Flame diameter

The effective diameter of the flame is calculated by

$$D = \sqrt{\frac{4Q}{\pi q_e}} \quad (4.69)$$

where Q is the fire power and q_e is the heat release rate of per square meter of the fire.

(d) Height of the flame

According to Zukoski model^[14,15], the flame height

$$H_f = 0.23Q^{0.4} - 1.02D \quad (4.70)$$

Calculated results of the flame height with different fire powers are listed in Table 4.10.

4.3.1.4 Temperature of the Flame

The fire flame temperature takes the average temperature of the inner and outer flame as

$$T_f = \left(\frac{T_1^4 + T_2^4}{2} \right)^{1/4} \quad (4.71)$$

where T_1 and T_2 are the temperature of inner flame and outer flame respectively. For the fiber type combustible material, T_1 and T_2 are approximately 1273 °C and 813 °C respectively.

Table 4.10 Height of the flame

Q	D						Q	D		
	2	3	4	5	6	7		5	6	7
1	1.61	0.59	-	-	-	-	14	-	4.36	3.34
2	2.77	1.75	0.73	-	-	-	15	-	4.65	3.63
3	-	2.60	1.58	0.56	-	-	16	-	4.93	3.91
4	-	3.29	2.27	1.25	0.23	-	17	-	5.2	4.18
5	-	3.88	2.86	1.84	0.82	-	18	-	5.46	4.44
6	-	-	3.38	2.36	1.34	0.32	19	-	-	4.7
7	-	-	3.86	2.84	1.82	0.8	20	-	-	4.94
8	-	-	4.3	3.28	2.26	1.24	21	-	-	5.18
9	-	-	-	3.68	2.66	1.64	22	-	-	5.41
10	-	-	-	4.06	3.04	2.02	23	-	-	5.64
11	-	-	-	4.41	3.39	2.37	24	-	-	5.86
12	-	-	-	4.75	3.73	2.71	25	-	-	6.07
13	-	-	-	-	4.05	3.03				

4.3.1.5 Blackness Factor

For ash type material combustion or incomplete combustion, the fire flame blackness factor ϵ_f takes the value of 0.8. For the steel structural component ϵ_f takes the value of 0.8. The blackness factor of smoke ϵ_g represents its ability to emit energy by radiation. For the smoke produced by the combustion of fiber type material ϵ_g takes the value of 0.8.

4.3.2 Parametric Study

4.3.2.1 Effects of the View Factor

As indicated by Eq.(4.57), with the increase in view factor, the energy transferred to the structural component Q_{fr} increases. As an example, for the fire of a fast growing fire type with flame plane area of 3 m×3 m and the heat release rate of 5 MW, effects of the view factor on the temperature elevation of the structural component is shown in Fig. 4.10. It clearly shows that with the increase in view factor, the structural component has a higher temperature^[16].

4.3.2.2 Effects of the Maximum Smoke Temperature

With the increase in the maximum smoke temperature T_g^{\max} the heat transferred to the structural component by radiation decreases, as stated by Eq.(4.55). The temperature difference $T - T'$ is studied to illustrate effects of the flame radiation on the

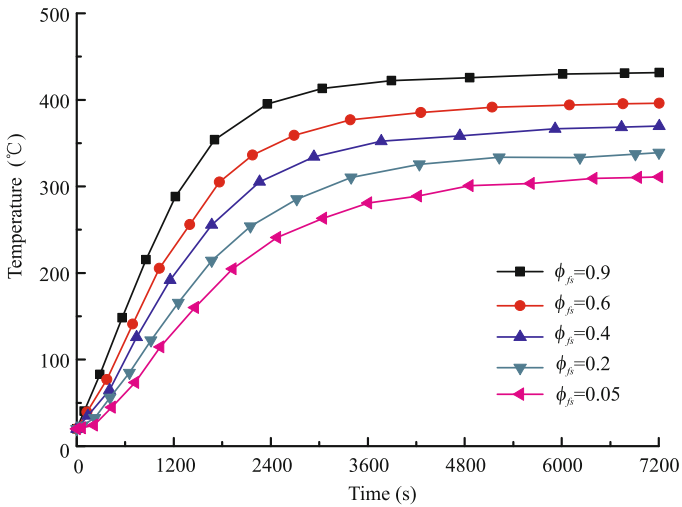


Fig. 4.10 Effects of the view factor on temperature evolution of structural component

temperature elevation of a structural component. T is the temperature of structural component considering effects of the flame radiation and T' is otherwise. Effects of T_g^{\max} on $T - T'$ are shown in Fig.4.11. The fire employed for this study is a fast growing fire with an area of 3 m×3 m and the fire power of from 2 MW to 25 MW. With the increase in T_g^{\max} , $T - T'$ decreases, as shown in Fig. 4.11.

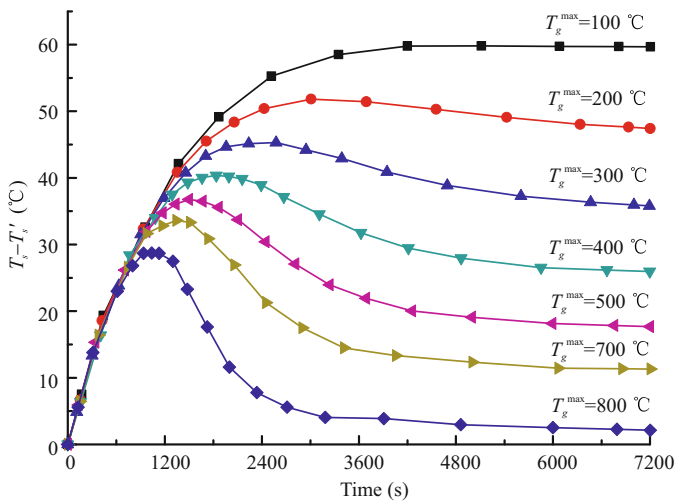


Fig. 4.11 Effects of the maximum smoke temperature

4.3.2.3 Effects of Exposure Area Factor

The exposure area factor ξ is the ratio between the area exposed to the total surface area of the structural component. With the increase in ξ , $T - T'$ increase, which means the effect of the flame radiation on the temperature elevation of a structural component increases, as shown in Fig. 4.12.

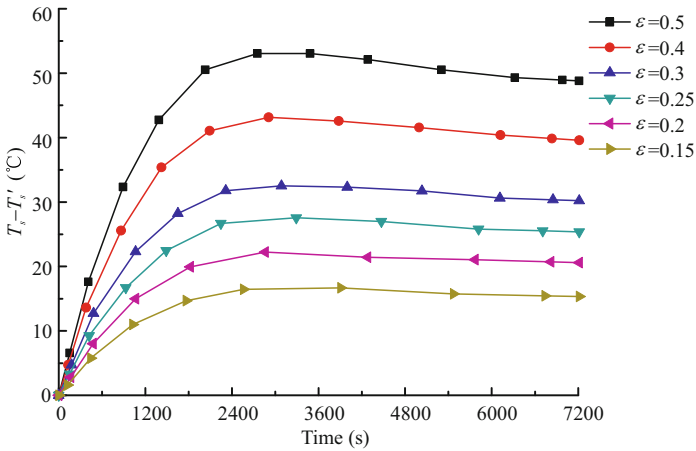


Fig. 4.12 Effects of the surface expose area factor

4.3.2.4 Effects of Configuration Factor

Eq.(4.54) and Eq.(4.59) show that the configuration factor of a structural component F_s/V_s affects the value of Q_{gr} and Q_{sc} greatly. When the temperature of the structural component is higher than that of the smoke, $Q_{gr} < 0$ and $Q_{sc} < 0$. Fig. 4.13 illustrates effects of the flame radiation to the temperature elevation of a structural component with different configuration factors. The fire is a fast growth fire with area of $3 \text{ m} \times 3 \text{ m}$ and fire power of 5 MW. It can be seen that with the increase of the configuration factor, the temperature difference $T - T'$ decreases.

4.3.3 Limit Value of Flame Radiation

According to the Table 3.2.1 of CECS200^[5], if the temperature difference of a structural component, including and not including effects of the flame radiation, is less than $20 \text{ }^\circ\text{C}$ after 1800 s, the heat transferred by radiation can be ignored.

Through examining effects of the view factor, the configuration factor, the effective area of a structural component exposed to the flame radiation and the flame temperature, the criteria for ignoring effects of the flame radiation on the temperature

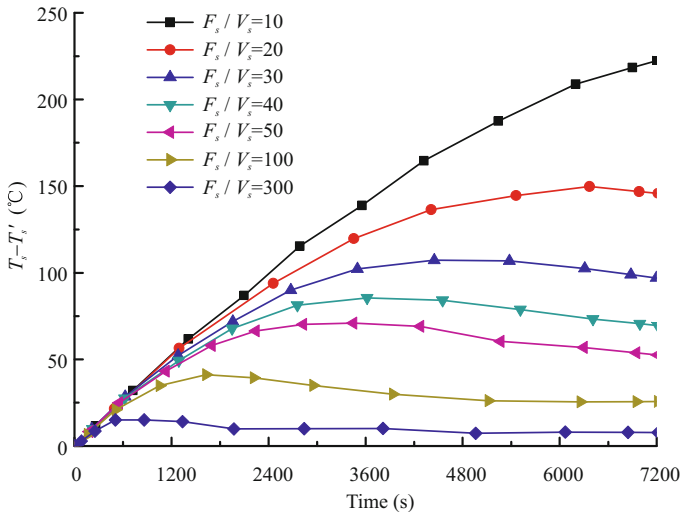


Fig. 4.13 Effects of the surface exposed area factor

elevation of a structural component is listed in Appendix C based on the analysis of 1,030 cases. If the view factor is less than the value listed in Appendix C, the effect of the flame radiation on the temperature elevation of a structural component is ignored^[17].

4.4 Example

Parameters of the studied fire in a large space building are

- the fire load of 250 MJ/m²;
- the fire power of 5 MW;
- the fire increase type of fast growing fire with growth factor α of 0.04689;
- the heat release rate q_e of 250 kW/m²;
- the dimension of the building of 32 m (length) \times 32 m (width) \times 15 m (height);
- the dimension of the opening of 10 m (length) \times 2 m (height) and 0 m above the floor;
- the configuration factor of the structural component F/V of 100;
- the effective area to the flame radiation ξ of 0.2;
- and the fire duration time of 2 h.

Calculate the temperature evolution of a structural component.

Answer:

(a) According to the simplified calculation method for the smoke temperature in a large space building fire, the maximum smoke temperature $T_g^{\max}=170$ °C. The effective fire diameter is

$$D = \sqrt{\frac{4 \times 5 \times 10^3}{3.15 \times 250}} = 5.05 \text{ m} \quad (4.72)$$

The square dimension of the flame is

$$a = \sqrt{\frac{5 \times 10^3}{250}} = 4.47 \text{ m} \quad (4.73)$$

The height of the flame is

$$H_f = 0.23 \times 5000^{0.4} - 1.02 \times 5.05 = 1.79 \text{ m} \quad (4.74)$$

The distance of the flame to the structural component surface is

$$C = 15 - 1.79 = 13.21 \text{ m} \quad (4.75)$$

Hence, the view factor is 0.044.

(b) From Appendix C, for 0.044 is less than 0.57, the effect of the flame radiation on the temperature elevation of structural component is ignored. The temperature elevation of the structural component is plotted in Fig. 4.14. And the temperature difference is lower than 20 °C, including and not including the effects of flame radiation.

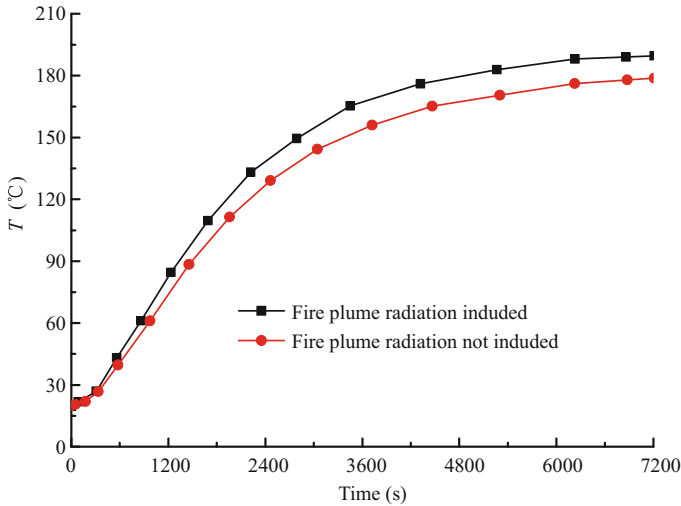


Fig. 4.14 Effects of flame radiation on the temperature evolution of a structural component

References

- [1] C. M. Yu. *Heat Transfer and Numerical Simulation*. Tsinghu University Press, 1982.

- [2] G. Q. Li, L. H. Han, G. B. Lou, and S. C. Jiang. *Steel and Steel-Concrete Composite Structures Fire Resistance Design*. China Architecture & Building Press, 2006.
- [3] International Organization for Standardization. *Fire-Resistance Tests, Elements of Building Construction, Part 1: General Requirements*. International Organization for Standardization, 1999.
- [4] U. Wickstrom. Temperature analysis of heavily-insulated steel structures exposed to fire. *Fire Safety Journal*, 9, 1995.
- [5] China Association for Engineering Construction Standardization. *Technical Code for Fire Safety of Steel Structures in Buildings CECS200-2006*. China Plan Press, 2006.
- [6] European Committee for Standardization. *EN1993-1-2. Eurocode 3: Design of Steel Structures, Part 1.2, General Rules, Structural Fire Design*. European Committee for Standardization, 2005.
- [7] D. Z. Ma and Y. Q. Li. Material properties of hot rolled steel members with heavy section under fire. *Industry Building*, 3, 1990.
- [8] X. Q. Kong. *Application of the finite element method in heat exchange (third edition)*. Science Press, 1998.
- [9] Y. Du and G. Q. Li. Simplified algorithm of steel member at elevated temperature in large space fire based on field model. *Fire Science and Technology*, 3, 2006.
- [10] Y. Du and G. Q. Li. Practical calculation method for temperature elevation of steel members on flame radiation in large space building fire. *Journal of Architecture and Civil Engineering*, 3, 2008.
- [11] Y. Du and G. Q. Li. Fire radiation effect on steel member at elevated temperature in large space fire. *Fire Safety Science*, 4, 2006.
- [12] Y. Du, Y. Z. Lu, and Q.I. Jiang. Simplified conditions of elevated temperature for structural members based on field model. *Fire Science and Technology*, 3, 2010.
- [13] Y. Du. *A Practical Approach for Fire Resistance Design of Large Space Building Grid Structures*. PhD thesis, Tongji University, 2007.
- [14] E. E. Zukoski, T. Kubota, and B. Cetegen. Entrainment in fire plumes. *Fire Science and Technology*, 3(3):107–121, 1981.
- [15] B. M. Cetegen, E. E. Zukoski, and T. Kubota. Entrainment and flame geometry of fire plumes. *Technical Report, No. PB-83-107847. California Institute of Technology, Pasadena (USA)*, 1982.
- [16] J. Q. Huang, G. Q. Li, P. Q. Bao, and K. Liu. Influence of flame radiation on temperature rising of steel members in large space fire. *Fire Science and Technology*, 5, 2008.
- [17] Y. Du and G. Q. Li. Standard for steel structures without fire protection in large space buildings fire. *Fire Science and Technology*, 7, 2008.

Fire-Resistance of Isolated Flexural Structural Components

5.1 Load-bearing Capacity of a Flexural Steel Component at High Temperatures

5.1.1 Strength of a Flexural Steel Component at High Temperatures . . .

When one of the following conditions is met, it is thought that the lateral torsional buckling of a flexural component is prevented and only the yield strength capacity of the flexural component is checked^[1] at high temperatures

- a rigid decking (reinforced concrete slab or steel plate) is connected to the compression flange of the flexural component;
- the ratio of unsupported length l_1 of the compression flange of a simply supported beam to its width b_1 does not exceed the value given in Table 5.1.

The bending strength of solid web member bent in its principal plane at high temperatures^[1] is checked by

$$\frac{M}{\gamma W_n} \leq \gamma_R f_{yT} \quad (5.1)$$

5.1.2 Lateral Torsional Buckling Strength of a Flexural Steel Component at High Temperatures

The bending moment capacity for overall stability of flexural member at ambient and high temperatures^[1] is expressed respectively through

$$M_{crT} = C_1 \beta_b \frac{\pi^2 EI_y}{l^2} \left[C_2 a + C_3 \beta + \sqrt{(C_2 a + C_3 \beta)^2 + \frac{I_\omega}{I_y} \left(1 + \frac{GI_t l^2}{\pi^2 EI_\omega} \right)} \right] \quad (5.2)$$

Table 5.1 Maximum value of l_1/b_1 allowed to prevent lateral torsional buckling of a flexural component

Steel Grade	Beams without intermediate lateral support		Beams with intermediate lateral support
	Loading at the upper flange	Loading at the lower flange	
	Q235	13.0	
Q345	10.5	16.5	13.0
Q390	10.0	15.5	12.5
Q420	9.5	15.0	12.0

Note: (a) The maximum l_1/b_1 values of beams made of steel other than Q235 be multiplied by $\sqrt{235/f_y}$; (b) For beams not having lateral supports within the span, l_1 is the span length. For those provided with lateral supports within the l_1 span, is the distance between these supports

$$M_{crT} = C_1 \beta_b \frac{\pi^2 E_T I_y}{l^2} \left[C_2 a + C_3 \beta + \sqrt{(C_2 a + C_3 \beta)^2 + \frac{I_\omega}{I_y} \left(1 + \frac{G_T I_t l^2}{\pi^2 E_T I_\omega} \right)} \right] \quad (5.3)$$

where C_1 , C_2 and C_3 are parameters related to the load type.

The bending moment capacity at high temperatures can also be expressed as

$$M_{crT} = \phi_{bT} W f_{yT} \quad (5.4)$$

Define the ratio of overall stability factor of a flexural steel component at high temperatures to that at ambient temperature as α_b . The partial factor of steel at high temperature is the same as that at ambient temperature and α_b can be calculated through

$$\alpha_b = \frac{\phi_{bT}}{\phi_b} = \frac{M_{crT} f_y}{M_{cr} f_{yT}} \quad (5.5)$$

Assume that the Poisson ratio of steel at high temperature is the same as that at ambient temperature

$$\frac{G_T}{E_T} = \frac{G}{E} \quad (5.6)$$

Then Eq.(5.5) can be rewritten as

$$\alpha_b = \frac{E_T}{E} \frac{f_y}{f_{yT}} \quad (5.7)$$

Obviously α_b depends only on the yield strength and Young's modulus of steel at high temperature. For structural steel, values of α_b at various temperatures are listed in Table 5.2.

The overall stability factor of a flexural steel component at high temperatures can be obtained with α_b as

Table 5.2 Values of α_b for a flexural component made of structural steel at elevated temperatures

Temperature (°C)	20	100	150	200	250	300	350	400	450	500
α_b	1.000	0.980	0.966	0.949	0.929	0.905	0.896	0.917	0.962	1.027
Temperature (°C)	550	600	650	700	750	800	850	900	950	1000
α_b	1.094	1.101	0.961	0.950	1.011	1.000	0.870	0.769	0.690	0.625

$$\varphi_{bT} = \alpha_b \varphi_b \quad (5.8)$$

The above overall stability factor is obtained through elastic stability theory. If $\varphi_{bT} > 0.6$, the flexural steel component buckles at plastic state and the overall stability factor should be modified by

$$\varphi'_{bT} = 1.07 - \frac{0.282}{\alpha_b \varphi_b} \quad (5.9)$$

The overall stability of a flexural steel component at high temperatures is checked by

$$\frac{M}{\varphi'_{bT} W} \leq f_{yT} \quad (5.10)$$

5.1.3 Critical Temperature of a Flexural Steel Component in Fire

With the elevation of temperatures, the load bearing capacity of a structural component degrades. The critical temperature of a structural component is the temperature at which the load bearing capacity of the structural component equals the applied load effect. For a flexural steel component, the critical temperature can be obtained through

$$\frac{M}{\varphi'_{bT} W} = \eta_T \gamma_R f \quad (5.11)$$

Define the load ratio R as the applied load effect to the load bearing capacity of the structural component at ambient temperature, i.e.

$$R = \frac{M}{\varphi'_b W f} \quad (5.12)$$

Substituting Eq.(5.11) into Eq.(5.12) gives

$$R = \frac{\varphi'_{bT}}{\varphi'_b} \eta_T \gamma_R \quad (5.13)$$

Given the overall stability factor of the flexural component at ambient temperature φ'_b and the load ratio R , the critical temperature of the flexural component can be obtained, as listed in Table 5.3.

Table 5.3 Critical temperature of a flexural steel component (°C)

R	ϕ'_b					
	≤ 0.5	0.6	0.7	0.8	0.9	1
0.3	669	669	672	674	675	676
0.35	650	650	652	653	654	655
0.4	634	634	635	635	636	636
0.45	621	620	620	619	618	618
0.5	610	608	606	604	602	600
0.55	600	596	591	588	585	583
0.6	586	580	575	571	568	565
0.65	569	563	557	553	550	548
0.7	550	543	538	534	532	530
0.75	528	522	517	515	513	511
0.8	500	497	495	494	493	492
0.85	466	466	470	471	472	472
0.9	423	423	441	446	449	450

After obtaining the critical temperature T_d , the thickness of fire protection can be obtained through

$$d_i = 5 \times 10^{-5} \times \frac{\lambda_i}{\left(\frac{T_d - 20}{t} + 0.2\right)^2 - 0.044} \frac{F_i}{V} \quad (5.14)$$

where t is required fire resistance time.

5.1.4 Example

Consider a hot rolled steel beam of section I36b with a span of 5 m

- the design strength of steel $f=215$ MPa;
- the surface area per unit length is 1.289 m²/m;
- the volume per unit length is 8.364×10^{-3} m³/m;
- the ratio of the surface exposed to fire is 0.8 and the effective fire exposure area $F_i=0.8 \times 1.289=1.031$ m²/m;
- the applied uniformly distributed load q is acting on the upper flange;
- the section modulus of the beam $W=920.8$ cm³;
- the overall stability factor of the beam at ambient $\phi'_b=0.73$ and
- the conductive factor of the fire protection material $\lambda_i=0.093$ W/(m·°C).

Design the fire resistance of the beam.

Instance I:

Knowing that the applied uniformly distributed load $q=30$ kN/m and the fire resistance time of the beam is 2.0 h, find the required thickness of fire protection.

Answer:

(a) The load ratio acting on the beam is

$$R = \frac{M}{\phi_b' W_f} = \frac{1}{8} \frac{30 \times 5^2 \times 10^6}{0.73 \times 920.8 \times 10^3 \times 215} = 0.649$$

(b) According to Table 5.3, the critical temperature of the beam is

$$T_d = 556.2 \text{ }^\circ\text{C}$$

(c) According to Eq.(5.14), the required fire protection thickness is

$$\begin{aligned} d_i &= 5 \times 10^{-5} \times \frac{\lambda_i}{\left(\frac{T_d - 20}{t} + 0.2\right)^2 - 0.044} \frac{F_i}{V} \\ &= 5 \times 10^{-5} \times \frac{0.093}{\left(\frac{556.2 - 20}{2.0 \times 3600} + 0.2\right)^2 - 0.044} \frac{1.031}{8.364 \times 10^{-3}} \\ &= 18.3 \text{ mm} \end{aligned}$$

Instance II:

Knowing that the applied uniformly distributed load $q=30$ kN/m the thickness of the fire protection $d_i=25$ mm, find the fire resistance time.

Answer:

(a) According to Table 5.3, the critical temperature of the beam is

$$T_d = 556.2 \text{ }^\circ\text{C}$$

(b) The fire resistance of the beam is

$$\begin{aligned} t &= \frac{T_d - 20}{-0.2 + \sqrt{5 \times 10^{-5} \times \frac{\lambda_i F_i}{d_i V} + 0.044}} \\ &= \frac{556.2 - 20}{-0.2 + \sqrt{5 \times 10^{-5} \times \frac{0.093}{0.025} \frac{1.031}{8.364 \times 10^{-3}} + 0.044}} \\ &= 2.54 \text{ h} \end{aligned}$$

Instance III:

Knowing that the applied uniformly distributed load $q=25$ kN/m, the thickness of fire protection is 30 mm and the required fire resistance time $t=2.5$ h, check whether the beam can meet the fire resistance requirement.

Answer I: Critical temperature method

(a) According to Eq.(5.13), the load ratio of beam is

$$R = \frac{M}{\phi_b' W f} = \frac{1}{8} \frac{25 \times 5^2 \times 10^6}{0.73 \times 920.8 \times 10^3 \times 215} = 0.541$$

According to Table 5.3, the critical temperature of the beam is

$$T_d = 592.9 \text{ }^\circ\text{C}$$

(b) The parameter of the fire protected beam is

$$B = \frac{\lambda_i F_i}{d_i V} = \frac{0.093}{0.03} \frac{1.031}{8.364 \times 10^{-3}} = 382.1 \text{ W}/(\text{m}^{-3} \cdot ^\circ\text{C})$$

and the temperature of the steel beam after 2.5 h of fire exposure is

$$T_s = \left(\sqrt{0.044 + 5 \times 10^{-5} \times 382.1} - 0.2 \right) \times 3 \times 3600 + 20 = 573.0 \text{ }^\circ\text{C}$$

and $T_s = 573.0 \leq T_d = 592.9$

Hence, the protected steel can meet the fire resistance requirement.

Answer II: Load-bearing method

(a) The temperature of the beam after 2.5 h fire exposure is

$$T_s = 573.0 \text{ }^\circ\text{C}$$

(b) The reduction factor of the yield strength and Young's modulus of steel at temperature 573.0 °C is

$$\frac{f_{yT}}{f_y} = 0.522 \text{ and } \frac{E_T}{E} = 0.580$$

According to Eq.(5.7), the reduction factor of the overall stability factor of the steel beam at high temperature is

$$\alpha_b = \frac{E_T}{E} \frac{f_y}{f_{yT}} = 0.580 \times \frac{1}{0.522} = 1.112$$

and

$$\alpha_b \phi_b = 1.112 \times 0.73 = 0.812 > 0.6$$

The beam will buckle in a plastic state. The overall stability factor should be modified as

$$\phi_{bT}' = 1.07 - \frac{0.282}{0.812} = 0.723$$

(c) The bending moment capacity of the beam at high temperature is

$$M_{crT} = \phi_{bT}' W f_{yT} = 0.723 \times 920.8 \times 10^3 \times 0.522 \times 1.1 \times 215 \times 10^{-6} = 82.2 \text{ kN} \cdot \text{m}$$

(d) Check $M_{crT} \geq M$.

The applied bending moment is

$$M = \frac{1}{8} q l^2 = \frac{1}{8} \times 25 \times 5^2 = 78.1 \text{ kN} \cdot \text{m}$$

and

$$M_{crT} \geq M$$

Hence, the beam can meet the fire resistance requirement.

5.2 Fire-resistance of Flexural Steel-Concrete Composite Components

Composite members exhibit enhanced strength and stiffness when compared to the contribution of their components acting separately. However, the steel component in a steel-concrete composite beam is sensitive to fire due to its strength and elastic modules will be reduced quickly when exposed to fire.

Six full-scale composite structural experiments were carried out by BRE in Cardington^[2,3,4]. Wang^[5] firstly conducted a 2-D model analysis on the composite beams in the Cardington test and a further theoretical study by Wang^[6] indicated the importance of the tensile membrane action in maintaining the robustness of the composite slab. Rose et al.^[7] using the 3D model simulation showed a good match between predicted and test deflections for the beam test, the plane frame test and the BRE corner test in the Cardington test.

Wang^[8] had also presented a novel way to significantly reduce the fire protection cost to a composite beam and only the steel lower flange and a fraction of the steel web are protected. Nadjai et al.^[9] described an experimental and numerical study at both ambient and elevated temperatures on the behavior of full-scale composite steel beams.

A procedure for finite element thermal analysis of composite steel and concrete beams was described and implemented by Fakury^[10] in a finite element based computer program. Benedettia^[11] presented an analytical procedure for the incremental thermal mechanical solution of simply supported composite beams.

The required fire protection to a steel component is traditionally determined based on results of standard fire tests. At present, analytical methods proposed in BS 5950 Part 8^[12] or Eurocode 4 Part 1.2^[13] may also be used. In the CECS200^[11], an analytical method is also provided to check the load bearing capacity of steel-concrete composite beams in fire.

5.2.1 Material Properties and Temperature Calculation of a Composite Beam

The strength reduction factor of concrete at elevated temperatures proposed in EC4^[13] may be used for this study. A fitting formula to calculate the reduction factor for concrete strength at elevated temperatures is given as

$$f_{cT} = \frac{f_c}{1 + \exp\left(\frac{T_c - 569}{157}\right)} \quad (5.15)$$

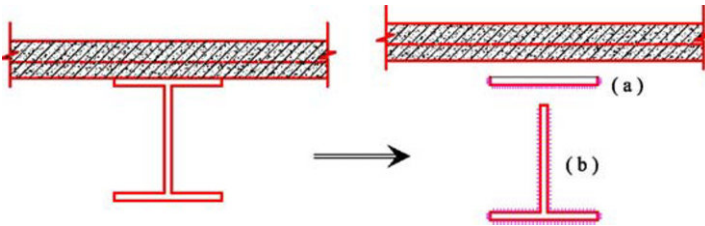
The average temperature of concrete slabs subjected to standard fire can be obtained from Table 5.4 given in CECS200^[11].

The temperature of H-shaped steel beam consisting of a steel-concrete composite beam subjected to a standard fire can be obtained by dividing the steel beam into two parts, i.e. the upper flange which is exposed to the fire with three sides and the inverse

Table 5.4 Average temperatures in concrete slabs subjected to a standard fire (°C)

Depth of slab (mm)	Fire duration (min)			
	30	60	90	100
≤ 50	405	635	805	910
≥ 100	265	400	510	600

T shape part including the web and lower flange which is exposed to the fire with all sides, as shown in Fig. 5.1. According to the section factor, the temperature of the steel part can be obtained from the Table 5.5 in CECS200^[1].

**Fig. 5.1** Simplified model for determining the temperature of a steel beam

5.2.2 Strength of a Composite Beam at High Temperature

The load bearing capacity of a composite beam in a fire is checked by^[1]

$$M \leq M_u^T \quad (5.16)$$

where

(a) for a simply-supported composite beam

$$M_u^T = M_R^+ \quad (5.17)$$

and (b) for a fixedly-supported composite beam

$$M_u^T = M_R^+ + M_R^- \quad (5.18)$$

A plastic approach using the yielding strength distribution over the cross section of the composite beam can be employed to determine the positive and negative moment bearing capacity. The yield stress of concrete and steel of a composite beam in a fire can be obtained through Eq.(5.16) when the temperature of the concrete slab and steel beam is determined.

Table 5.5 Temperature of a bare steel members exposed to the ISO834 Standard fire (°C)

Time (min)	T_g (°C)	Section factor F/V (m^{-1})									
		10	20	30	40	50	100	150	200	250	300
0	20	20	20	20	20	20	20	20	20	20	20
5	576	32	44	56	67	78	133	183	229	271	309
10	678	54	86	118	148	178	311	416	496	552	590
15	739	81	138	193	246	295	491	609	669	697	711
20	781	112	197	277	350	416	638	724	752	763	767
25	815	146	261	365	456	533	737	786	798	802	805
30	842	182	327	453	556	636	799	824	830	833	834
35	865	221	396	538	646	721	838	852	856	858	859
40	885	261	464	618	723	787	866	874	877	879	880
45	902	302	531	690	785	835	888	893	896	897	898
50	918	345	595	752	834	871	906	911	913	914	915
55	932	388	655	805	871	898	922	926	928	929	929
60	945	432	711	848	900	919	936	940	941	942	943
65	957	475	762	883	923	936	949	952	954	954	955
70	968	518	807	911	941	951	961	964	965	966	966
75	979	561	846	933	956	963	972	974	976	976	977
80	988	603	880	952	969	975	982	984	986	986	987
85	997	643	908	968	981	985	992	994	995	995	996
90	1006	683	933	981	991	995	1001	1003	1004	1004	1004

5.2.3 Critical Temperature of a Composite Beam

Define the load ratio as

$$R = \frac{M}{M_u} \quad (5.19)$$

where M_u is the ultimate moment capacity of a composite beam at normal temperature.

According to the required fire duration of a composite beam, the temperature of the concrete slab T_c can be obtained through Table 5.4. Given an initial exposure time of the steel beam (usually 10 min), the temperature of the steel beam is obtained with Table 5.5. Then the ultimate moment capacity of the composite beam at elevated temperature M_u^T is obtained at the given temperature. If M_u^T is larger than M , then increase the fire exposure time until the temperature of lower flange reaches a temperature T_{cr} at which M_u^T is equal to M . Fig. 5.2 shows the flowchart of steps associated with the determination of the critical temperature calculation.

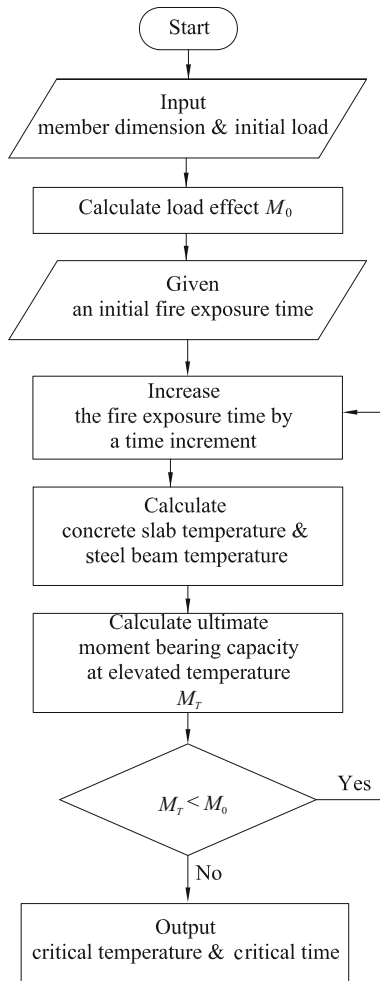


Fig. 5.2 Flow chart showing steps associated with the critical temperature calculation

5.2.4 Parametric Study

In order to investigate parameters affecting the critical temperature of a composite beam, parametric studies are carried out. Parameters include the composite beam dimension, the strength of concrete and steel, the slab depth, the effective width of the concrete slab and the required fire duration. The analyzed composite beam is shown in Fig. 5.3. The rib height of the steel deck is 75 mm. The thickness of concrete slab is within the range of 50 mm to 100 mm and the effective width of the concrete slab is from 1200 mm to 1800 mm. The required fire duration is often 30 min, 60 min, 90 min or 120 min.

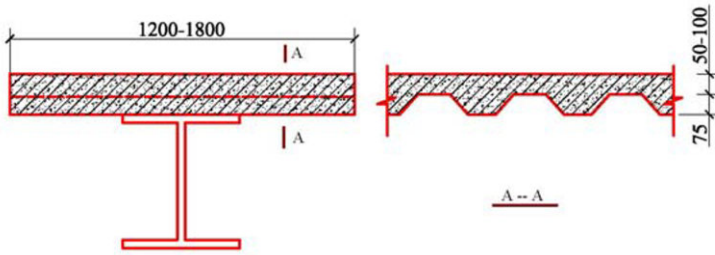


Fig. 5.3 Dimension of the composite slab (mm)

5.2.4.1 Dimension of the Composite Beam

Critical temperatures of composite beams with six sets of dimensions are calculated at different load levels with a fixed fire duration of 60 min. Results are plotted in Fig. 5.4. The slab depth and effective width of concrete slab are 80 mm and 1500 mm respectively, the steel and concrete grades are Q235 and C35 respectively.

From Fig. 5.4, it is shown that the steel beam dimension has little influence on the critical temperature of a composite beam simply or fix-ended.

5.2.4.2 Strength of the Concrete and Steel

Critical temperatures of composite beams with various grades of steel and concrete are analyzed at different load levels. Analyzed results are plotted in Fig. 5.5 and Fig. 5.6. The studied steel beam is H 350×175×7×11 with the fire duration of 60 min and the slab depth and effective width of 80 mm and 1500 mm respectively.

From Fig. 5.5 and Fig. 5.6, it is observed that the grade of steel and concrete has little influence on the critical temperature of both pin- and fix-ended composite beams.

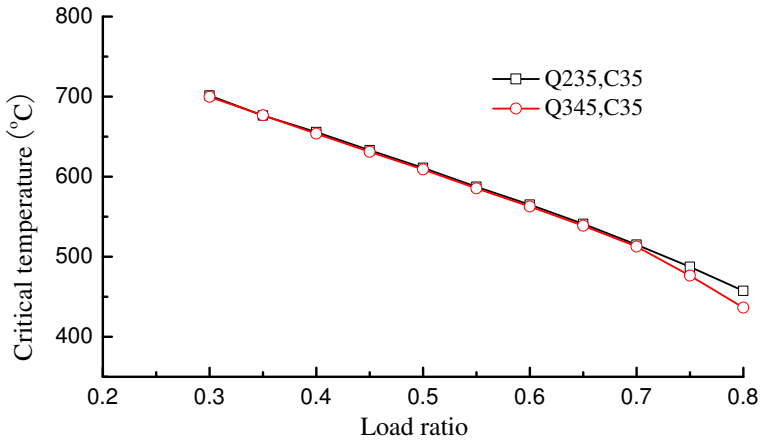
5.2.4.3 Depth of the Concrete Slab

Critical temperatures of composite beams with different depth of slabs are analyzed at various load levels and plotted in Fig. 5.7. The steel beam is H 350×175×7×11 with the effective width of slab of 1500 mm and the steel and concrete grades of Q235 and C35 respectively fire duration of 60 min.

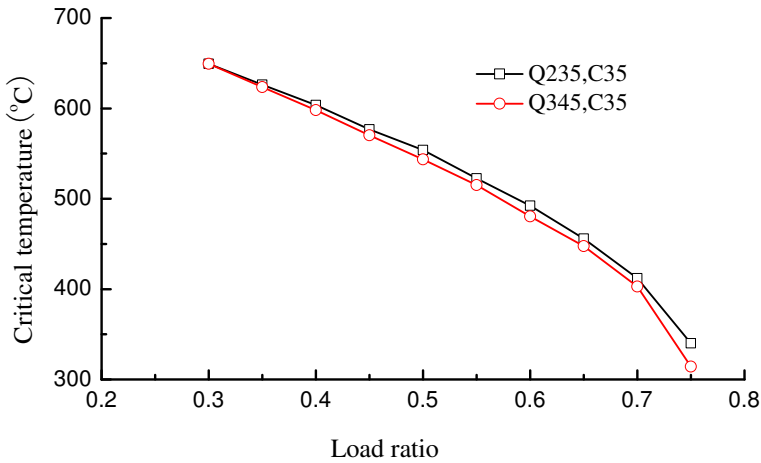
Fig. 5.7 clearly shows that the depth of concrete slab has a significant influence on critical temperatures of both pin- and fix-ended composite beams. At a given load level, the composite slab with a thicker slab has a higher critical temperature.

5.2.4.4 Effective Width of the Concrete Slab

Critical temperatures of composite beams with different effective slab width are analyzed at various load levels and plotted in Fig. 5.8. The steel beam is



(a) Critical temperatures of simply supported composite beams



(b) Critical temperatures of fix-ended composite beams

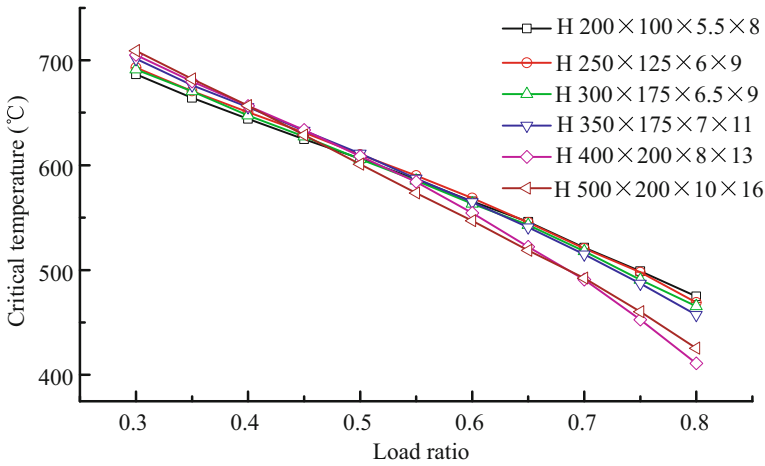
Fig. 5.4 Influence of the steel beam dimension on critical temperatures of composite beams with various load levels

H 350×175×7×11 with the depth of slab of 80 mm and the steel and concrete grades of Q235 and C35 respectively fire duration of 60 min.

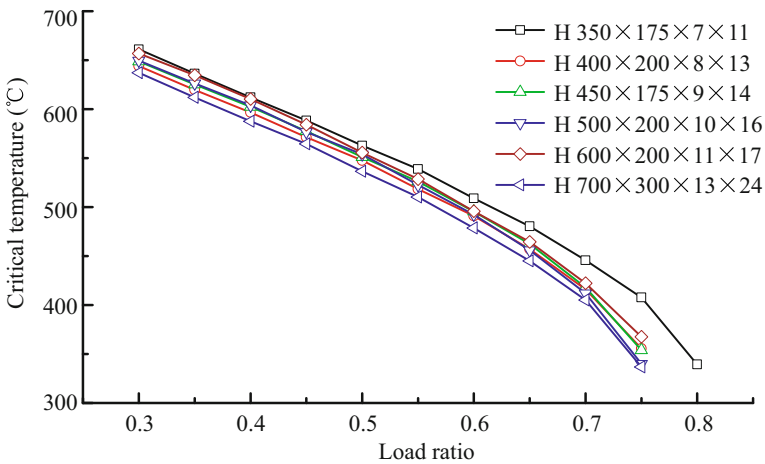
The effective slab width has little influence on the critical temperature of composite beams at low load levels. At high load level, the composite beam with the larger effective width has a higher critical temperature as shown in Fig. 5.8.

5.2.4.5 Fire Duration of Composite Beams

Critical temperatures of composite beams in different fire durations are analyzed at various load levels and plotted in Fig. 5.9. The steel beam is H 350×175×7×11 with



(a) Critical temperatures of simply supported composite beams

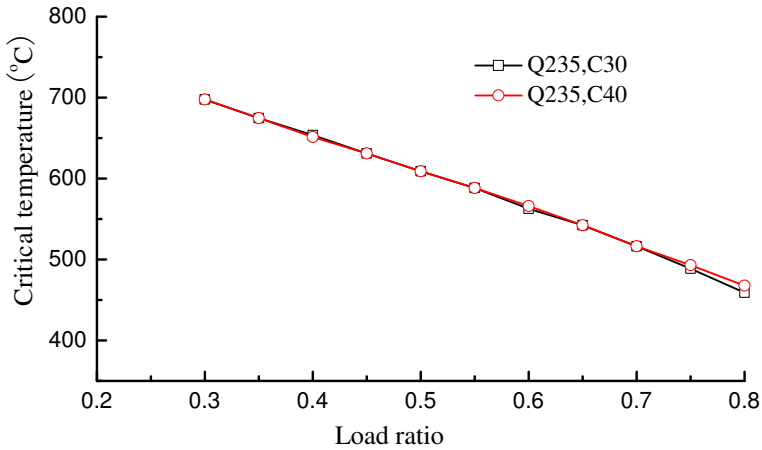


(b) Critical temperatures of fix-ended composite beams

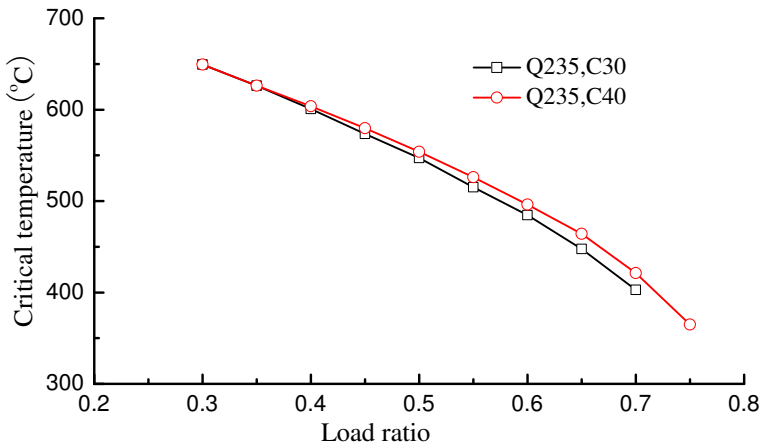
Fig. 5.5 Influence of the steel strength on critical temperatures of composite beams at various load levels

the depth and effective width of slab of 80 mm and 1500 mm respectively and the steel and concrete grades of Q235 and C35 respectively.

Fig. 5.9 shows that the required fire duration has great influence on the critical temperature of a composite beam. For a simply supported composite beam with fire exposure time less than 60 min, the fire duration has little influence on the critical temperature.



(a) Critical temperatures of simply supported composite beams



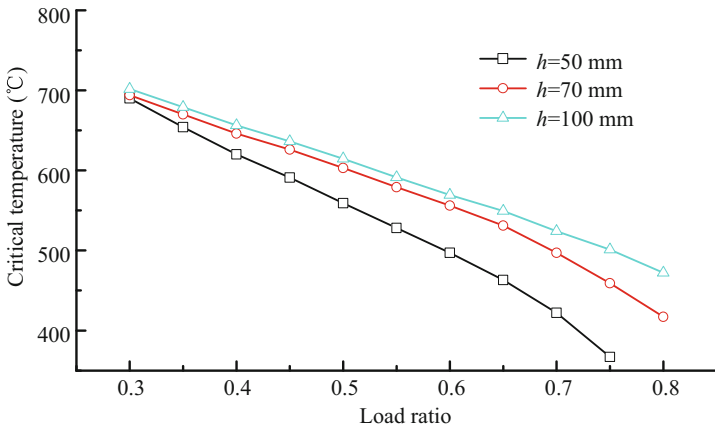
(b) Critical temperatures of fix-ended composite beams

Fig. 5.6 Influence of the concrete strength on critical temperatures of composite beams at various load levels

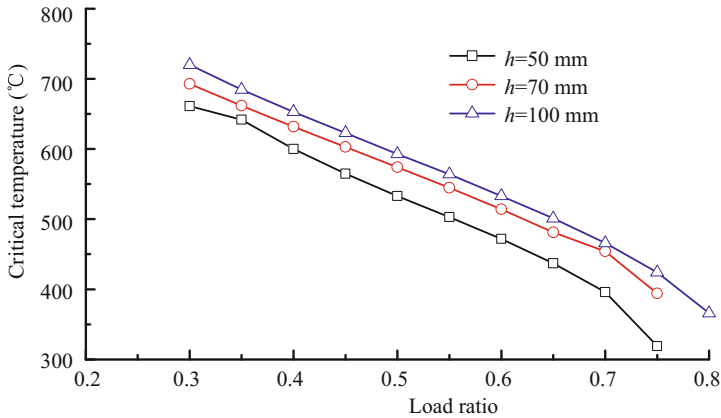
5.2.5 Simplified Approach for the Fire Resistance Design of Composite Beams

5.2.5.1 Critical Temperature

Parametric studies showed that only the slab depth and the required fire duration have great influence on the critical temperature of a composite beam. The critical temperature of composite beams with various depth of slab and fire duration at various load level for pin-ended and fix-ended composite beams are listed in Table D-1 and D-2 in Appendix D.



(a) Critical temperatures of simply supported composite beams



(b) Critical temperatures of fix-ended composite beams

Fig. 5.7 Influence of the slab depth on critical temperatures of composite beams at various load levels

5.2.5.2 Determination of the Fire Protection Thickness

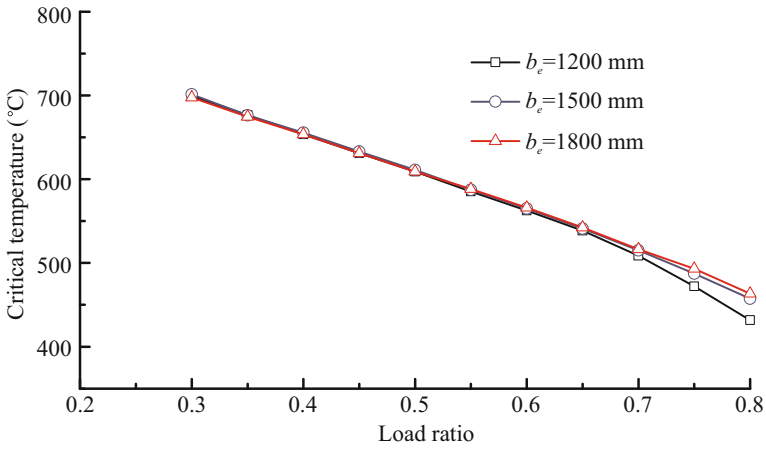
The temperature of a steel component with fire protection is calculated by

$$T_s = (\sqrt{0.044 + 5 \times 10^{-5} B} - 0.2)t + 20 \tag{5.20}$$

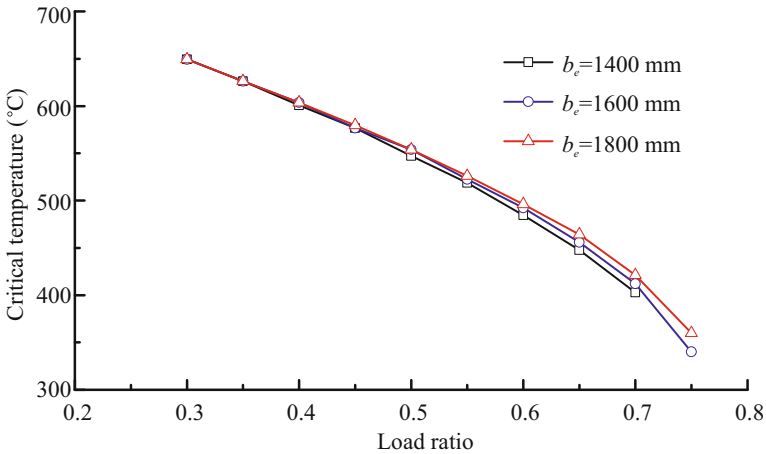
where B is the comprehensive coefficient of heat conductivity given by

$$B = \frac{\lambda_i F}{d_i V} \tag{5.21}$$

The thickness of fire protection is obtained through



(a) Critical temperatures of simply supported composite beams



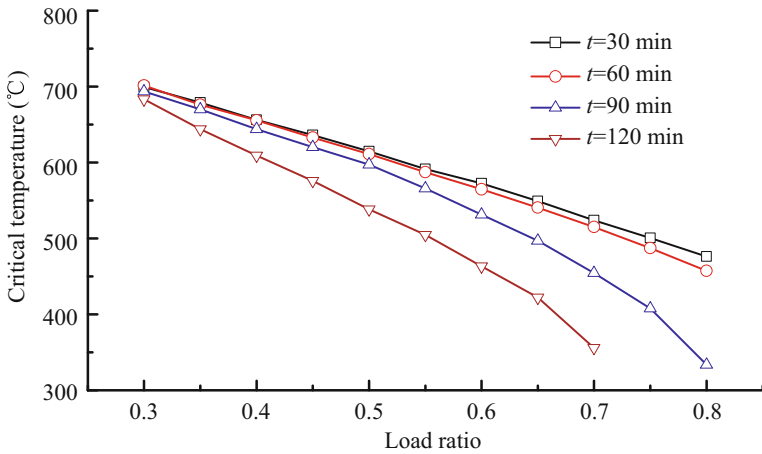
(b) Critical temperatures of fix-ended composite beamf

Fig. 5.8 Influence of the effective slab width on critical temperatures of composite beams at various load levels

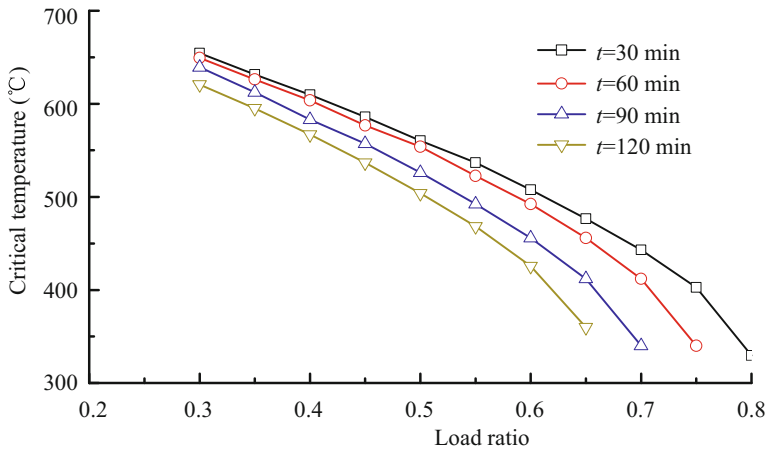
$$d_i = \frac{5 \times 10^{-5} \lambda_i}{\left(\frac{T_{cr} - 20}{t} + 0.2\right) - 0.044} \frac{F}{V} \quad (5.22)$$

5.2.6 Example and Comparison

An example is presented to demonstrate the application of the fire resistance design procedure for composite beams, and comparisons are made between the CECS200^[1] and the simplified approach proposed.



(a) Critical temperatures of simply supported composite beams



(b) Critical temperatures of fix-ended composite beams

Fig. 5.9 Influence of the fire durations on critical temperatures of the composite beams at various load levels

5.2.6.1 Composite Beam Studied

The depth and effective width of the concrete slab are 100 mm and 1500 mm with concrete grade C30 respectively. The steel deck is GH-344 and the rib height is 76 mm with the steel grade of Q235. The span of the composite beam is 4 m. The design load is 90 kN/m and fire duration requirement is 90 min. The heat conductivity of the fire protection is 0.1 W/(m·°C).

5.2.6.2 Code Approach

The moment at the beam middle span

$$M = \frac{ql^2}{8} = \frac{90 \times 4^2}{8} = 180 \text{ kN} \cdot \text{m}$$

Assume that the depth of fire protection is 19 mm. Then the temperature of the upper flange of the steel beam with fire protection is 385 °C and that of the lower flange and web is 648 °C. Thus the ultimate moment resistance capacity is obtained as 196 kN·m, which is larger than M . The fire protection thickness may be adopted as 19 mm.

5.2.6.3 Proposed Simplified Approach

According to CECS200^[1], the ultimate moment bearing capacity is 452 kN·m, and then the load level is 0.4 determined by Eq.(5.19). And according to Table D-1, the critical temperature of the composite beam is 654 °C.

The fire protection thickness is 19.4 mm determined through Eq.(5.22).

5.2.6.4 Comparison between Code and Simplified Approach

Although the fire protection thickness determined through the code and the simplified approaches nearly equal each other, the simplified approach is much easier for application. In the simplified approach, we do not need to calculate the ultimate moment bearing capacity of a composite beams in a fire, which is difficult and complex for engineers.

5.2.7 Experimental Validation

The simplified approach is validated by an experiment conducted by Zhou^[14] on a full-scale simply-supported composite beam with the load level of 0.7. The width and depth of the concrete slab is 1350 mm and 100 mm respectively with the grade of C30. The steel beam is H 300×150×8×8 with the grade of Q235B.

The test set-up and failure of the composite beam are shown in Fig. 5.10 and Fig. 5.11 respectively. The deflection of the composite beam at mid-span is shown in Fig. 5.12. Measured temperatures of steel beam in section 2-2 and 3-3 are shown in Fig. 5.13 and Fig. 5.14 respectively. The deflection at mid-span increases rapidly after the composite beam is exposed to the fire for 40 min. Hence the critical temperature of the composite beam is about 500 °C taking the average temperature of the lower flange and the web of the steel beam at 40 min of fire exposure.

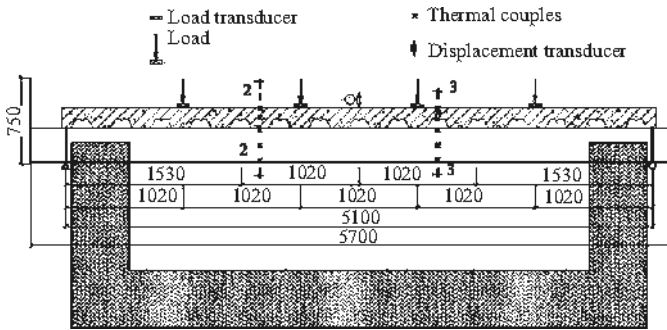


Fig. 5.10 Test set-up (mm)



Fig. 5.11 Failure of the composite beam

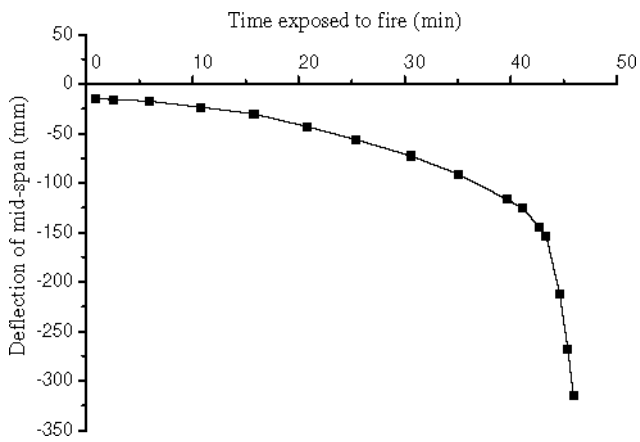


Fig. 5.12 Measured deflections at the mid-span of the composite beam

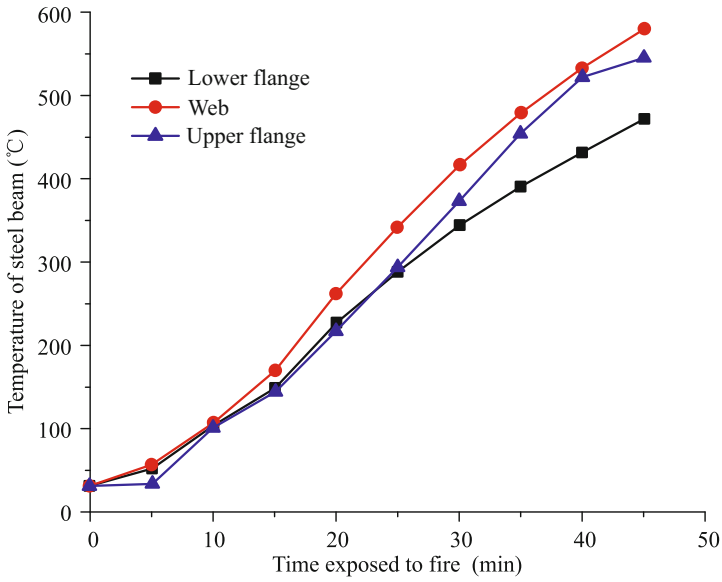


Fig. 5.13 Measured temperatures of the composite beam across section 2-2

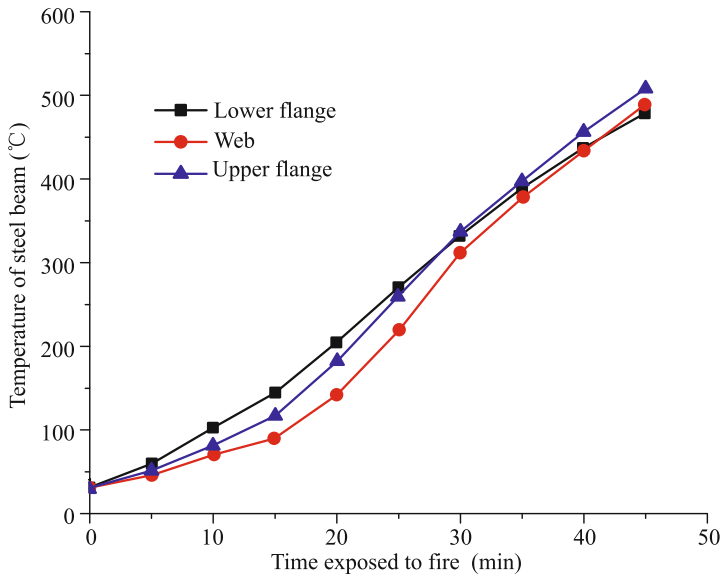


Fig. 5.14 Measured temperatures of the composite beam across section 3-3

References

- [1] China Association for Engineering Construction Standardization. *Technical Code for Fire Safety of Steel Structures in Buildings (CECS200-2006)*. China Plan Press, 2006.
- [2] M. Gillie, A. S. Usmani, and J. M. Rotter. A structural analysis of the first cardington test. *Journal of Constructional Steel Research*, 57(6):581–601, 2001.
- [3] M. Gillie, A. S. Usmani, and J. M. Rotter. A structural analysis of the cardington british steel corner test. *Journal of Constructional Steel Research*, 58(4):427–442, 2002.
- [4] T. Lennon and D. Moore. The natural fire safety concept, full-scale tests at cardington. *Fire Safety Journal*, 38(7):623–643, 2003.
- [5] Y. C. Wang, T. Lennon, and D. B. Moore. The behavior of steel frames subject to fire. *Journal of Constructional Steel Research*, 35:291–322, 1995.
- [6] Y. C. Wang. Tensile membrane action in slabs and its application to the cardington fire tests. *Proceedings of the Second Cardington Conference, March, BRE*, 1996.
- [7] P. S. Rose, I. W. Burgess, R. J. Plank, and C. G. Bailey. The influence of floor slabs on the structural behavior of composite frames in fire. *Journal of Constructional Steel Research*, 46(1-3), 1998.
- [8] Y. C. Wang. Composite beams with partial fire protection. *Fire Safety Journal*, 30:315–332, 1998.
- [9] A. Nadjaia, O. Vassart, F. Ali, D. Talamona, A. Allam, and M. Hawes. Performance of cellular composite floor beams at elevated temperatures. *Fire Safety Journal*, 42:489–497, 2007.
- [10] R. H. Fakury, E. B. Las Casas, F. Pacifico F. Jr., and L. M. P. Abreu. Design of semi-continuous composite steel-concrete beams at the fire limit state. *Journal of Constructional Steel Research*, 61:1094–1107, 2005.
- [11] A. Benedettia and E. Mangoni. Analytical prediction of composite beams response in fire situations. *Journal of Constructional Steel Research*, 63:221–228, 2007.
- [12] British Standard Institution. *British Standard BS 5950, Part 8, Code of Practice for Fire Resistance Design*. British Standard Institution, 2000.
- [13] European Committee for Standardization. *EN1994-1-2. Eurocode 4: Design of Composite Steel and Concrete Structures, Part 1-2: General Rules, Structural Fire Design*. European Committee for Standardization, 2005.
- [14] H. Y. Zhou. *Theoretical and Experimental Research on Fire Resistance of Steel-Concrete Composite Beams*. PhD thesis, Tongji University, 2004.

Fire-Resistance of Isolated Compressed Steel Components

The objective of this chapter is to describe how fire resistance and design calculation is carried out for isolated steel columns. Herein below, the approach provided by the CECS200^[1] is adopted as the main source of information for the objects.

6.1 Fire Resistance of Axially Compressed Steel Components

6.1.1 Load Bearing Capacity of Axially Compressed Steel Components

6.1.1.1 Assumption

For calculating the buckling resistance of an axially compressed steel component in a fire, the following assumptions^[2,3] are adopted:

- the steel component is subjected to ISO834^[4] standard fire;
- the temperature distributions across the section and along the component are both uniform;
- the yield strength reduction factor of steel at high temperatures described in CECS200^[1] is adopted;
- the distribution of residual stress over cross-section at high temperatures is the same as that recommended for ambient design^[5].

6.1.1.2 Critical Stress of an Axially Compressed Structural Component at High Temperatures

When calculating the critical stress of an axially compressed structural component, the initial geometric imperfection of the component is^[6]

$$y_0 = \delta_0 \sin\left(\frac{\pi x}{l}\right) \quad (6.1)$$

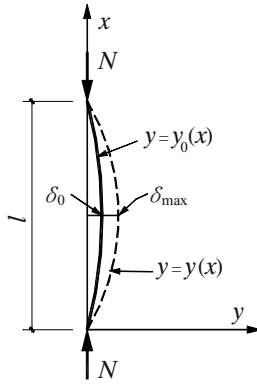


Fig. 6.1 Mechanical model of an axially compressed component

where δ_0 is the maximum initial deflection of the component, as shown in Fig. 6.1. The overall stability factor of the axially compressed component at elevated temperatures is obtained through using the same approach as that at ambient temperature.

Under the axial load N , the lateral deflection of the component^[7] is

$$y_0 = \frac{\delta_0}{1 - N/N_{ET}} \sin\left(\frac{\pi x}{l}\right) \tag{6.2}$$

and

$$N_{ET} = \sigma_{ET} A \tag{6.3}$$

$$\sigma_{ET} = \frac{\pi^2 E_T}{\lambda^2} \tag{6.4}$$

The maximum deflection of the component is

$$\delta_{max} = y|_{x=l/2} = \frac{\delta_0}{1 - N/N_{ET}} \tag{6.5}$$

The additional bending moment^[8] at the middle of the component due to the second order effect is

$$M = N \delta_{max} \tag{6.6}$$

So the maximum stress in the column section is

$$\sigma = \frac{N \delta_{max}}{W} + \frac{N}{A} \tag{6.7}$$

where W is the section modulus. Substituting Eq.(6.3) into Eq.(6.5) gives

$$\sigma = \frac{N}{A} \left[\frac{\frac{\delta_0 A}{W}}{1 - \frac{N}{A \sigma_{ET}}} + 1 \right] \tag{6.8}$$

Let

$$e_0 = \frac{\delta_0 A}{W} \quad (6.9)$$

where e_0 is called as the initial eccentricity ratio that is independent of the temperature variation.

The ultimate buckling limit of the component is defined when the steel yield in the component section^[9] is

$$\sigma_{crT} \left(\frac{e_0}{1 - \frac{\sigma_{crT}}{\sigma_{ET}}} + 1 \right) = f_{yT} \quad (6.10)$$

where σ_{crT} is the critical nominal compressive stress of the component at high temperatures and defined by

$$\sigma_{crT} = \frac{N_{crT}}{A} \quad (6.11)$$

Through solving Eq.(6.10), σ_{crT} is obtained as

$$\sigma_{crT} = \frac{1}{2} \left\{ (1 + e_0)\sigma_{ET} + f_{yT} - \sqrt{[(1 + e_0)\sigma_{ET} + f_{yT}]^2 - 4f_{yT}\sigma_{ET}} \right\} \quad (6.12)$$

If σ_{ET} and f_{yT} take values at ambient temperature respectively, Eq.(6.9) gives the critical stress at ambient temperature as

$$\sigma_{crT} = \frac{1}{2} \left\{ (1 + e_0)\sigma_E + f_y - \sqrt{[(1 + e_0)\sigma_E + f_y]^2 - 4f_y\sigma_E} \right\} \quad (6.13)$$

For determining σ_{cr} and σ_{crT} , the initial eccentricity of the component described by the China Steel Structural Design Code^[5] is employed as

(a) for the section type A

$$e_0 = 0.152\bar{\lambda} - 0.014 \quad (6.14)$$

(b) for the section type B

$$e_0 = 0.3\bar{\lambda} - 0.035 \quad (6.15)$$

(c) for the section type C

$$e = \begin{cases} 0.595\bar{\lambda} - 0.094, & \text{if } \bar{\lambda} > 1.05 \\ 0.302\bar{\lambda} + 0.216, & \text{if } \bar{\lambda} \leq 1.05 \end{cases} \quad (6.16)$$

(d) for the section type D

$$e = \begin{cases} 0.915\bar{\lambda} - 0.132, & \text{if } \bar{\lambda} > 1.05 \\ 0.432\bar{\lambda} + 0.375, & \text{if } \bar{\lambda} \leq 1.05 \end{cases} \quad (6.17)$$

where

$$\lambda = \frac{\lambda}{\pi} \sqrt{\frac{f_y}{E}} \quad (6.18)$$

6.1.1.3 Overall Stability Factor of an Axially Compressed Component

The critical stress of an axially compressed component at high temperatures and ambient temperature can be expressed as^[10]

$$\sigma_{crT} = \varphi_T f_{yT} \quad (6.19)$$

and

$$\sigma_{cr} = \varphi f_y \quad (6.20)$$

From Eq.(6.20) and Eq.(6.20), the modified factor of the overall stability factor at high temperature is introduced as

$$\alpha_c = \frac{\varphi_T}{\varphi} = \frac{\sigma_{crT} f_y}{\sigma_{cr} f_{yT}} \quad (6.21)$$

The value of α_c relevant to the temperature and slenderness ratio of the component is listed in Table 6.1^[11].

Table 6.1 Modified factor of the overall stability factor α_c of an axially compressed column

Temperature (°C)	Slenderness $\lambda \sqrt{f_y/235}$					
	10	50	100	150	200	250
100	1.000	0.999	0.992	0.986	0.984	0.983
150	1.000	0.998	0.985	0.976	0.972	0.971
200	1.000	0.997	0.978	0.964	0.958	0.956
250	0.999	0.996	0.968	0.949	0.942	0.938
300	0.999	0.994	0.957	0.931	0.921	0.917
350	0.999	0.994	0.952	0.924	0.914	0.909
400	0.999	0.995	0.963	0.940	0.931	0.928
450	1.000	0.998	0.984	0.973	0.969	0.968
500	1.000	1.002	1.011	1.019	1.022	1.023
550	1.001	1.004	1.036	1.064	1.075	1.080
600	1.001	1.005	1.039	1.069	1.080	1.086
650	1.000	0.998	0.983	0.972	0.968	0.966
700	1.000	0.997	0.978	0.964	0.959	0.957
750	1.000	1.001	1.005	1.008	1.009	1.010
800	1.000	1.000	1.000	1.000	1.000	1.000

6.1.1.4 Load Bearing Capacity of an Axially Compressed Component at High Temperature

The load bearing capacity of an axially compressed component at high temperatures can be checked with^[11]

$$\frac{N}{\phi_T A} \leq f_{yT} \quad (6.22)$$

6.1.2 Critical Temperature of an Axially Compressed Component

The critical temperature of the axially compressed steel component is the temperature at which the applied axial force equals the load bearing capacity of the component. It is obtained by solving

$$\frac{N}{\alpha_c \phi A} = \eta_T \gamma_R f \quad (6.23)$$

Rewrite the above equation as

$$\frac{N}{\phi A f} = \gamma_R \alpha_c \eta_T \quad (6.24)$$

and define

$$R = \frac{N}{\phi f A} \quad (6.25)$$

R is called the load ratio of the axially compressed component. Given the load ratio and slenderness of the column, the critical temperature can then be obtained through solving Eq.(6.24). For the convenience of engineering application, the critical temperatures of the axially compressed steel component with various load ratios and slenderness are listed in Table 6.2^[1].

When the critical temperature of the component is obtained, the thickness of fire protection is obtained as

$$d_i = 5 \times 10^{-5} \frac{\lambda_i}{\left(\frac{T_d - 20}{t} + 0.2 \right)^2 - 0.044} \frac{F_i}{V} \quad (6.26)$$

6.1.3 Example

A H-section steel column is studied with

- the cross section area of $21.52 \times 10^3 \text{ mm}^2$ made of Q235 steel;
- the section type of b ;
- the buckling length around the x - and y -axis both of 8.0 m;
- the radius of gyration $r_x=217.6 \text{ mm}$ and $r_y=99.6 \text{ mm}$, respectively;
- the slenderness ratio $\lambda_x=36.8$ and $\lambda_y=80.3$;
- the overall stability factor at ambient temperature $\phi=0.688$;
- the yield strength of steel at ambient temperature of 235 MPa;
- parameters of the fire protection material $\lambda_i=0.1 \text{ W/(m}\cdot\text{K)}$, $\rho_i=680 \text{ kg/m}^3$ and $c_i= 1000 \text{ J/(kg}\cdot\text{K)}$, and
- the section factor $F_i/V=59.7 \text{ m}^{-1}$.

Table 6.2 Critical temperature T_d of an axially compressed steel column ($^{\circ}\text{C}$)

Load ratio R	Slenderness $\lambda \sqrt{f_y}/235$			
	≤ 50	100	150	≥ 200
0.3	676	674	672	672
0.35	655	653	652	651
0.4	636	636	636	636
0.45	618	620	622	622
0.5	600	605	608	609
0.55	582	589	594	596
0.6	565	571	577	579
0.65	547	554	560	562
0.7	529	535	542	545
0.75	511	515	520	522
0.8	492	494	496	497
0.85	472	471	469	468
0.9	451	444	437	433

Perform the fire resistance design of the column.

Case I: The design axial force is 2400 kN and the fire resistance requirement is 2.5 h. Find the thickness of fire protection.

Answer:

(a) The load ratio of the column is

$$R = \frac{N}{\phi f A} = \frac{2400 \times 10^3}{0.688 \times 21.52 \times 10^3 \times 215} = 0.754$$

Through Table 6.2, the critical temperature of the column $T_d = 511.8^{\circ}\text{C}$.

(b) The thickness of fire protection is

$$\begin{aligned} d_i &= 5 \times 10^{-5} \frac{\lambda_i}{\left(\frac{T_d - 20}{t} + 0.2\right)^2 - 0.044} \frac{F_i}{V} \\ &= 5 \times 10^{-5} \times \frac{0.1}{\left(\frac{511.8 - 20}{2.5 \times 3600} + 0.2\right)^2 - 0.044} \times 59.7 \\ &= 14.2 \text{ mm} \end{aligned}$$

On the other hand,

$$\begin{aligned} \mu &= \frac{\rho_i c_i d_i F_i}{\rho_s c_s V} \\ &= \frac{680 \times 1000 \times 0.0143}{7850 \times 600} \times 59.7 \\ &= 0.123 < 0.5 \end{aligned}$$

The fire protection is lightweight fire protection and the thickness solved is accepted.

Case II: The applied axial load is 2000 kN and the thickness of fire protection is $d_i=25$ mm. Find the fire resistance time of the column.

Answer:

(a) According to Eq.(6.25), the load ratio of the column is

$$R = \frac{N}{\phi f A} = \frac{2000 \times 10^3}{0.688 \times 21.52 \times 10^3 \times 215} = 0.628$$

And based on Table 6.2, the critical temperature of the column is

$$T_d = 558.9 \text{ }^\circ\text{C}$$

(b) The fire resistance time is calculated through

$$\begin{aligned} t &= \frac{T_d - 20}{-0.2 + \sqrt{5 \times 10^{-5} \frac{\lambda_i F_i}{d_i V} + 0.044}} \\ &= \frac{558.9 - 20}{-0.2 + \sqrt{5 \times 10^{-5} \times \frac{0.1}{0.02} \times 59.7 + 0.044}} \\ &= 3.50 \text{ h} \end{aligned}$$

Case III: The applied axial force is 2700 kN, the fire protection thickness $d_i=18$ mm and fire resistance time is 3 h. Check whether the column satisfies the fire resistance requirement.

Answer I: Using critical temperature method

(a) According to Eq.(6.25), the load ratio of the column is

$$R = \frac{N}{\phi f A} = \frac{2700 \times 10^3}{0.688 \times 21.52 \times 10^3 \times 215} = 0.848$$

And based on Table 6.2, the critical temperature of the column is

$$T_d = 472.3 \text{ }^\circ\text{C}$$

(b) The parameter B of the studied column is

$$B = \frac{\lambda_i F_i}{d_i V} = \frac{0.1}{0.018} \times 59.7 = 331.7 \text{ W}/(\text{m}^3 \cdot \text{ }^\circ\text{C})$$

And the column temperature after 3 h fire exposure is

$$\begin{aligned} T_s &= \left(\sqrt{0.044 + 5 \times 10^{-5} B} - 0.2 \right) \times 3 \times 3600 + 20 \\ &= 518.3 \text{ }^\circ\text{C} > T_d = 472.3 \text{ }^\circ\text{C} \end{aligned}$$

The column does not satisfy the fire resistance requirement.

Answer II: Using Load bearing capacity method

(a) The temperature of the column after 3h fire exposure is

$$T_s = 518.3^\circ\text{C}$$

(b) According to Table 6.1, the reduction factor of the overall stability factor is

$$\alpha_c = 1.013$$

The overall stability factor at the high temperature is

$$\varphi_T = \alpha_c \varphi = 1.013 \times 0.688 = 0.697$$

And the reduction factor of steel at temperature T_s is

$$\begin{aligned} \eta_T &= 1.24 \times 10^{-8} T_s^3 - 2.096 \times 10^{-5} T_s^2 + 9.228 \times 10^{-3} T_s - 0.2168 \\ &= 0.662 \end{aligned}$$

The load bearing capacity of the column at temperature T_s is

$$\begin{aligned} N_{ET} &= \varphi_T \gamma_R \eta_T f A \\ &= 0.697 \times 21.52 \times 10^3 \times 0.662 \times 1.1 \times 215 \times 10^{-3} \\ &= 2348 \text{ kN} \end{aligned}$$

obviously

$$N_{ET} < N$$

The column does not satisfy the fire resistance requirement.

6.2 Design Method for a Structural Component under the Combined Axial Force and Bending Moment

6.2.1 Stability of a Structural Component under the Combined Axial Force and Bending Moment

According to the China Steel Structure Design Code^[5], both the overall stability of the component around the major and minor axis should be checked at ambient temperature by

(a) when bending around the major axis (x -axis)

$$\frac{N}{\varphi_x A} + \frac{\beta_{mx} M_x}{\gamma_x W_x (1 - 0.8N/N'_{Ex})} + \eta \frac{\beta_{ly} M_y}{\varphi'_{by} W_y} \leq f \quad (6.27)$$

and (b) when bending around the minor axis (y -axis)

$$\frac{N}{\varphi_y A} + \eta \frac{\beta_{lx} M_x}{\varphi'_{bx} W_x} + \frac{\beta_{my} M_y}{\gamma_y W_y (1 - 0.8N/N'_{Ey})} \leq f \quad (6.28)$$

Similarly, the load bearing capacity of the component under the combined axial force and bending moment at elevated temperatures is checked with^[2]

(a) when bending around the major axis (x -axis)

$$\frac{N}{\varphi_{xT}A} + \frac{\beta_{mx}M_x}{\gamma_x W_x (1 - 0.8N/N'_{ExT})} + \eta \frac{\beta_{ly}M_y}{\varphi'_{by}W_y} \leq f_{yT} \quad (6.29)$$

and (b) when bending around the minor axis (y -axis)

$$\frac{N}{\varphi_{yT}A} + \eta \frac{\beta_{lx}M_x}{\varphi'_{bx}W_x} + \frac{\beta_{my}M_y}{\gamma_y W_y (1 - 0.8N/N'_{EyT})} \leq f_{yT} \quad (6.30)$$

where α_c is the modified factor of overall stability factor of axially compressed component at elevated temperatures as listed in Table 6.1.

6.2.2 Cross-Sectional Strength of the Structural Component under the Combined Axial Force and Bending Moment at Elevated Temperatures

The cross-sectional strength of a structural component subjected to the combined axial force and bending moment at high temperatures is checked by

$$\frac{N}{A_n} \pm \frac{M_x}{\gamma_x W_{nx}} \pm \frac{M_y}{\gamma_y W_{ny}} \leq \eta_T \gamma_R f \quad (6.31)$$

6.2.3 Critical Temperature of the Structural Component Subjected to the Combined Axial Force and Bending Moment

Define the load ratio of a structural component subjected to the combined axial force and bending moment as

(a) for bending around the x -axis

$$R_x = \frac{1}{f} \left[\frac{N}{\varphi_x A} + \frac{\beta_{mx}M_x}{\gamma_x W_x (1 - 0.8N/N'_{Ex})} + \eta \frac{\beta_{ly}M_y}{\varphi'_{by}W_y} \right] \quad (6.32)$$

and (b) for bending around the y -axis

$$R_y = \frac{1}{f} \left[\frac{N}{\varphi_y A} + \eta \frac{\beta_{lx}M_x}{\varphi'_{bx}W_x} + \frac{\beta_{my}M_y}{\gamma_y W_y (1 - 0.8N/N'_{Ey})} \right] \quad (6.33)$$

Define the eccentricity of the component when bending around the x -axis as

$$e_{x1} = \frac{\beta_{mx}M_x}{\gamma_x W_x (1 - 0.8N/N'_{Ex})} \frac{\varphi_x A}{N} \quad (6.34)$$

$$e_{x2} = \frac{\eta \beta_{ly}M_y}{\varphi'_{by}W_y} \frac{\varphi_x A}{N}$$

The applied axial force on the column bending around x -axis can then be expressed by R_x , e_{x1} and e_{x2} as

$$N = \frac{R_x \phi_x f A}{1 + e_{x1} + e_{x2}} \quad (6.35)$$

With using Eqs. (6.31), (6.33), (6.34) and (6.35), Eq.(6.29) is rewritten as

$$\frac{R_x}{1 + e_{x1} + e_{x2}} \left(\frac{\phi_x}{\phi_{xT}} + e_{x1} \frac{1 - 0.8N/N'_{Ex}}{1 - 0.8N/N'_{ExT}} + e_{x2} \frac{\phi'_{by}}{\phi'_{byT}} \right) = \eta_T \gamma_R \quad (6.36)$$

Given λ_x , e_{x1} , e_{x2} and R_x , the critical temperature of the component T_{dx} when bending around x -axis is obtained through Eq.(6.36). Calculated results are listed in Table E-1 in Appendix E.

Similarly, when the component bends around the y -axis, the eccentricity is calculated through

$$e_{y1} = \frac{\beta_{my} M_y}{\gamma_y W_y (1 - 0.8N/N'_{Ey})} \frac{\phi_y A}{N} \quad (6.37)$$

$$e_{y2} = \frac{\eta \beta_{lx} M_x}{\phi'_{bx} W_x} \frac{\phi_y A}{N}$$

The applied axial force on the column bending around y -axis can then be expressed by R_y , e_{y1} and e_{y2}

$$N = \frac{R_y \phi_y f A}{1 + e_{y1} + e_{y2}} \quad (6.38)$$

Eq.(6.30) is rewritten as

$$\frac{R_y}{1 + e_{y1} + e_{y2}} \left(\frac{\phi_y}{\phi_{yT}} + e_{y1} \frac{1 - 0.8N/N'_{Ey}}{1 - 0.8N/N'_{EyT}} + e_{y2} \frac{\phi'_{bx}}{\phi'_{bxT}} \right) = \eta_T \gamma_R \quad (6.39)$$

Given λ_y , e_{y1} , e_{y2} and R_y , the critical temperature of column T_{dy} when bends around y -axis is obtained by Eq.(6.39). Results obtained are also listed in Table E-1 in Appendix E^[1].

If the column fails due to the compressive yield failure, the critical temperature should be calculated with the cross-sectional strength criteria. Define the load ratio as

$$R = \frac{1}{f} \left(\frac{N}{A_n} \pm \frac{M_x}{\gamma_x W_{nx}} \pm \frac{M_y}{\gamma_y W_{ny}} \right) \quad (6.40)$$

Given load ratio R , the critical temperature T_{d0} is obtained through Eq.(6.31), which is listed Table 6.3^[1].

The critical temperature of the component takes the minimum value of T_{dx} , T_{dy} and T_{d0} as

$$T_d = \min\{T_{dx}, T_{dy}, T_{d0}\} \quad (6.41)$$

Table 6.3 Critical temperature of a steel column subjected to the combined axial force and bending moment fails by compressed squash T_{d0} ($^{\circ}\text{C}$)

R	0.30	0.35	0.40	0.45	0.50	0.55	0.60	0.65	0.70	0.75	0.80	0.85	0.90
T_d	676	656	636	617	599	582	564	546	528	510	492	472	452

6.2.4 Example

A H-section steel column with

- the cross section area of $21.52 \times 10^3 \text{ mm}^2$ made of Q235 steel;
- the section type of type b ;
- the section modulus $W_x = 3973 \text{ cm}^3$;
- the slenderness ratio of the column $\lambda_x = 55.0$ and $\lambda_y = 70.0$;
- the overall stability factors $\varphi_x = 0.833$ and $\varphi_y = 0.751$;
- the yield strength of steel at ambient temperature of 235 MPa;
- the applied axial force and bending moment $N = 1080 \text{ kN}$ and $M_x = 248.5 \text{ kN}\cdot\text{m}$;
- the equivalent moment factor $\beta_{mx} = \beta_{tx} = 1.0$;
- the conduction factor of fire protection material $\lambda_y = 0.09 \text{ W}/(\text{m}\cdot\text{K})$;
- the density of fire protection material $\rho_f = 680 \text{ kg}/\text{m}^3$;
- the specific heat of fire protection material of $1000 \text{ J}/(\text{kg}\cdot\text{K})$ and
- the section factor of $F_i/V = 128.7 \text{ m}^{-1}$.

Perform the fire resistance design of the column.

Case I: The fire resistance requirement of the column is 3 h. Find the thickness of the fire protection.

Answer:

(a) According to Eq.(6.40), the load ratio R is

$$\begin{aligned}
 R &= \frac{1}{f} \left[\frac{N}{A_n} + \frac{M_x}{\gamma_x W_{nx}} \right] \\
 &= \frac{1}{215} \left[\frac{1080 \times 10^3}{21600} + \frac{248.5 \times 10^6}{1.05 \times 4973 \times 10^3} \right] \\
 &= 0.454
 \end{aligned}$$

According to Table 6.3, the critical temperature due to compressive squash $T_{d0} = 615.6$ $^{\circ}\text{C}$.

(b) Determine R_x , e_{x1} and e_{x2} as

$$\begin{aligned}
 N'_{Ex} &= \frac{\pi^2 EA}{1.1\lambda_x^2} = \frac{3.14^2 \times 2.05 \times 10^5 \times 21600}{1.1 \times 55^2} = 1.313 \times 10^7 \text{ N} \\
 R_x &= \frac{1}{f} \left[\frac{N}{\varphi_x A} + \frac{\beta_{mx} M_x}{\gamma_x W_x (1 - 0.8N/N'_{Ex})} \right] \\
 &= \frac{1}{215} \left[\frac{1080 \times 10^3}{0.8 \times 21600} + \frac{1.0 \times 248.5 \times 10^6}{1.05 \times 4973 \times 10^3 \times (1 - 0.8 \times 1080/13130)} \right] \\
 &= 0.516 \\
 e_{x1} &= \frac{\beta_{mx} M_x}{\gamma_x W_x (1 - 0.8N/N'_{Ex})} \frac{\varphi_x A}{N} \\
 &= \frac{1.0 \times 248.5 \times 10^6}{1.05 \times 4973 \times 10^3 \times (1 - 0.8 \times 1080/13130)} \times \frac{0.833 \times 21600}{1080 \times 10^3} \\
 &= 0.849 \\
 e_{x2} &= 0
 \end{aligned}$$

According to Table E-1 in Appendix E, the critical temperature of the column buckling around x -axis is

$$T_{dx} = 588.9 \text{ }^\circ\text{C}$$

(c) Calculate R_y , e_{y1} and e_{y2} as

$$\begin{aligned}
 \varphi'_{bx} &= 1.07 - \frac{\lambda_y^2}{44000} \frac{f_y}{235} \\
 &= 1.07 - \frac{70^2}{44000} \frac{235}{235} \\
 &= 0.959 \\
 R_y &= \frac{1}{f} \left[\frac{N}{\varphi_y A} + \eta \frac{\beta_{tx} M_x}{\varphi'_{bx} W_x} \right] \\
 &= \frac{1}{215} \left[\frac{1080 \times 10^3}{0.751 \times 21600} + 1.0 \times \frac{1.0 \times 248.5 \times 10^6}{0.959 \times 4973 \times 10^3} \right] \\
 &= 0.552 \\
 e_{y1} &= 0 \\
 e_{y2} &= \frac{\eta \beta_{tx} M_x}{\varphi'_{bx} W_x} \frac{\varphi_y A}{N} \\
 &= \frac{1.0 \times 1.0 \times 248.5 \times 10^6}{0.959 \times 4973 \times 10^3} \frac{0.751 \times 21600}{1080 \times 10^3} \\
 &= 0.783
 \end{aligned}$$

According to Table E-1 in appendix E, the critical temperature for the column buckling around y -axis is

$$T_{dy} = 577.6 \text{ }^\circ\text{C}$$

(d) The critical temperature of the column is

$$T_d = \min\{T_{dx}, T_{dy}, T_{d0}\} = 577.6 \text{ }^\circ\text{C}$$

The required thickness of fire protection is

$$\begin{aligned}
 d_i &= 5 \times 10^{-5} \frac{\lambda_i}{\left(\frac{T_d - 20}{t} + 0.2\right)^2} - 0.044 \frac{F_i}{V} \\
 &= 5 \times 10^{-5} \times \frac{0.09}{\left(\frac{577.6 - 20}{3.0 \times 3600} + 0.2\right)^2} - 0.044 \frac{2.78}{0.0216} \\
 &= 30 \text{ mm}
 \end{aligned}$$

Case II: The thickness of fire protection $d_i=20$ mm and fire resistance requirement $t=2.5$ h. Check whether the column can satisfy the fire resistance requirement.

Answer I: With the load bearing capacity method

(a) The parameter B of the studied column is

$$B = \frac{\lambda_i F_i}{d_i V} = \frac{0.09}{0.02} \times \frac{2.78}{0.0216} = 579.2 \text{ W/(m}^3 \cdot \text{°C)}$$

and the temperature of the column after 2.5h fire exposure is

$$\begin{aligned}
 T_s &= (\sqrt{0.044 + 5 \times 10^{-5} B})t + 20 \\
 &= (\sqrt{0.044 + 5 \times 10^{-5} \times 579.2}) \times 2.5 \times 3600 + 20 \\
 &= 651 \text{ °C}
 \end{aligned}$$

(b) The yield strength reduction factor of the steel at temperature T_s is

$$\begin{aligned}
 \eta_T &= 1.24 \times 10^{-8} T_s^3 - 2.096 \times 10^{-5} T_s^2 + 9.228 \times 10^{-3} T_s - 0.2168 \\
 &= 1.24 \times 10^{-8} \times 651^3 - 2.096 \times 10^{-5} \times 651^2 + 9.228 \times 10^{-3} \times 651 - 0.2168 \\
 &= 0.329
 \end{aligned}$$

Check the cross-section strength of the column as

$$\begin{aligned}
 \sigma &= \frac{N}{A_n} + \frac{M_x}{\gamma_x W_{nx}} = \frac{1080 \times 10^3}{21600} + \frac{248.5 \times 10^6}{1.05 \times 4973 \times 10^3} \\
 &= 97.6 \text{ N/mm}^2 \\
 &> \eta_T \gamma_R f = 0.329 \times 1.1 \times 215 = 77.8 \text{ N/mm}^2
 \end{aligned}$$

and it is accepted.

(c) The yield strength reduction factor of steel at the temperature T_s is

$$\begin{aligned}
 \eta_T &= 1.24 \times 10^{-8} T_s^3 - 2.096 \times 10^{-5} T_s^2 + 9.228 \times 10^{-3} T_s - 0.2168 \\
 &= 1.24 \times 10^{-8} \times 651^3 - 2.096 \times 10^{-5} \times 651^2 + 9.228 \times 10^{-3} \times 651 - 0.2168 \\
 &= 0.329
 \end{aligned}$$

The elastic modulus reduction factor of steel at the temperature T_s is

$$E_T = \frac{1000 - T_s}{6T_s - 2800} E = \frac{1000 - 651}{6 \times 651 - 2800} E = 6.469 \times 10^4 \text{ N/mm}^2$$

and

$$\begin{aligned}
 N'_{ExT} &= \frac{\pi^2 E_T A}{1.1 \lambda_x^2} \\
 &= \frac{3.14^2 \times 6.469 \times 10^4 \times 21600}{1.1 \times 55^2} \\
 &= 4.145 \times 10^6 \text{ N}
 \end{aligned}$$

The overall stability reduction factor of the column under axial compressed load is

$$\alpha_c = 0.997$$

And the overall stability factor of the column is

$$\varphi_{xT} = \alpha_c \varphi_x = 0.997 \times 0.833 = 0.831$$

The load bearing capacity of the column bending around x -axis is

$$\begin{aligned}
 \sigma_T &= \frac{N}{\varphi_{xT} A} + \frac{\beta_{mx} M_x}{\gamma_x W_x (1 - 0.8N/N'_{ExT})} \\
 &= \frac{1080 \times 10^3}{0.831 \times 21600} + \frac{1.0 \times 248.5 \times 10^6}{1.05 \times 4973 \times 10^3 \times (1 - 0.8 \times 1080/4145)} \\
 &= 120.29 \text{ N/mm}^2 \\
 &> \eta_T \gamma_{Rf} = 0.329 \times 1.1 \times 215 = 77.8 \text{ N/mm}^2
 \end{aligned}$$

which is accepted.

(d) According to Table 6.1, the reduction factor for the overall stability factor of an axially compressed column is

$$\alpha_c = 0.992$$

And the overall stability factor at high temperature is

$$\varphi_{yT} = \alpha_c \varphi_y = 0.992 \times 0.751 = 0.745$$

The lateral torsional stability factor of a bending component at ambient temperature is

$$\varphi_{bx} = 1.07 - \frac{\lambda_y^2}{44000} \frac{f_y}{235} = 1.07 - \frac{70^2}{44000} \times \frac{235}{235} = 0.959$$

The reduction factor for the lateral torsional stability factor of the bending component is

$$\alpha_b = 0.961$$

and the lateral torsional stability factor of the bending component at high temperature is

$$\alpha_b \varphi_{bx} = 0.961 \times 0.959 = 0.992 > 0.6$$

which means the column buckles plastically. The lateral torsional stability factor should be modified as

$$\varphi'_{bxT} = 1.07 - \frac{0.282}{\alpha_b \varphi_{b,x}} = 1.07 - \frac{0.282}{0.922} = 0.855$$

The check equation for the overall stability of the column at high temperature bending around y-axis is

$$\begin{aligned}\sigma_T &= \frac{N}{\varphi_{yT}A} + \eta \frac{\beta_{tx}M_x}{\varphi'_{bxT}W_x} \\ &= \frac{1080 \times 10^3}{0.745 \times 21600} + 1.0 \times \frac{1.0 \times 248.5 \times 10^6}{0.855 \times 4973 \times 10^3} \\ &= 119.5 \text{ N/mm}^2 \\ &> \eta_T \gamma_{Rf} = 0.329 \times 1.1 \times 215 = 77.8 \text{ N/mm}^2\end{aligned}$$

which is not accepted. The columns will fail by lateral torsionally buckling around y-axis.

Answer II: With critical temperature method

(a) The temperature of the column after 2.5 h fire exposure

$$T_s = 651 \text{ }^\circ\text{C}$$

(b) The critical temperature of the column

$$T_d = 577.6 \text{ }^\circ\text{C}$$

(c) Obviously,

$$T_s > T_d$$

The fire resistance of the column is not satisfied.

References

- [1] China Association for Engineering Construction Standardization. *Technical Code for Fire Safety of Steel Structures in Buildings (CECS200-2006)*. China Plan Press, 2006.
- [2] G. Q. Li, L. H. Han, G. B. Lou, and S. C. Jiang. *Steel and Steel-Concrete Composite Structures Fire Resistance Design*. China Architecture & Building Press, 2006.
- [3] G. Q. Li, J. L. He, and S. C. Jiang. Fire-resistant experiment and theoretical calculation of steel columns. *Building Structure*, (9), 2000.
- [4] International Organization for Standardization. *Fire-Resistance Tests - Elements of Building Construction, Part 1: General Requirements*. International Organization for Standardization, 1999.
- [5] Ministry of Housing and Urban-Rural Development of China. *Code for Design of Steel Structures (GB50017-2003)*. China Plan Press, 2003.
- [6] S. F. Chen. *Principle of Steel Structure Design*. China Science Press, 2005.
- [7] J. Chen. *Stability of Steel Structures: Theory and Design*. China Science Press, 2001.

- [8] P. J. Wang and G. Q. Li. Post-buckling behavior of axially restrained steel columns in fire. *Journal of Tongji University (Natural Science)*, (4), 2008.
- [9] G. Q. Li and J. J. Li. *Advanced Analysis and Design of Steel Frames*. John Wiley & Sons, Ltd., 2007.
- [10] G. Q. Li, M. Yang, and Z. X. Wang. A practical approach for fire-resistant calculation and design of steel columns. *Industry Construction*, (2), 1995.

Fire-Resistance of Restrained Flexural Steel Components

7.1 Fire-Resistance of a Restrained Steel Beam

Before 1990, research on fire-resistance of steel structures was mainly focused on isolated members. In 1990, a fire occurred in a partly completed 14-storey office building at Broadgate in London^[1,2]. The investigation after the fire showed that behavior of a beam was strongly influenced by the restraint provided by the surrounding structural components. Although the possible beneficial effects of the catenary action of the beam or the membrane action of the composite slab were not evident because relatively low steel temperatures less than 600 °C were reached during the fire, interactions between different structural members in a completed structure subjected to a fire drew the attention of researchers. In 1996, a program of full-scale fire tests was completed on an eight-storey steel-framed building in the UK at Cardington Laboratory, to investigate the behavior of a real steel framed structure under real fire conditions. The typical “runaway” failure of an isolated steel beam in the standard fire test did not occur to the steel frame beam, even though the temperature of the bottom flange of the beam had exceeded 800 °C, which indicated that a steel beam in a framed structure, with the aid of restraint from surrounding members, has better fire-resistant capability than an individual steel beam^[3,4,5,6,7]. The local buckling of the bottom flange occurred near the beam-to-column connection during heating, because of tremendous compression stress at this place resulting from the restrained thermal expansion. Damage of beam-to-column connections was also observed due to thermal contraction of the beam during cooling^[8,9,10,11,12,13], as shown in Fig. 7.1.

It is necessary to carry out additional experiments to obtain more detailed understanding of behavior of a restrained steel beam subjected to a fire. Considering that it will be very expensive to perform a fire test on steel beams in a completed steel structure, the experiment on a restrained steel beam is often employed for simulating behavior of a beam in a completed structure.

By this method, Li^[8,9], Liu et al.^[14,15,16], Cong^[17] and Li et al.^[18] have conducted some fire tests on restrained steel beams. Huang and Tan^[19] and Yin and Wang^[20,21,22] analyzed the restrained steel beam using finite-element methods. A simplified method was proposed by Yin and Wang^[20,21,22] to predict the behavior

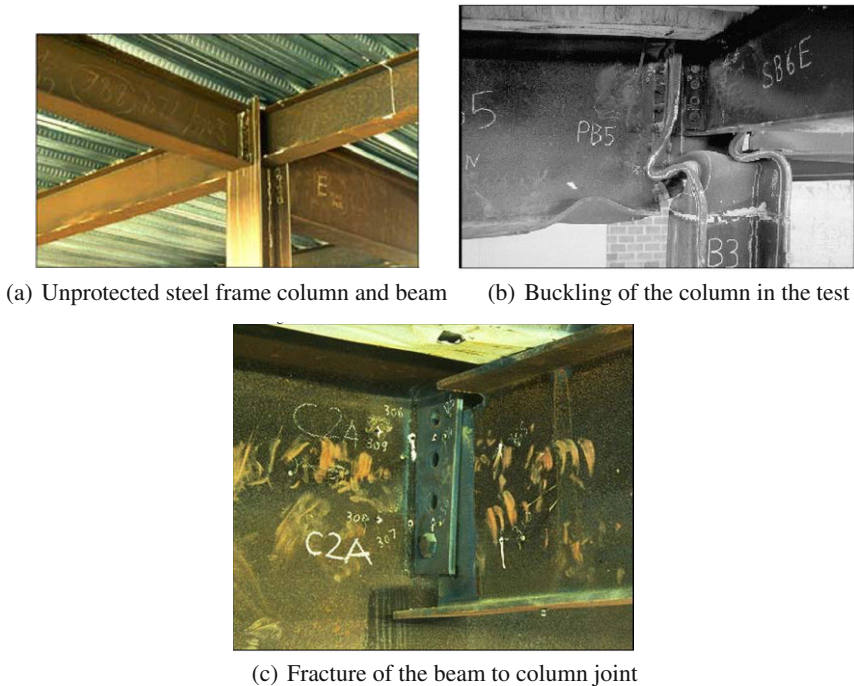


Fig. 7.1 Failure of restrained structural components in a fire

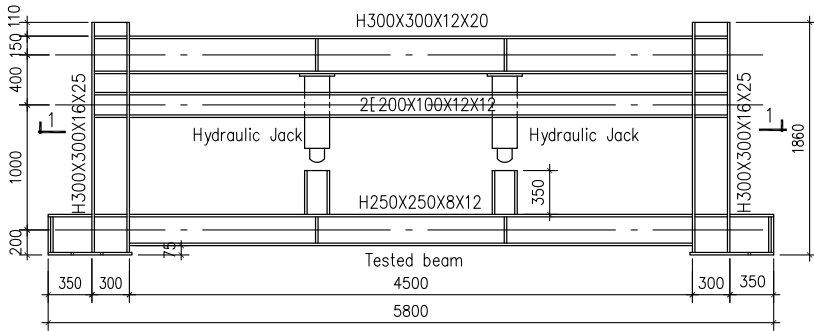
of a restrained steel beam subjected to fire. Li and Guo^[9] studied the behavior of a restrained steel beam during cooling phase and a theoretical method was proposed.

Although lots of experimental and theoretical research on restrained steel beams has been carried out, the damage of beam-to-column connection has not been investigated in detail and behavior of the restrained beam during cooling was seldom addressed. Fire tests on two restrained steel beams with rigid beam-to-column connections were carried out at the Fire Laboratory of Tongji University^[8] to investigate behavior of the restrained steel beam during the heating and cooling phase in a fire.

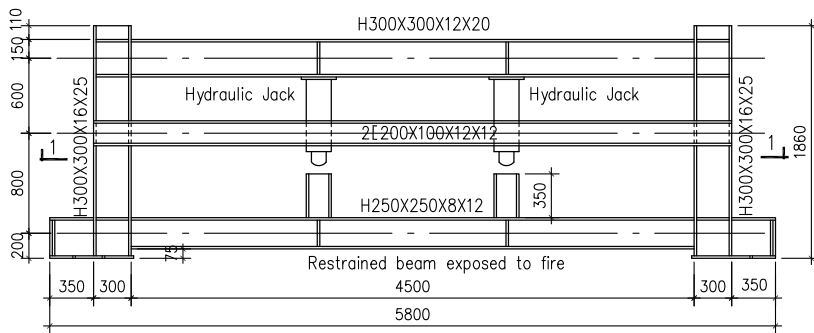
7.1.1 Fire Test of Restrained Steel Beams

7.1.1.1 Test Arrangement

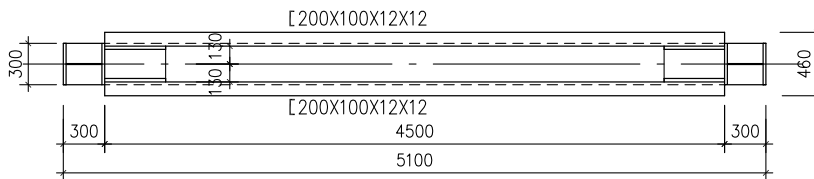
The test set-up is shown in Fig. 7.2. The bottom H-beam was the tested restrained beam and the top H-beam and the double channel beam are to provide the axial restraint and were out of the furnace. The restrained beam was made of Q235 steel with yield strength of 271 MPa, and all the other members were made of Q345 steel with yield strength of 331 MPa.



(a) Set up of test 1



(b) Set up of test 2



(c) 1-1 section plan view

Fig. 7.2 Test set-up of the restrained steel beam in a fire (mm)

In order to simulate the heat-sink effect of the concrete slab, the top flange of the restrained steel beam was wrapped by ceramic fiber blanket with a thickness of 3 mm and 10 mm for specimen 1 and specimen 2, respectively.

Two concentrated loads were applied symmetrically on the restrained beam by hydraulic jacks and the load ratio was 0.7 (130 kN). When the deflection of the beam reached about $l/16$, the fire was stopped.

7.1.1.2 Installation of Instruments

The temperature, the lateral deflection and the internal force of restrained beam were measured during the test. Although the top H-beam and the double channel beams were not exposed to fire, their strain can be obtained through strain gauges and then the internal force can be calculated.

Arrangements of thermocouples, displacement transducers and strain gauges are shown in Fig. 7.3. Three displacement transducers were fixed at $l/4$, $l/2$ and $3l/4$ along the restrained beam span to record vertical deflections and two displacement transducers were fixed at the two ends of the restrained beam to measure horizontal displacements. The arrangement of thermocouples are shown in Fig. 7.3. The distribution of strain gauges was shown in Fig. 7.4 and Fig. 7.5. The full view of the test with instruments is shown in Fig. 7.6.

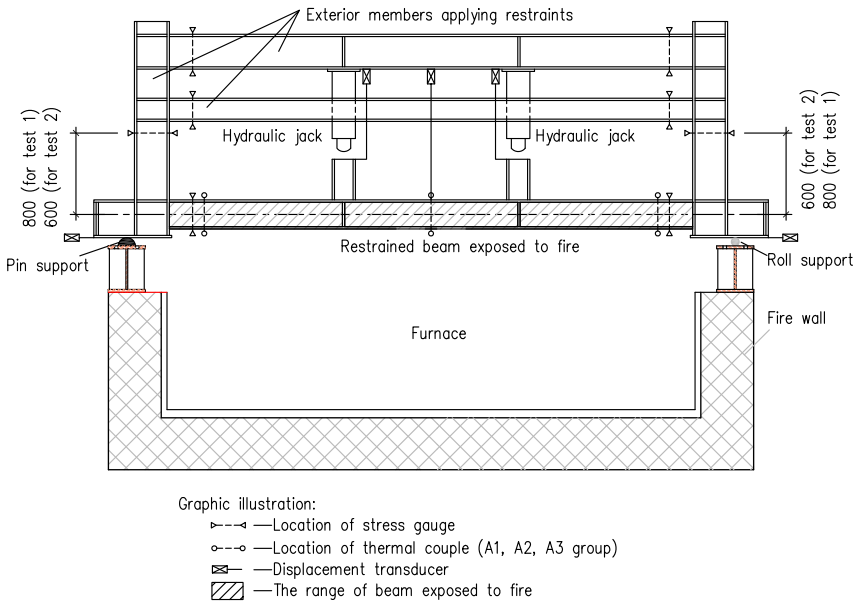


Fig. 7.3 Installation of instruments (mm)

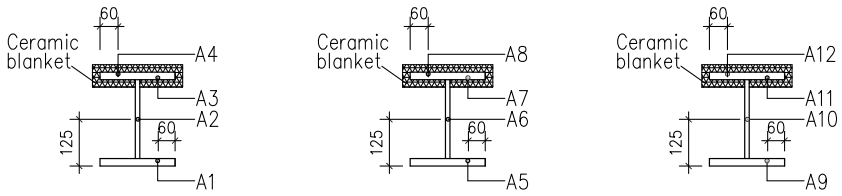


Fig. 7.4 Distribution of thermo-couples over the cross section of the restrained beam (mm)

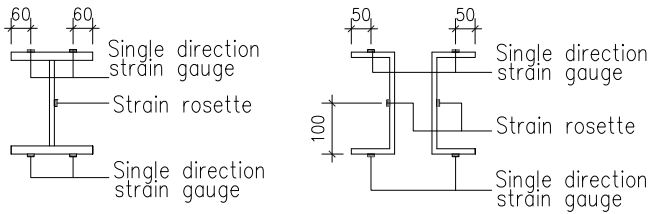


Fig. 7.5 Distribution of strain gauges over the cross section of members (mm)



Fig. 7.6 Full view of the test set-up

7.1.1.3 Failure of the Restrained Beam

The restrained beam experienced very large deflection in the fire test. Appearance of specimen 1 after test is shown in Fig. 7.7. Local buckling occurred at the bottom flange near the support, as shown in Fig. 7.8. The distance between the buckling zone and the beam support ranged from 150 mm to 250 mm, and the largest displacement in the buckling zone reached 65 mm. Damage to the beam-to-column connection was not observed.



Fig. 7.7 Deflection of the restrained beam



Fig. 7.8 Local buckling of the restrained beam

7.1.1.4 Tests Results

• Temperature results

Temperature-time curves of the fire, the bottom flange, the web and top flange of the restrained beam are shown in Fig. 7.9 to Fig. 7.12. The heating period of test 1 and 2 was 19 min and 21 min respectively, and the temperature measurement stopped at 148 min and 282 min after the fire was turned off for test 1 and 2, respectively.

From Fig. 7.9 to Fig. 7.12, it can be found that temperatures of the bottom flange and the web of the restrained beam in the same section were close to each other, and the temperature of the top flange increased more slowly than that of the bottom flange. After the fire stopped, the temperature of the bottom flange decreased rapidly, while the temperature of the top flange still increased for a period of time.

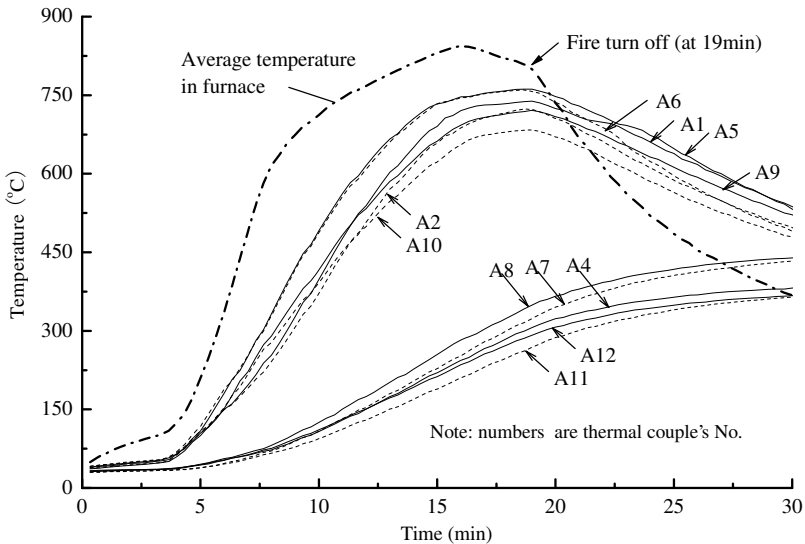


Fig. 7.9 Measured temperatures of test 1 in 30 min

• Measured deflections

During the fire test, the deflection against time is shown in Fig. 7.13. In heating phase the deflection increased rapidly. After the fire stopped, especially 10 min later, the variation in the deflection was very small.

During the first 10 min after the fire stopped, the deflection of the restrained beam still increased slowly. This might result from two reasons. The first is that the temperature of the top flange still increased in this period of time. And the second is that the deflection increased so quickly that the load could not catch it. The actual load was lower than the required value, while 10 min later after the fire went out, the change in deflection was very small.

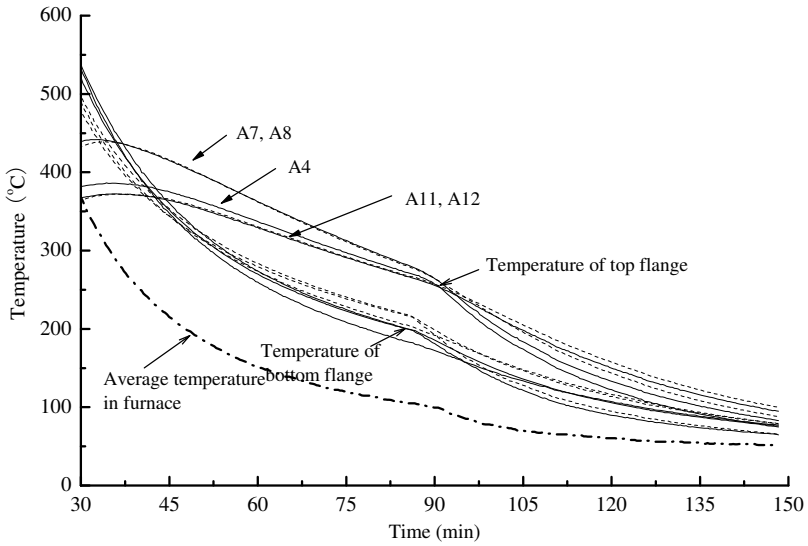


Fig. 7.10 Measured temperatures of test 1 after 30 min

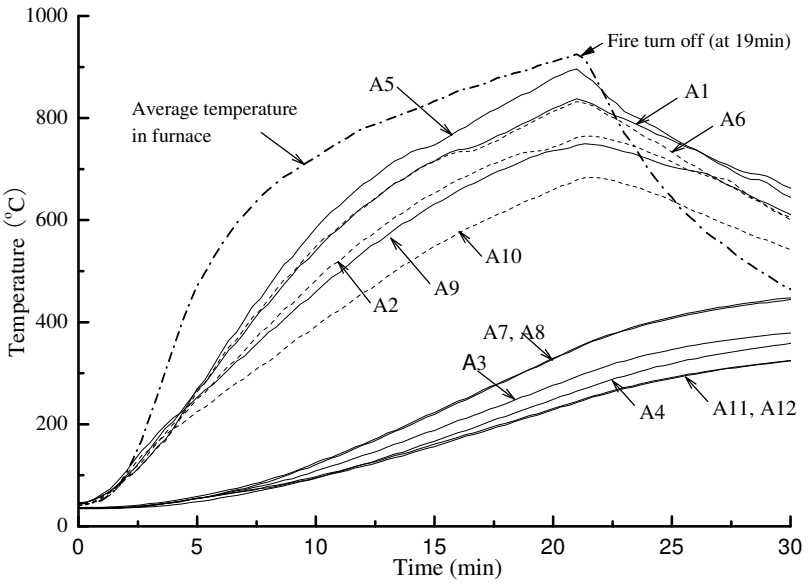


Fig. 7.11 Measured temperatures of test 2 in 30 min

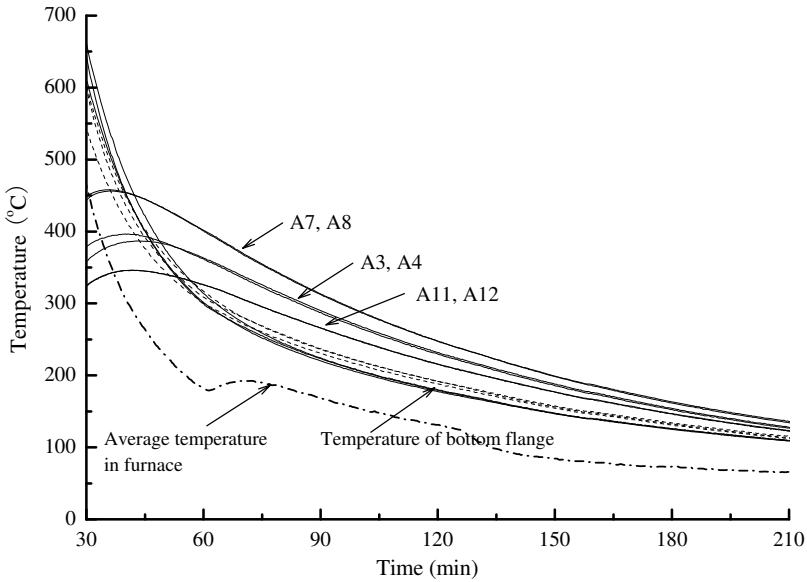


Fig. 7.12 Measured temperatures of test 2 after 30 min

Fig. 7.13 shows that the catenary action occurred when the deflection exceeded about $1/20$ of the beam span, which slowed down the deflection increase. For an isolated beam with a load ratio of 0.7, it will collapse when the temperature reaches $500\text{ }^{\circ}\text{C}$, while for the restrained beams with the same load ratio, they still had load bearing capacity though the highest temperature had exceeded $700\text{ }^{\circ}\text{C}$.

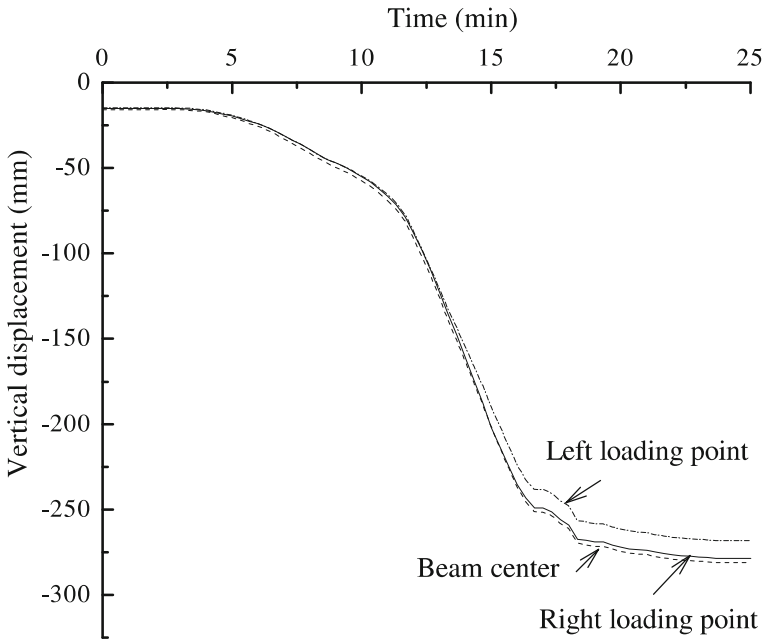
• Horizontal displacements at the beam ends

Horizontal displacements at the ends of tested beam are shown in Figs. 7.14 and 7.15.

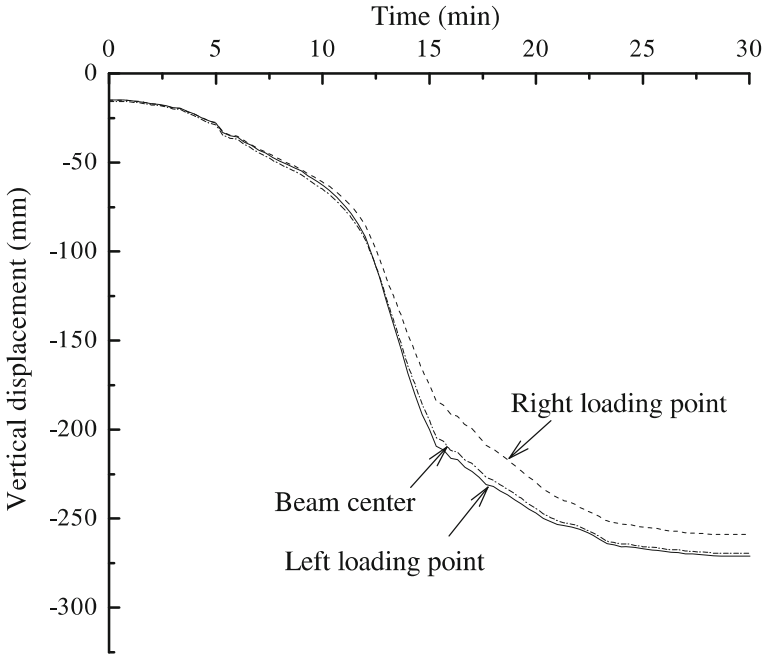
At the beginning of the fire test, the right beam end moved toward outside for the expansion of the beam. But 10 min after, the beam end began to move inside resulting a large deflection of the beam. About 14 min later, the beam returned to its original length. After the fire went out, the beam end kept moving toward the inside because of the contraction of steel during cooling. The horizontal displacement of specimen 1 was larger than that of specimen 2 because the restraint stiffness in test 1 was smaller than that in test 2.

7.1.1.5 Axial Forces in the Restrained Beam

The axial restraint stiffness of the beam in test 1 and test 2 was 39.5 kN/mm and 68.3 kN/mm , respectively. The axial force in the restrained beam can be calculated through the axial restraint stiffness multiplied by the horizontal displacement and is shown in Figs. 7.16 and 7.17.



(a) Deflection of test specimen 1



(b) Deflection of test specimen 2

Fig. 7.13 Deflections of the restrained beam in the fire test

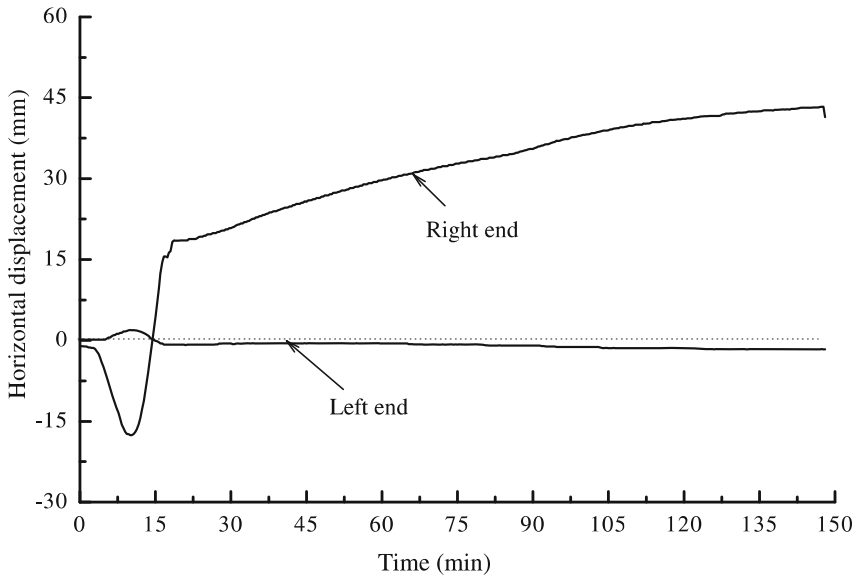


Fig. 7.14 Horizontal displacements at the restrained beam ends in test 1

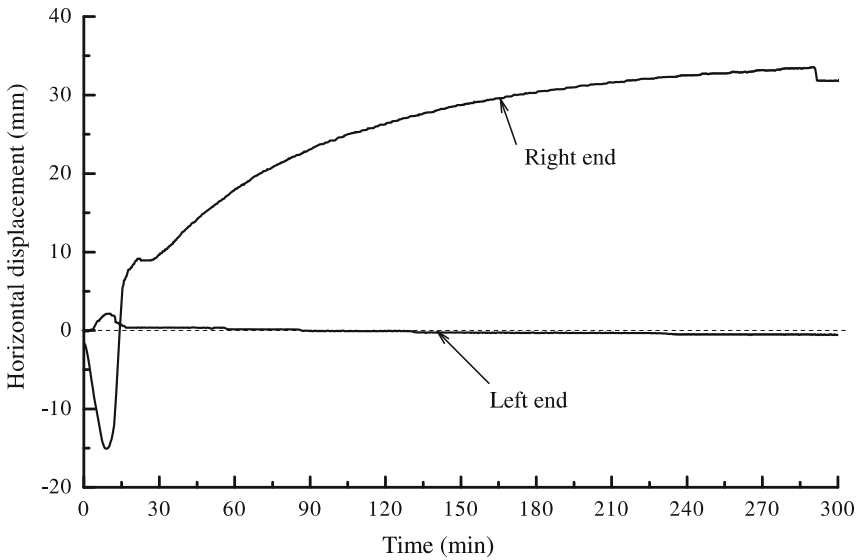


Fig. 7.15 Horizontal displacements at the restrained beam ends in test 2

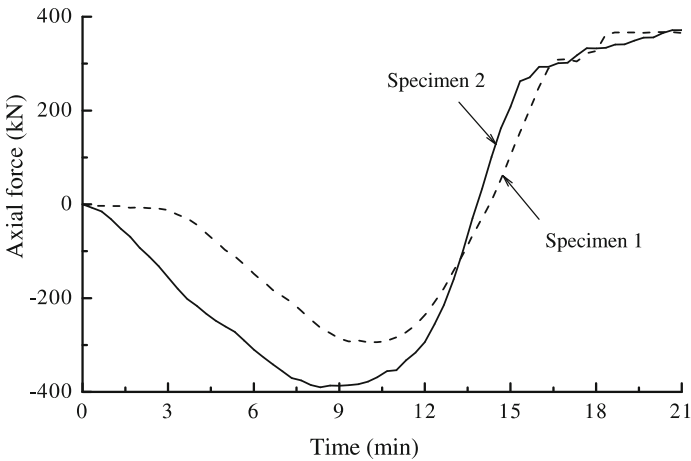


Fig. 7.16 Variation of the axial forces in restrained beams in 20 min

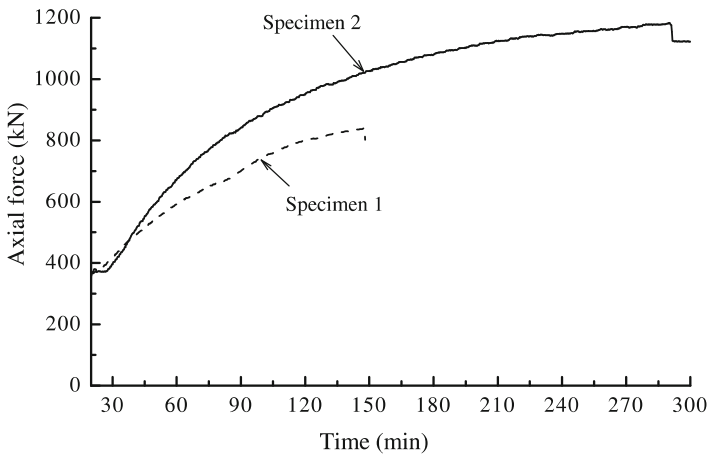


Fig. 7.17 Variation of the axial forces in restrained beams after 20 min

At the beginning of the fire test, the axial compression force was produced because of the restrained thermal expansion. At 8–9 min, the axial compression force began to decrease. At about 14 min, the axial force in the beam changed into tension due to the dominance of catenary action.

Since the axial restrain stiffness in test 2 was larger than that in test 1, the maximum value of the axial compression force and tension force in specimen 2 was observed to be larger than that in specimen 1.

7.1.2 Analysis and Design for Fire-Resistance of a Restrained Steel Beam

Observations from experiments indicate that the restrained steel beam has better fire-resistant capacity than an isolated beam^[23]. Over the past ten years, behavior of the restrained steel beam during heating has been investigated through experimental and theoretical studies^[18,14], and some practical and simplified approaches for predicting behavior of the restrained steel beam have been proposed^[21,22]. On the other hand, damage of connections of the restrained beam are noticeable in fire, which is thought to be mainly caused by the enormous axial tensile force resulting from temperature decreasing. Fig. 7.18 illustrates the damage in beam-column connections found in the fire attacked tall steel building in Taipei Science and Technology Park^[23]. Few researches on the performance of a restrained steel beam during the cooling have been conducted, except some studies on the strain reversal of steel during cooling carried out by El-Rimawi et al.^[24] and Bailey et al.^[10].



Fig. 7.18 Damage to the beam-column connection by a fire

7.1.2.1 Behavior of a Restrained Steel Beam During the Heating and Cooling Phase in a Fire

Behavior of a restrained beam in a fire during the heating phase can be divided into 4 stages according to the development of the axial force on the beam, as shown in Fig. 7.19. The deflection development of the restrained beam in accordance with each stage is shown in Fig. 7.20. The 4 stages are

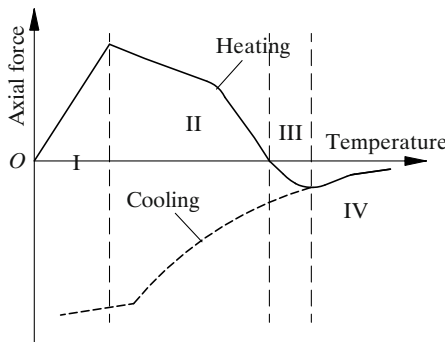
Stage I: A compressive axial force is induced in the beam because thermal expansion is restrained and it increases with temperature elevation. At the end of stage I, the axial force reaches the maximum value.

Stage II: The compressive force on the beam begins to decrease. At the end of this stage the compressive force is reduced to zero and the deflection increases sharply.

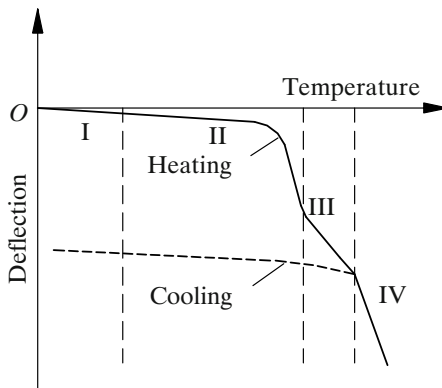
Stage III: The axial force changes into tension, and the rate of the deflection is slowed down, which indicates that catenary action takes into effect. At the end of stage III the tensile axial force reaches the maximum value.

Stage IV: The axial tensile force begins to decrease and the rate of the deflection increases again.

In stages II to IV, a plastic strain is produced and accumulated in the beam with the temperature increasing. When the temperature begins to decrease, because the plastic strain cannot recover and the beam is restrained at the ends, the contraction force in the beam will be increased, as indicated by the dashed line in Fig. 7.19(a). At the same time, the recovery of the elastic modulus of steel together with the effect of increasing tensile axial force, reduce the deflection of the beam, as shown by the dashed lines in Fig. 7.19(b).



(a) Development of the axial force



(b) Development of the deflection

Fig. 7.19 Axial force and deflection development of the restrained beam during fire

7.1.2.2 Equilibrium of the Restrained Steel Beams in Large Deflection State

Restrained steel beams in a fire condition can undergo very large deflection. The effect of geometric non-linearity, which is normally ignored when studying an isolated beam, must be considered. A typical model of a restrained beam is shown in Fig. 7.20.

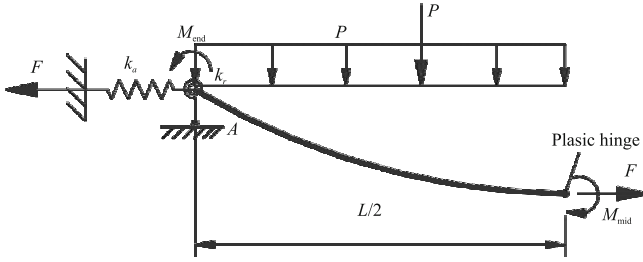


Fig. 7.20 Mechanical model of a restrained steel beam

The equilibrium equation of moments involving the effect of geometric non-linearity is expressed as

$$M_{\text{end}} + M_{\text{mid}} - M_q + F\delta = 0 \quad (7.1)$$

The axial force on the beam can be determined by

$$F = (\alpha l \Delta T - \lambda \frac{\delta^2}{L}) k_{e,a} \quad (7.2)$$

where $k_{e,a}$ is the effective axial stiffness of the beam expressed as

$$\frac{1}{k_{e,a}} = \frac{2}{K_a} + \frac{1}{k_{bT}} \quad (7.3)$$

7.1.2.3 Stiffness of the Restrained Steel Beam

The axial stiffness of the restraint k_a is assumed to be temperature independent, but the axial stiffness of the beam k_{bT} varies widely in different stages. In order to simplify the study, the temperature distribution over the beam cross-section is assumed to be uniform. Three states are discussed as follows

- **Elastic state with small deflection**

Assume that the beam is in an elastic state and its deflection is very small. The axial stiffness of the beam is approximately determined by

$$k_{b,T} = \frac{E_T A}{L} \quad (7.4)$$

• **Elastic state with large deflection**

When the deflection of the beam is very large, the effect of deflection on the axial stiffness of a beam must be taken into account. The following approximate approach is proposed to determine the axial stiffness of the beam.

For a simply supported and curved beam shown in Fig. 7.21, the horizontal displacement of the beam under horizontal force P is determined by

$$\Delta_P = P \int_0^l \frac{\sqrt{1+f'^2(x)}f^2(x)}{E_T I} dx + \int_0^l \frac{P}{E_T A \sqrt{1+f'^2(x)}} dx \quad (7.5)$$

where $f'(x)$ is the first derivative of function $f(x)$ and $f(x)$ is the profile of the beam, as proposed by Yin and Wang^[21,22].

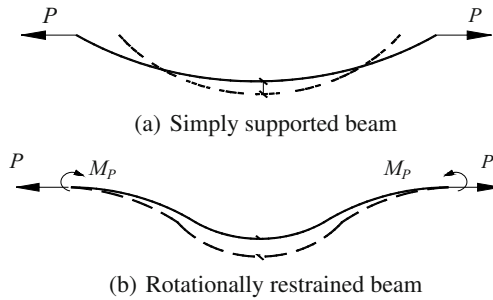


Fig. 7.21 Curved beam

In Eq.(7.5), the first part is the deflection induced by the moment and the second part is that induced by the axial force.

If the rotation of the beam is restrained, as shown in Fig. 7.21, the moment M_P will be induced at the ends under the axial force P . Based on the virtual work principle, the following equation is obtained

$$\int_0^l \frac{M_P \bar{M}}{E_T I} ds - \int_0^l \frac{f(x) P \bar{M}}{E_T I} ds = 0 \quad (7.6)$$

where \bar{M} is the virtual unit moment.

The moment M_P can be worked out through Eq.(7.6) and expressed as

$$M_P = \frac{P \int_0^l \sqrt{1+f'^2(x)}f(x)dx}{\int_0^l \sqrt{1+f'^2(x)}dx} \quad (7.7)$$

If the beam ends are rotationally restrained, the expression of M_P may be modified as

$$M_P = \frac{k_{e,r} L P \int_0^l \sqrt{1+f'^2(x)}f(x)dx}{EL \int_0^l \sqrt{1+f'^2(x)}dx} \quad (7.8)$$

where $k_{e,r}$ is the effective stiffness of the restrained beam and is determined with

$$\frac{1}{k_{e,r}} = \frac{L}{EI} + \frac{2}{k_r} \quad (7.9)$$

M_p also induces horizontal displacement of the ends and the total horizontal displacement of the beam with rotational restraint is determined by

$$\begin{aligned} \Delta_P = P \int_0^l \frac{\sqrt{1+f'^2(x)}f^2(x)}{E_T I} dx + \int_0^l \frac{P}{E_T A \sqrt{1+f'^2(x)}} dx \\ - \frac{k_{e,r} L P \int_0^l \sqrt{1+f'^2(x)}f(x) dx}{EL \int_0^l \sqrt{1+f'^2(x)} dx} \int_0^l \frac{\sqrt{1+f'^2(x)}f(x)}{E_T I} dx \end{aligned} \quad (7.10)$$

Then the axial stiffness of the curved beam considering the effect of deflection is determined by

$$\begin{aligned} \frac{1}{k_{b,T}} = \frac{\Delta_P}{P} = \int_0^l \frac{\sqrt{1+f'^2(x)}f^2(x)}{E_T I} dx + \int_0^l \frac{1}{E_T A \sqrt{1+f'^2(x)}} dx \\ - \frac{k_{e,r} L \int_0^l \sqrt{1+f'^2(x)}f(x) dx}{EL \int_0^l \sqrt{1+f'^2(x)} dx} \int_0^l \frac{\sqrt{1+f'^2(x)}f(x)}{E_T I} dx \end{aligned} \quad (7.11)$$

• Plastic state with large deflection

According to plastic theory, the relationship between the moment M and axial force F at the plastic hinge in the beam is expressed as

(a) for the neutral axis in the web

$$\frac{M}{M_p} + \omega \left(\frac{F}{F_p} \right)^2 = 1 \quad (7.12)$$

(b) for the neutral axis in the flange

$$\zeta \frac{M}{M_p} + \left| \frac{F}{F_p} \right| = 1 \quad (7.13)$$

where ω and ζ are factors relevant to the type of the cross-section of the beam, given by

$$\omega = \frac{(2 + \mu_t)^2}{\mu_t(4 + \mu_t)}, \text{ and } \zeta = \frac{4 + \mu_t}{2(2 + \mu_t)} \quad (7.14)$$

μ_t is the ratio of the cross-sectional area of the web to that of one flange.

For a beam without rotational restraints at the ends, $M_{\text{end}} = 0$. Eq.(7.1) changes to

$$F \delta = M_{\text{mid}} + M_q \quad (7.15)$$

Work out the expression of M_{mid} from Eq.(7.12) and Eq.(7.13), and substitute it into Eq.(7.15). The derivative of F with respected to δ is obtained by

(a) for the neutral axis in the web

$$\frac{dF}{d\delta} = -\frac{F}{2\omega \frac{M_p F}{F_p^2} + \delta} \quad (7.16)$$

(b) for the neutral axis in the flange

$$\frac{dF}{d\delta} = -\frac{F}{\frac{M_p}{\zeta F + p} + \delta} \quad (7.17)$$

Given that the temperature is kept constant, the relationship between the relative displacement of the two ends u and the deflection at the mid span of the beam δ is expressed as

$$u = \lambda \frac{\delta^2}{L} \quad (7.18)$$

Then

$$\frac{du}{d\delta} = 2\lambda \frac{\delta}{L} \quad (7.19)$$

Therefore, according to the differential Eq.(7.16), Eq.(7.17) and Eq.(7.19), the axial stiffness of the beam with plastic hinge and large deflection can be determined by

(a) for the neutral axis in the web

$$k_{bt,p} = \frac{dF}{du} = -\frac{F}{2\omega \frac{M_p F}{F_p^2} + \delta} \frac{L}{2\lambda \delta} \quad (7.20)$$

(b) for the neutral axis in the flange

$$k_{bt,p} = \frac{dF}{du} = -\frac{F}{\frac{M_p}{\zeta F_p} + \delta} \frac{L}{2\lambda \delta} \quad (7.21)$$

Similarly, for a beam with end rotation fully restrained, the axial stiffness of the beam with plastic hinge and large deflection is derived as

(a) for the neutral axis in the web

$$k_{bT,p} = \frac{dF}{du} = -\frac{F}{4\omega \frac{M_p F}{F_p^2} + \delta} \frac{L}{2\lambda \delta} \quad (7.22)$$

(b) for the neutral axis in the flange

$$k_{bT,p} = \frac{dF}{du} = -\frac{F}{2 \frac{M_p}{\zeta F_p} + \delta} \frac{L}{2\lambda \delta} \quad (7.23)$$

7.1.2.4 Analysis of the Restrained Beam During the Cooling Phase in a Fire

For simplicity, the temperature distribution over the cross-section of the beam is assumed to be uniform.

• Stress-strain relationship during the cooling phase

The stress-strain relationship of steel is supposed to be linear when unloading, as shown in Fig. 7.22. According to the proposal by El-Rimawi et al.^[24], the stress-strain relationship of steel during cooling can be assumed to follow the path shown in Fig. 7.23. At temperature T_1 or T_2 , the elastic modulus of steel is E_{T_1} or E_{T_2} , and the stress may increase up to f_{yT_1} or f_{yT_2} . If the strain in the steel reaches ε_{T_1} with a stress of f_{yT_1} at T_1 then the temperature begins to decrease from T_1 to T_2 , and the change in the strain and stress of the steel can be divided into two steps

- unload at temperature T_1 , and the strain decreases to ε_y with a slope equal to E_{T_1} ;
- decrease the temperature to T_2 and then increase the load, and the strain and stress increase again with a slope equal to E_{T_2} . When the stress reaches f_{yT_1} , the corresponding strain is ε_{T_2} , which is equal to $\varepsilon_{T_1} - f_{yT_1}/E_{T_1} + f_{yT_1}/E_{T_2}$.

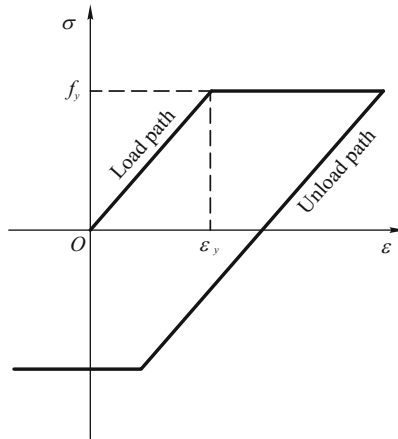


Fig. 7.22 Stress-strain curve of steel when unloading

• Behavior of the restrained beam during cooling

When the steel temperature decreases from T_1 to T_2 , the elastic modulus and yield strength recover, which increases the stiffness and the load bearing capacity of the beam. At the same time, a contraction force ΔF will be produced, as shown in Fig. 7.24(a).

In order to study the behavior of a restrained beam during cooling, a temperature negative incremental approach is employed. The completed process of cooling can

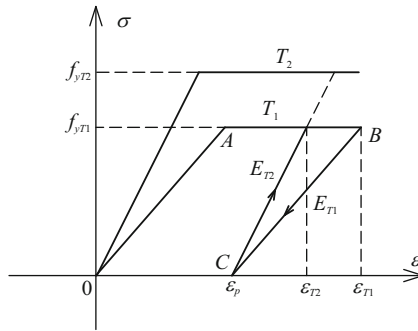


Fig. 7.23 Reversal of stress in steel during cooling

be divided into many decrements. In each temperature decrement, $\Delta T = T_2 - T_1$, the analysis of a beam is divided into four steps:

- Step 1:** the applied vertical load is unloaded at temperature T_1 , with the axial force in the beam and moment at the beam ends being kept constant;
- Step 2:** the steel temperature decreases from T_1 to T_2 and the beam contracts. The steel elastic modulus and yield strength recover, as shown in Fig. 7.24(b);
- Step 3:** apply load on the beam by the previous value; and
- Step 4:** the incremental tensile axial force Δf resulting from contraction is applied at the beam ends, as shown in Fig. 7.24(c).

• **Deflection induced by recovery of elastic modulus of steel**

Because the plastic strain cannot be recovered during the cooling phase, the beam remains as a bowed beam. The deflection reversal of the restrained beam resulting from the recovery of the steel elastic modulus during steps 1 to 3 is determined according to the process shown in Fig. 7.25.

For an isolated bowed beam with a profile function $f(x)$, as shown in Fig. 7.25, the applied vertical load will induce an increment of deflection $d_{P,T}$ determined by

$$d_{P,T} = \frac{P c_L}{E_T} \tag{7.24}$$

where c_L is a factor dependent on the span of the beam and the type of the vertical load on the beam.

If horizontal restraints are applied on the ends of the bowed beam (Fig. 7.26), the deflection increment will produce an axial force F_u . The horizontal tensile force F_u will induce a decrement of deflection $d_{F,T}$. Then the deflection increment will be reduced to d_T .

According to the law of energy conservation, $d_{F,T}$ is determined by

- (a) for a simply-supported beam

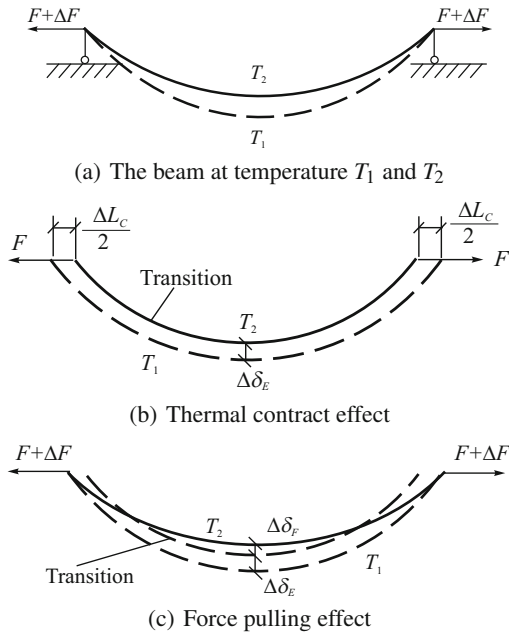


Fig. 7.24 Behavior of the restrained beam during cooling

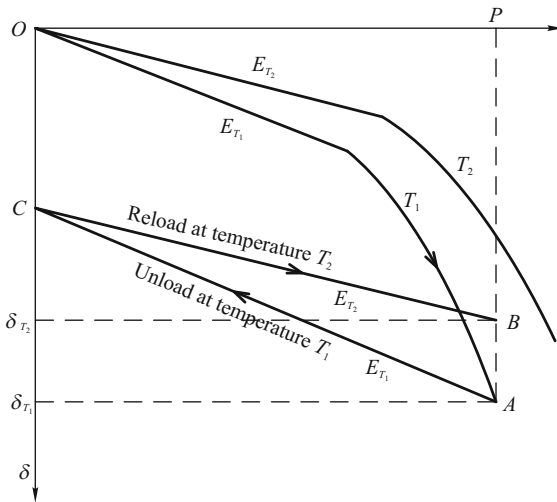


Fig. 7.25 Deflection reversal resulting from the recovery of elastic modulus

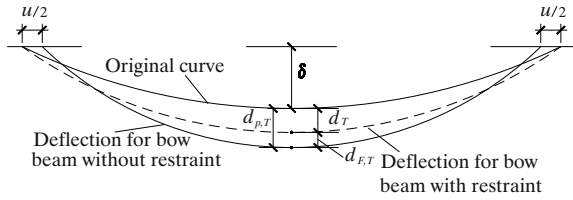


Fig. 7.26 Deflection the beam by bowing effects

$$d_{F,T} = \frac{2F_u}{E_T I} \int_0^{L/2} \left(\frac{1}{2}x\right) f(x) \sqrt{1 + f'^2(x)} dx \quad (7.25)$$

(b) for a rotationally restrained beam

$$d_{F,T} = \frac{2F_u}{E_T I} \int_0^{L/2} \left(\frac{L}{8} - \frac{x}{2}\right) \left[\frac{\int_0^L \sqrt{1 + f'^2(x)} f(x) dx}{\int_0^L \sqrt{1 + f'^2(x)} dx} - f(x) \right] \sqrt{1 + f'^2(x)} dx \quad (7.26)$$

The above equations can be simplified as

$$d_{F,T} = \frac{2F_u}{E_T I} C_d \quad (7.27)$$

where

(a) for a simply-supported beam

$$d_{F,T} = \int_0^{L/2} \left(\frac{1}{2}x\right) f(x) \sqrt{1 + f'^2(x)} dx \quad (7.28)$$

(b) for a rotationally restrained beam

$$d_{F,T} = \int_0^{L/2} \left(\frac{L}{8} - \frac{x}{2}\right) \left[\frac{\int_0^L \sqrt{1 + f'^2(x)} f(x) dx}{\int_0^L \sqrt{1 + f'^2(x)} dx} - f(x) \right] \sqrt{1 + f'^2(x)} dx \quad (7.29)$$

The horizontal displacement of the beam end u can be expressed approximately as

$$u = \frac{2\lambda \delta_T}{L} d_T \quad (7.30)$$

Considering the relationship of $d_{p,T}$, d_T , $d_{F,T}$ and F_u , gives

$$d_T + d_{F,T} = d_{p,T} \quad (7.31)$$

and

$$F_u = uk_g = \frac{2\lambda \delta_T}{L} d_T k_g \quad (7.32)$$

substituting Eq.(7.32) into Eq.(7.27) gives

$$d_{F,T} = \frac{4\lambda \delta_T}{E_T I L} d_T k_g C_d \quad (7.33)$$

and substituting Eq.(7.33) into Eq.(7.31), d_T can be worked out as

$$d_T = \frac{d_{P,T}}{1 + \frac{4\lambda \delta_T}{E_T I L} k_g C_d} \quad (7.34)$$

At temperature T_1 , the unloading will lead to a deflection reduction d_{T_1} . At temperature T_2 , reloading will induce a deflection increase d_{T_2} . Then the deflection reversal resulting from the recovery of the elastic modulus of steel is determined by

$$\begin{aligned} \delta_{rev,E} = d_{T_1} - d_{T_2} &= \frac{\frac{pCL}{E_{T_1}}}{1 + \frac{4\lambda \delta_{T_1}}{E_{T_1} I L} k_g C_d} - \frac{\frac{pCL}{E_{T_2}}}{1 + \frac{4\lambda \delta_{T_2}}{E_{T_2} I L} k_g C_d} \\ &= \frac{\frac{pCL}{E_{T_1}}}{1 + \frac{4\lambda \delta_{T_1}}{E_{T_1} I L} k_g C_d} - \frac{\frac{pCL}{E_{T_2}}}{1 + \frac{4\lambda \delta_{T_1}}{E_{T_2} I L} k_g C_d} \end{aligned} \quad (7.35)$$

where δ_{T_1} and δ_{T_2} show the mid-span deflection of the beam at temperature T_1 and T_2 , respectively. It should be noted that because the difference between δ_{T_1} and δ_{T_2} is relatively small, δ_{T_2} in the second part of the above equation is substituted by δ_{T_1} .

Given that the axial restraint stiffness is not larger than $0.1k_b$ and

$$\frac{4\lambda \delta_{T_1}}{E_{T_1} I L} k_g C_D \approx 0$$

$$\frac{4\lambda \delta_{T_1}}{E_{T_2} I L} k_g C_D \approx 0$$

then Eq.(7.35) can be simplified as

$$\begin{aligned} \delta_{rev,E} &= \frac{pCL}{E_{T_1}} - \frac{pCL}{E_{T_2}} \\ &= \frac{pCL}{E_0} \left(\frac{E_0}{E_{T_1}} - \frac{E_0}{E_{T_2}} \right) \\ &= d_0 \left(\frac{E_0}{E_{T_1}} - \frac{E_0}{E_{T_2}} \right) \end{aligned} \quad (7.36)$$

• Contraction force generated by temperature decrease

In the second step as shown in Fig. 7.24(c), because the steel strength recovers with the temperature decreasing, as shown in Fig. 7.27, and the strain induced by ΔF is

in reverse, the axial displacement of the beam ends is assumed to change elastically at the beginning. During the temperature decrease from T_1 to T_2 , if the plastic hinge occurs, the complete relative displacement change of the ends due to ΔF can be divided into two parts, i.e. the elastic part Δu_e and the plastic part Δu_p . Accounting for the geometric compatibility, the following equation must be satisfied

$$\Delta u_e + \Delta u_p = \alpha L \Delta T \tag{7.37}$$

where $\Delta T = T_2 - T_1$, and ΔF is determined by

$$\Delta F = \Delta u_e k_{e,ae} + \Delta u_p k_{e,ap} \tag{7.38}$$

where $k_{e,ae}$ is the effective axial restraint stiffness when the beam is in an elastic state and $k_{e,ap}$ is the effective axial restraint stiffness when the beam is in a plastic state.

• **Moment at the beam ends during cooling**

For beams with the end fully rotationally restrained, when the temperature decreases from T_1 to T_2 , the incremental axial tension force will lead to a the change of moment at the beam ends.

If a the plastic hinge does not occur, the change in the moment can be determined by Eq.(7.39) according to Eq.(7.8) as

$$\Delta M_{\text{end}} = \frac{\Delta F \int_0^l \sqrt{1 + f'^2(x)} f(x)(d) x}{\int_0^l \sqrt{1 + f'^2(x)} dx} \tag{7.39}$$

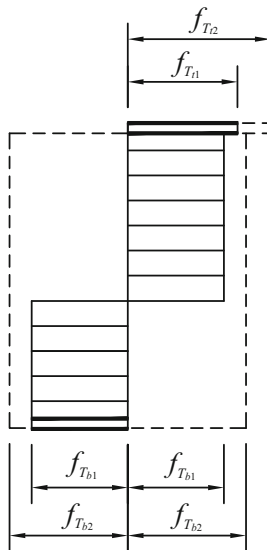


Fig. 7.27 Recovery of the steel strength with the temperature decreasing

Then the moment at T_2 is expressed as

$$M_{\text{end},T_2} = M_{\text{end},T_1} - \Delta M_{\text{end}} \quad (7.40)$$

Given that there is a plastic hinge, the moment at the beam ends can be worked out from Eq.(7.12) and Eq.(7.13) as

(a) for the neutral axis in the web

$$M_{\text{end},T_2} = \left[1 - \omega \left(\frac{F}{F_p} \right)^2 \right] M_p \quad (7.41)$$

(b) for the neutral axis in the flange

$$M_{\text{end},T_2} = \left[1 - \left| \frac{F}{F_p} \right| \right] \frac{M_p}{\zeta} \quad (7.42)$$

• Deflection reversal due to the contraction force

When the steel temperature decreases from T_1 to T_2 , and if ΔF is not so large as to create a plastic hinge in the beam, the deflection reversal of the beam induced by ΔF is obtained with the energy conservation principle by

$$\delta_{\text{rev},F} = \frac{2\Delta F}{E_{T_2} I} C_d \quad (7.43)$$

• Total deflection during cooling

When the temperature decreases from T_1 to T_2 , given that the plastic hinge does not occur, the total deflection of the beam at temperature T_2 is determined by

$$\delta_{T_2} = \delta_{T_1} - \delta_{\text{rev},E} - \delta_{\text{rev},F} \quad (7.44)$$

If a plastic hinge occurs, the deflection of the beam has to be worked out through the equilibrium equation of the beam.

For a pin supported beam, the deflection of the beam at temperature T_2 is derived from Eq.(7.1) as

$$\delta_{T_2} = \frac{M_q + M_{\text{mid}}}{F} \quad (7.45)$$

where M_{mid} is worked out from Eq.(7.12) and Eq.(7.13).

Similarly, for a beam with ends fully rotationally restrained, the deflection of the beam at temperature T_2 is expressed, assuming M_{mid} equals M_{end} , as

$$\delta_{T_2} = \frac{M_q + 2M_{\text{end},T_2}}{F} \quad (7.46)$$

The behavior of a restrained beam during the cooling phase can then be analyzed following the steps presented above, until the steel temperature decreases to an ambient temperature.

7.1.2.5 Validation

The performance of a heated restrained steel beam during cooling is predicted by this method and compared with results obtained by the FE method. The beam is H 400×200×8×13 of steel Q235 with a span of 8m. The FEM analysis is carried out by ANSYS^[25]. In the FE analysis, a shell element is employed to simulate the flanges and web of the beam.

Four types of restraints are applied to the beam. In the first and second type, the beam ends are pin supported and the axial restraint stiffness is $0.1k_b$ and $0.4k_b$, respectively. The uniformly distributed load on the beam is 26.25 kN/m. In the third and fourth type of restraint, the beam ends are fixed and the axial restraint stiffness is $0.2k_b$ and $0.4k_b$ respectively. The uniformly distributed load on the beam is 35.5 kN/m.

For the beam with the first and second types of restraint, the development of the deflection and the axial force predicted by the proposed method and the FE method are compared in Fig. 7.28 to Fig. 7.29. For a beam with the third and fourth types of restraint, the development of the deflection, the axial force and the moment at the ends predicted by the proposed method and the FE method are compared in Fig. 7.30 to Fig. 7.32. It can be seen that results by the method proposed and the FEM method are in good agreement.

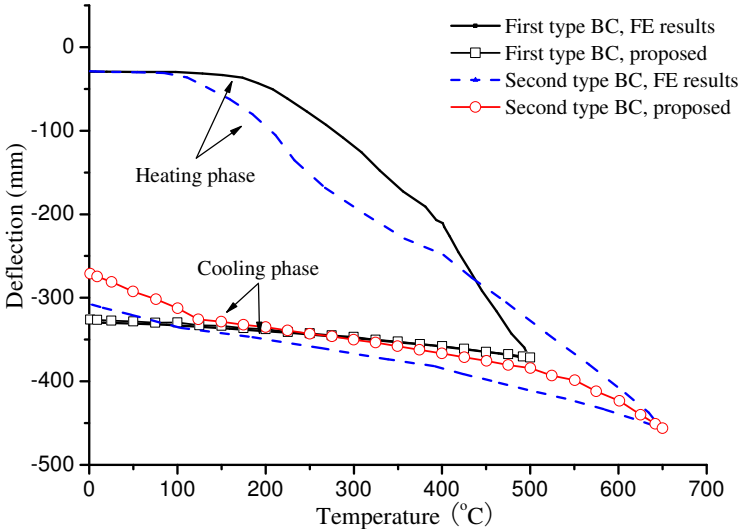


Fig. 7.28 Comparison of deflections predicted by the FE method and the proposed method (hinged support)

That axial tensile force increases as the temperature decreases. The beam with a larger axial restraint stiffness has a bigger increment in the axial tensile force.

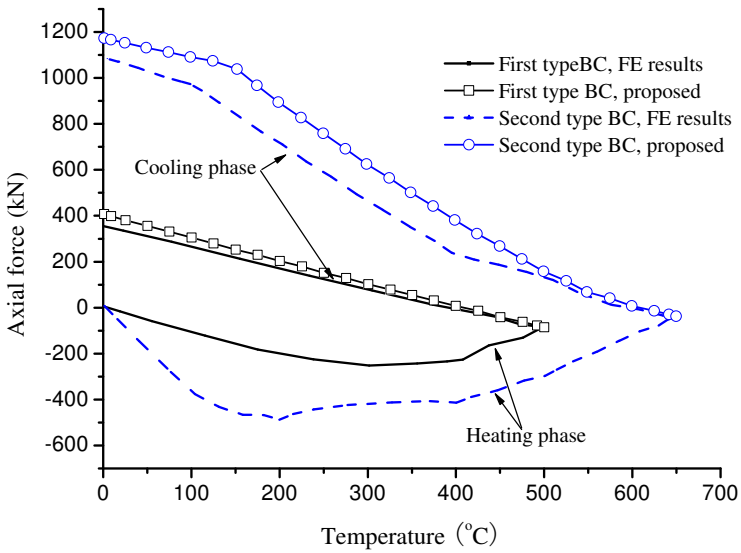


Fig. 7.29 Comparison of axial forces predicted by the FE method and the proposed method (pin supported)

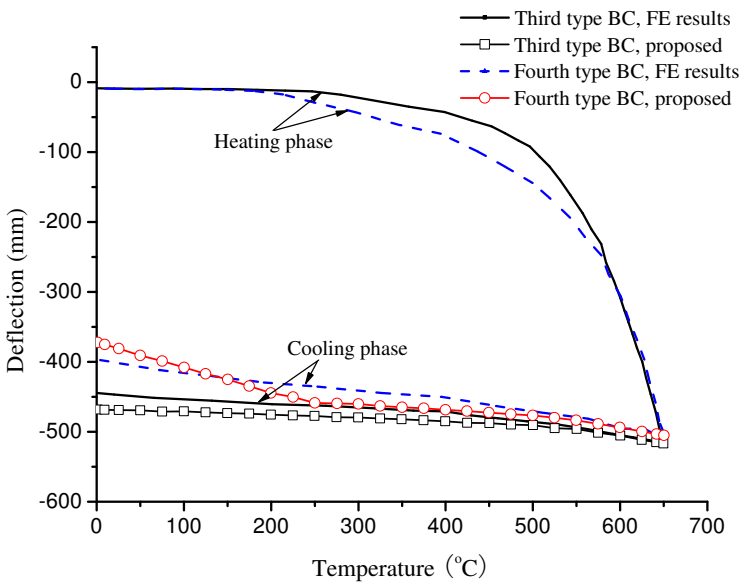


Fig. 7.30 Comparison of deflections predicted by the FE method and the proposed method (fix ended)

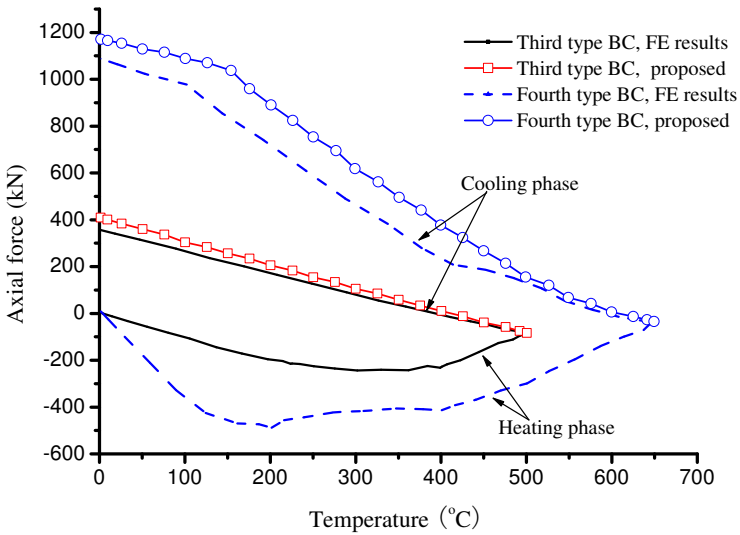


Fig. 7.31 Comparison of axial forces predicted by the FE method and the proposed method (fix ended)

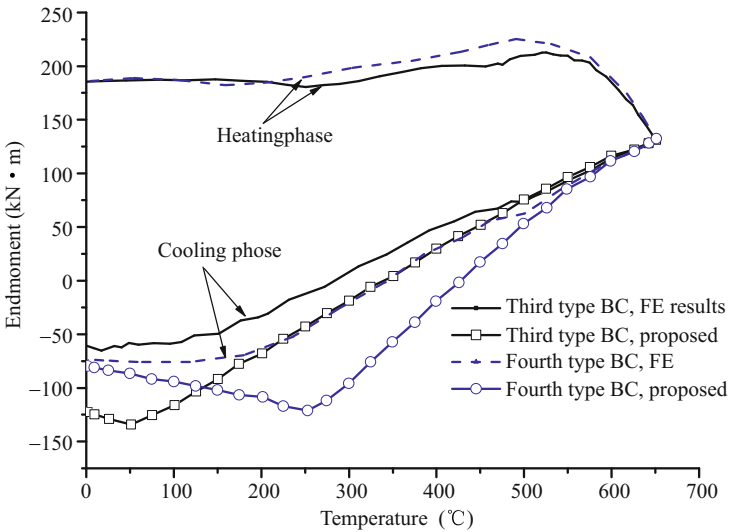


Fig. 7.32 Comparison of end moments predicted by the FE method and the proposed method (fix ended)

However, too large an axial tensile force will produce a plastic hinge in the restrained steel beam. The increased rate of the axial force will decrease and the deflection reversal will increase sharply.

In addition, if the rotation is restrained at the beam ends, the moments at the beam ends will vary reversely. Eventually, the moments at the beam can change to negative. Together with the effect of the axial tensile force, the negative moment may lead to tremendous tensile stress at the bottom flange near the beam ends.

7.2 Fire Resistance of Steel-Concrete Composite Beams

7.2.1 Fire Test on Restrained Steel-Concrete Composite Beams

The fire-resistance of a composite beam has been a research concern recently years [26,27,28,29,30,31]. Benedetti [32] proposed an analytical method for predicting the fire-resistance of composite beams. Wang [33] studied behavior of a composite beam with partial fire protection. In order to propose a simplified design method for the fire-resistance of steel-concrete composite beams, a series of tests were carried out [34,35] to study

- the temperature elevation of a steel-concrete composite beam;
- the failure model and failure mechanism of restrained steel-concrete composite beams and
- the effectiveness of the simplified design method proposed.

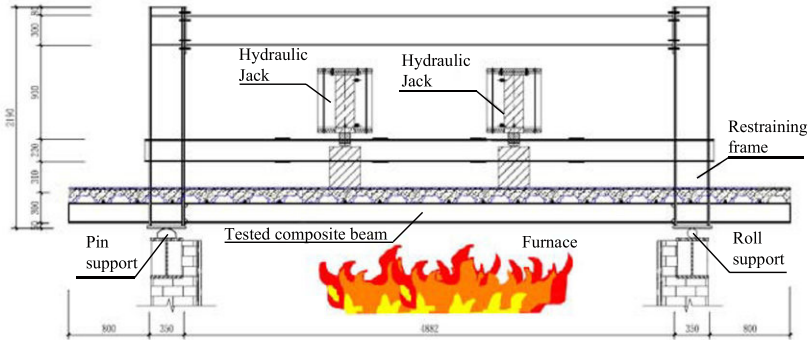
7.2.1.1 Test Design

The span of the steel-concrete composite beam is 5.23 m [34] and the depth of the steel deck is 76 mm. The detailed description of the specimen is listed in Table 7.1.

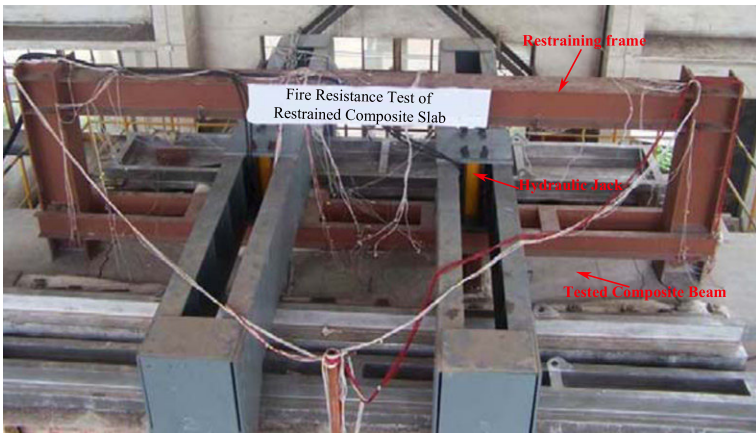
Table 7.1 Parameters of the test specimen

No.	Steel beam	Depth of concrete slab	Concrete Grade	Reinforcement	Boundary condition	Applied load (Load ratio)
CB150	HN200×100	150 mm	C30	φ8135	Pinned	40 kN (0.49)
CB125	HN200×100	125 mm	C30	φ8200	Rigid	60 kN (0.52)

The column of the restraint frame is H 350×300×8×20 and the beam of the restraint frame is H 300×300×10×14. Two steel channels were welded at 1/3 of the height of the column to provide a restraint stiffness of 85 kN/mm, as shown in Fig. 7.33 and Fig. 7.34. Positions of the LVDTs for measuring the axial displacement and the lateral deflection are shown in Fig. 7.35. Positions of the thermal couples for measuring the temperature are shown in Figs. 7.36, 7.37 and 7.38.



(a) Layout of the test set-up



(b) Picture of the test set-up

Fig. 7.33 Test set-up

Two concentrated loads are applied on the beam at $1/3$ and $2/3$ span with a load ratio of 0.49 and 0.52 in test CB150 and CB125 respectively. The fire temperature follows the ISO 834 standard fire.

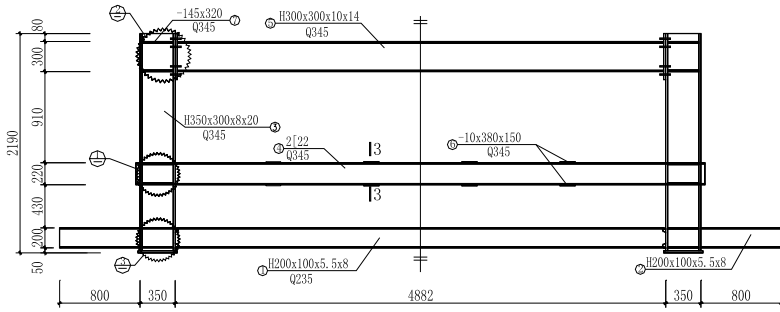


Fig. 7.34 Restraint frame (mm)

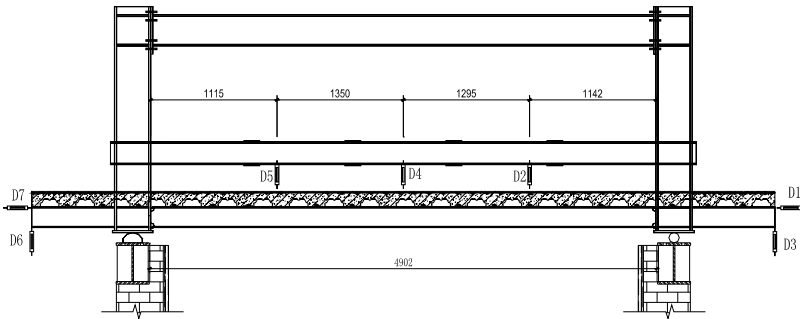


Fig. 7.35 Locations of LVDT (mm)

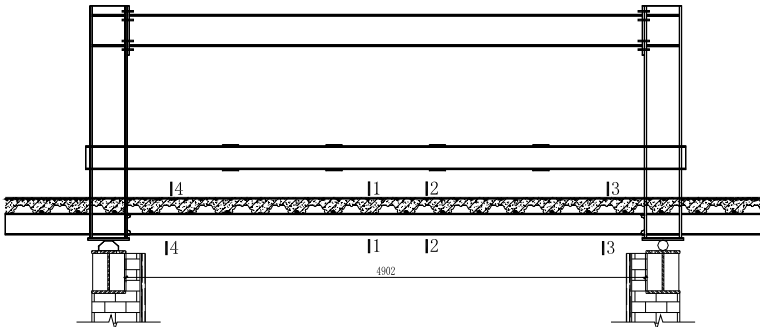


Fig. 7.36 Locations of thermal couples (mm)

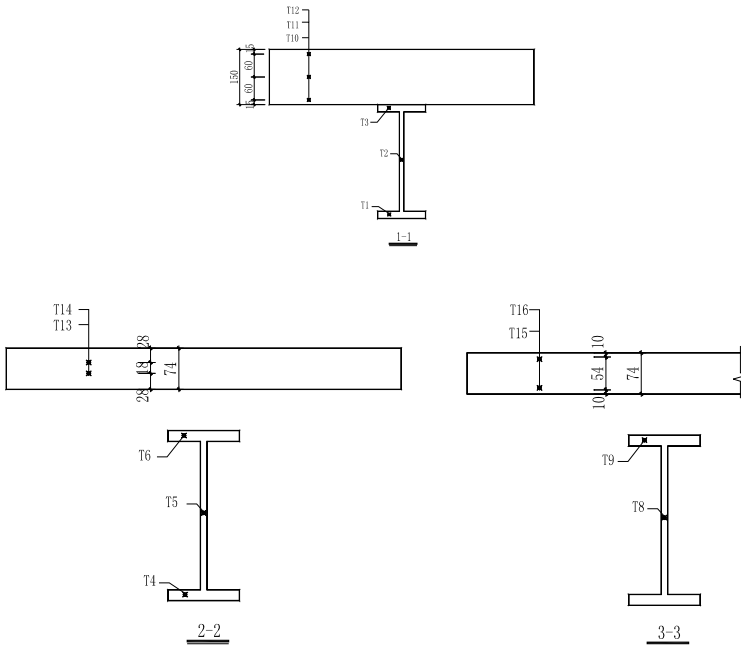


Fig. 7.37 Positions of thermal couples over cross-section of specimen CB150 (mm)

7.2.1.2 Material Strength

The materials for making the test specimen are listed in Table 7.2.

Table 7.2 Material strength (MPa)

Concrete	Reinforcement		Steel plate		
	φ8	φ12	–5 mm	–8 mm	–20 mm
43.1	316	421	300	277	333

7.2.1.3 Test Results

• Specimen CB150

With the elevation of temperature, cracks perpendicular to the beam appeared at the beam end. After about 40 min of the test, water exuded through cracks in the slab. At about 70 min after the test, the concrete slab temperature reached about 130 °C and all the water had evaporated, as shown in Fig. 7.39 and Fig. 7.40. Cracks in the

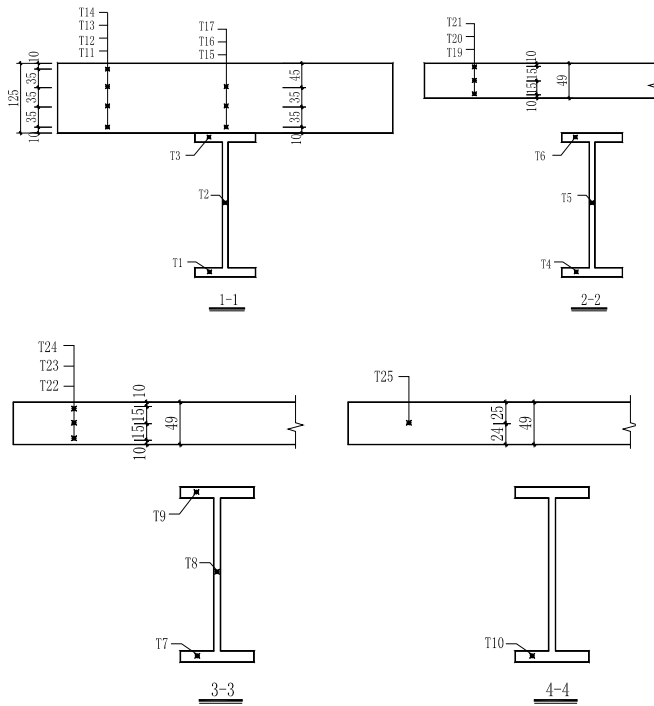


Fig. 7.38 Positions of thermal couples over cross-section of specimen CB125 (mm)

concrete slab mainly existed between the load point and the support of the beam. After the fire test, there was local buckling on both the flange and web of the steel beam. The fire protection of the steel beam was destroyed due to the large local deformation.

The local buckling of the beam web and flange will cause destruction and a decrease in fire protection. Fig. 7.41 shows that the length of the destroyed fire protection was about three times the flange width. After the drop in fire protection, the temperature of the steel beam will increase quickly. Due to the large deflection of the beam, there are some cracks in the fire protection at the beam's middle span. However, there is still fire protection on the beam.

After the fire test, with the decrease in temperature, the deflection of the beam only recovers by about 40 mm. When the temperature of the beam is reduced to about 150 °C, there is a great sound of fracture in the furnace produced by the fracture of the beam-column joint, as shown in Fig. 7.40.

• Specimen CB125

Water is exuded after about 40 min and water evaporates out after about 70 min in test CB125.



Fig. 7.39 Water exudes through cracks in the slab in the test CB150 (mm)



Fig. 7.40 Breaking of the joint in test CB150



Fig. 7.41 Local buckling of the steel beam in test CB150



Fig. 7.42 Deformation of the web and high strength bolt in test CB150

Since the steel beam was rigidly connected to the reaction frame, the compression force in specimen CB125 was greater than that in specimen CB150. The local buckling of the flange was more serious than in specimen CB150, as shown in Fig. 7.43.

No cracks appeared between the two load points in test CB150. However, cracks appeared in the CB125, as shown in Fig. 7.44. This is due to the centenary action which caused a tensile force in the beam and tensional cracks in the concrete slab.

The deflection of the composite beam recovered about 50mm after the test and the joint did not causes a break.



Fig. 7.43 Local buckling of the flange of in test CB125

7.2.1.4 Temperature Results

● Specimen CB150

The measured fire temperature in test CB150 is shown in Fig. 7.45. About 5 min later, the measured fire temperature and the ISO834 fire curve agree very well.



Fig. 7.44 Cracks in the concrete slab in test CB125

Measured temperatures of the steel beam and concrete slab are shown in Fig. 7.46 and Fig. 7.47, respectively. The measured temperatures of T_1 and T_4 , T_2 and T_5 are nearly identical to each other, which shows that the concrete slab has negligible influence on the temperature elevation of the bottom flange and web of the steel beam. The measured temperature of T_3 is about 60 °C lower than that of T_6 , which shows that the concrete will influence the temperature elevation of the upper flange of the steel beam.

Thermal couple T_{10} was 15 mm from the bottom of the concrete slab. The maximum measured temperature was 580 °C. However, the maximum temperature at 75 mm (T_{11}) and 135 mm (T_{12}) from the bottom of the concrete slab was only about 180 °C.

Measured concrete temperatures through T_{14} and T_{13} are shown in Fig. 7.37 and Fig. 7.38. The maximum temperature was 280 °C.

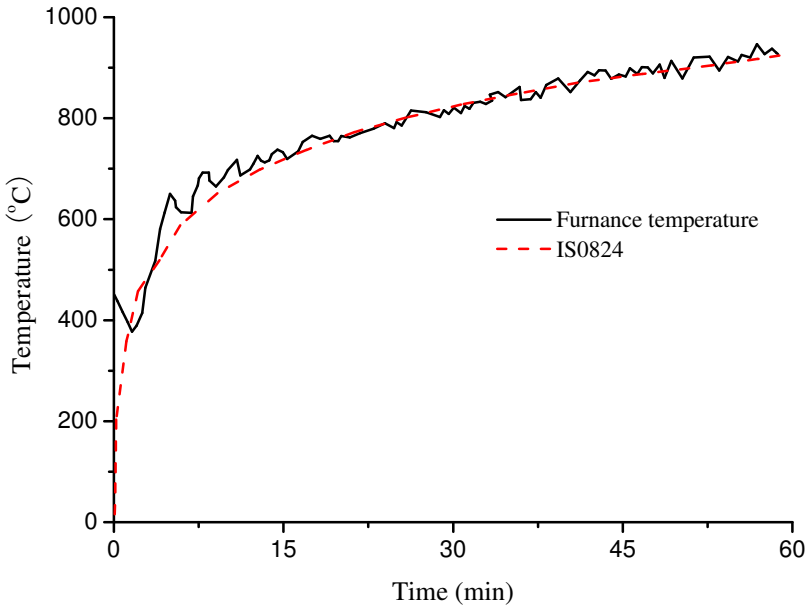


Fig. 7.45 Fire temperatures in test CB150

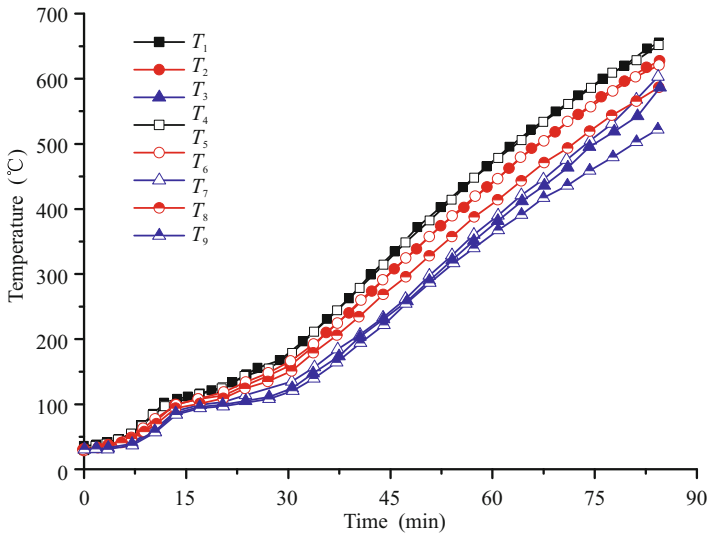


Fig. 7.46 Temperatures of the steel beam in test CB150

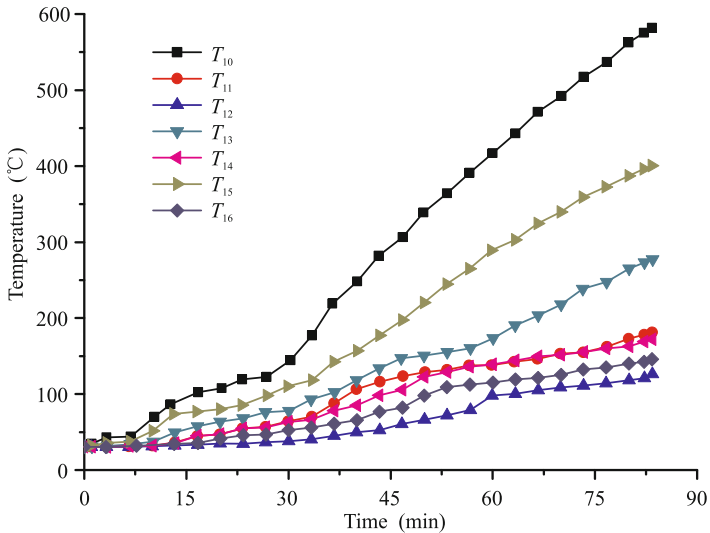


Fig. 7.47 Temperatures of the concrete slab in test CB150

• Specimen CB125

The fire temperature in test CB125 is shown in Fig. 7.48 and measured temperatures of the steel beam and concrete slab are shown in Fig. 7.49 and Fig. 7.50 respectively.

Temperatures of $T_7 - T_{10}$ increased suddenly after 3200 s of the test, as shown in Fig. 7.49, which means the fire protection at this position was broken.

Except for temperatures of T_{11} and T_{19} , which are only 15 mm from the bottom of the concrete slab, the measured temperatures of all the other thermal couples are lower than 500 °C.

7.2.1.5 Displacement Results

Locations of the LVDTs are shown in Fig. 7.35. Axial displacements at two ends of the test beam and axial deformations of the specimen CB150 and CB125 are shown in Fig. 7.51 and Fig. 7.52 respectively. Deflections of the specimens CB150 and CB125 are shown in Fig. 7.53 and Fig. 7.54 respectively. Axial deformations of both specimens increase till deflections reach a certain level, then decrease with the further development of the deflections due to the catenary action of the restrained beam.

7.2.2 Analysis of Restrained Steel-Concrete Composite Beams

7.2.2.1 Axial Stiffness of a Composite Beam and Axial Force in the Composite Beam

Assume the axial stiffness of a half span steel-concrete beam is k and the horizontal displacement of the support is δ_h , so the axial force in the composite beam

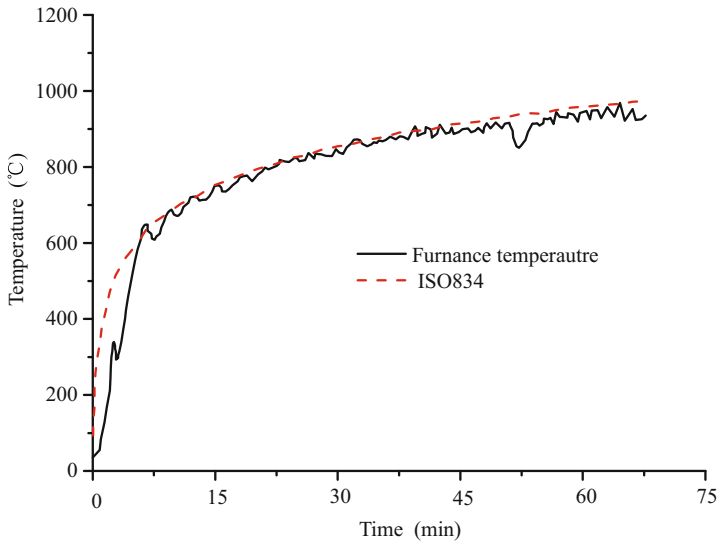


Fig. 7.48 Fire temperatures in test CB125

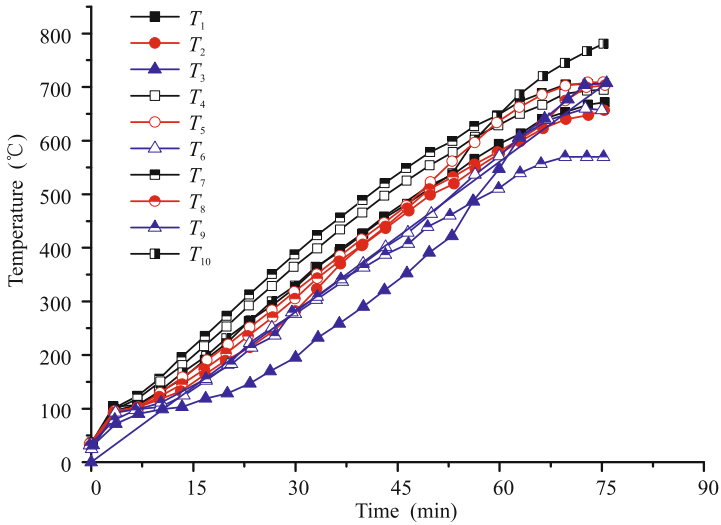


Fig. 7.49 Temperatures of steel beam in test CB12

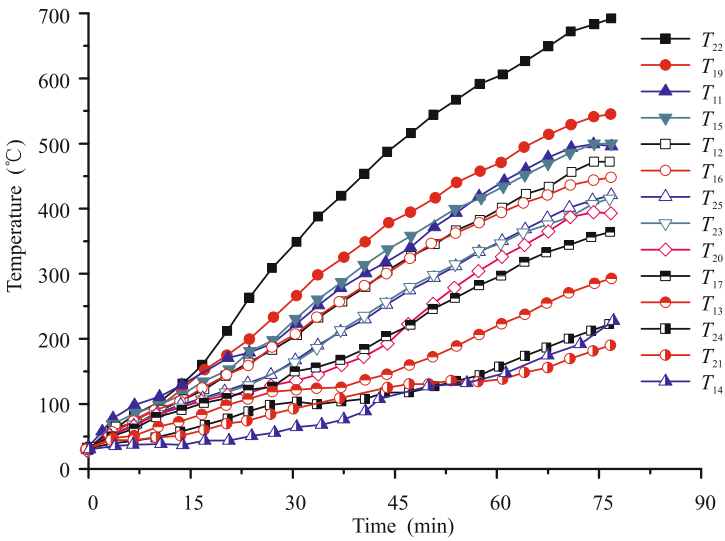


Fig. 7.50 Temperatures of the concrete slab in test CB125

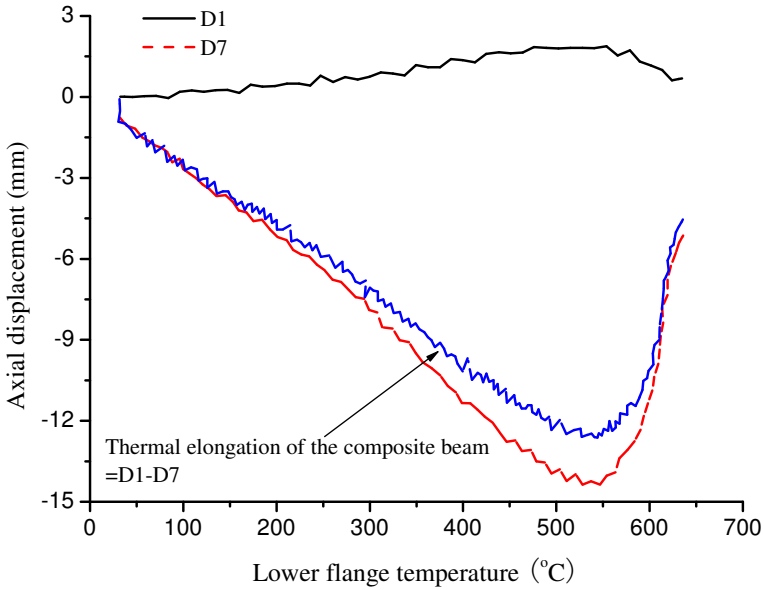


Fig. 7.51 Axial displacements and deformations of test CB150

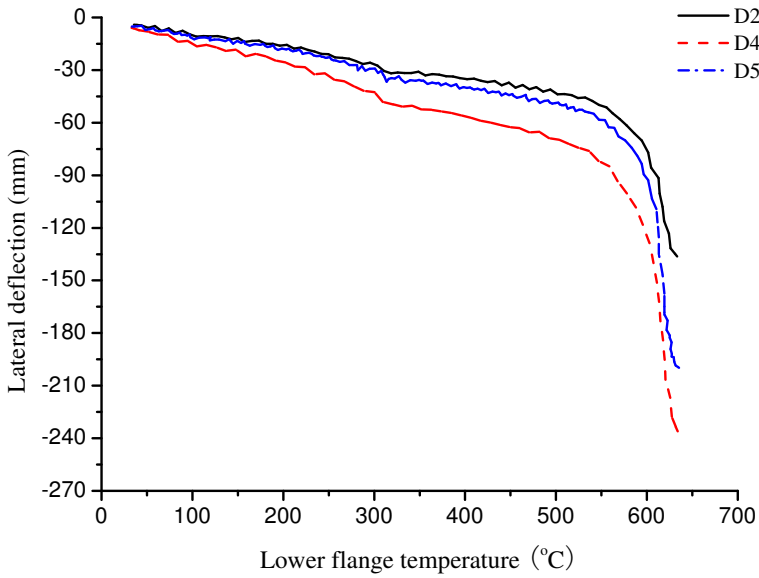


Fig. 7.52 Deflections of the test CB150

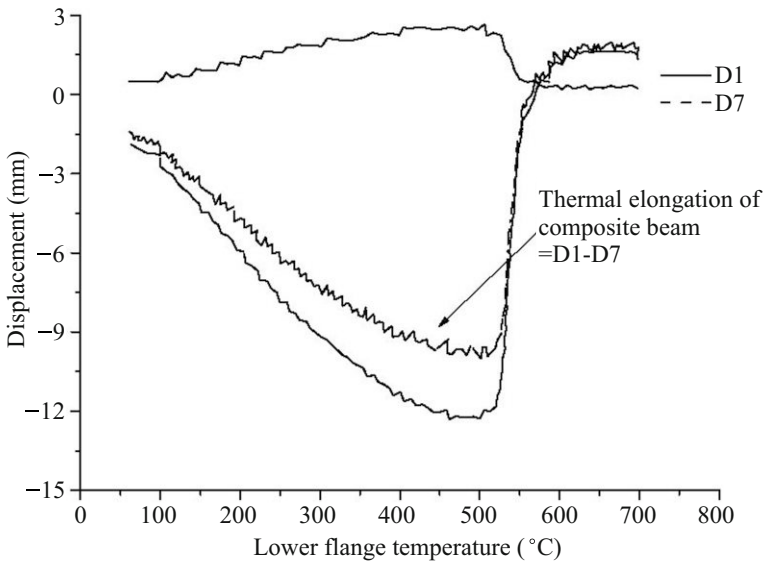


Fig. 7.53 Axial displacements and deformations of test CB125

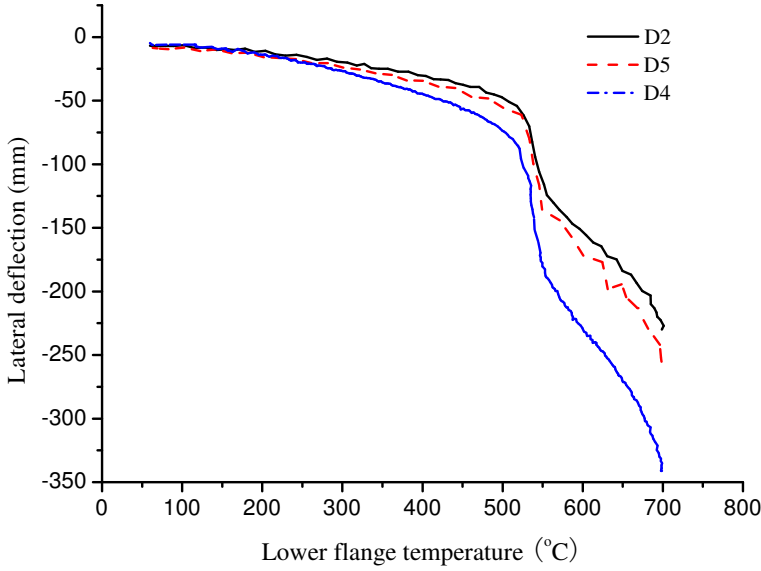


Fig. 7.54 Deflections of test CB125

$$F_T = k\delta_h \tag{7.47}$$

where k is the axial stiffness and δ_h is the support displacement.

• **Axial stiffness of the composite beam**

The axial stiffness of a half span composite beam is calculated by

$$k = \frac{1}{\frac{1}{k_{bT}} + \frac{1}{k_a}} = \frac{k_{bT}k_a}{k_{bT} + k_a} \tag{7.48}$$

where k_{bT} is the axial stiffness of the composite beam at temperature T and is obtained through

(a) when the composite beam is under compression

$$k_{bT} = \alpha_c \alpha_k \frac{E_{sT}A_{se} + E_{cT}A_{ce} + E_{sbT}A_{sb}}{L/2} \tag{7.49}$$

(b) when the composite beam is under tension

$$k_{bT} = \frac{E_{sT}A_{se} + E_{sbT}A_{sb}}{L/2} \tag{7.50}$$

where A_{ce} is the cross-sectional area of the concrete slab in an elastic state represented by height x_{ce} in Fig. 7.55, A_{se} is the cross-sectional area of the steel beam in an elastic state represented by height b in Fig. 7.55, α_k is a factor for considering the influence of cracks in a concrete slab in a continuous composite beam and $\alpha_k=0.7$,

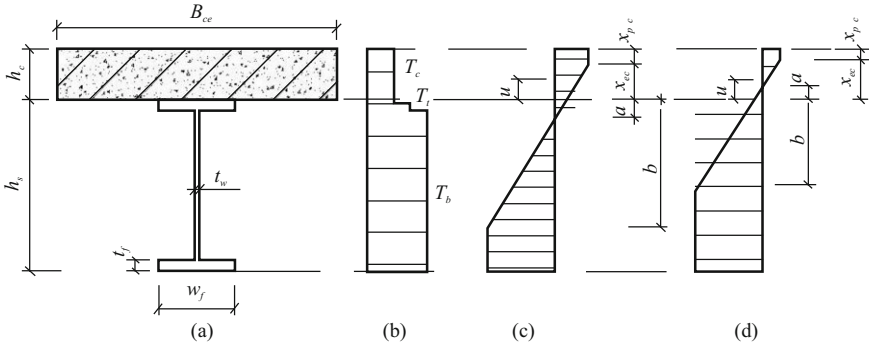


Fig. 7.55 Temperature and stress-distribution in the cross section of a composite beam: (a) cross section of the composite beam; (b) temperature distribution in the cross section; (c) stress distribution in the concrete slab and (d) stress distribution in the steel beam

α_c is a factor for considering the connection stiffness of the steel beam-column connection. For the bolted connection $\alpha_c=0.1$ and for the welded connection $\alpha_c=1.0$.

• **Support displacement**

The horizontal displacement at the beam support is caused by the bowing effect of the beam deflection and the thermal expansion of the beam due to temperature elevation.

The deflection of the composite beam

$$\omega(x) = \delta_m(2Lx^3 - x^4 - L^3x) + f_T(x) \tag{7.51}$$

For a composite beam with rotational restraint stiffness k_r at the support, the deflection can be determined through

$$f_T(x) = - \left(1 - \frac{k_r}{2E_T I/L} \right) \frac{\alpha_s T T_b - \alpha_c T T_t}{h_c + 2h_r + h_s} (x^2 - Lx) \tag{7.52}$$

Let

$$\kappa_T = \left(1 - \frac{k_r}{2E_T I/L} \right) \frac{\alpha_s T T_b - \alpha_c T T_t}{h_c + 2h_r + h_s} \tag{7.53}$$

and Eq. (7.52) is simplified as

$$f_T(x) = -\kappa_T(x^2 - Lx) \tag{7.54}$$

The horizontal displacement at the beam support due to the beam deflection is obtained by

$$\begin{aligned} \delta_h &= \int_0^{L/2} \sqrt{1 + \left(\frac{d\omega(x)}{dx} \right)^2} dx - \frac{1}{2}L - \frac{1}{2}\alpha L\Delta T \\ &= \frac{\pi^2 \delta_m^2}{8L} - \left(1 - \frac{\sin(\kappa_T L/2)}{\kappa_T L/2} \right) - \frac{1}{2}\alpha L\Delta T \end{aligned} \tag{7.55}$$

where α is the thermal expansion of the composite beam. For simplicity, the temperature difference in the steel and concrete is neglected. The thermal expansion of the composite beam is determined by

$$\alpha = \frac{E_{sT}A_{se}\alpha_{sT} + E_{cT}A_{ce}\alpha_{cT}}{E_{sT}A_{se} + E_{cT}A_{ce}} \quad (7.56)$$

The horizontal displacement of the composite beam due to temperature elevation is obtained through

$$\delta_{hT} = \frac{E_{sT}A_{se}\alpha_{sT}T_s + E_{cT}A_{ce}\alpha_{cT}T_c}{E_{sT}A_{se} + E_{cT}A_{ce}} \frac{L}{2} \quad (7.57)$$

7.2.2.2 Analysis of the Local Buckling in the Lower Flange of the Steel Beam

Local buckling in the lower flange near the support has been found in fire tests and fire investigations, as shown in Fig. 7.43.

The analysis of the local buckling of the lower flange of the beam is shown in Fig. 7.56. Assume the buckling length in the lower flange to be L_f . The work of the axial force on the lower flange out of plan displacement equals that of the bending moment on the plastic hinge rotation in the buckling region as

$$2 \int_0^{w_f/2} t_f \sigma_x \frac{\pi^2 \delta^2(z)}{4L_f(z)} dz = \int_0^{w_f/2} t_f^2 f_{stbend} \arctan\left(\frac{\delta(z)}{L_f(z)/2}\right) dz + \int_0^{w_f/2} t_f^2 f_{stbend} \arctan\left(\frac{L_f(z)/2}{\delta(z)}\right) dz \quad (7.58)$$

where $\delta(z)$ is the displacement of the lower flange at position z and $\delta(z)=2z\Delta/w_f$, Δ is the maximum displacement of the lower flange as shown in Fig. 7.56, $L_f(z)$ is the buckling length of the lower flange at the position z and $L_f(z)=2zL_f/w_f$, L_f is the maximum buckling length of the lower flange as shown in Fig. 7.56.

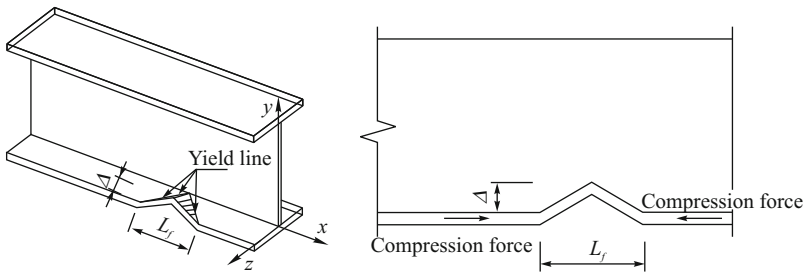


Fig. 7.56 Local buckling of the lower flange

Eq.(7.58) is simplified as

$$\frac{\pi^2 \Delta^2 t_f w_f \sigma_x}{8L_f} = \frac{1}{2} t_f^2 w_f f_{stbend} \left(\arctan\left(\frac{2\Delta}{L_f}\right) + \arctan\left(\frac{L_f}{2\Delta}\right) \right) \quad (7.59)$$

The axial force in the lower flange is determined through

$$F_{\text{lower}} = \sigma_x t_f w_f \quad (7.60)$$

and the axial force in the lower flange is obtained by

$$F_{\text{lower}} = \frac{f_{\text{stbend}} w_f^2 t_f^2}{4\pi \Delta^2} \quad (7.61)$$

With the increase in Δ , the axial force in the lower flange decreases.

The arc length of the buckled lower flange is the sum of the thermal expansion of the lower flange $\alpha_s L_f T_{\text{bend}}$ and horizontal shortening due to the rotation of the beam $\kappa_e L_f h_s$ as

$$L_{\text{arc}} = \alpha_s L_f T_{\text{bend}} + \kappa_e L_f h_s \quad (7.62)$$

Assume the buckled flange follows a polynomial curve. The maximum buckled length

$$L_{\text{arc}} = \frac{\pi^2 \Delta^2}{4L_f} \quad (7.63)$$

Substituting Eq.(7.63) into Eq.(7.62) gives

$$\frac{\pi^2 \Delta^2}{4L_f} = \alpha_s L_f T_{\text{bend}} + \kappa_e L_f h_s \quad (7.64)$$

Usually, the buckling length equals the flange width

$$L_f = w_f \quad (7.65)$$

Then Eq.(7.61) is rewritten as

$$F_{\text{lower}} = \frac{\pi f_{\text{stbend}} t_f^2}{16(\alpha_s T_{\text{bend}} + \kappa_e h_s)} \quad (7.66)$$

The yield axial force of the lower flange

$$F_{\text{yield}} = A_s f_{\text{stbend}} \quad (7.67)$$

When

$$F_{\text{lower}} < F_{\text{yield}} \quad (7.68)$$

or

$$\frac{\pi}{16(\alpha_s T_{\text{bend}} + \kappa_e h_s)} < \frac{w_f}{t_f} \quad (7.69)$$

the lower flange buckles.

7.2.3 Practical Design Method for a Restrained Steel-Concrete Composite Beam

7.2.3.1 Governing Equations

The governing equation for a fire resistance of a restrained composite beam is

$$M_f \leq F_T \delta_v + M_m + M_e \quad (7.70)$$

7.2.3.2 Temperatures of the Composite Beam

When calculating the temperature of the lower flange of a steel beam and the concrete slab, the heat conduction from the top flange to the web and lower flange is ignored. When calculating the temperature of the upper flange of a steel beam, the heat sink effect of the concrete slab is considered, as shown in Fig. 7.57.

The incremental type equation for calculating the upper flange temperature is

$$\Delta T_s = \frac{\alpha_c + \alpha_f}{\rho_s c_s V_s + \rho_c c_c V_c} F_s (T_g - T_s) \Delta t \tag{7.71}$$

where F_s is the area exposed to fire per unit length and $F_s = w_f + 2t_f - t_w$.

The temperature distribution over the cross section of the composite beam is assumed to be that shown in Fig. 7.57. The temperature in the steel beam with profiled concrete slab is assumed to be uniform and the temperature in the upper flange of the steel beam is different from that in the web and lower flange of the steel beam in a composite beam with a flat slab.

The average temperature of the concrete slab is determined through

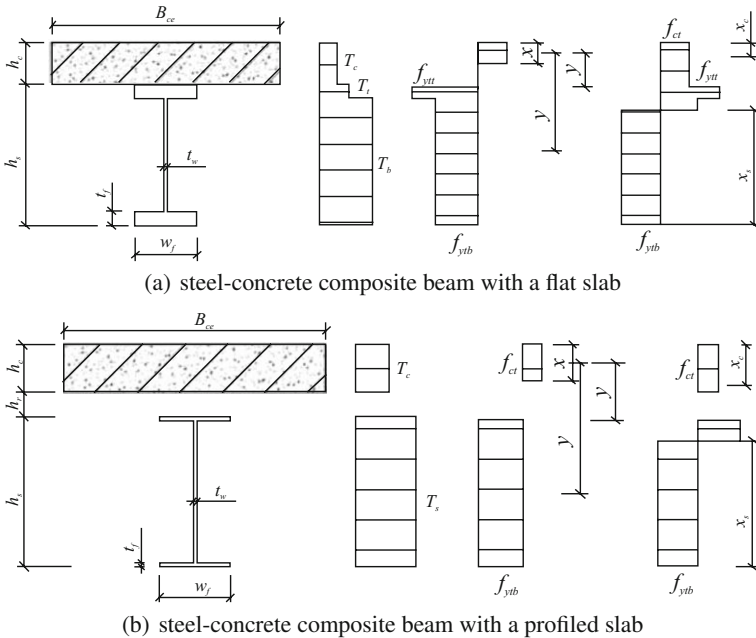


Fig. 7.57 Temperature distribution across the section in the composite beam

$$\Delta T_c = \left[\frac{0.6 \exp(-w_2/w_4) - 0.1}{h} d + 1 \right] \cdot \left[T_0 + \frac{1}{8} \exp \left(\frac{0.05 + 0.135(t/20) - 0.005(t/20)^2 - d}{0.007 + 0.0145(t/20) - 0.0005(t/20)^2} \right) \right] \quad (7.72)$$

where d is the depth of the concrete slab over the profiled steel deck as shown in Fig. 7.58, w_2 and w_4 are parameters of the profiled steel sheet as shown in Fig. 7.58.

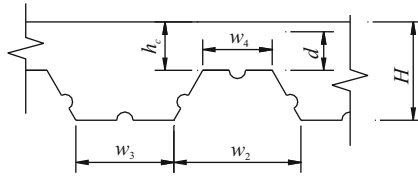


Fig. 7.58 Profiled steel deck concrete slab

7.2.4 Axial Force in the Composite Beam

Effects of the load ratio, the restraint stiffness ratio, the ratio of steel beam area to the concrete slab area, the reinforcement ratio and the temperature gradient on the ultimate tensile force in the beam are as follows:

- the tensile force in the composite beam exposed to a fire at the centenary action phase increases with the increase in the load ratio. However, the ultimate tensile force is nearly the same, which equals the tensile capacity of the steel beam at high temperature;
- the restraint stiffness has minor effects on the tensile force in the composite beam;
- the tensile force in the composite beam increases along with the ratio between the steel beam area and the concrete slab area;
- the reinforcement has little effect on the tensile force; and
- the temperature gradient has little effect on the tensile force.

Hence the tensile force of the composite beam depends on the cross sectional area of the steel beam.

For simplicity, the tensile force takes the following value

- (a) for the composite beam with a profiled concrete slab

$$F_T = F_{s0.5} = 0.5 f_{yt\text{bend}} A_s \quad (7.73)$$

- (b) for the composite beam with a flat concrete slab

$$F_T = F_{s0.5} = f_{yt\text{bend}} A_f + \frac{1}{2} f_{yt\text{bend}} A_s \quad (7.74)$$

7.2.4.1 Deflection of the Composite Beam

Effects of the load ratio, the restraint stiffness ratio, the ratio of steel beam area to the concrete slab area, the reinforcement ratio and the temperature gradient on the deflection of the restrained composite beam are as follows:

- the composite beam with a smaller load ratio has greater deflection;
- the composite beam with smaller restraint stiffness has greater deflection;
- the deflection of the beam increases with the increase in the ratio between the cross-sectional area of the steel beam and the concrete slab;
- the reinforcement ratio has little effects on the deflection;
- the temperature gradient has great effect on the deflection.

The fire test shows that the deflection of the restrained composite beam could reach $l/15$ of its span. On the safety side, the following design value of the deflection can be taken for checking the fire resistance of the restrained composite beam

$$\delta_v = L/15 \quad (7.75)$$

where L is the span of the beam.

7.2.4.2 Hogging and Sagging Moment Resistance Capacity

• Sagging moment resistance capacity

Since temperatures in the steel beam are higher than those in the concrete slab and the strength of the steel beam degrades more than the concrete slab, the natural axis of the section at high temperature generally lies in the concrete slab. Assume that half of the steel beam bears the moment and the other half bears the axial force formed in the composite beam due to the catenary action, and that the temperature over the cross section of the concrete slab is uniformly distributed. As shown in Fig. 7.59, the sagging moment resistance capacity of the composite beam is calculated by

$$M_m = B_{ce} x f_{cT} y \quad (7.76)$$

where

$$x = \frac{0.5 A_s f_{yT} \text{bend}}{B_{ce} f_{cT}} \quad (7.77)$$

• Hogging moment resistance capacity

The concrete will crack at the hogging moment region. When calculating the hogging moment resistance capacity of the composite beam, the contribution of the concrete is ignored. At the same time, the lower flange of the steel beam will buckle at high temperature. Only the contribution of the web and upper flange of the steel beam and the reinforcement in the concrete slab are included. To consider the interaction between the axial force and bending moment, the area of the reinforcement, the upper flange and the web of the steel beam that contribute to the axial force resistance should be subtracted from the section area when calculating the moment inertia of the

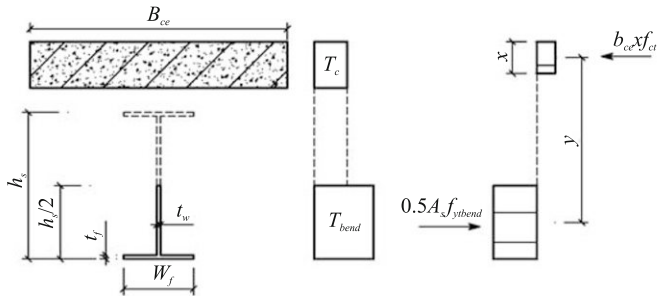


Fig. 7.59 Sagging moment resistance capacity of a composite beam

section, see Fig. 7.60 and Fig. 7.61. The order of this subtraction is the reinforcement first, then the upper flange of the steel beam, and then the web of the steel beam.

The hogging moment is calculated by

$$M_e = W_{epp} f_{yrbend} \tag{7.78}$$

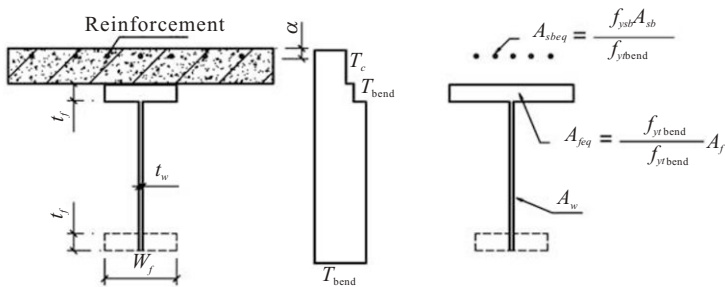


Fig. 7.60 Hogging moment resistant capacity of the composite beam with a profiled concrete slab

7.2.4.3 Calculating Steps

The fire resistance of a restrained steel-concrete composite beam is estimated through the following steps

- determine the requirement of the fire resistance time of the composite beam and calculate the temperature distribution across the section of the beam;
- calculate the material properties of the steel and concrete at high temperature and the equivalent moment inertia of the section;

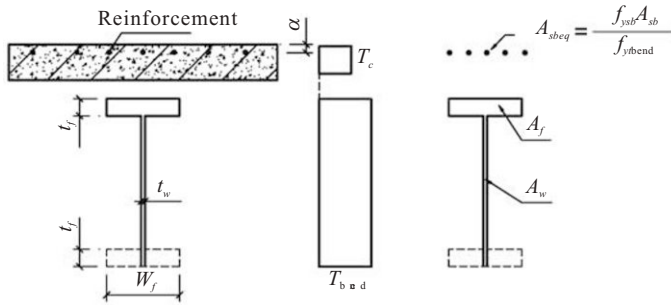


Fig. 7.61 Hogging moment resistance capacity of composite beam with a flat concrete slab

- calculate the axial force in the composite beam and the deflection of the beam with $\delta_v=L/15$ to obtain the bending moment resistance provided by catenary action as $F_T \delta_v$;
- calculate the sagging moment resistance;
- calculate the hogging moment resistance;
- check the fire resistance of the restrained composite beam.

7.2.4.4 Verification of the Proposed Method by Fire Test Results

The proposed method is verified by fire test results described above. The calculated deflection and axial force are shown in Fig. 7.62 and Fig. 7.63 respectively. The calculated deflection and axial force in the test specimen CB150 is shown in Fig. 7.64 and Fig. 7.65 respectively. Comparisons of results show that the proposed method has enough precision.

7.2.4.5 Worked Example

The test CB125 is selected as an example. The steel beam is H 200×100×5.5×8 made of Q235B steel. The depth of the concrete deck is 125 mm with a strength of 40 MPa and the reinforcement in the concrete slab is 10φ8 with a yield strength of 270 MPa. The applied bending moment is 97.6 kN·m.

Answer:

(a) Assume that the temperature of the steel beam in the hogging moment region is 600 °C and that of the concrete slab is 420 °C;

(b) The cross sectional area of the steel beam is 26.12 cm² and the axial force in the composite beam is

$$F_T = F_{s0.5} = 0.5\eta f_y A_s = 0.5 \times 0.40 \times 270 \times 2612 = 141.1 \text{ kN}$$

The maximum deflection at the middle span of the composite beam

$$L/15 = 4880/15 = 325 \text{ mm}$$

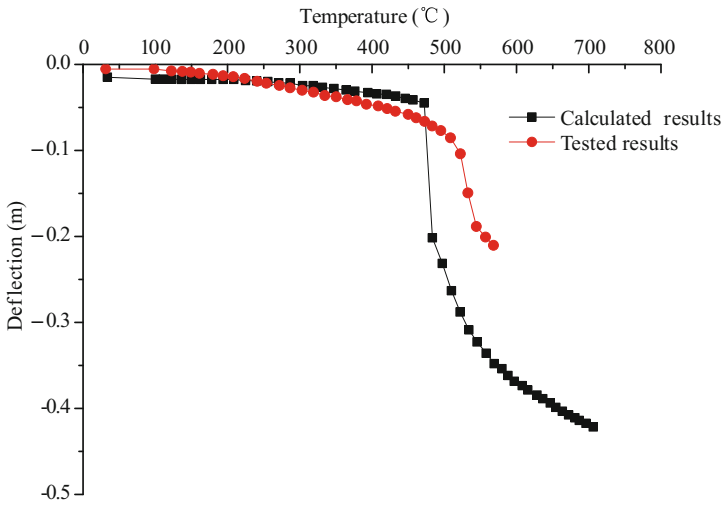


Fig. 7.62 Calculate and tested deflections of test CB125

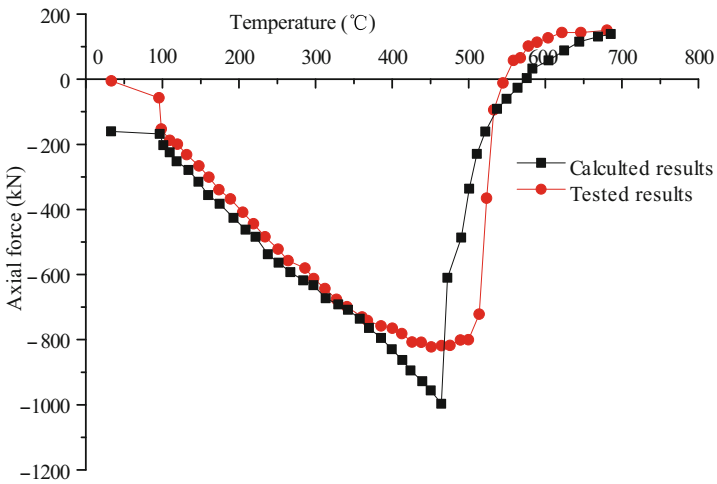


Fig. 7.63 Calculated and tested axial forces of test CB125

The bending moment provided by the catenary action

$$F_{30.5}L/15 = 141.1 \times 0.325 = 46.0 \text{ kN}\cdot\text{m}$$

(c) The compression strength of concrete at a temperature of 420 °C

$$f_{c,T} = 0.72 \times 40 = 28.8 \text{ MPa}$$

the height of the compression region of the concrete slab

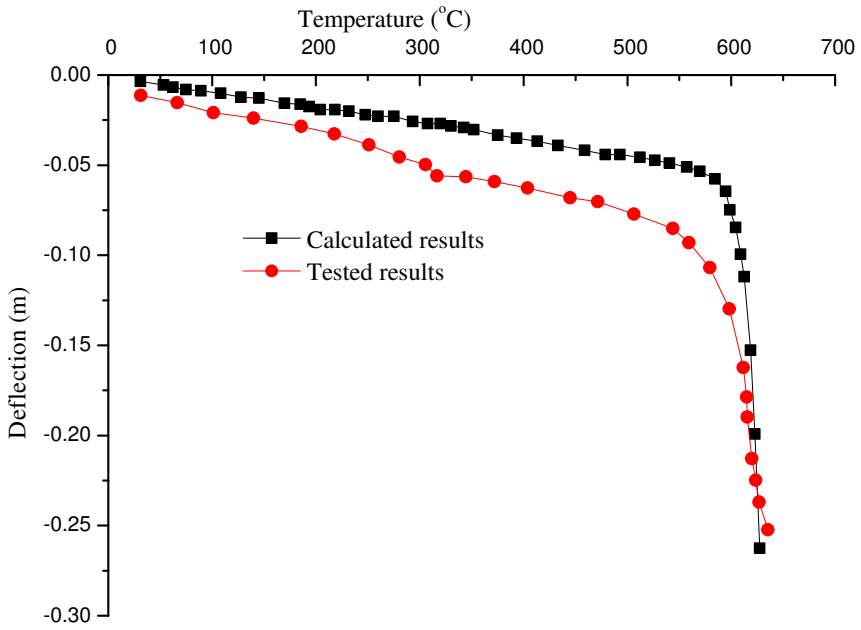


Fig. 7.64 Calculated and tested deflections of test CB150

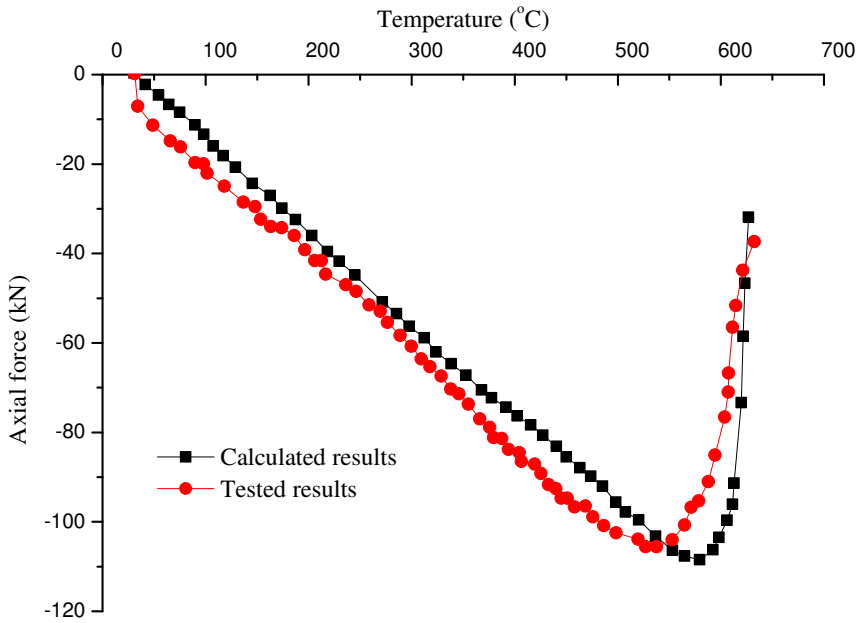


Fig. 7.65 Calculated and tested axial forces of test CB150

$$x = \frac{0.5A_s f_{ytb}}{B_{ce} f_{cT}} = \frac{0.5 \times 2612 \times 0.4 \times 270}{1350 \times 28.8} = 3.63 \text{ mm}$$

The hogging moment resistance

$$\begin{aligned} M_m &= B_{ce} x f_{cT} y \\ &= 1350 \times 3.63 \times 28.8 \times \left(200 - \frac{100 \times 5.5 \times 50}{100 \times 5.5 + 100 \times 8} + 125 - \frac{3.63}{2} \right) \\ &= 42.7 \text{ kN}\cdot\text{m} \end{aligned}$$

(d) The axial force in the composite beam

$$F_{s0.5} = 131 \text{ kN}$$

and the yield force of the reinforcement in the concrete slab

$$F_{sb} = 0.873 \times 270 \times 502 = 118 \text{ kN} < F_{s0.5}$$

which means a part of the steel beam is under tensile stress.

$$A_{st} = (141100 - 118000) / (0.05 \times 270) = 1696.9 \text{ mm}^2$$

Hence the moment inertia of the left section of the composite beam

$$W_{epb} = 600.6 \text{ mm}^3$$

The sagging moment resistance is

$$W_{epb} f_{ytbend} = 600.6 \times 0.05 \times 270 = 8108.2 \text{ N}\cdot\text{mm}$$

The sagging moment resistance is very small if the catenary action effect is considered.

(e) The fire resistance of the composite beam

$$M_f = 97.6 > F_T \delta_v + M_m + M_e = 46.0 + 42.7 = 88.7$$

The applied bending moment is bigger than the bending moment resistance. The assumed temperature is too high.

(f) Make a new assumption. The temperature of the steel beam is 540 °C and recalculate. At this time, the fire resistance of the composite beam is satisfied. The critical temperature of the composite beam is 540 °C.

(g) If the catenary action effect is not included, the calculated critical temperature of the composite beam is 510 °C. Which means the critical temperature of the composite beam is increased by 30 °C if the catenary action effect is included.

References

- [1] A. D. Weller. *Broadgate Phase 8: Fire, 22 June 1990. Summary Report of Damage and Repair*. Building Research Establishment PD 21/92, 1992.

- [2] Steel Construction Institute. *Investigation of Broadgate Phase 8 Fire, Report of Fire Engineering Consultant Ltd.* SCI Fire Engineering Group, UK, 1991.
- [3] Y. C. Wang. An analysis of the global structural behaviour of the cardington steel-framed building during the two bre fire tests. *Engineering Structures*, 22(5):401–412, 2000.
- [4] C. Bailey. Computer modelling of the corner compartment fire test on the large-scale cardington test frame. *Journal of Constructional Steel Research*, 48(1):27–45, 1998.
- [5] M. Gillie, A. S. Usmani, and J. M. Rotter. A structural analysis of the first cardington test. *Journal of Constructional Steel Research*, 57(6):581–601, 2001.
- [6] M. Gillie, A. S. Usmani, and J. M. Rotter. A structural analysis of the cardington british steel corner test. *Journal of Constructional Steel Research*, 58(4):427–442, 2002.
- [7] T. Lennon and D. Moore. The natural fire safety concept—full-scale tests at cardington. *Fire Safety Journal*, 38(7):623–643, 2003.
- [8] S. X. Guo. *The Behaviour of Restrained Steel Beam During Heating and Cooling and the Damage of Beam-to-Column Connection*. PhD thesis, Tongji University, 2006.
- [9] G. Q. Li and S. X. Guo. Experiment on restrained steel beams subjected to heating and cooling. *Journal of Constructional Steel Research*, 64(3):268–274, 2008.
- [10] C. G. Bailey, I. W. Burgess, and R. J. Plank. Analyses of the effects of cooling and fire spread on steel-framed buildings. *Fire Safety Journal*, 26(4):273–293, 1996.
- [11] C. K. Iu, S. L. Chan, and X. X. Zha. Nonlinear pre-fire and post-fire analysis of steel frames. *Engineering Structures*, 27(11):1689–1702, 2005.
- [12] K. H. Lien, Y. J. Chiou, R. Z. Wang, and P. A. Hsiao. Nonlinear behavior of steel structures considering the cooling phase of a fire. *Journal of Constructional Steel Research*, 65(8-9), 2009.
- [13] P. J. Wang, G. Q. Li, and S. X. Guo. Effects of the cooling phase of a fire on steel structures. *Fire Safety Journal*, 43(6):451–458, 2008.
- [14] T. C. H. Liu, M. K. Fahad, and J. M. Davies. Experimental investigation of behaviour of axially restrained steel beams in fire. *Journal of Constructional Steel Research*, 58(9):1211–1230, 2002.
- [15] T. C. H. Liu. Effect of connection flexibility on fire resistance of steel beams. *Journal of Constructional Steel Research*, 45(1):99–118, 1998.
- [16] T. C. H. Liu and K. M. Chiang. Influence of connection flexibility on fire resistance of structural steel frames. In: S.L. Chan and J.G. Teng (editors), *Advances in Steel Structures (ICASS '96)*, pages 405–410. Pergamon, Oxford, 1996.
- [17] S. P. Cong, S. T. Liang, and Y. L. Dong. Experimental investigation of behaviors of simply supported steel beam in fire. *Journal of Southeast University (Natural Science Edition)*, 35(1):66–69, 2005.

- [18] G. Q. Li, J. L. He, and S. C. Jiang. Fire-resistant experiment and theoretical calculation of a steel beam. *China Civil Engineering Journal*, 32(4):23–26, 2000.
- [19] Z. F. Huang, K. H. Tan, and S. K. Ting. Structural response of a steel beam within a frame during a fire. In: S.L. Chan, J.G. Teng, and K.F. Chung (editors), *Advances in Steel Structures (ICASS '02)*, pages 1111–1118. Elsevier, Oxford, 2002.
- [20] Y. Z. Yin and Y. C. Wang. A numerical study of large deflection behaviour of restrained steel beams at elevated temperatures. *Journal of Constructional Steel Research*, 60(7):1029–1047, 2004.
- [21] Y. Z. Yin and Y. C. Wang. Analysis of catenary action in steel beams using a simplified hand calculation method, part 1: theory and validation for uniform temperature distribution. *Journal of Constructional Steel Research*, 61(2):183–211, 2005.
- [22] Y. Z. Yin and Y. C. Wang. Analysis of catenary action in steel beams using a simplified hand calculation method, part 2: validation for non-uniform temperature distribution. *Journal of Constructional Steel Research*, 61(2):213–234, 2005.
- [23] G. B. Lou, G. Q. Li, L. H. Han, and S. C. Jiang. *Steel and Steel-Concrete Composite Structures Fire Resistance Design*. China Architecture & Building Press, 2006.
- [24] J. A. El-Rimawi, I. W. Burgess, and R. J. Plank. The treatment of strain reversal in structural members during the cooling phase of a fire. *Journal of Constructional Steel Research*, 37(2):115–135, 1996.
- [25] ANSYS. *ANSYS Analysis User's Manual*. ANSYS Inc., 2007.
- [26] R. H. Fakury, E. B. Las Casas, F. Pacico Jr., and L. M. P. Abreu. Design of semi-continuous composite steel-concrete beams at the fire limit state. *Journal of Constructional Steel Research*, 61(8):1094–1107, 2005.
- [27] A. M. Sanad, J. M. Rotter, A. S. Usmani, and M. A. O'Connor. Composite beams in large buildings under fire, numerical modelling and structural behaviour. *Fire Safety Journal*, 35(3):165–188, 2000.
- [28] A. Y. Elghazouli and B. A. Izzuddin. Response of idealised composite beam-slab systems under fire conditions. *Journal of Constructional Steel Research*, 56(3):199–224, 2000.
- [29] A. Y. Elghazouli and B. A. Izzuddin. Analytical assessment of the structural performance of composite floors subject to compartment fires. *Fire Safety Journal*, 36(8):769–793, 2001.
- [30] A. Y. Elghazouli, B. A. Izzuddin, and A. J. Richardson. Numerical modelling of the structural fire behaviour of composite buildings. *Fire Safety Journal*, 35(4):279–297, 2000.
- [31] J. Kruppa and B. Zhao. Fire resistance of composite beams to eurocode 4 part 1.2. *Journal of Constructional Steel Research*, 33(1-2):51–69, 1995.
- [32] A. Benedetti and E. Mangoni. Analytical prediction of composite beams response in fire situations. *Journal of Constructional Steel Research*, 63(2):221–228, 2007.

- [33] Y. C. Wang. Composite beams with partial fire protection. *Fire Safety Journal*, 30(4):315–332, 1998.
- [34] Y. Z. Wang. *Behavior and Design of Composite Beam in Fire with Considering Global Structure Effect*. PhD thesis, Tongji University, 2006.
- [35] H. Y. Zhou. *Theoretical and Experimental Research on Fire Resistance of Steel-Concrete Composite Beams*. PhD thesis, Tongji University, 2004.

Fire-Resistance of Restrained Steel Columns

Traditionally, the fire resistance of a steel column is obtained through a standard fire resistance test conducted on a simply supported compressive specimen subjected to the standard fire exposure, such as ISO834^[1]. Although the standard fire resistance test is a convenient way for grading the relative fire performance of different types of structural members, for a number of reasons it is not very effective in developing our understanding of realistic structural behavior in a fire. An important shortcoming is that standard fire resistance tests are carried out on the individual structural member, not on a complete structure. Therefore, structural interactions cannot be assessed. The Broadgate fire^[2,3] and the series of Cardington fire tests and the following theoretical analysis^[4,5,6] have all shown that strong interactions exist among slabs, columns and beams. An effective way of studying structural interactions in a fire is to perform fire tests on restrained steel members.

The Broadgate^[2,3] and Cardington^[4,5,6] frames employed nominally pinned joints. In seismic zones such as China, typical beam-column connections are rigid or semi-rigid, as shown in Fig. 8.1. Rigid connections may provide greater restraint to columns than pin connections. Therefore, much more attention should be paid to the behavior of a column restrained in a rigidly connected frame exposed to fire.

8.1 Fire Test on Restrained Steel Columns with Axial and Rotational Restraint

So far, many restrained column fire tests have been carried out by Simms et al.^[7,8], Ali et al.^[9] and Tan et al.^[10]. However, these fire tests have not considered the post-buckling behavior of a restrained steel column. Fire tests carried out by Rodrigues et al.^[11] used only small scale steel plates. Although fire tests carried out by Wang and Davies^[12], Ali and O'Connor^[13] considered effects of both the axial restraint and rotational restraint, they did not include the post-buckling phase. Many research results^[14,15,16] have shown that the buckling temperature of a restrained column can be much lower than the unrestrained one if the post-buckling behavior is not considered, but the failure temperature can increase if post-buckling is included.



Fig. 8.1 Typical beam-column connection in a framed structure

Until now, research on restrained columns has mainly focused on columns under axial load only. In a steel frame, columns are usually under combined axial load and bending moment. Fire tests of Rodrigues et al.^[11] and numerical studies of Valente et al.^[17] have incorporated the eccentricity of axial load. However, in a real structure, the bending moment can come from many sources in addition to the load eccentricity. Further fire tests on restrained steel columns loaded with combined axial force and bending moment are still necessary.

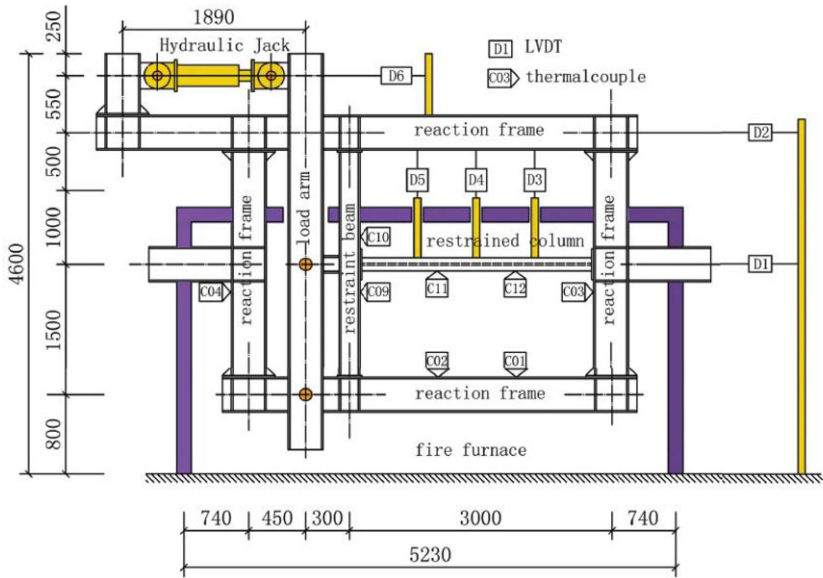
8.1.1 Test Set-Up and Test Specimen

The test set-up is shown in Fig. 8.2(a). It is composed of a tested restrained column, a restraint beam to provide the axial and rotational restraint, a load arm and a testing frame that all components are installed on. The axial force was applied on the restrained column through the load arm^[18,19], as shown in Fig. 8.2.

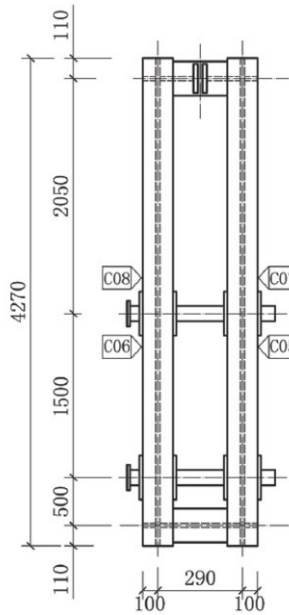
The tested column connects to the testing frame and the restraint beam by using extended end plate connection and bends around its minor axis. The axial and rotational restraints are provided by the bending of the restraint beam.

The restrained column was 3 m long with a section of HN200×100. The measured yield strength and Young's modulus of steel at ambient temperature were 360 N/mm² and 2.025×10⁵ N/mm² respectively. According to GB50017^[20], the flexural buckling strength of the test column $N_{cr,0}=394.2$ kN and the applied axial force on the column was 236.7 kN. Hence, the axial load ratio of the test column were $\rho_N=N/N_{cr,0}=0.6$. The initial imperfection was simulated using a 1000 N laterally concentrated load acting at the column mid-span.

The restraint beam was 3 m long, pin-ended at both ends bending around its major axis. The measured yield strength and Young's modulus of steel at ambient



(a) Test frame



(b) Load arm

Fig. 8.2 Test set-up (mm)

temperature were 245 N/mm^2 and $1.95 \times 10^5 \text{ N/mm}^2$ respectively. The dimension of the restraint beam was

- H180×200 in Test 01: the flange width and overall depth were 180 mm and 200 mm, the flange and web thickness were 12 mm and 6 mm, respectively;
- H180×240 in Test 02: the flange width and overall depth were 180 mm and 200 mm, the flange and web thickness were 12 mm and 6 mm, respectively.

The restraint stiffness is listed in Table 8.1. The axial restraint stiffness was $k_l = 48E_b I_b / l_b^3$, the rotational restraint stiffness provided by the restraint beam $k_r = 12E_b I_b / l_b$. E_b and I_b are Young's modulus and the moment of inertia of the restraint beam respectively. l_b is the length of the restraint beam, $k_{c,0} = E_c A_c / l_c$ is the axial stiffness of the restrained column at ambient temperature, $k_{r,0} = 4E_c I_c / l_c$ is the rotational stiffness of restrained column at ambient temperature, E_c and A_c are Young's modulus and cross-section area, l_c is the column length, $\beta_l = k_l / k_{c,0}$ and $\beta_r = k_r / k_{r,0}$ are the axial and rotational restraint stiffness ratios respectively.

Table 8.1 Restraint stiffness

No.	Section	Axial restraint (N/mm)			Rotational restraint (N/mm)		
		k_l	$k_{c,0}$	β_l	k_r	$k_{r,0}$	β_r
Test 01	H180×12×200×6	1.49×10^4	1.61×10^5	0.093	3.36×10^{10}	3.11×10^8	107.8
Test 02	H180×12×240×6	2.23×10^4		0.138	5.02×10^{10}		161.1

Parts of the restraint beam, the testing frame and the load arm were in the furnace. The restraint beam was fire protected by wrapping up in a 10 mm thick ceramic fibre blanket. The testing frame and the load arm were protected using a layer of 40 mm thick sprayed fire-protection coating plus a layer of 10 mm thick ceramic fiber fire-protection blanket.

8.1.2 Displacement and Temperature Acquisition

Linear Variable Displacement Transducers (LVDTs) were used to measure the column axial displacement and the lateral deflection. Positions of LVDTs are shown in Fig. 8.2(a). D1 and D2 were used to measure the deformation of the testing frame, D3, D4 and D5 were to measure the lateral displacement of the tested column. Specially fabricated probes were used to transfer the column lateral deflection outside of the furnace, as shown in Fig. 8.3. The axial displacement of the restrained column was measured through the lateral displacement of the load arm top and the amplification factor was 2.3667.

Furnace temperatures and specimen temperatures were closely monitored by thermocouples. C01 to C12 in Fig. 8.2(a) and Fig. 8.2(b) indicate positions of thermocouples. D1 to D6 are Linear Variable Displacement Transducers.

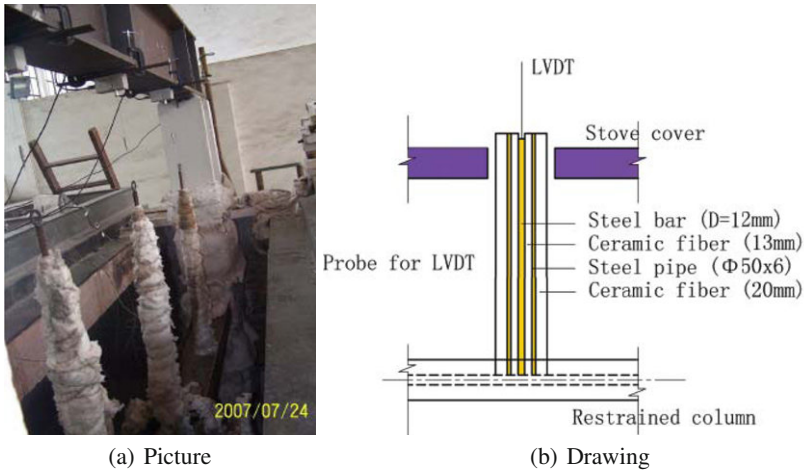


Fig. 8.3 Installation of probe for LVDT

8.1.3 Test Schedule

The test schedule was as follows:

- (1) apply 1000 N lateral load at the middle span of tested column;
- (2) apply 236.7 kN axial force to the column;
- (3) tighten high strength bolts at the two ends of restraint beam;
- (4) start fire;
- (5) the axial load was maintained constant during the fire test;
- (6) when the temperature of the tested column reaches 800 °C, stop the fire.

8.1.4 Test Results

8.1.4.1 Furnace Temperatures

The fire temperature was designed to follow the ISO834 standard fire curve^[1]. Measured temperatures of the two tests are shown in Fig. 8.4. Recorded temperature-time curves were very close to the standard fire curve.

8.1.4.2 Temperatures of the Reaction Frame and the Load Arm

Measured temperatures of the reaction frame and the load arm were not exceeding 90 °C, confirming that the two layered fire protection was very effective.

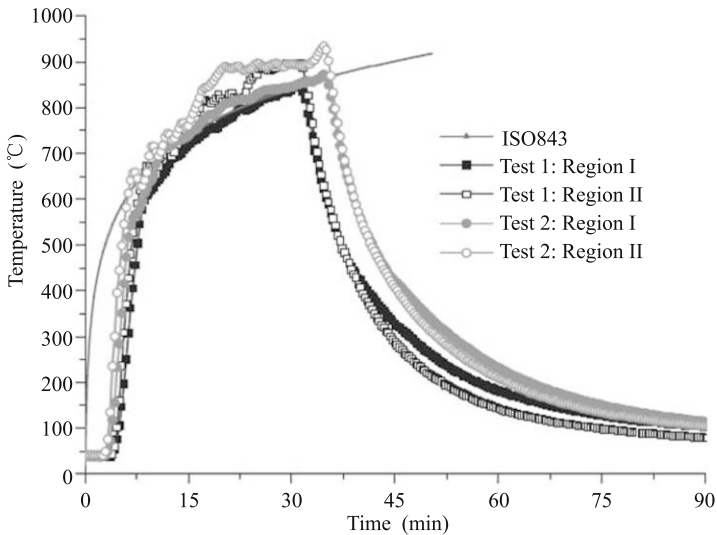


Fig. 8.4 Fire temperatures

8.1.4.3 Temperatures of the Restraint Beam

The lower part of the restraint beam was in the furnace (section C09 in Fig. 8.2(a)), with fire protection of a 10 mm thick ceramic fibre blanket. And the upper part of the restraint beam was outside of the furnace (section C10 in Fig. 8.2(a)) without fire-protection. Measured temperatures of the restraint beam are shown in Fig. 8.5.

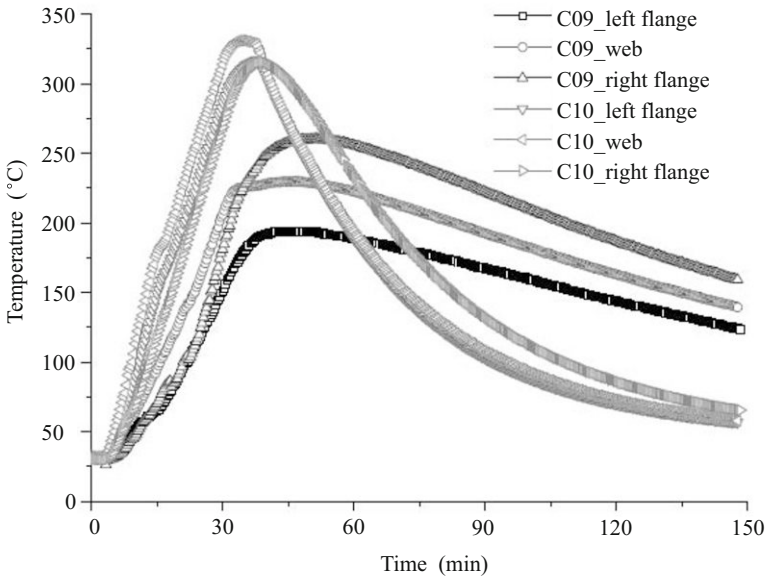
The higher temperature in the upper part of the restraint beam was due to leakage of hot smoke from the furnace. The non-uniform temperature distribution along the restraint beam was taken into consideration when calculating the restraint stiffness.

8.1.4.4 Temperatures of the Restrained Column

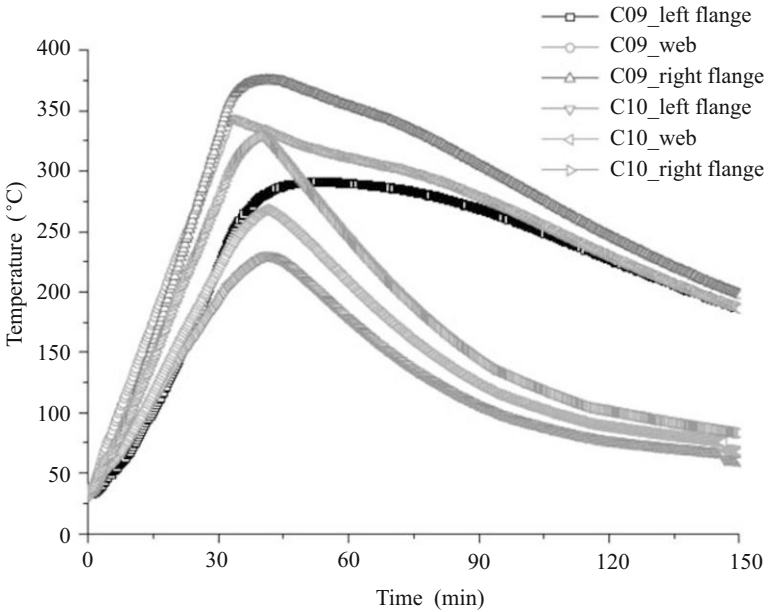
The restrained column was not fire protected. The section factor (F/V) was as great as 424.6 m^{-1} . Its temperature increased very quickly in the test, being almost the same as the fire temperature, see Fig. 8.6. Temperatures at position C11 and C12 were nearly the same, which means a uniform temperature distribution along the tested column.

8.1.4.5 Displacements of the Reaction Frame

Displacements of the reaction frame were shown in Fig. 8.7. The maximum displacement was only about 3 mm, which was much smaller than the lateral deflection and axial displacement of the tested column, as shown in Fig. 8.8 and Fig. 8.9. Thus the testing frame was treated as rigid and its deformation is ignored.

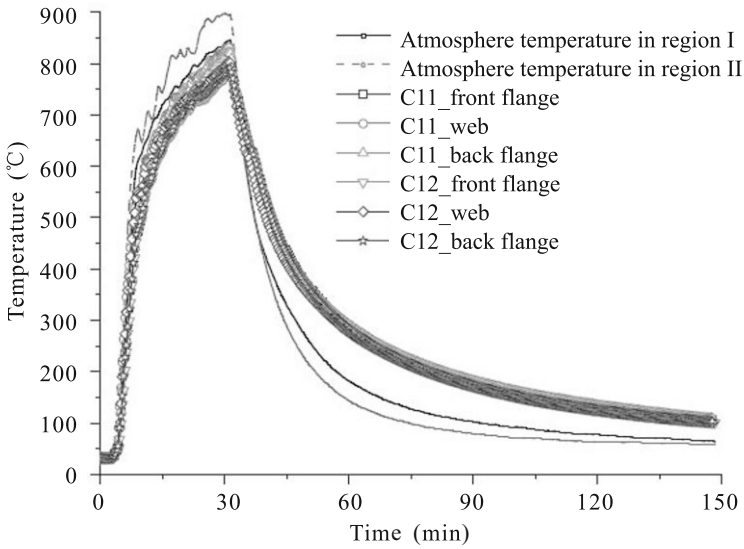


(a) Measured temperatures of the restraint beam in Test 01

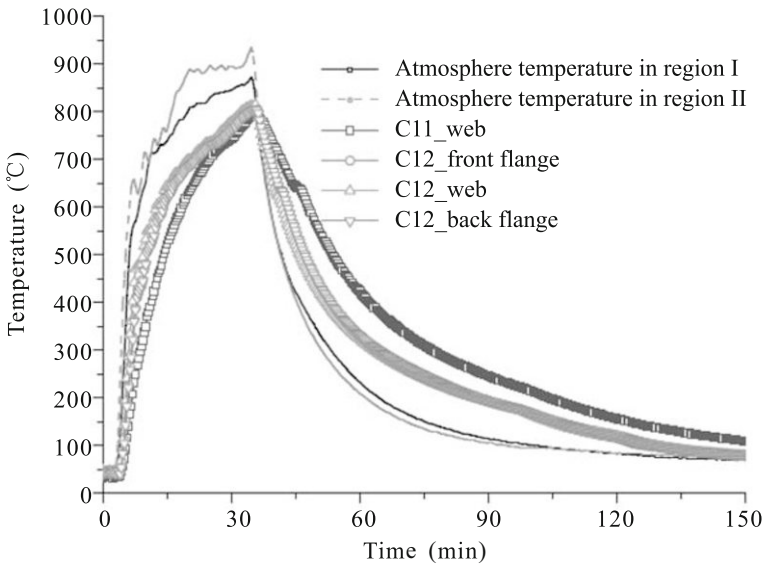


(b) Measured temperatures of the restraint beam in Test 02

Fig. 8.5 Measured temperatures of the restraint beam



(a) Measured temperatures of the restrained column in Test 01



(b) Measured temperatures of the restrained column in Test 02

Fig. 8.6 Measured temperatures of the restrained column

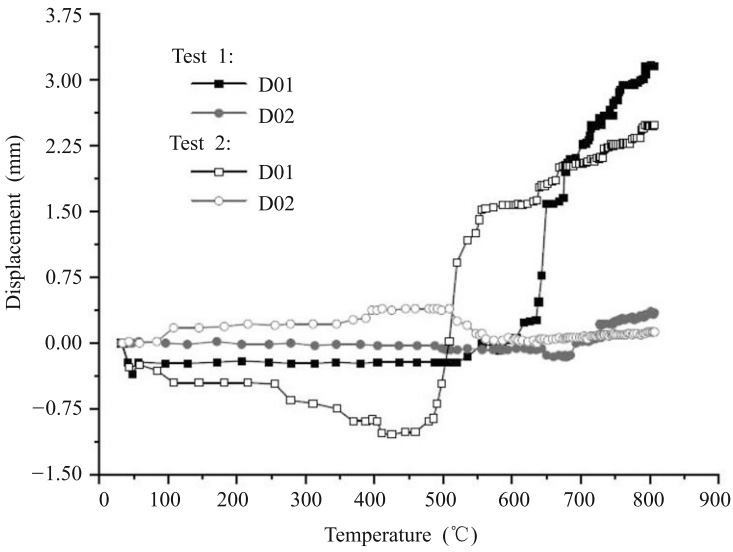


Fig. 8.7 Deformations of the reaction frame

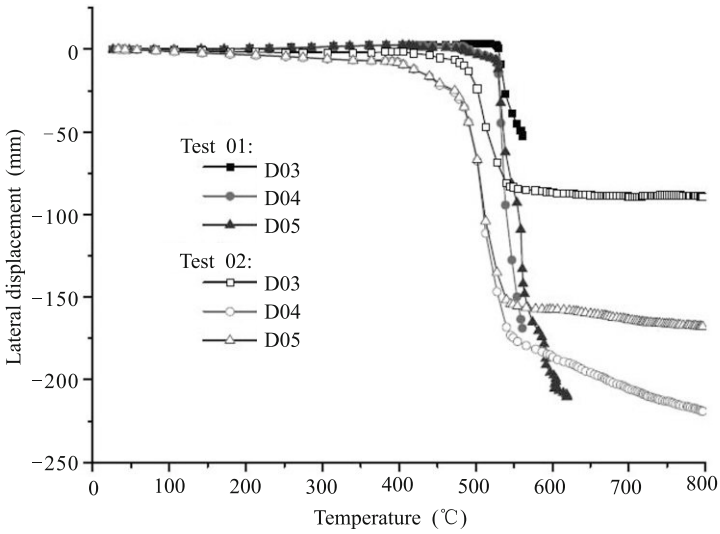


Fig. 8.8 Lateral deflections of the restrained column

8.1.4.6 Lateral Deflections of the Restrained Column

Fig. 8.8 shows the lateral deflections of the restrained column with the elevation in temperature. The lateral deflection remained very small before the column buckled. When the column temperature reached the buckling temperature, being 530 °C for the column in Test 01 and 490 °C for the column in Test 02, the column lateral deflection increased suddenly. Then a new stable state was reached. In the column Test 01, the LVDTs stopped working after the column buckled.

The axial restraint stiffness ratio is 0.093 in Test 01 and 0.138 in Test 02. The axial restraint would influence the lateral deflection of the column in two ways:

- The deflection of the restrained column with greater axial restraint stiffness (the column in Test 02) started to increase from a relatively low temperature, as shown in Fig. 8.8. This was caused by a faster increase in its axial force which in turn caused a bigger second-order bending moment.
- The restrained column with a greater axial restraint stiffness could find a new equilibrium state with a smaller deflection. For the column in Test 02, when the new stable state was reached, the lateral deflection at the mid-span of the column was about 180 mm. However, for the column in Test 01, the new stable state was not reached even when the mid-span deflection exceeded 200 mm.

8.1.4.7 Axial Displacements of the Restrained Column

The temperature at which the axial deformation of a restrained column reaches its maximum value is defined as the buckling temperature, because shortening of the column under heating indicates a sudden large lateral deflection and buckling. As shown in Fig. 8.9, the buckling temperatures of the column in Test 01 and Test 02 were 530 °C and 490 °C respectively. Maximum axial deformations of the column in Test 01 and Test 02 were about 38.5 mm and 24.0 mm respectively when they buckled. The start of column shortening was accompanied by a high shortening rate. Due to the axial restraint, a new equilibrium state was found after which the rate of column shortening slowed down. For the column with greater restraint stiffness, the new stable state was reached at a smaller displacement. As shown in Fig. 8.9, axial deformations of the column in Test 01 and Test 02 were 75.2 mm and 40.5 mm respectively when the new stable states were reached.

Rodrigues et al.^[11], Franssen^[14], Neves et al.^[15] and Wang^[16] all define the failure temperature of a restrained column as the temperature at which the axial force of a restrained column returns to its initial value. Following this definition, the failure temperatures of the column in Test 01 and Test 02 were 549.7 °C and 515.8 °C respectively. The differences between the buckling and failure-temperature of the restrained column were only about 20 °C. The improvement in failure temperature of the tested column is not obvious by taking into consideration the post-buckling phase. However, this difference will increase with a reduction in the load ratio or an increase in the axial restraint stiffness^[11,14,15,16].

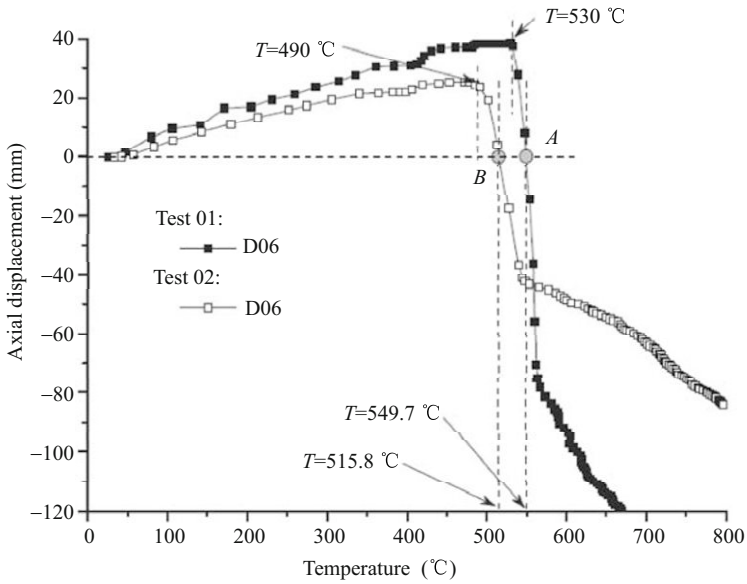


Fig. 8.9 Axial deformations of the restrained column

8.1.4.8 Residual Deflection of the Restrained Column

The residual deformation of a tested column after tests is shown in Fig. 8.10. The restrained column experienced very large deflection in tests and the lateral deflection only recovered a little. The residual deflection was about 300 mm.

The rotational restraint reduces the buckling length of the column. The CECS200^[21] simply adopts the effective length factor prescribed in the ambient temperature design code^[22]. However, it can be seen from Fig. 8.10 that the effective length factor of the column was about 0.5.



(a) Residual deflection of the restrained column in Test 01



(b) Residual deflection of the restrained column in Test 02

Fig. 8.10 Residual deflection of the restrained column

8.1.5 Numerical Simulation of the Fire Test

The general finite element software ABAQUS^[23] was used to simulate the fire test. The restrained column is simulated by using the linear beam element B31. The spring element SPRING2 was used to model the axial or rotational restraint.

Geometrically nonlinear static problems sometimes involve buckling or temporary failure behavior, where the load-displacement response shows a negative stiffness and the structure must release strain energy to remain in equilibrium. ABAQUS provides an automatic mechanism for stabilizing unstable quasi-static problems through the automatic addition of volume-proportional damping to the model^[23].

8.1.5.1 Numerical Simulations of the Restraint Beam

The numerical analysis of the fire test was performed in two steps. Firstly the restraint beam was analyzed to obtain the restraint stiffness and secondly the restrained column was analyzed using the calculated restraint stiffness. Analytical models of the restraint beam and the restrained column are shown in Fig. 8.11.

The force-displacement of the restraint beam was obtained by ABAQUS using recorded temperatures and deflection results, as shown in Fig. 8.12. The high temperature material model provided in EN1993-1-2^[22] was used here. Calculated axial restraint stiffness was 1.42×10^4 N/m and 2.12×10^4 N/m respectively, which was nearly the same as hand calculated results, as listed in Table 8.1.

8.1.5.2 Numerical Simulations of the Restrained Column

The restraint provided by the restraint beam was represented by a spring element when simulating the restrained column. An energy dissipation factor sensitivity study was carried out to choose the proper value for simulating behavior of a restrained

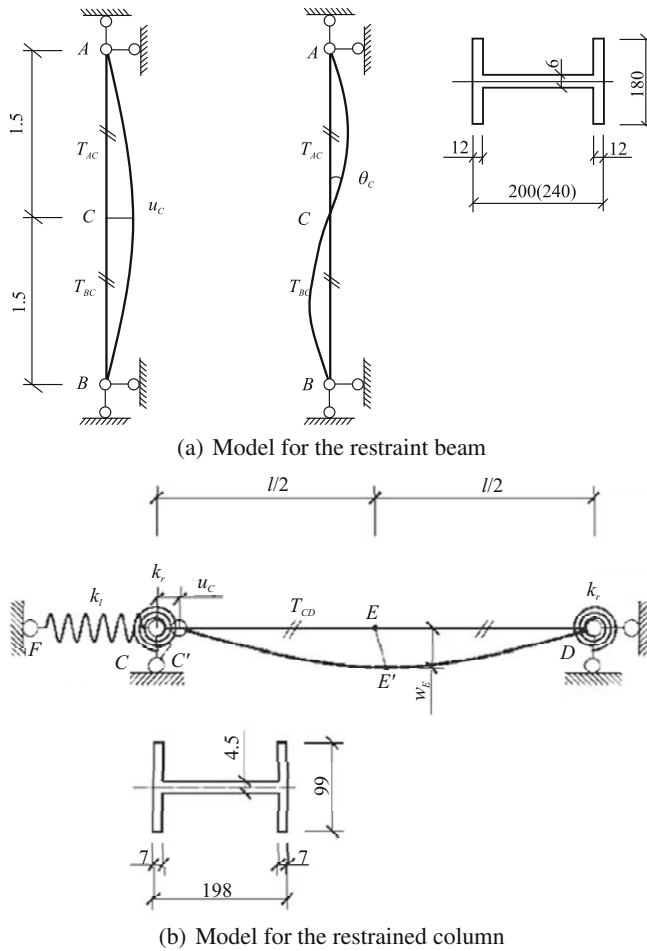


Fig. 8.11 Models for the restraint beam and the restrained column (mm)

column in a fire. The initial imperfection of the column follows a half sine curve with at the deflection of $L/1000$ at mid-span.

The energy dissipation factor α_d has a default value of 0.2×10^{-3} that is suitable for most applications, but the appropriate value is problem dependent and the user has the option of specifying a non-default value to achieve good accuracy if necessary. Its proper value should be determined by trial and error. Here, the restrained column was analyzed using five energy damping factors, 0.2×10^{-1} , 0.2×10^{-2} , 0.2×10^{-3} (default value), 0.2×10^{-4} and 0.2×10^{-5} . The element type was B31 and the column was divided into 32 elements. Calculated results are shown in Fig. 8.13 and Fig. 8.14.

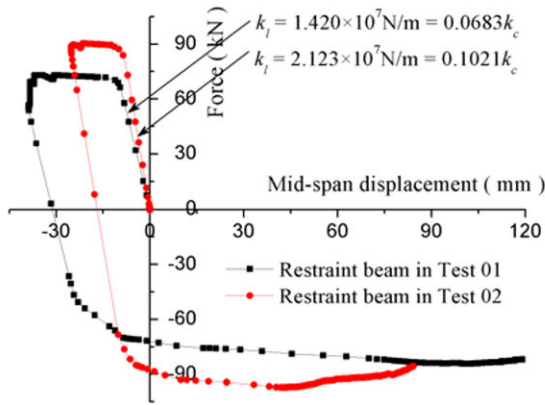


Fig. 8.12 Restraint force-displacement curves of the restraint beam

The lateral deflection of the tested column from ABAQUS simulation agrees well with test results, as shown in Fig. 8.13(b) and Fig. 8.14(b). However, there is a big gap between the tested axial displacement and analysis results, as shown in Fig. 8.13(a) and Fig. 8.14(b). It may be caused by the error in axial restraint stiffness. The actual axial restraint stiffness is less than that assumed in ABAQUS simulation because of the thermal bowing.

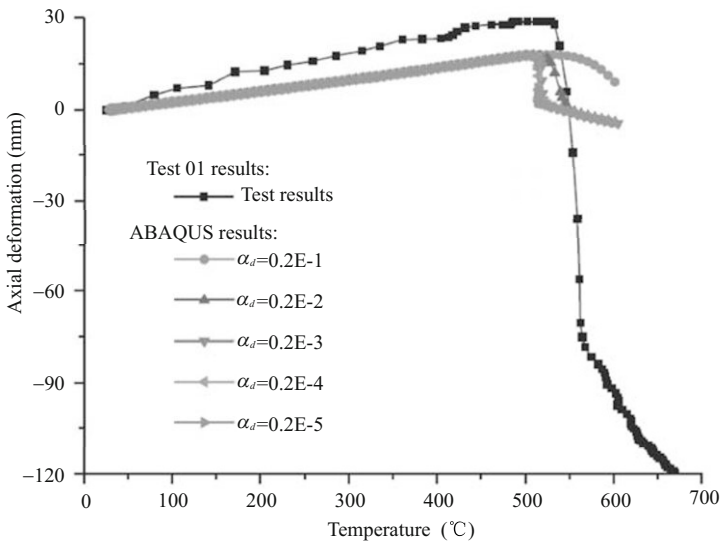
8.2 Parametric Study of Restrained Steel Columns in a Fire

Wang^[16], Franssen^[14], Neves et al.^[15] studied behavior of the axially restrained steel column under axial load in a fire. Huang et al.^[24,25], Valente and Neves^[17] have numerically explored behavior of the steel column with both axial and rotational restraints exposed to a fire. Huang and Tan^[26] investigated effects of the bending moment on behavior for both axially and rotationally restrained columns. However, these parametric studies of the restrained steel columns are mainly focused on the behavior of the axial force-temperature evolution curves and lateral deflection-temperature evolution curves. More systematic studies including

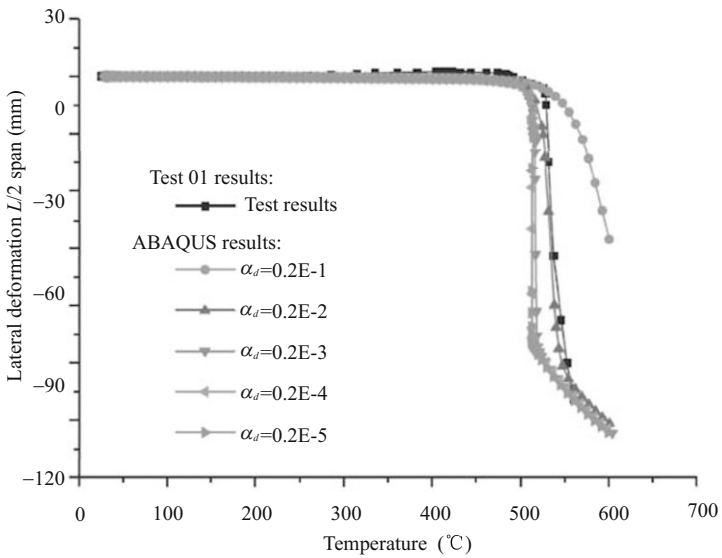
- the failure temperature;
- the difference between the failure temperature of an unrestrained column and restrained columns; and
- the difference between the failure temperature and the buckling temperature of a restrained column

are still necessary.

Results of parametric studies will form the basis of a simplified calculation method for evaluating the fire-resistance of a restrained steel column.

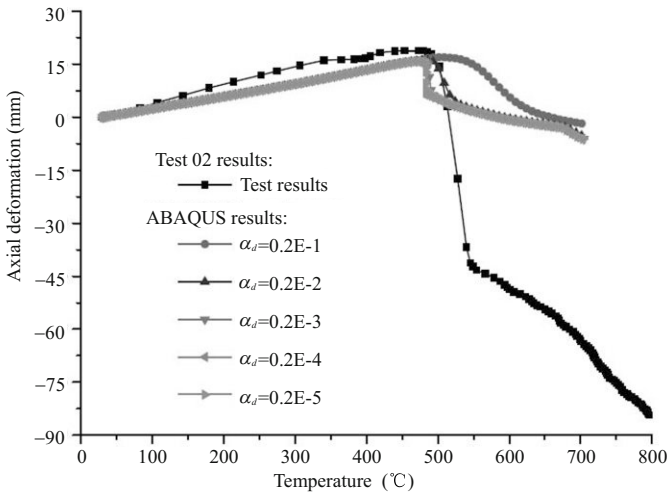


(a) Axial displacement

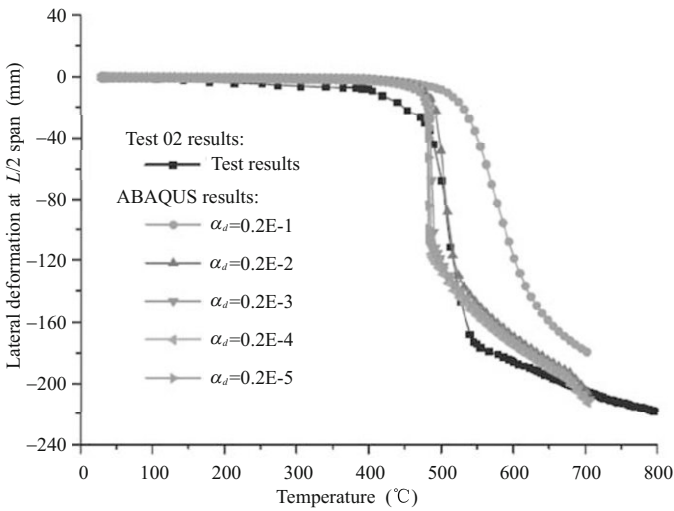


(b) Lateral deflection

Fig. 8.13 Analysis results of the restrained column in Test 01



(a) Axial displacement



(b) Lateral deflection

Fig. 8.14 Analysis results of the restrained column in Test 02

8.2.1 Parameters

For the restrained steel column under axial load only, studied parameters include

- the axial load ratio ρ_N ;
- the axial restraint stiffness ratio β_l and
- the slenderness ratio λ .

For the restrained steel column under combined axial load and bending moment, studied parameters include

- the axial load ratio ρ_N ;
- the bending moment load ratio ρ_M ;
- the axial restraint stiffness ratio β_I ;
- the slenderness ratio λ and
- the ratio between two end moments α_M .

8.2.1.1 Parameter Definition

The axial load ratio ρ_N is defined as

$$\rho_N = \frac{P_0}{N_{cr,0}} \quad (8.1)$$

where P_0 is the design axial force of a steel column in a fire situation, $N_{cr,0}$ is the flexural buckling resistance of the steel column at ambient temperature calculated according to GB50017^[20].

The bending moment load ratio ρ_M for a restrained column under combined axial load and bending moment is defined as

$$\rho_M = \frac{M_x}{M_b} \quad (8.2)$$

where M_x is the numerically larger one of the two end bending moments M_1 and M_2 , M_b is the bending moment resistance of the column under combined axial force and bending moment calculated according to GB50017^[20] as

$$M_b = \left(1.0 - \frac{P_0}{N_{cr,0}}\right) \frac{\gamma_x W_{1x} \left(1.0 - 0.8 \frac{P_0}{N'_{EX}}\right)}{\beta_{mx}} \quad (8.3)$$

By substituting Eq.(8.1) into Eq.(8.3), M_b is reformulated as

$$M_b = (1.0 - \rho_N) \frac{\gamma_x W_{1x} \left(1.0 - 0.8 \rho_N \frac{N_{cr,0}}{N'_{EX}}\right)}{\beta_{mx}} \quad (8.4)$$

where β_{mx} is the equivalent moment factor^[20] given by

$$\beta_{mx} = 0.65 - 0.35 \alpha_M \quad (8.5)$$

α_M is the ratio between two end moments as

$$\alpha_M = \frac{M_1}{M_2} \quad (8.6)$$

which is positive if the column is bending in double curvature and negative if the column is bending in single curvature and N'_{EX} is a parameter given by

$$N'_{EX} = \frac{\pi^2 EA}{1.1\lambda^2} \quad (8.7)$$

The axial restraint stiffness ratio β_l and rotational restraint ratio β_r are defined as

$$\beta_l = \frac{k_l}{k_{c,0}} \quad (8.8)$$

and

$$\beta_r = \frac{k_r}{k_{r,0}} \quad (8.9)$$

8.2.1.2 Failure Criteria

The buckling temperature of a restrained column $T_{res,b}$ is the temperature at which the column buckles and the axial compressive force in the column reaches its maximum value and starts to reduce. And the failure temperature of a restrained column $T_{res,f}$ is the temperature at which the axial force in the column returns to its initial value to support the design load effect. If large deformation is permitted for a framed structure exposed fire, the design objective can adopt the failure temperature. Otherwise, the design objective should adopt the buckling temperature.

The failure temperature of an unrestrained column $T_{free,f}$ is the temperature at which the column fails to resist its initial load effects. It can be treated as a special case of a restrained column when the axial restraint stiffness equals zero. The current structural fire design codes^[21,22] have described methods to calculate $T_{free,f}$.

The cross-section of the column for parametric studies was H200×14×250×10. The yield strength and Young's modulus of steel at ambient temperature are 235 N/m² and 2.05×10^5 N/m² respectively. The elevated temperature material properties follow the recommendation of ENV1993-1-2^[22]. Parametric studies were performed using the calibrated ABAQUS^[23] model.

8.2.2 Parametric Study on a Restrained Steel Column under Axial Load Only in a Fire

8.2.2.1 Failure Temperature

With the increase in the axial load ratio, $T_{res,f}$ decreases. But for the column with different axial restraint stiffness ratios, the decrease in $T_{res,f}$ is different. For example, as shown in Fig. 8.15, for the column without any axial restraint, when ρ_N increases from 0.1 to 0.9, $T_{res,f}$ drops from 750 °C to 350 °C; but for the column with β_l of 0.5, $T_{res,f}$ drops from 680 °C to 100 °C.

The relationship between λ and $T_{res,f}$ is very complicated, as shown in Fig. 8.15(c). For columns with β_l less than 0.01, with an increase in λ , $T_{res,f}$ decreases

first; but when λ is greater than 80, $T_{res,f}$ increases with the increase in λ . This has been noticed by Wang^[16] and is due to the greatest reduction in the stiffness of the column when the column slenderness is at a medium value. For columns with high axial restraint stiffness, the phenomenon disappears. The column is governed by the increasing force so columns with greater slenderness generally have lower failure temperatures.

8.2.2.2 Difference between Failure Temperatures of the Unrestrained and Restrained Column

Fig. 8.16 shows $T_{free,f}-T_{res,f}$ against ρ_N . For the column with β_l less than 0.002, $T_{free,f}-T_{res,f}$ is very small, being only about 60 °C for the column with ρ_N of 0.1 and only 10 °C for the column with ρ_N greater than 0.3. That is to say, effects of β_l on the failure temperature of a restrained column are insignificant when β_l is small. For columns with β_l greater than 0.05, the axial restraint causes a great reduction in the column failure temperature.

8.2.2.3 Difference between Buckling and Failure Temperatures of a Restrained Column

For a column with small β_l , such as those with β_l less than 0.02, $T_{res,f}-T_{res,b}$ is very small, say less than 50 °C, furthermore it is not affected by ρ_N and λ , as shown in Fig. 8.17. For a column with high axial load, $T_{res,f}-T_{res,b}$ depends on ρ_N . For example, for the column with β_l of 0.5 in Fig. 8.17(a), when ρ_N is 0.1, $T_{res,f}-T_{res,b}$ is about 500 °C. And when ρ_N is 0.8, $T_{res,f}-T_{res,b}$ is only 50 °C. That is to say, for a lightly loaded column the column can find the new stable position much more easily than a heavily loaded column, and the failure temperature of a restrained column can be improved from its buckling temperature. $T_{res,f}-T_{res,b}$ keeps on increasing with an increase in axial restraint stiffness, as shown in Fig. 8.17(b).

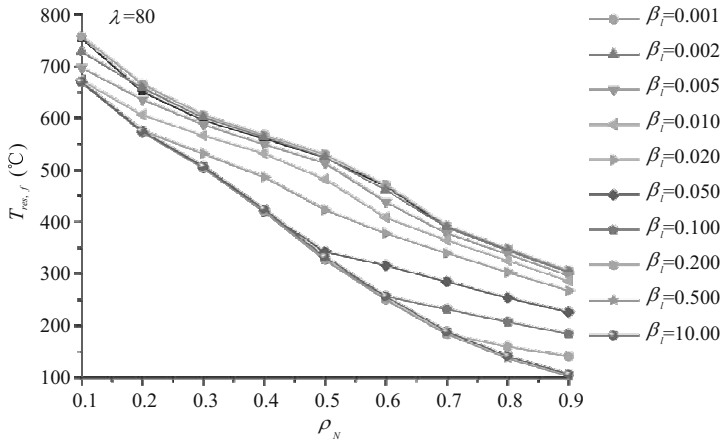
For a column with high axial restraint stiffness, $T_{res,f}-T_{res,b}$ will decrease firstly and then increase with an increase in λ , as shown in Fig. 8.17(c). The minimum value of $T_{res,f}-T_{res,b}$ occurs when λ is about 100.

8.2.3 Parametric Study of a Restrained Column under Combined Axial Load and Bending Moment in a Fire

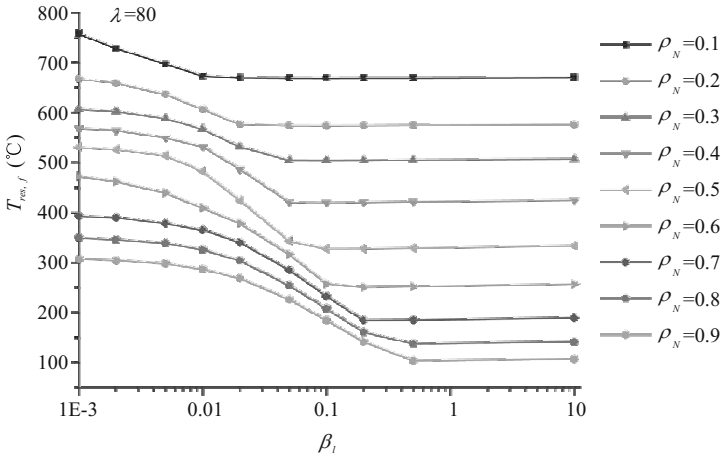
8.2.3.1 Failure Temperature

From Fig. 8.18(a) and Fig. 8.18(b), it can be seen that with the increase in ρ_N and ρ_M , $T_{res,f}$ decreases. The failure temperature of a restrained column with great axial restraint stiffness is much lower than that with small axial restraint stiffness^[18,27].

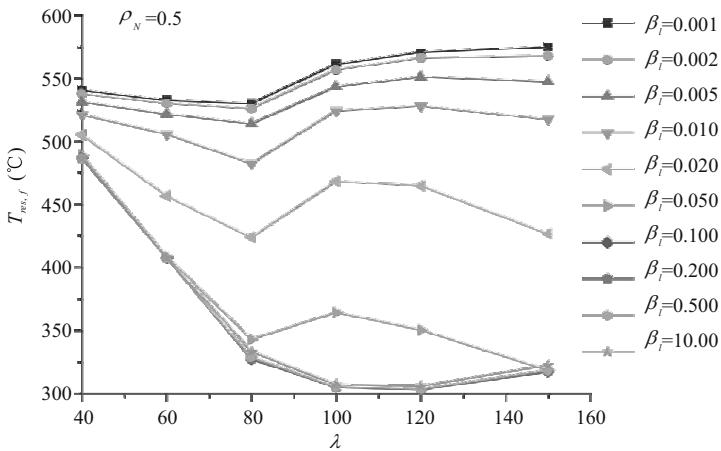
Fig. 8.18(c) shows that when β_l increases, $T_{res,f}$ also decreases; but when β_l is greater than a critical value, here it is 0.1, $T_{res,f}$ is not affected by β_l any more, as shown in Fig. 8.18(c).



(a) Effects of the axial load



(b) Effects of the axial restraint stiffness



(c) Effects of the slenderness

Fig. 8.15 Failure temperatures of the restrained column under axial load only

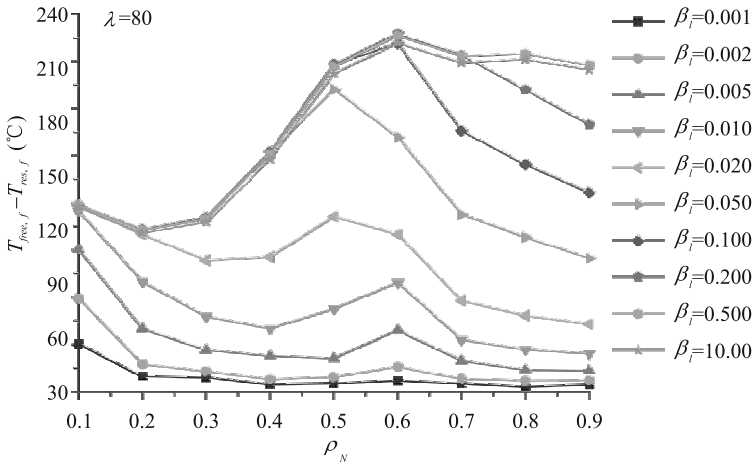


Fig. 8.16 Difference between failure temperatures of the unrestrained and restrained column

When the column slenderness increases from 40 to 60, $T_{res,f}$ decreases; however, when λ is greater than 60, $T_{res,f}$ does not change much when λ increases, see Fig. 8.18(d).

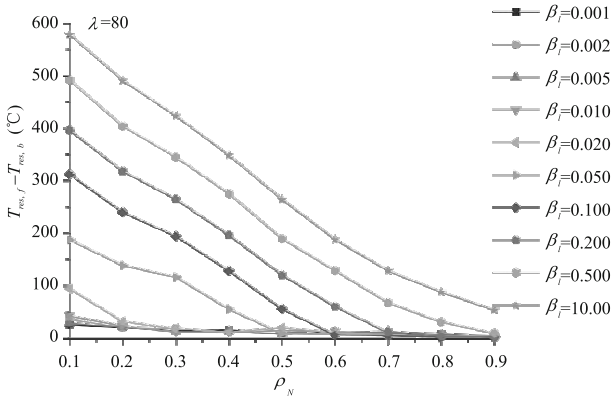
Effects of α_M on $T_{res,f}$ depend on β_l . As shown in Fig. 8.18(e), for columns with smaller β_l , $T_{res,f}$ decreases more with the increase in α_M . So for the column with $\beta_l=0.001$, when α_M increases from -1.0 to 1.0 , the decrease in $T_{res,f}$ is about 100°C ; however, for the column with $\beta_l=0.050$, the decrease in $T_{res,f}$ is about 20°C .

8.2.3.2 Difference between Failure Temperatures of the Unrestrained and Restrained Column

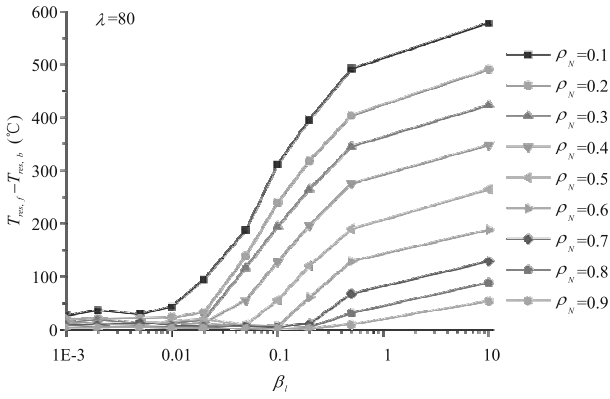
For columns with β_l less than 0.02, $T_{free,f}-T_{res,f}$ is not affected by ρ_N , as shown in Fig. 8.19(a), indicating that it is not necessary to consider effects of axial restraint. For the column with β_l greater than 0.02, $T_{free,f}-T_{res,f}$ increases with an increase in ρ_N , and the maximum difference can reach 150°C at the particular bending moment ratio. Contrary to the effect of the axial load ratio, an increase in the bending moment ratio will reduce the temperature difference, as shown in Fig. 8.19(b). That is to say, for columns with greater bending moments, the effect of axial restraint on the failure temperature of a restrained column becomes less significant.

$T_{free,f}-T_{res,f}$ increases with an increase in β_l , as shown in Fig. 8.19(c). However, when β_l is greater than 0.1, $T_{free,f}-T_{res,f}$ is not sensitive to β_l .

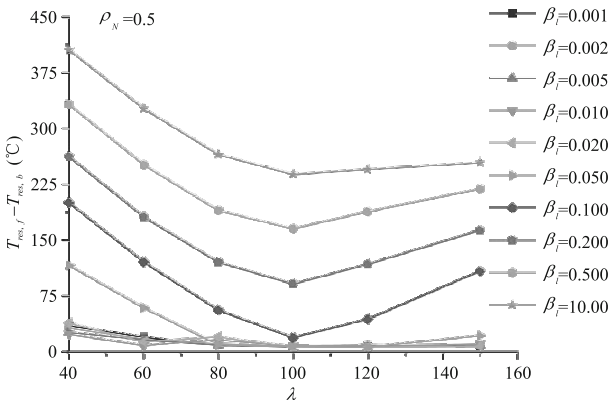
For columns with β_l less than 0.02, $T_{free,f}-T_{res,f}$ is not sensitive to λ , as shown in Fig. 8.19(d). $T_{free,f}-T_{res,f}$ slightly decreases with an increase in α_M , as shown in Fig. 8.19(e).



(a) Effects of the axial load

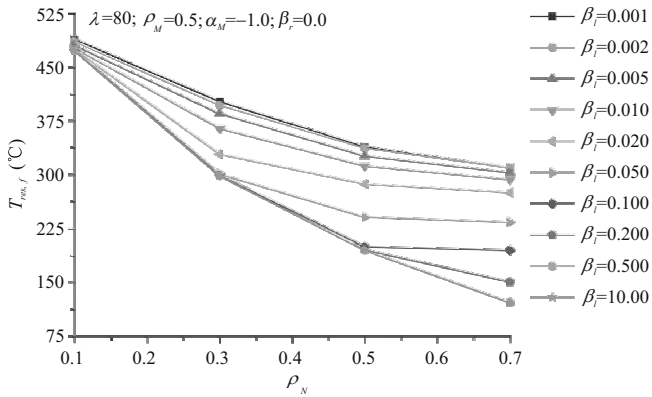


(b) Effect of the axial restraint stiffness

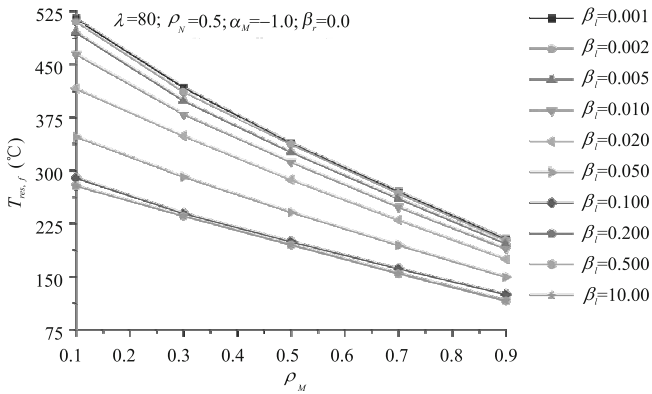


(c) Effects of the slenderness

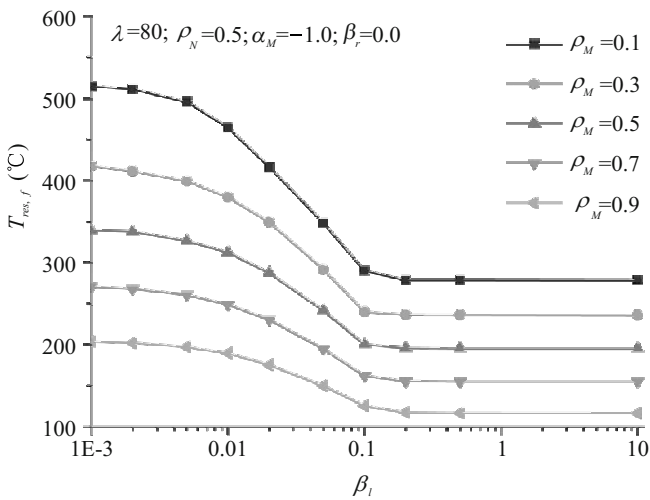
Fig. 8.17 Difference between failure and buckling temperatures of the restrained column



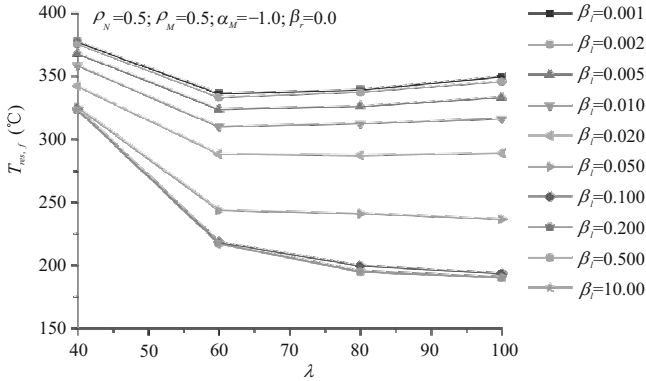
(a) Effects of the axial load



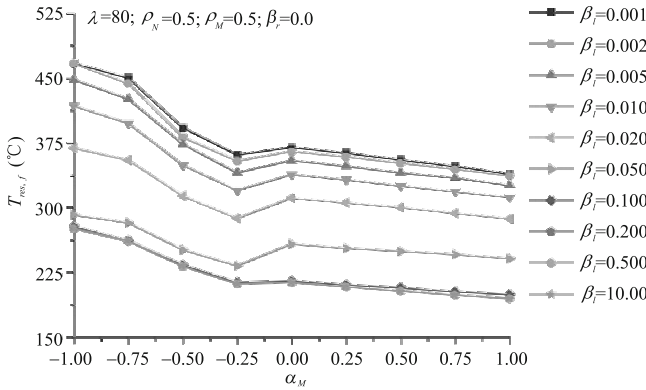
(b) Effect of the bending moment



(c) Effect of the axial restraint



(d) Effect of the slenderness



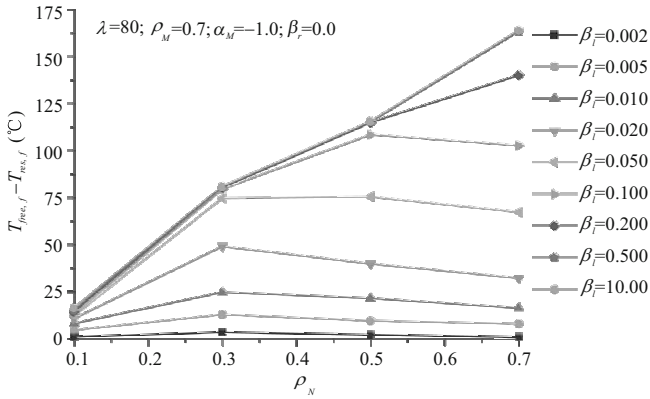
(e) Effect of the end moment ratio

Fig. 8.18 Failure temperatures of the restrained column under combined axial load and bending moment

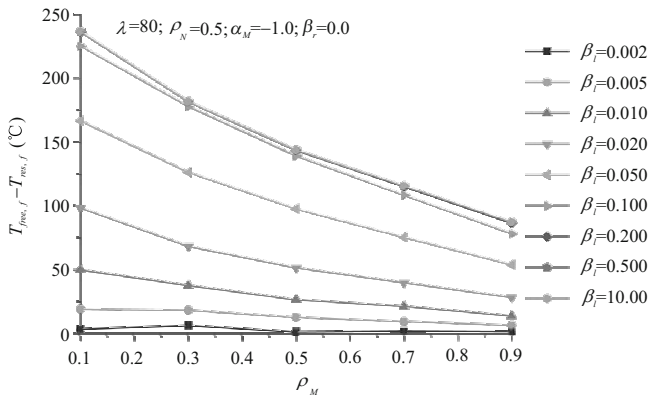
8.2.3.3 Difference between Failure- and Buckling-temperatures of Restrained Column

For columns with a small β_l , such as for columns with β_l less than 0.02, $T_{res,f}-T_{res,b}$ is small, generally less than 50 °C, and it is not affected by ρ_N , ρ_M , λ and α_M , as shown in Fig. 8.20. For columns with high β_l , $T_{res,f}-T_{res,b}$ depends on ρ_N , or ρ_M . For example, as shown in Fig. 8.20(a) and Fig. 8.20(b), for a column with β_l of 0.5, when ρ_N is 0.1, the temperature difference is about 225 °C; when ρ_N is 0.7, the difference is only 25 °C.

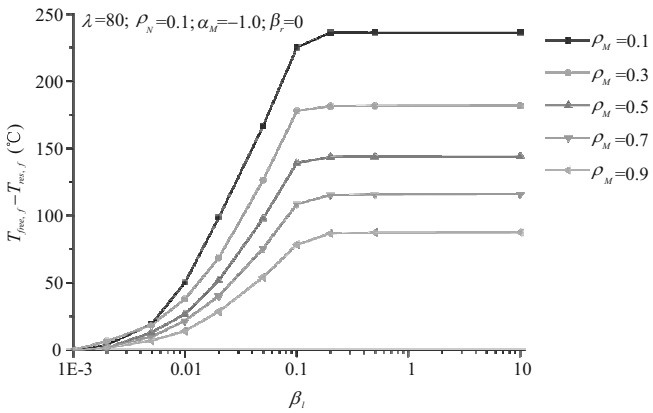
With an increase in β_l , $T_{res,f}-T_{res,b}$ increases, as shown in Fig. 8.20(c). It is different to $T_{free,f}-T_{res,f}$, as shown in Fig. 8.20(c). This is because, with the increase in β_l , both the buckling temperature and failure temperature of the restrained column decrease. However, after β_l reaches the critical value, there is no further reduction in the column failure temperature; but the column buckling temperature keeps on reducing.



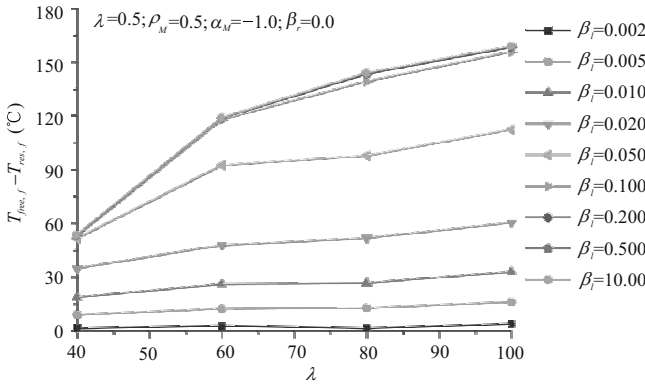
(a) Effects of the axial load



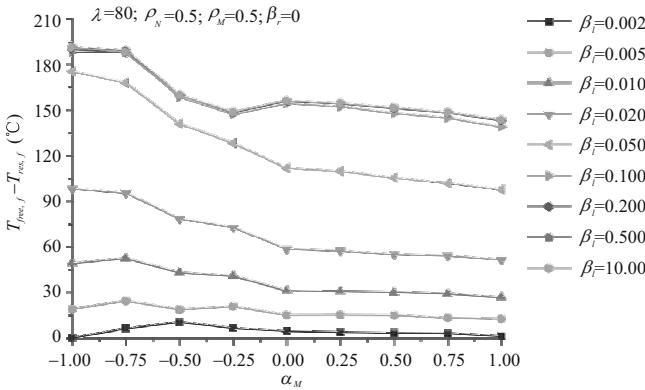
(b) Effect of the bending moment



(c) Effect of the axial restraint



(d) Effect of the slenderness



(e) Effect of the end moment ratio

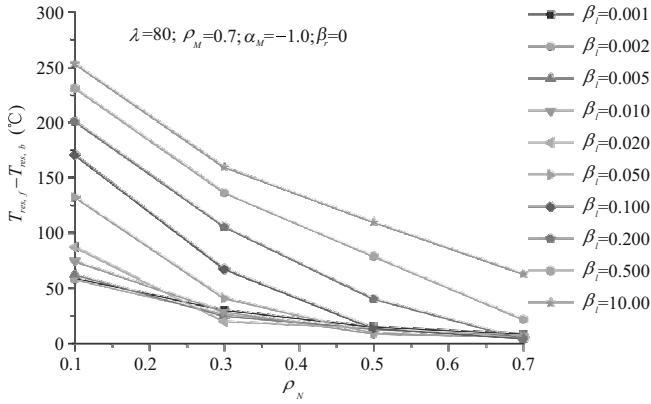
Fig. 8.19 Difference between failure temperatures of the unrestrained and restrained column under combined axial force and bending moment

For columns with high β_l , $T_{res,f}-T_{res,b}$ decrease firstly with the increase in λ . When λ is greater than 60, it decreases at a slow rate, as shown in Fig. 8.20(d).

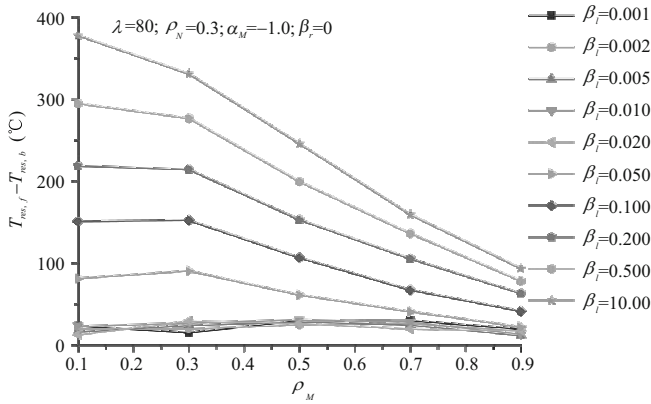
$T_{res,f}-T_{res,b}$ decreases with the increase in α_M , as shown in Fig. 8.20(e). However, if β_l is less than 0.1, which is it in most realistic structures, effects of α_M are small with the temperature differences being less than 20 °C.

8.3 Simplified Design Method for Restrained Steel Columns in a Fire

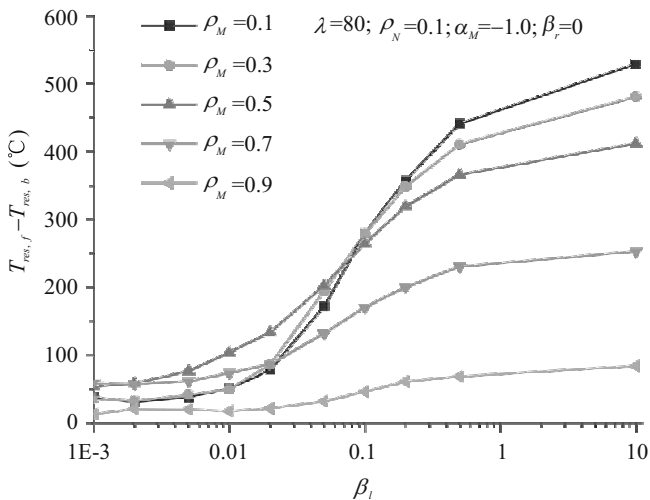
Present fire resistance design codes^[21,22] are mainly based on isolated structural members, which only adopt the design procedure at ambient temperature by using the reduced strength and stiffness of steel at elevated temperatures. Only a limited consideration is given to interactions among structural members under fire conditions.



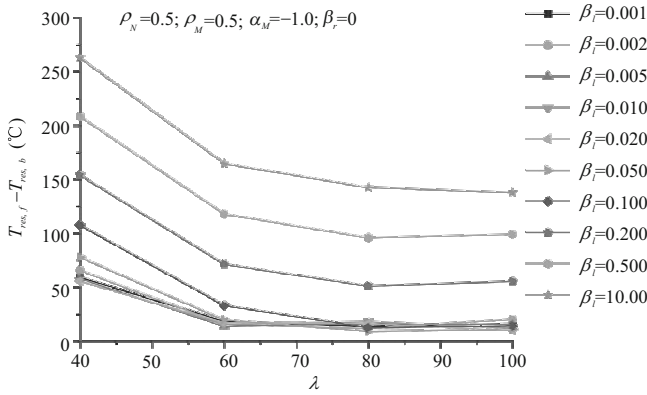
(a) Effects of the axial load



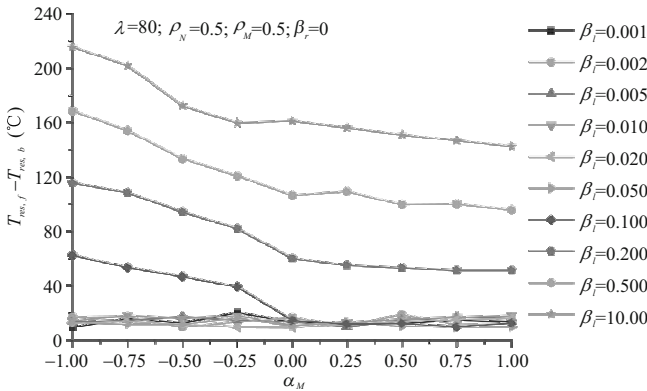
(b) Effect of the bending moment



(c) Effect of the axial restraint



(d) Effect of the slenderness



(e) Effect of the end moment ratio

Fig. 8.20 Difference between failure and buckling temperatures of the restrained column under combined axial load and binding moment

EN1993-1-2^[22] includes the effect of structural continuity in a fire by reducing the column buckling length. As presented above, the axial restraint to the column causes a reduction in the buckling and failure temperature of the steel column. Design methods should consider the effects of the axial restraint.

Elastic methods have been developed to predict the buckling temperature of restrained columns in a fire. Huang and Tan^[24] proposed a Rankine Approach for determining the buckling temperature of an axially and rotationally restrained column. Tan and Yuan^[28] calculated the buckling temperature of an axially restrained column with longitudinal non-uniform temperature distribution using the Euler Equation. However, since the failure temperature of a restrained column is reached in the post-buckling phase, elastic theory is not applicable.

If one accepts that the fire resistant design objective of the restrained steel column is met when the column load carrying capacity is sufficient to sustain its initial load,

then the column failure temperature may be defined as that at which the column axial load returns to its original level. Thus, the restrained steel column has two ultimate states in a fire situation as failure model I and failure model II. And correspondingly, there are two critical temperatures for the restrained steel column, the buckling temperature and the failure temperature. These two temperatures are illustrated in Fig. 8.21 and the buckling temperature will not exceed the failure temperature. If a large structural deformation in a fire is not permitted or to avoid the dynamic effects of sudden column buckling, then the column should be designed so that its temperature rise does not exceed the buckling temperature; otherwise, the column may be designed to sustain the failure temperature.

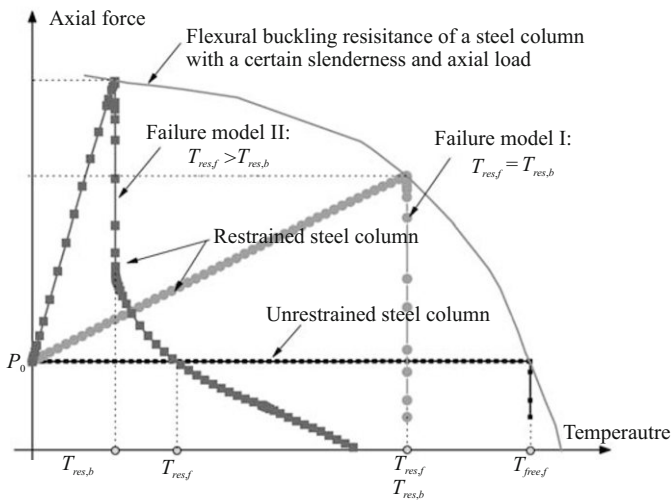


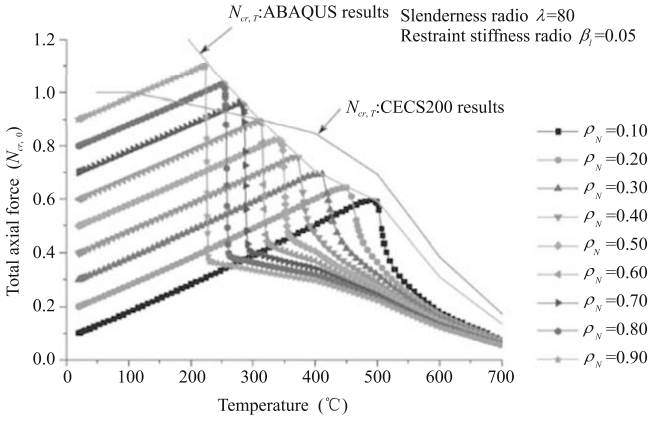
Fig. 8.21 Failure models of a restrained steel column in a fire

8.3.1 Design Method for Restrained Columns under Axial Load Only in a Fire

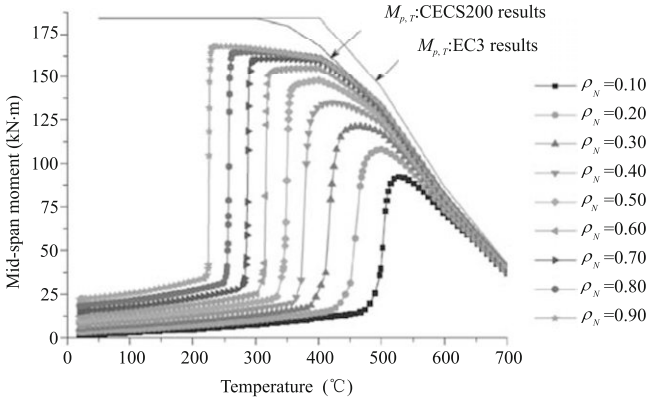
8.3.1.1 Structural Responses of the Restrained Column under Axial Load Only

Fig. 8.22 shows simulation results of a series of restrained steel columns in a fire. As shown in Fig. 8.22(a) and Fig. 8.22(b), before a restrained column buckles, the axial force in the restrained column increases linearly and bending moments remain small. Therefore, the restrained column can be treated as an axially loaded column with increased axial force due to the restraint thermal expansion^[18,29,30].

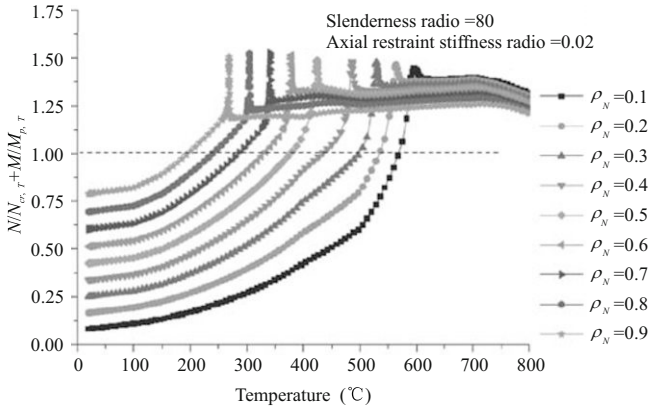
After the column buckles, the axial force in the restrained column is reduced and the bending moment increases significantly. The restrained column is loaded under the combined axial force and bending moment. To characterize the column



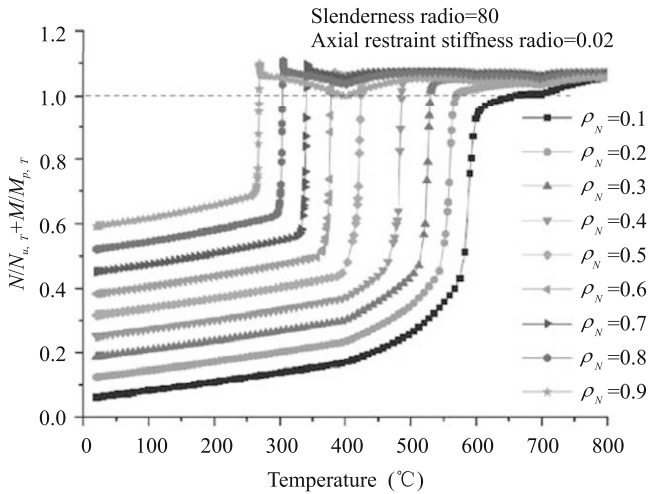
(a) Axial force-temperature evolution curve



(b) Bending moment-temperature evolution curve



(c) $N/N_{cr,T}+M/M_{p,T}$ -temperature evolution curve

(d) $N/N_{u,T}+M/M_{p,T}$ -temperature evolution curve**Fig. 8.22** Behavior of the restrained column under axial load only in a fire

loading condition, a number of axial load-bending moment interaction curves may be used. For simplicity, the linear form is considered in this study. The axial force-bending moment interaction curves may be represented by either $N/N_{cr,T}+M/M_{p,T}$ or $N/N_{u,T}+M/M_{p,T}$, as shown in Fig. 8.22(c) and Fig. 8.22(d). Where N and M are the axial force and mid-span bending moment in the column, $N_{cr,T}$ is the flexural buckling resistance of the column at elevated temperature calculated by CECS200^[21], $N_{u,T}$ and $M_{p,T}$ are the axial yield strength and plastic bending moment capacity of the column at elevated temperature respectively. From Fig. 8.22(c) it can be seen that, if $N/N_{cr,T}+M/M_{p,T}$ is used to represent the column axial force-bending moment interaction relationship, its value is much greater than 1.0 when the column fails. However, if $N/N_{u,T}+M/M_{p,T}$ is used to represent the axial force-bending moment interaction relationship, when the column fails, its value is approaching 1.0, as shown in Fig. 8.22(d). This clearly suggests that the restrained column fails because the cross-section of the column has reached its plastic resistance. This will be used in the following section to develop a practical design method.

8.3.1.2 Design Method for the Buckling Temperature of a Restrained Column under Axial Load Only

• Design equation

Before the restrained column buckles, it can be designed as an axially loaded column. Compared to the design equation of an unrestrained column in a fire, the only difference is that the axial force should include the additional axial force due to axial restraint. The design equation is

$$\frac{N}{N_{cr,T}} = 1.0 \tag{8.10}$$

and

$$N = P_0 + k_l u_l \tag{8.11}$$

where u_l is the axial displacement of the column calculated by

$$u_l = \frac{k_c}{k_c + k_l} \left(\epsilon_{th} l - \frac{P_0}{k_c} + \frac{P_0}{k_{c,0}} \right) \tag{8.12}$$

Since the buckling temperature is unknown, an iterative procedure should be followed.

The buckling temperature of the restrained column $T_{res,b}$ should not be higher than the failure temperature of the unrestrained column under the initial axial force $T_{free,f}$

$$T_{res,b} < T_{free,f} \tag{8.13}$$

• **Verification of the buckling temperature equation**

Fig. 8.23 compares ABAQUS predicted column buckling temperatures and those calculated by using Eq.(8.10).

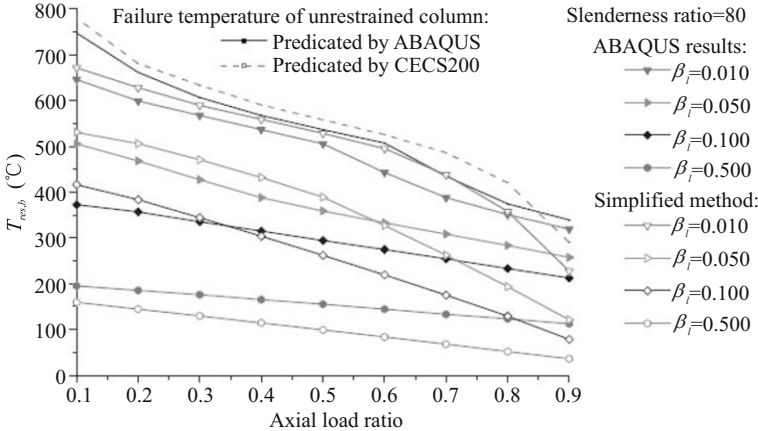


Fig. 8.23 Verification of the buckling temperature equation for the restrained column under axial load

Generally speaking, the buckling temperature $T_{res,b}$ predicted by Eq.(8.10) and ABAQUS agree well for columns with a small ρ_N and a small β_l . As shown in Fig. 8.23, when β_l is less than 0.05, $T_{res,b}$ predicted by Eq.(8.10) is slightly greater than that by ABAQUS, the difference being about 20 °C. When β_l is greater than 0.10, $T_{res,b}$ predicted by Eq.(8.10) is lower than that by ABAQUS. The maximum difference is about 150 °C, which occurs when β_l is 0.1 and ρ_N is 0.9.

8.3.1.3 Design Method for the Failure Temperature of a Restrained Columns under Axial Load

• **Design equation**

After the column buckles, it is loaded under the combined axial force and bending moment. The design equation is

$$\frac{N}{N_{cr,T}} + \frac{N.w}{M_{p,T}} = 1.0 \tag{8.14}$$

According to the definition of the failure temperature of a restrained column

$$N = P_0 \tag{8.15}$$

w is the lateral deflection of the restrained column at failure. The column lateral deflection causes an additional column shortening u_c and they are related in the following way

$$u_c = \xi \frac{w^2}{l} \tag{8.16}$$

where ξ is a parameter which depends on the shape of the deflection curve. For example, if the deflection curve is a parabolic, $\xi=8/3$.

u_c and the displacement of the axial restraint u_l satisfy

$$\begin{cases} u_l + u_c = \varepsilon_{th}l + \frac{P_0}{k_{c,0}} \\ k_l u_l = \Delta P \\ k_c u_c = p_0 + \Delta P \end{cases} \tag{8.17}$$

Considering Eq.(8.16), the relationship between u_s and w is expressed as

$$u_l = \alpha \frac{w^2}{l} \tag{8.18}$$

hence,

$$w = \sqrt{\frac{u_c l}{\alpha}} \tag{8.19}$$

α is a function of λ , β_l and ρ_N

$$\alpha = \alpha(\lambda, \beta_l, \rho_N) \tag{8.20}$$

The expression of α can be obtained by curve fitting ABAQUS simulation results, as shown in Fig. 8.24, as

$$\begin{aligned} \alpha &= c_{\rho_l} c_{\beta_l} c_{\lambda} \geq 2.5 \\ c_{\rho_N} &= 1.18 \rho_N + 0.54 \\ c_{\beta_l} &= 45.96 e^{-\frac{\beta_l}{23.07}} - 5.77 e^{-\frac{\beta_l}{25.21}} - 38.85 \\ c_{\lambda} &= 18.42 e^{-\frac{\beta_l}{30.36}} + 2.11 \end{aligned} \tag{8.21}$$

The failure temperature of a restrained column $T_{res,f}$ should be lower than the failure temperature of an unrestrained column under the same load $T_{free,f}$, but higher than the buckling temperature of a restrained column $T_{res,b}$ as

$$T_{res,b} \leq T_{res,f} \leq T_{free,f} \quad (8.22)$$

• Verification of the failure temperature equation by ABAQUS

To assess the accuracy of the proposed method for calculating $T_{res,f}$, a comparison is made between Eq.(8.14) predictions and ABAQUS simulations.

The comparison is shown in Fig. 8.25. For columns with ρ_N less than 0.6, $T_{res,f}$ obtained by Eq.(8.14) and those by ABAQUS simulation agree well, as shown in Fig. 8.25. For columns with higher ρ_N , if β_l is less than 0.02, $T_{res,f}$ calculated by Eq.(8.14) agree well with those of the ABAQUS simulation, as shown in Fig. 8.25. Otherwise, there exist differences between failure temperatures predicted by the two methods. For example, for the column with ρ_N of 0.9 and β_l of 0.05, $T_{res,f}$ predicted by Eq.(8.14) is about 100 °C and that by ABAQUS is about 220 °C, as shown in Fig. 8.25. This large difference is primarily due to the difference between the ABAQUS simulation result and CECS200 calculation of column failure temperature at high loads. Fortunately, Eq.(8.14) tends to predict safe (lower) results. Also in practice, the initial axial load ratio rarely exceeds 0.6.

The failure temperatures of an unrestrained column under different axial load ratios are also shown in Fig. 8.25. It is clear to see that $T_{res,f}$ is lower than $T_{free,f}$. The column with a greater the axial load ratio and axial restraint stiffness ratio has a lower failure temperature.

8.3.2 Design Methods for the Restrained Columns under Combined Axial Load and Bending Moment

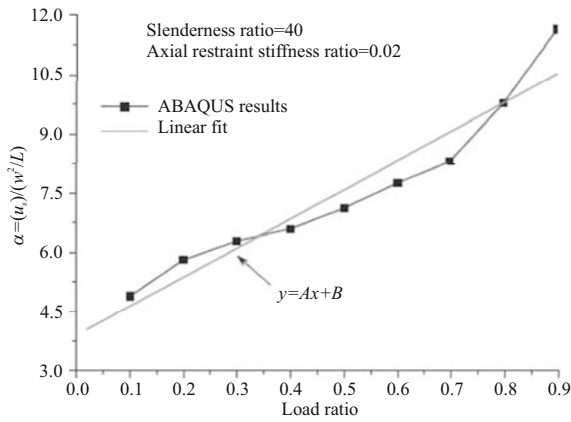
8.3.2.1 Structural Responses of the Restrained Column under Combined Axial Load and Bending Moment

As shown in Fig. 8.26(a) and Fig. 8.26(b), before the restrained column buckles, the axial force in the restrained column increases linearly and the bending moment changes little. Hence, for determining the buckling temperature of a restrained column, the design equation for the unrestrained column can be used, but with increased column axial load due to the restraint thermal expansion.

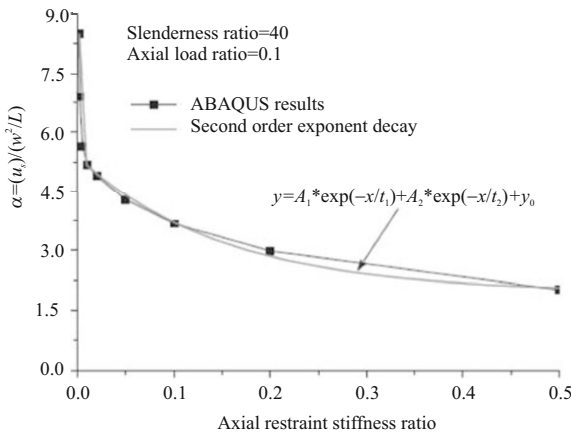
After buckling, the axial force in the restrained column drops and the bending moment increases. Again, as shown in Fig. 8.26(c) and Fig. 8.26(d), the $N/N_{cr,T} + M/M_{p,T}$ interaction curve is more appropriate for defining the ultimate failure state than the $N/N_{u,T} + M/M_{p,T}$ interaction curve.

8.3.2.2 Design Method for the Buckling Temperature of a Restrained Column under Combined Axial Load and Bending Moment

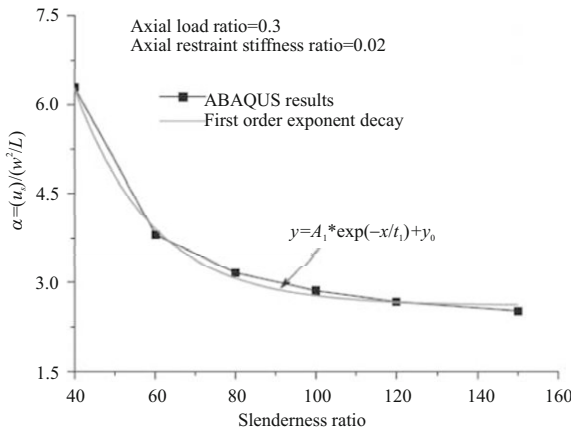
• Design equation



(a) Relationship between α and ρ_N



(b) Relationship between α and β_t



(c) Relationship between α and λ

Fig. 8.24 Relationship between α and ρ_N, β_t, λ

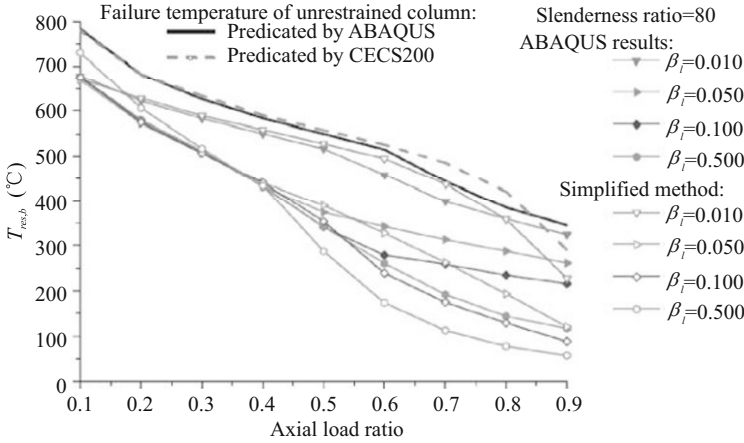


Fig. 8.25 Verification of the failure temperature equation of a restrained column under axial load

Before the restrained column buckles, the axial force increases linearly and the bending moment changes little. The design equation is

$$\frac{N}{N_{cr,T}} + \frac{\beta_{mx}M_x}{\gamma_x W_{1x} \left(1.0 - 0.8 \frac{N}{N'_{EX}} \right)} = 1.0 \tag{8.23}$$

where

$$N'_{EX} = \frac{\pi^2 EA}{1.1 \lambda^2} \tag{8.24}$$

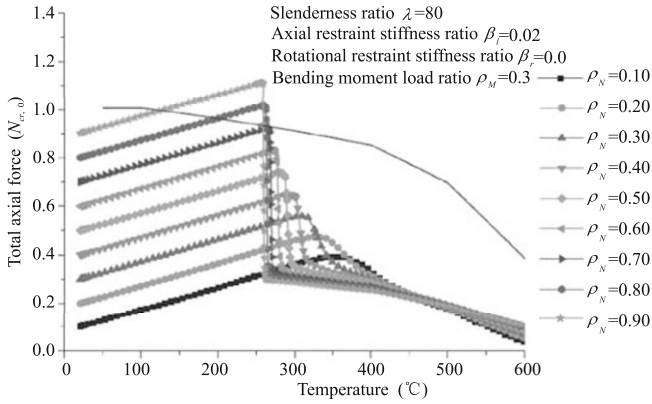
N is calculated by Eq.(8.11), γ_x is the plastic factor of the section. W_{1x} is the elastic modulus of the cross-section.

The buckling temperature of the restrained column should not be higher than the failure temperature of the unrestrained column.

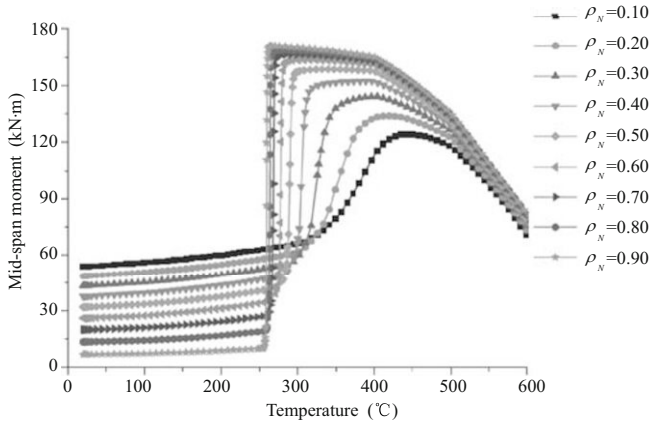
• **Verification of the buckling temperature equation**

To check the accuracy of the proposed method, ABAQUS simulations have been run. Calculated results are shown in Fig. 8.27.

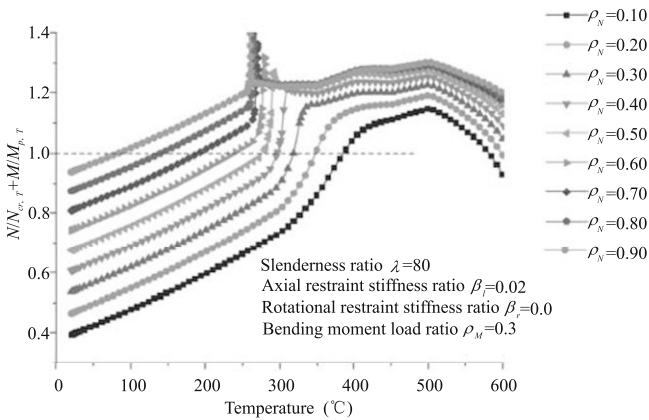
From Fig. 8.27(a), it can be seen that, for columns with β_l less than 0.05, $T_{res,b}$ predicted by Eq.(8.23) is greater than that by ABAQUS by about 80 °C. However, for columns with β_l greater than 0.1, $T_{res,b}$ predicted by Eq.(8.23) is less than that of ABAQUS by about 50 °C. The difference between buckling temperature predicted by ABAQUS and Eq.(8.23) becomes greater for columns with bigger ρ_N , as shown in Fig. 8.27(a) and Fig. 8.27(b). Again the difference is primarily due to the difference between the ABAQUS simulation result and CECS200 calculation of unrestrained column buckling resistance at high temperature. Fortunately, in practice the initial axial load ratio rarely exceeds 0.6.



(a) Axial force-temperature evolution curves



(b) Bending moment-temperature evolution curves



(c) $N/N_{cr,T} + M/M_{p,T}$ -temperature evolution curves

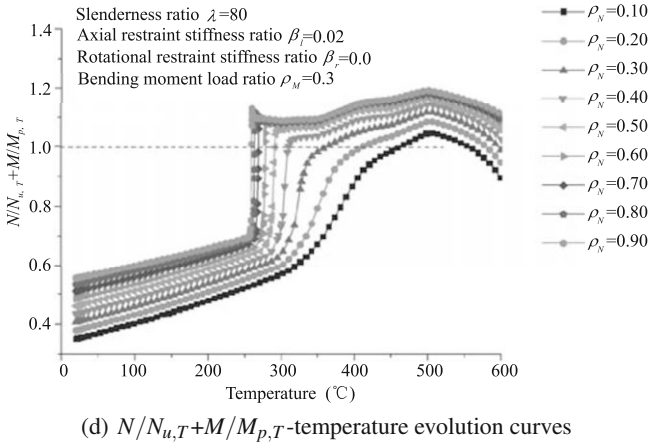


Fig. 8.26 Behavior of restrained column under the combined axial load and bending moment in a fire

For columns with α_M greater than -0.25 , $T_{res,b}$ predicted by Eq.(8.23) agree well with that by the ABAQUS simulation, as shown in Fig. 8.27(c).

8.3.2.3 Design Method for the Failure Temperature of a Restrained Column under Combined Axial Load and Bending Moment

• Design equation

The design equation for the failure temperature of the restrained column is

$$\frac{N}{N_{u,T}} + \frac{Nw + \beta_{mx}M_x}{M_{p,T}} = 1.0 \quad (8.25)$$

where N is calculated by Eq.(8.15). Similar to the restrained column under axial load, the maximum column lateral deflection is calculated by

$$w = \sqrt{\frac{u_l l}{\alpha}} \quad (8.26)$$

where u_l is calculated using Eq.(7), α is a function of ρ_N , ρ_M , β_l , λ and α_M as

$$\alpha = \alpha(\rho_N, \rho_M, \beta_l, \lambda, \alpha_M) \quad (8.27)$$

The expression of α is obtained by curve fitting ABAQUS results (Fig. 8.28):

$$\begin{aligned} \alpha &= c_{\rho_N} c_{\rho_M} c_{\beta_l} c_{\lambda} c_{\alpha_M} \geq 2.5 \\ c_{\rho_N} &= 1.10\rho_N + 0.06 \\ c_{\rho_M} &= -1.60\rho_M + 2.10 \\ c_{\beta_l} &= 4.72e^{-\frac{\beta_l}{0.002}} + 205.35e^{-\frac{\beta_l}{136.81}} - 203.32 \\ c_{\lambda} &= 10.87e^{-\frac{\lambda}{406.80}} - 7.70 \end{aligned} \quad (8.28)$$

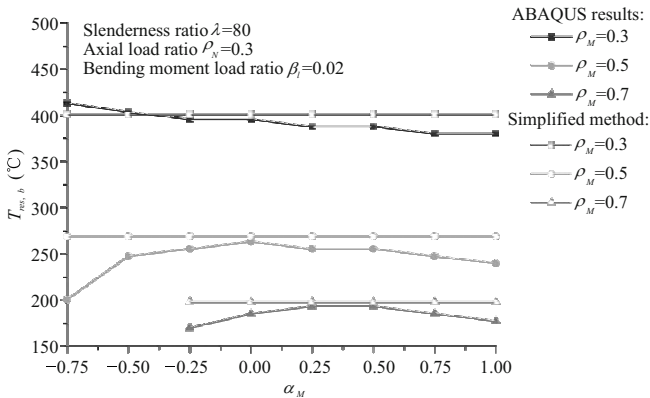
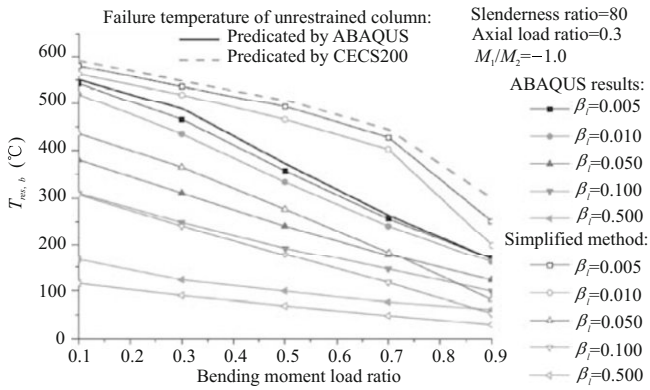
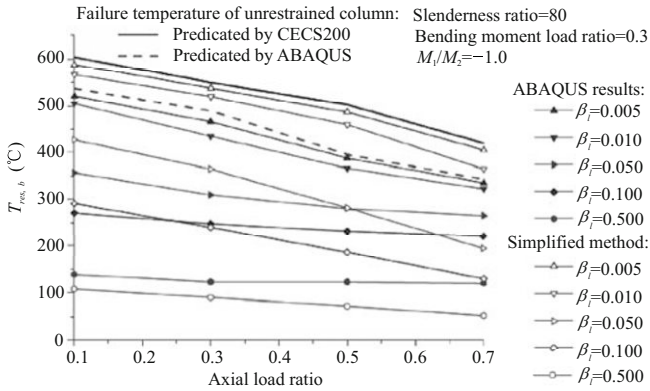
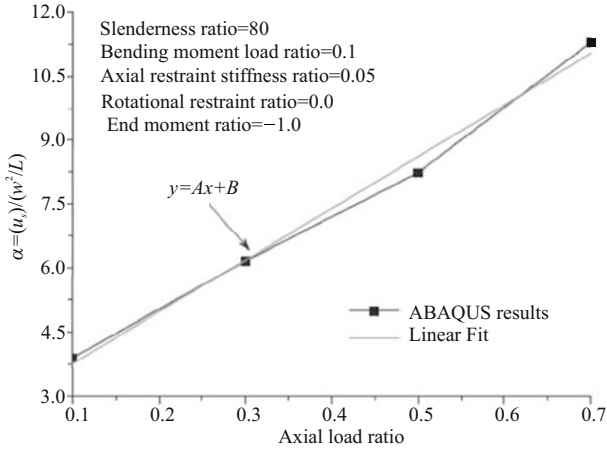
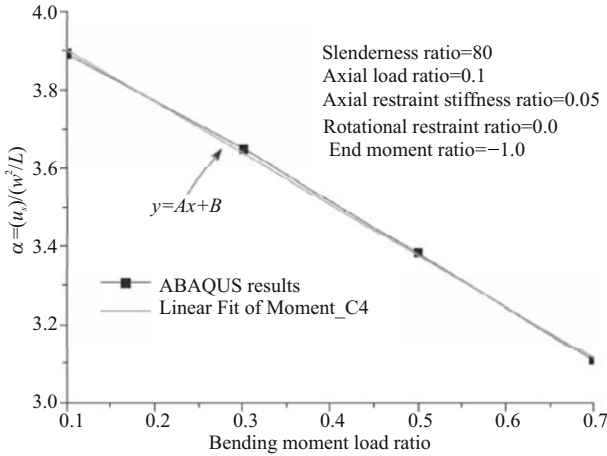


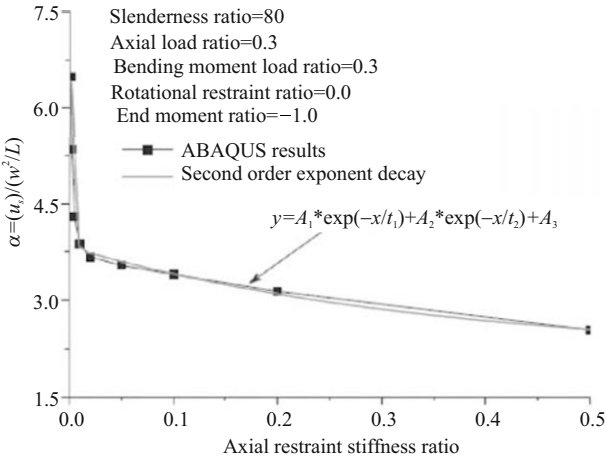
Fig. 8.27 Verification of the buckling temperature equation for a restrained column under combined axial load and bending moment



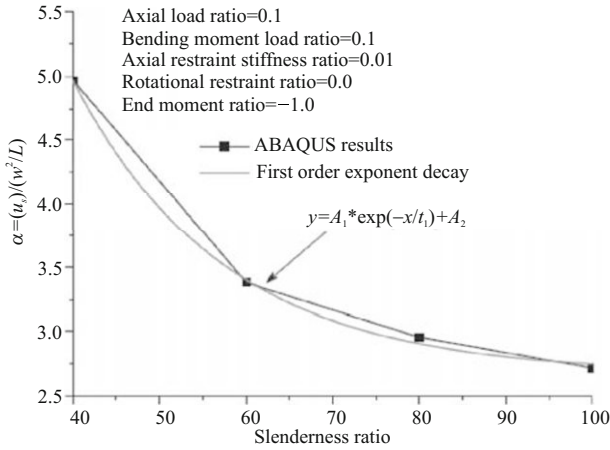
(a) Relationship between α and ρ_N



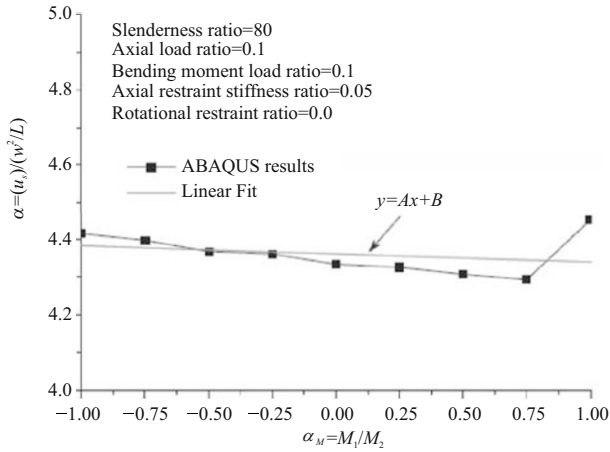
(b) Relationship between α and ρ_M



(c) Relationship between α and β_I



(d) Relationship between α and λ



(e) Relationship between α and α_M

Fig. 8.28 Relationship between α and $\rho_N, \rho_M, \beta_l, \lambda, \alpha_M$

• Verification of the failure temperature equation by ABAQUS simulation

To check the accuracy of the proposed method, ABAQUS simulations have been carried out. Fig. 8.29 compares the column failure temperature obtained by Eq.(8.25) and from ABAQUS simulation.

For columns with β_L lower than 0.02, $T_{res,f}$ predicted by Eq.(8.25) is greater than that from the ABAQUS simulation. With an increasing load ratio, the difference between the failure temperature obtained by the two methods increases, as shown in Fig. 8.29(a) and Fig. 8.29(b). For columns with greater β_l , $T_{res,f}$ predicted by Eq.(8.25) is slightly lower than those by ABAQUS.

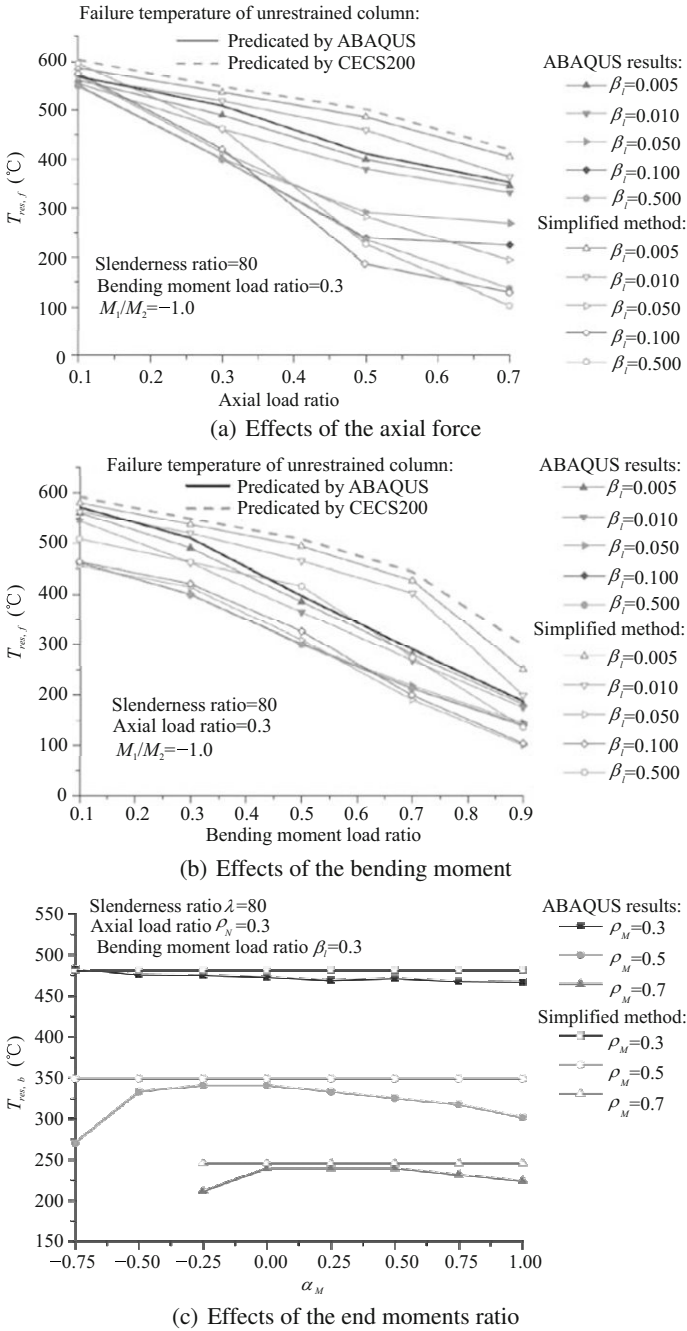


Fig. 8.29 Verification of the failure temperature equation for a restrained column under combined axial load and bending moment

Except for $\alpha_M = -0.75$, $T_{res,f}$ predicted by Eq.(8.25) is not affected by α_M , as shown in Fig. 8.29(c). Eq.(8.25) gives a slightly higher failure temperature.

● **Verification of the failure temperature equation by fire tests**

The comparison of $T_{res,f}$ predicated by Eq.(8.25) and fire test results are listed in Table 8.2. It can be seen that $T_{res,f}$ calculated by Eq.(8.25) is a little lower than the tested result, which shows that the proposed method is precise enough, and falls on the safe side.

Table 8.2 Comparison of tested- and calculated-failure temperatures

Test No.	$T_{res,f}$ (°C)		Error
	Proposed	Tested	
Test 01	469.4	549.7	-14.6%
Test 02	470.2	515.8	-8.5%

8.4 Fire-Resistance of Restrained Columns with Non-Uniform Temperature Distribution

A few numerical studies have been carried out to investigate effects of partial fire protection damage. Wang et al.^[31] conducted finite element analysis to predict the temperature distribution of steel columns with partial fire protection loss and found that the length and location of fire protection loss has little impact on the temperature distribution over the length of a steel component. Wang et al.^[32] proposed a method to predict the stability capacity of a restrained steel column based on the principle of minimum potential energy .

Tomecek and Milke^[33] carried out a two-dimensional finite element study to investigate effects of fire protection loss on the fire resistance of steel columns, and showed that a 4% loss of protection resulted in a 15% reduction in the critical time for a one-hour rated W10×49 column and a 40% reduction in the time for a two-hour rated W10×49 column. Ryder et al.^[34] conducted a three-dimensional finite element analysis on a steel column with partial fire protection damage and showed that the fire resistance of the column can be severely diminished if even a small portion of the protection is removed. Kang et al.^[35] carried out a numerical study to investigate the fire resistance reduction of protected steel beams caused by partial loss of fire protection and found that partial loss of fire protection can cause a significant moment capacity reduction.

Results of a heat-transfer analysis of steel columns with partial loss of fire protection using the finite element method were presented by Milke^[36]. Analytical results indicated that for a given exposure time the area of the protection loss and the size of

the column were found to have an appreciable effect upon the thermal response of the column regardless of the protection thickness. And the area of the missing protection seems to be the primary factor in the temperature rise of the column. Fontana^[37] and Knobloch^[38] studied the fire behavior using a three-dimensional finite element heat transfer and structural model, taking into account geometrical nonlinearities, local temperature distributions, thermal strains and temperature dependent material properties. Results confirmed that local damage to fire protection is a decisive factor in the fire resistance of steel columns and it is important to avoid fire protection that has been damaged by periodical repairs by using robust fire protection systems. Stephen Pessiki^[39] performed an analysis to examine the behavior of steel H columns in a fire with damaged spray-applied fire resistant material subjected to concentric axial compression. The conclusions stated that the removal of even relatively small amounts of fire resistant material from the column flange causes a dramatic decrease in column axial load capacity for fire resistance duration in excess of 30 minutes. A simplified approach in the temperature domain using the critical temperature criteria for steel columns was used in ASTM E119^[40] to calculate the fire resistance of steel columns with partially missing fire protection.

It seems that the finite element method has been employed by nearly all the previous researchers to study the temperature distribution and fire resistance of steel members suffering from partial loss of fire insulation material. Although the FEM is powerful, it is not straightforward for understanding the failure mechanism of steel members in a fire with a partial loss of fire protection. Experimental study and theoretical investigation with a simple model are necessary for identifying the fire-resistance of restrained columns with partial fire protection damage.

8.4.1 Test Arrangement and Instrumentation

The experimental set-up^[41] is shown in Fig. 8.2. Four displacement transducers were employed in the experiment: one was used to measure the axial displacement and the other three for measuring the lateral displacement of the specimen. Nine thermocouples were utilized to measure the temperature of the specimen: three were used to measure the temperature on the portion without fire protection and the other six for the portion with fire protection. The arrangement of thermocouples and displacement transducers is shown in Fig. 8.30.

8.4.1.1 Specimen

The specimen is 2.7 m long with a cross section of H140×100×6×6. Young's Modulus of steel was 202000 N/mm², the yield strength was 272 N/mm², the ultimate strength was 413 N/mm² and maximum elongation was 18%. The applied axial load keeps constant with the load ratio of 0.55. The load ratio is defined as the ratio of the load on the steel column to column buckling resistance at the normal temperature.

The specimens were protected with 20 mm thick of fire protection. At the two ends of the column, the fire protection is moved away to simulate the partial loss of

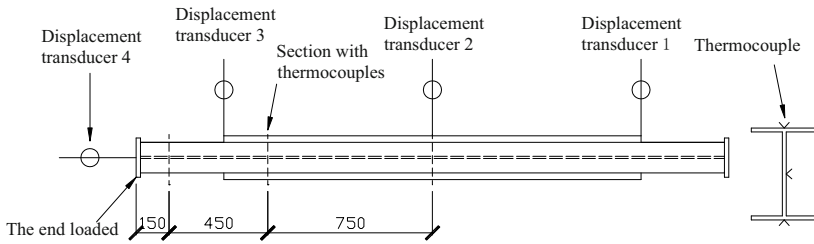


Fig. 8.30 Thermocouples and displacement transducers arrangement (mm)

fire protection. The length of fire protection loss is 7% and 14% of the column length with approximately 190 mm and 380 mm length respectively, as shown in Fig. 8.31.

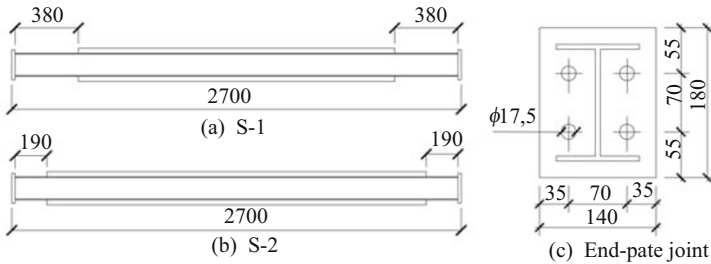


Fig. 8.31 Specimen (mm)

8.4.2 Temperature Distribution

The temperature in the portion of the steel column with and without fire protection are shown in Fig. 8.32 and Fig. 8.33. The column temperature with fire protection initially rose much more slowly than that without fire protection. The difference increased to almost 500 °C in 25 min.

8.4.2.1 Axial Displacements and Failure Temperatures

Fig. 8.34 and Fig. 8.35 show the development of axial displacement against time and column temperature respectively. For the specimen S-1, the axial displacement increases rapidly and the buckling occurs at 15 min. However, for the specimen S-2, the buckle time was 40 min due to the length of the fire protection loss being short. As can be seen from Fig. 8.35, the critical temperatures of specimens S-1 and S-2 are 500 °C and 750 °C respectively.

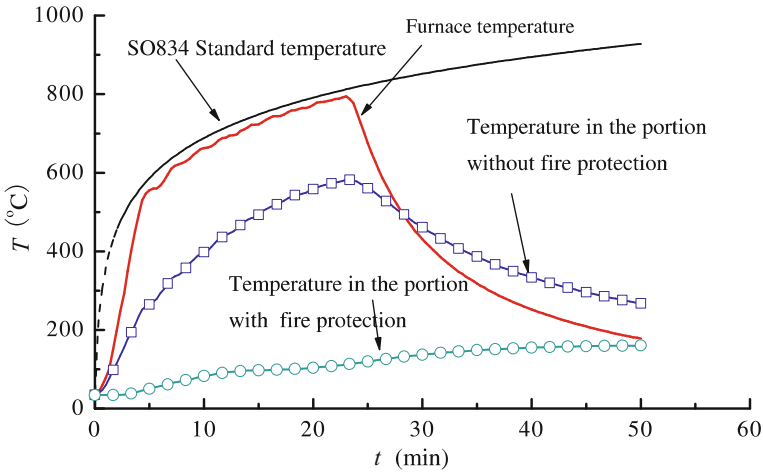


Fig. 8.32 Temperature time curves of the Specimen S-1

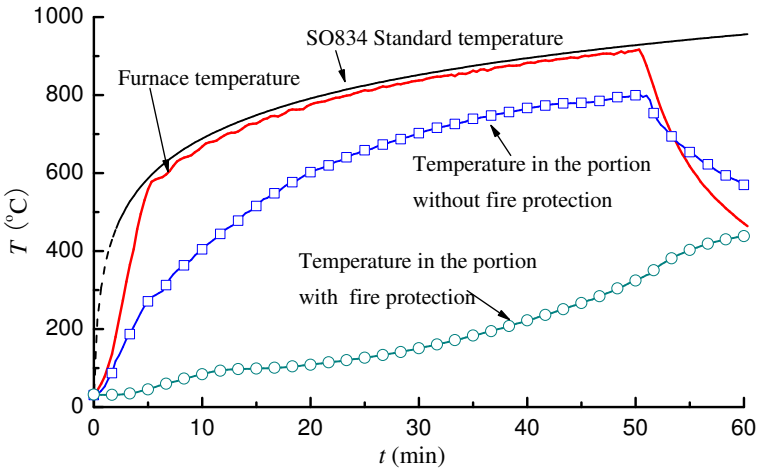


Fig. 8.33 Temperature-time curves of the Specimen S-2

8.4.2.2 Failure of Specimens

Fig. 8.36 and Fig. 8.37 show the failure of the specimens. The column buckled in the portion without fire protection.

8.4.3 Continuum Model

Fig. 8.38 shows the mechanical model of a steel column without fire protection at the two ends^[42,43,44,45]. The initial flexure of the column may be expressed by

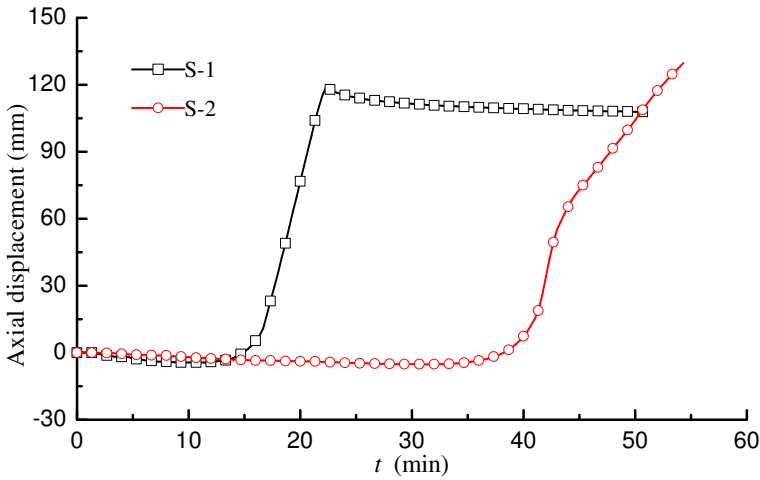


Fig. 8.34 Axial displacement time curve of the specimens

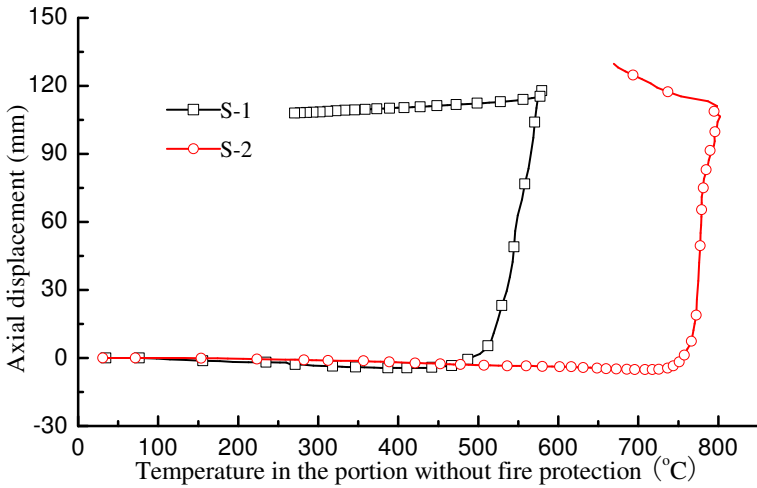


Fig. 8.35 Axial displacement temperature curve of the specimens

$$y_0 = a_0 \sin\left(\frac{\pi x}{l}\right) \tag{8.29}$$

where a_0 is the initial imperfection at the mid-span of the column.

If the lateral displacements of the column at the location without fire protection and with fire protection are y_1 and y_2 respectively, the following equation can be obtained as

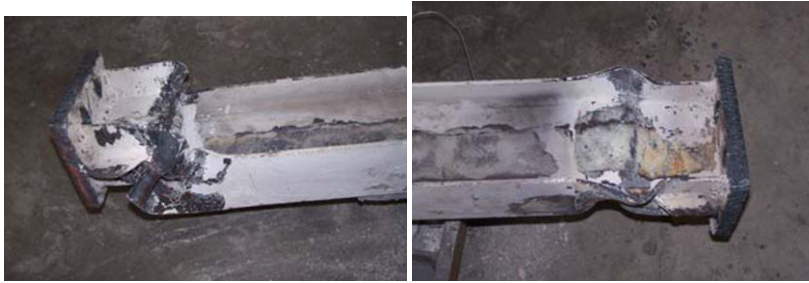
$$\begin{cases} E_{T_1} I (y_1 - y_0) + P (y_1 + e_0) = 0, & \text{when } 0 \leq y \leq l' \\ E_{T_2} I (y_2 - y_0) + P (y_2 + e_0) = 0, & \text{when } l' \leq y \leq l/2 \end{cases} \tag{8.30}$$



(a) End A

(b) End B

Fig. 8.36 Failure of the Specimen S-1



(a) End A

(b) End B

Fig. 8.37 Failure of the Specimen S-2

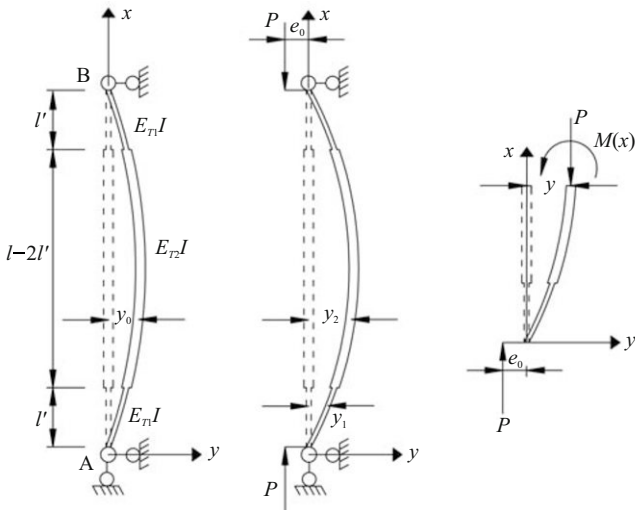


Fig. 8.38 Mechanical model of the steel column with partial fire protection damage

Considering the displacement at the two ends is zero and the rotation of the cross section of the column continues through the overall length, the following boundary conditions are adopted as

$$\begin{aligned} y_1(0) &= 0; & y_1(l') &= y_2(l') \\ y_1'(l') &= -y_2'(l'); & y_2'(l/2) &= 0 \end{aligned} \quad (8.31)$$

For convenience, the following parameters are defined as

$$\begin{aligned} \mu &= \frac{l'}{l}; & \varepsilon &= \frac{a_0}{l}; & \eta &= \frac{e_0}{h_c} \\ P_{cr1} &= \frac{\pi^2 E_{T_1} I}{l^2}; & P_{cr2} &= \frac{\pi^2 E_{T_2} I}{l^2} \\ \alpha &= \sqrt{\frac{P}{P_{cr1}}}; & \beta &= \sqrt{\frac{P}{P_{cr2}}} \end{aligned} \quad (8.32)$$

The solution to Eq.(8.30) is given as

$$\begin{cases} y_1 = C_1 \sin\left(\frac{\alpha\pi x}{l}\right) + C_2 \cos\left(\frac{\alpha\pi x}{l}\right) + \frac{a_0}{1-\alpha^2} \sin\left(\frac{\pi x}{l}\right) - e_0 \\ y_2 = C_3 \sin\left(\frac{\beta\pi x}{l}\right) + C_4 \cos\left(\frac{\beta\pi x}{l}\right) + \frac{a_0}{1-\beta^2} \sin\left(\frac{\pi x}{l}\right) - e_0 \end{cases} \quad (8.33)$$

where parameters C_1 , C_2 , C_3 and C_4 are determined by employing the boundary condition Eq.(8.31), given by

$$\begin{aligned} C_1 &= \frac{A \left[\beta \tan\left(\frac{\beta\pi}{2}\right) \cos(\mu\beta\pi) - \beta \sin(\mu\beta\pi) \right] - B \left[\cos(\mu\beta\pi) + \tan\left(\frac{\beta\pi}{2}\right) \sin(\mu\beta\pi) \right]}{C \sin(\mu\alpha\pi) - \alpha D \cos(\mu\alpha\pi)} \\ C_2 &= e_0 \\ C_3 &= \frac{[\alpha A \cos(\mu\alpha\pi) - B \sin(\mu\alpha\pi)] \tan\left(\frac{\beta\pi}{2}\right)}{C \sin(\mu\alpha\pi) - \alpha D \cos(\mu\alpha\pi)} \\ C_4 &= \frac{\alpha A \cos(\mu\alpha\pi) - B \sin(\mu\alpha\pi)}{C \sin(\mu\alpha\pi) - \alpha D \cos(\mu\alpha\pi)} \end{aligned} \quad (8.34)$$

and

$$\begin{aligned} A &= a_0 \left[\frac{1}{1-\beta^2} - \frac{1}{1-\alpha^2} \right] \sin(\mu\pi) - e_0 \cos(\mu\alpha\pi) \\ B &= a_0 \left[\frac{1}{1-\beta^2} - \frac{1}{1-\alpha^2} \right] \cos(\mu\pi) - e_0 \sin(\mu\alpha\pi) \\ C &= \beta \tan\left(\frac{\beta\pi}{2}\right) \cos(\mu\beta\pi) - \beta \sin(\mu\beta\pi) \\ D &= \cos(\mu\beta\pi) + \tan\left(\frac{\beta\pi}{2}\right) \sin(\mu\beta\pi) \end{aligned} \quad (8.35)$$

If we take yielding at the as the failure criteria of the column in a fire, the ultimate load capacity of the column with partial loss of fire protection is predicted by

$$\begin{cases} \frac{P}{A} + \frac{P\alpha_{\max 1}}{W} = f_{yT_1} \\ \frac{P}{A} + \frac{P\alpha_{\max 2}}{W} = f_{yT_2} \end{cases} \quad (8.36)$$

where $\alpha_{\max 1} = y_1(l')$ and $\alpha_{\max 2} = y_1(l/2)$.

8.4.4 Experiment Study

8.4.4.1 Specimens

The cross section area of the specimens $A=1968 \text{ mm}^2$ with the moment inertia $I_x=6438976 \text{ mm}^4$ and $I_y=1002304 \text{ mm}^4$. The slenderness of the column $\lambda_x=47.2$ and $\lambda_y=119.6$. The stable factor $\varphi_x=0.87$. Therefore, the load capacity of the column is $N=234 \text{ kN}$. The load ratio is adopted as 0.55 and the load acting on the steel column $P=129 \text{ kN}$.

8.4.4.2 Yielding Load of the Specimen at Elevated Temperature

According to the equation

$$\varphi_T f_{yT} A = P$$

the yielding critical temperature is obtained as $T_{y,cr}=692 \text{ }^\circ\text{C}$.

For specimen S-1, the column failed at $500 \text{ }^\circ\text{C}$ and is lower than $T_{y,cr}$, which may cause global stability failure. For specimen S-2, the failure temperature is $750 \text{ }^\circ\text{C}$ and is higher than $T_{y,cr}$, which may cause strain hardening of the steel at elevated temperature.

8.4.4.3 Global Stability Study

For the specimen with partial fire protection loss, the yielding may occur on the boundary of fire protection damage or at the mid-span. Fig. 8.39 and Fig. 8.40 show the critical temperature of the two specimens.

As is shown in Fig. 8.39, the temperature at which the mid-span yielding is $865 \text{ }^\circ\text{C}$ and the boundary of the fire protected part yielding is $665 \text{ }^\circ\text{C}$. Therefore, the failure temperature of specimen S-1 is $665 \text{ }^\circ\text{C}$. As shown in Fig. 8.40, the temperature at which the mid-span yielding and the boundary of fire protected part yielding are $960 \text{ }^\circ\text{C}$ and $680 \text{ }^\circ\text{C}$ respectively. Hence the failure temperature of the specimen S-2 is $680 \text{ }^\circ\text{C}$.

8.4.4.4 Comparison between Experimental and Analytical Results

The critical temperatures obtained by experiment and analysis are shown in Table 8.3. For specimen S-1, the critical temperature measured in the experiment is lower than both the yielding temperature and the temperature predicated by the analysis,

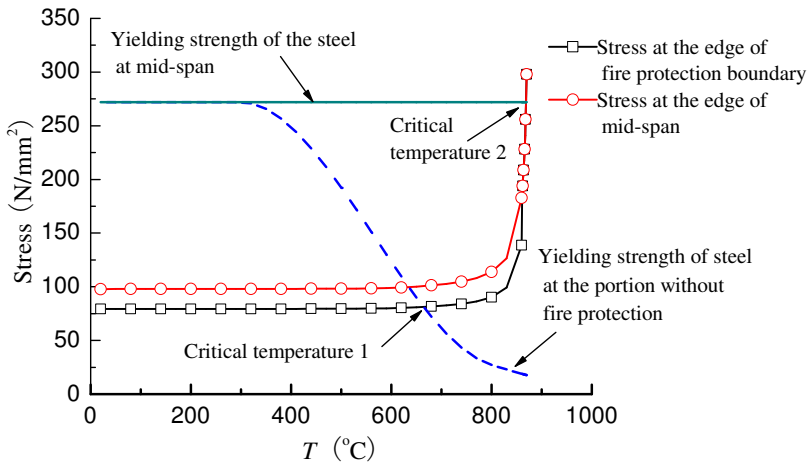


Fig. 8.39 Critical temperature of the specimen S-1

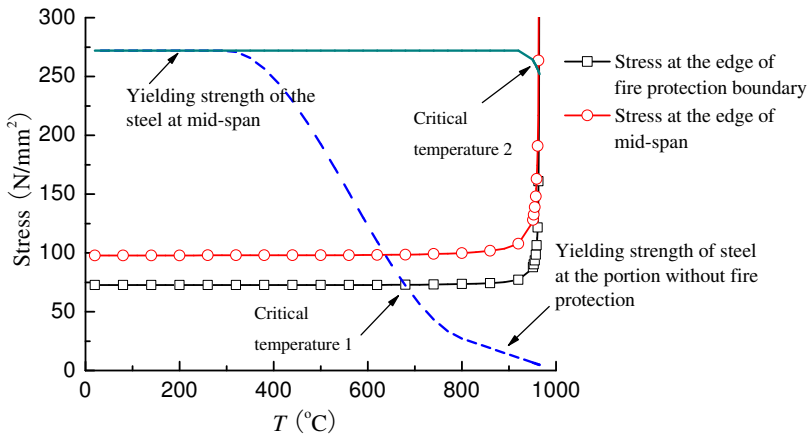


Fig. 8.40 Critical temperature of the specimen S-2

Table 8.3 Comparison of results between experiment and analysis

Test No.	Experimental results	Analytical results		
		Failure yielding	by continuum model	T_{cr}
S-1	500 °C	692 °C	665 °C	665 °C
S-2	750 °C	692 °C	680 °C	680 °C

which may be due to the fact that specimen S-1 has a greater imperfection and leads to the failure occurring earlier. Furthermore, some load eccentricity may exist at the loaded end of the specimen.

For specimen S-2, the measured critical temperature is higher than both the yielding temperature and the critical temperature predicated by analysis. This may result from the rotational restraint and the strain hardening of the steel in a large deflection state.

8.4.4.5 Influences of the Load Eccentricity Ratio on the Critical Temperature

The relationship between the critical temperature and load eccentricity ratio is plotted in Fig. 8.41. The critical temperature will decrease with the increase in the load eccentricity ratio. For specimen S-1, the critical temperature is 500 °C with a load eccentricity ratio of 12%.

8.4.4.6 Influence of the Rotational Restraint on the Critical Temperature

The deflection of specimens with pin-ends and fixed-ends at the boundary of the fire protected part and the mid-span are plotted in Fig. 8.42 and Fig. 8.43, respectively. Deflections increased suddenly at the critical temperature. For the specimens with the pin-ends, critical temperatures are 620 °C and 680 °C respectively for S-1 and S-2. And for the specimens with the fixed ends, critical temperatures are 675 °C and 695 °C respectively for S-1 and S-2.

From analytical results, some conclusions may be drawn:

- the boundary condition has little influence on the critical temperature; and
- the rotational restraint has great influence on the critical temperature of a specimen with a greater length unprotected.

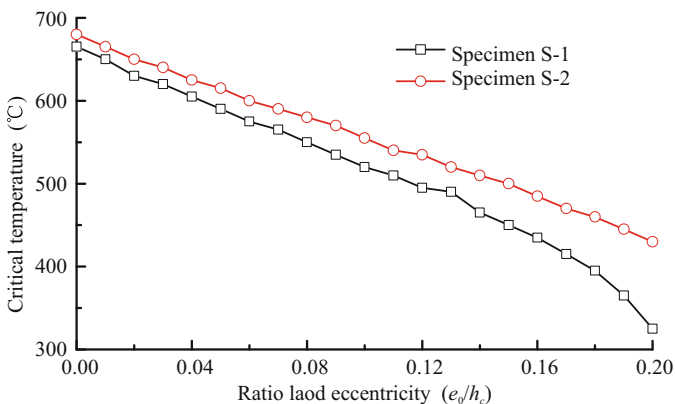


Fig. 8.41 Influences of the load eccentricity ratio

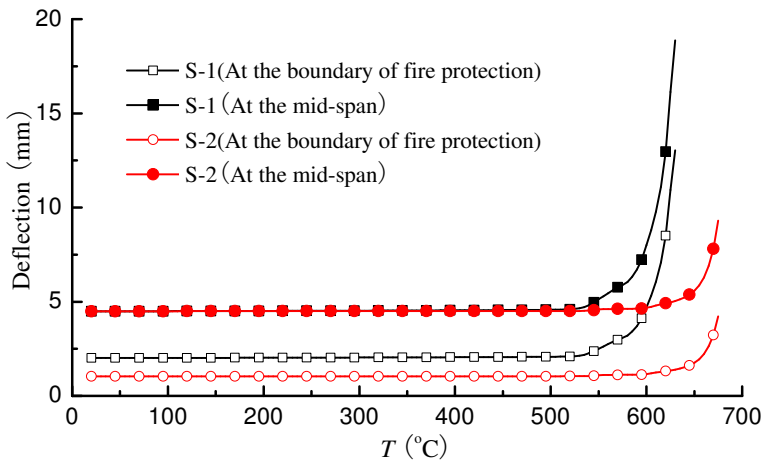


Fig. 8.42 Deflection temperature curves of the specimens with pinned ends

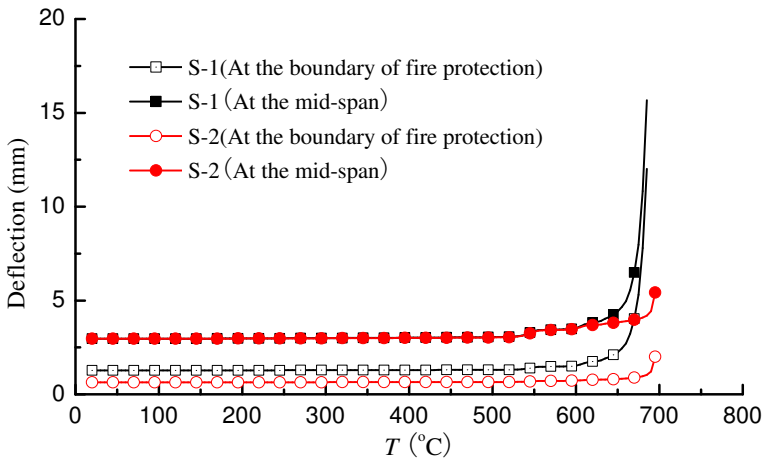


Fig. 8.43 Deflection-temperature curves of the specimens with fixed ends

References

- [1] International Organization for Standardization. *Fire-Resistance Tests – Elements of Building Construction, Part 1: General Requirements*. International Organization for Standardization, 1999.
- [2] A. D. Weller. *Broadgate Phase 8: Fire, 22 June 1990. Summary Report of Damage and Repair*. Building Research Establishment PD 21/92, 1992.
- [3] Steel Construction Institute. *Investigation of Broadgate Phase 8 Fire, Report of Fire Engineering Consultant Ltd*. SCI Fire Engineering Group, UK, 1991.

- [4] C. G. Bailey. Computer modelling of the corner compartment fire test on the large-scale cardington test frame. *Journal of Constructional Steel Research*, 48(1):27–45, 1998.
- [5] C. G. Bailey. The influence of the thermal expansion of beams on the structural behaviour of columns in steel-framed structures during a fire. *Engineering Structures*, 22(7):755–768, 2000.
- [6] Y. C. Wang and D. B. Moore. The effect of frame continuity on the critical temperature of steel columns. In *Proceedings of the 3rd international KEREN-SKY conference on global trends in structural engineering*, Singapore, 1994.
- [7] W. I. Simms, D. J. O’Connor, F. Ali, and M. Randall. An experimental investigation on the structural performance of steel columns subjected to elevated temperatures. *Journal of Applied Fire Science*, 5(4):269–284, 1996.
- [8] W. I. Simms. *An Experimental Investigation of Axially Restrained Steel Columns in Fire*. PhD thesis, University of Ulster, 1997.
- [9] F. Ali, A. Nadjai, and D. Talamona. Effect of rotational restraint on performance of steel columns in fire. *Journal of Applied Fire Science*, 13(1):21–34, 2004.
- [10] K. H. Tan, W. S. Toh, Z. F. Huang, and G. H. Phng. Structural responses of restrained steel columns at elevated temperatures. part 1: Experiments. *Engineering Structures*, 29(8):1641–1652, 2007.
- [11] J. P. Correia Rodrigues, I. Cabrita Neves, and J. C. Valente. Experimental research on the critical temperature of compressed steel elements with restrained thermal elongation. *Fire Safety Journal*, 35(2):77–98, 2000.
- [12] Y. C. Wang and J. M. Davies. An experimental study of non-sway loaded and rotationally restrained steel column assemblies under fire conditions: Analysis of test results and design calculations. *Journal of Constructional Steel Research*, 59(3):291–313, 2003.
- [13] F. Ali and D. O’Connor. Structural performance of rotationally restrained steel columns in fire. *Fire Safety Journal*, 36(7):679–691, 2001.
- [14] J. M. Franssen. Failure temperature of a system comprising a restrained column submitted to fire. *Fire Safety Journal*, 34(2):191–207, 2000.
- [15] I. C. Neves. The critical temperature of steel columns with restrained thermal elongation. *Fire Safety Journal*, 24(3):211–227, 1995.
- [16] Y. C. Wang. Postbuckling behavior of axially restrained and axially loaded steel columns under fire conditions. *Journal of Structural Engineering*, 130(3):371–380, 2004.
- [17] J. C. Valente and I. C. Neves. Fire resistance of steel columns with elastically restrained axial elongation and bending. *Journal of Constructional Steel Research*, 52(3):319–331, 1999.
- [18] P. J. Wang. *Theory and Experimental Studies on Restrained Steel Columns in Fire*. PhD thesis, Tongji University, 2009.
- [19] G. Q. Li, P. J. wang, and Y. C. Wang. Behaviour and design of restrained steel column in fire, part 1: Fire test. *Journal of Constructional Steel Research*, 66(8-9):1138–1147, 2010.

- [20] Ministry of Housing and Urban-Rural Development of China. *Code for Design of Steel Structures (GB50017-2003)*. China Plan Press, 2003.
- [21] China Association for Engineering Construction Standardization. *Technical Code for Fire Safety of Steel Structures in Buildings (CECS200-2006)*. China Plan Press, 2006.
- [22] European Committee for Standardization. *EN1993-1-2. Eurocode 3: Design of Steel Structures, Part 1.2, General Rules, Structural Fire Design*. European Committee for Standardization, 2005.
- [23] ABAQUS. *ABAQUS Analysis User's Manual*. Dassault Systmes, 2007.
- [24] Z. F. Huang and K. H. Tan. Rankine approach for fire resistance of axially and-flexurally restrained steel columns. *Journal of Constructional Steel Research*, 59(12):1553–1571, 2003.
- [25] Z. F. Huang, K. H. Tan, and S. K. Ting. Heating rate and boundary restraint effects on fire resistance of steel columns with creep. *Engineering Structures*, 28(6):805–817, 2006.
- [26] Z. F. Huang and K. H. Tan. Effects of external bending moments and heating schemes on the responses of thermally restrained steel columns. *Engineering Structures*, 26(6):769–780, 2004.
- [27] P. J. wang, G. Q. Li, and Y. C. Wang. Behaviour and design of restrained steel column in fire, part 2: Parameter study. *Journal of Constructional Steel Research*, 66(8-9):1148–1154, 2010.
- [28] K. H. Tan and W. F. Yuan. Buckling of elastically restrained steel columns under longitudinal non-uniform temperature distribution. *Journal of Constructional Steel Research*, 64(1):51–61, 2008.
- [29] P. J. wang, G. Q. Li, and Y. C. Wang. Behaviour and design of restrained steel column in fire, part 3: practical design method. *Journal of Constructional Steel Research*, 66(11):1422–1430, 2010.
- [30] P. J. Wang, Y. C. Wang, and G. Q. Li. A new design method for calculating critical temperatures of restrained steel column in fire. *Fire Safety Journal*, doi:10.1016/j.firesaf.2010.07.002, 2010.
- [31] J. Wang and G. Q. Li. Effect of local damage of fire insulation on temperature distribution of steel members subjected to fire. *Structural Engineers*, 21(5):30–35, 2005.
- [32] W. Y. Wang, P. J. Wang, and G. Q. Li. Stable bearing capacity for restrained steel column after damage of fire protection in fire. *Chinese Quarterly of Mechanics*, (3), 2008.
- [33] D. V. Tomecek and J. A. Milke. A study of the effect of partial loss of protection on the fire resistance of steel columns. *Fire Technology*, 29(1):4–21, 1993.
- [34] N. L. Ryder, S. D. Wolin, and J. A. Milke. An investigation of the reduction in fire resistance of steel columns caused by loss of spray-applied fire protection. *Journal of Fire protection Engineering*, 12(1):31–44, 2002.
- [35] Y. Kang, G. V. Hadjisophocleous, and H. A. Khoo. The effect of partial fire protection loss on the fire resistance reduction of steel beams. *Fourth International Workshop Structures in Fire, Aveiro. Portugal*, pages 63–73, 2006.

- [36] J. A. Milke. Analyses of the impact of loss of spray-applied fire protection on the fire resistance of steel columns. *Fire Safety Science-Proceedings of the Seventh International Symposium, Worcester, USA*, 2003.
- [37] M. Fontana and M. Knobloch. Fire resistance of steel columns with partial loss of fire protection. *Proceedings of the IABSE Symposium Shanghai 2004 Metropolitan Habitats and Infrastructure, IABSE Report Vol. 88, Shanghai, China*, 2004.
- [38] M. Knobloch, M. Fontana, and E. Raveglia. Partial loss of fire protection and structural collapse of high-rise buildings. *International Congress Fire safety in tall buildings, University of Cantabria, Santander, Spain*, 2006.
- [39] S. Pessiki, K. Kwon, and B. J. Lee. Fire load behavior of steel building columns with damaged spray-applied fire resistive material. *Fourth international workshop Structures in fire, Aveiro, Portuga*, 2006.
- [40] American Society of Testing and Material. *ASTM E-119: Standard Test Method for Fire Tests of Building Constructions and Materials*. ASTM Philadelphia, 2000.
- [41] W. Y. Wang. *Critical Temperature of Axially Restrained Steel Columns with Partial Fire Retardant Coating Damage*. PhD thesis, Tongji University, 2008.
- [42] G. Q. Li, W. Y. Wang, and S. W. Chen. Stability capacity of restrained steel columns after damage of fire retardant coating in fire. *Engineering Mechanics*, 25(12):72–78, 2008.
- [43] W. Y. Wang and G. Q. Li. Critical temperature of axially restrained steel columns with partial fire retardant coating damage. *Journal of Chongqing Jianzhu University*, 32(1), 2010.
- [44] W. Y. Wang and G. Q. Li. Behavior of steel columns in a fire with partial damage to fire protection. *Journal of Constructional Steel Research*, 65(6):1392–1400, 2009.
- [45] G. Q. Li and W. Y. Wang. A simple approach for modeling fire-resistance of steel columns with locally damaged fire protection. *Engineering Structures*, 31(3):617–622, 2009.

Fire-Resistance of Composite Concrete Slabs

The contribution of a steel deck to support the sagging moment is usually employed when designing the composite slab. However, the fire resistance of the steel sheet in the composite slab is a big concern. The traditional fire-resistance design of the composite slab is based on the fire resistance test. Nevertheless, the test can not include all the parameters that affect the fire resistance of the slab. Furthermore, the boundary conditions and loads on the composite slab in the fire test may be different from those in the real structure, which means that the fire resistance obtained from the test can not represent the resistance in the real structure.

Traditionally, the floor slab is used to support loads through a bending mechanism that is based on the small deflection theory. However, through the investigation of real fire disasters and fire experiments, it was noted that the composite floor slab^[1,2] showed higher load bearing capacity than expected using the traditional bending mechanism method for fire resistance design. The membrane action occurs at the large deflection of the slab, when edges of the slab are vertically and horizontally restrained. It is also possible for the membrane action to occur when the slab is vertically supported without horizontal restraint. The membrane action can enhance the load bearing capacity of the slab by changing the load bearing mechanism from a bending model with a small deflection to a membrane model with a large deflection.

9.1 Fire-resistance Design Method for Composite Concrete Slabs Based on Small Deflection Theory

9.1.1 Studied Slabs

When modeling behaviors of a composite slab in a fire, the following characteristics should be considered

- the temperature distribution the cross-section of the composite concrete slab is non-uniform and should be treated separately;

- the bond strength between the concrete and steel deck degrades with the elevation of temperature; and
- the non-linear temperature distribution will cause additional stress in the section of the slab.

The fire resistance of a single span and two continuous span composite slabs are studied. Parameters investigated include the applied load, the depth of composite slab, the thickness of the steel deck, and the reinforcement in the concrete^[3]. The Finite Element Method (FEM) is used for this investigation^[4,5].

The dimension of the profiled steel deck is shown in Fig. 9.3 and Table 9.1. The grade of concrete is C25 and C50, and the reinforcement for the hogging moment region is $\phi 10@100$ and $\phi 8@100$, respectively. Analytical results^[4,5] of the fire resistance time are listed in Table 9.2 and Table 9.3.

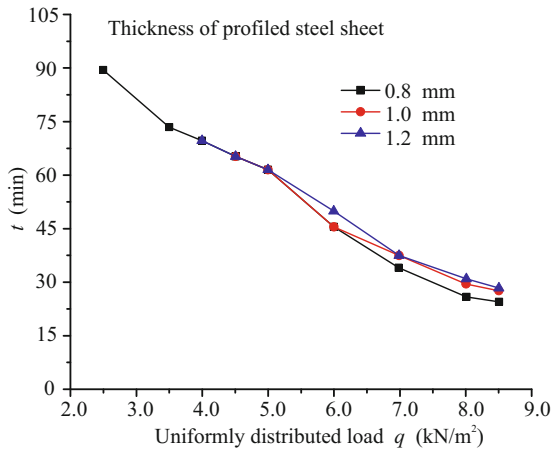


Fig. 9.1 Fire endurance of the single span composite slab with different thickness of profiled steel deck and composite slab depth of 150 mm

Table 9.1 Section properties of the steel sheet

Cover width (mm)	Rib height (mm)	Thickness (mm)	Section inertia I (cm ⁴)	Section modulus W (cm ³)
688	76	0.8	119.88	28.54
		1.0	149.85	35.68
		1.2	179.82	42.85

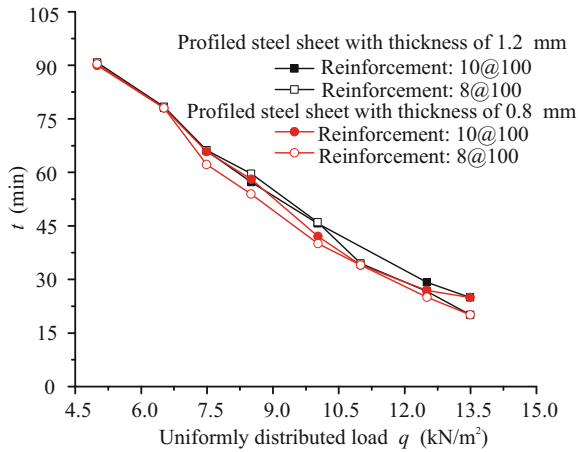


Fig. 9.2 Fire endurance of the two-span composite slab with different reinforcement and composite slab depth of 150 mm

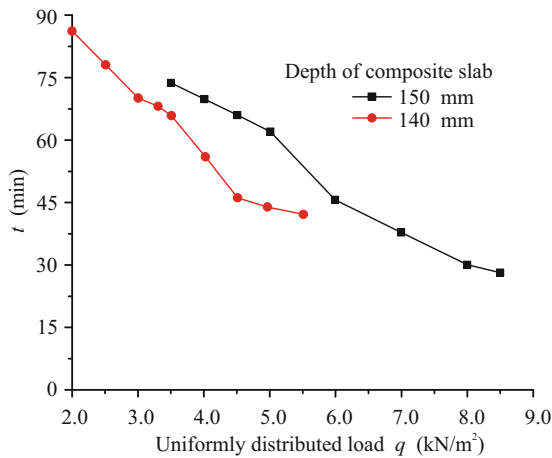


Fig. 9.3 Fire endurance of single span composite slab with different composite slab depth and of profiled steel deck thickness of 1.0 mm

9.1.2 Parametric Studies

9.1.2.1 Effects of the Profiled Steel Deck Thickness on the Fire Resistance of a Composite Slab

The fire endurance time of the composite slab with different thickness of profiled steel deck is nearly the same, as shown in Fig. 9.1 and Fig. 9.2. This is because the profiled steel sheet is exposed to fire directly, and the temperature elevation is not affected by the steel sheet on account of its thinness. The temperature of the

Table 9.2 Fire endurance time of single span composite slabs

No.	t (mm)	h (mm)	f_c	q (kN/m ²)	t_{cr} (min)	No.	t (mm)	h (mm)	f_c	q (kN/m ²)	t_{cr} (min)
SS-01	0.8	150	C25	2.50	90	SS-19	1.2	150	C25	4.00	70
SS-02	0.8	150	C25	3.50	74	SS-20	1.2	150	C25	4.50	66
SS-03	0.8	150	C25	4.00	70	SS-21	1.2	150	C25	5.00	62
SS-04	0.8	150	C25	4.50	66	SS-22	1.2	150	C25	6.00	50
SS-05	0.8	150	C25	5.00	62	SS-23	1.2	150	C25	7.00	38
SS-06	0.8	150	C25	6.00	46	SS-24	1.2	150	C25	8.00	31
SS-07	0.8	150	C25	7.00	34	SS-25	1.2	150	C25	8.50	27
SS-08	0.8	150	C25	8.00	26	SS-26	1.0	140	C25	2.00	86
SS-09	0.8	150	C25	8.50	25	SS-27	1.0	140	C25	2.50	78
SS-10	1.0	150	C25	3.50	74	SS-28	1.0	140	C25	3.00	70
SS-11	1.0	150	C25	4.00	70	SS-29	1.0	140	C25	3.50	66
SS-12	1.0	150	C25	4.50	66	SS-30	1.0	140	C25	4.50	46
SS-13	1.0	150	C25	5.00	62	SS-31	1.0	140	C25	5.50	42
SS-14	1.0	150	C25	6.00	46	SS-32	1.0	140	C25	6.00	27
SS-15	1.0	150	C25	7.00	38	SS-33	1.0	150	C50	6.00	62
SS-16	1.0	150	C25	8.00	30	SS-34	1.0	150	C50	8.00	50
SS-17	1.0	150	C25	8.50	26	SS-35	1.0	150	C50	10.00	30
SS-18	1.2	150	C25	3.50	74						

t is the thickness of steel sheet; h is the height of composite slab; f_c is concrete grade; q is the applied uniformly distributed load; t_{cr} is fire endurance

steel sheet can reach 750 °C in 30 min in the ISO834 standard fire exposure^[6]. The steel almost loses its strength at such high temperature^[7], and the bond between the concrete slab and the steel sheet is also almost completely lost. The fire resistance of the composite slab is mainly determined by the concrete slab.

9.1.2.2 Effects of the Slab Depth on the Fire Resistance of a Composite Slab

The slab depth has great influences on the fire resistance of the composite slab, as shown in Fig. 9.3. Because of the reduction in the composite slab depth between the concrete slab and the profiled steel deck, the fire resistance of the composite slab is dominated by the concrete slab. Because concrete has low thermal conductivity, the concrete slab with larger depth has a greater low temperature region and in turn has a larger load bearing capacity at high temperature.

Table 9.3 Fire endurance of two continuous span composite slabs

No.	t (mm)	h (mm)	f_y	f_c	q (kN/m ²)	t_{cr} (min)
DS-01	1.2	150	$\phi 10@100$	C25	5.00	90
DS-02	1.2	150	$\phi 10@100$	C25	6.50	78
DS-03	1.2	150	$\phi 10@100$	C25	7.50	66
DS-04	1.2	150	$\phi 10@100$	C25	8.50	62
DS-05	1.2	150	$\phi 10@100$	C25	10.0	46
DS-06	1.2	150	$\phi 10@100$	C25	12.5	29
DS-07	1.2	150	$\phi 10@100$	C25	13.5	25
DS-08	1.2	150	$\phi 8@100$	C25	5.00	90
DS-09	1.2	150	$\phi 8@100$	C25	6.50	78
DS-10	1.2	150	$\phi 8@100$	C25	7.50	66
DS-11	1.2	150	$\phi 8@100$	C25	8.50	62
DS-12	1.2	150	$\phi 8@100$	C25	10.0	46
DS-13	1.2	150	$\phi 8@100$	C25	11.0	34
DS-14	1.2	150	$\phi 8@100$	C25	12.5	26
DS-15	1.2	150	$\phi 8@100$	C25	13.5	20
DS-16	0.8	150	$\phi 10@100$	C25	5	90
DS-17	0.8	150	$\phi 10@100$	C25	6.5	78
DS-18	0.8	150	$\phi 10@100$	C25	7.5	66
DS-19	0.8	150	$\phi 10@100$	C25	8.5	62
DS-20	0.8	150	$\phi 10@100$	C25	10	42
DS-21	0.8	150	$\phi 10@100$	C25	11	34
DS-22	0.8	150	$\phi 10@100$	C25	12.5	27
DS-23	0.8	150	$\phi 10@100$	C25	13.5	25
DS-24	0.8	150	$\phi 8@100$	C25	5	90
DS-25	0.8	150	$\phi 8@100$	C25	6.5	78
DS-26	0.8	150	$\phi 8@100$	C25	7.5	62
DS-27	0.8	150	$\phi 8@100$	C25	8.5	58
DS-28	0.8	150	$\phi 8@100$	C25	10	42
DS-29	0.8	150	$\phi 8@100$	C25	11	34
DS-30	0.8	150	$\phi 8@100$	C25	12.5	25
DS-31	0.8	150	$\phi 8@100$	C25	13.5	20

f_y is the reinforcement for the hogging moment

9.1.2.3 Effects of the Reinforcement in the Hogging Moment Region on the Fire Resistance of a Composite Slab

From Fig. 9.4 it can be seen that the reinforcement in the hogging moment region of the composite slab with continuous span has little effect on the fire endurance. For the low conductivity of concrete, the temperature of the reinforcement bar does not exceed 200 °C in a fire. The yield strength and the elastic modulus of the steel reinforcement are nearly the same as that at ambient temperature. The failure of the composite slab is mainly due to the failure of the concrete instead of the reinforcement.

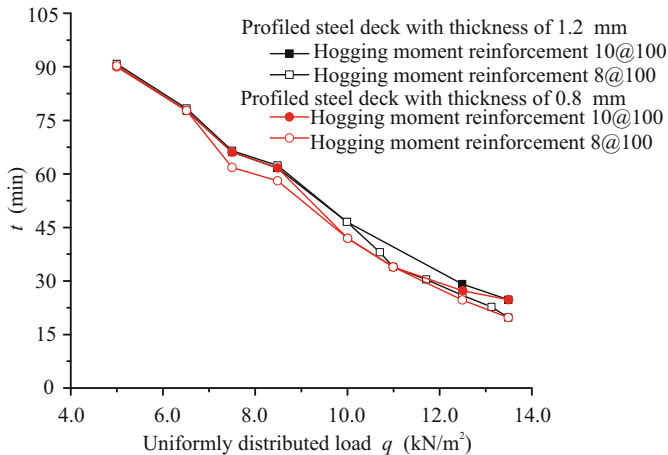


Fig. 9.4 Fire endurance of the composite slab with different reinforcement in the hogging moment region

9.1.2.4 Effects of the Concrete Grade on Fire Resistance of a Composite Slab

From Fig. 9.5 it can be seen that the composite slab with a higher concrete grade has a longer fire endurance time.

9.1.2.5 Effects of the Applied Load on the Fire Resistance of a Concrete Composite Slab

Effects of the applied load on the fire resistance of a concrete composite slab are shown in Fig. 9.1 to Fig. 9.5. It can be seen that, with the increase in the applied load, the fire endurance time decreases nearly linearly.

9.1.3 Simplified Design Method

The fire resistance of composite slabs is not severely affected by the thickness of a profiled steel deck and the reinforcement in the hogging moment region. It is mainly

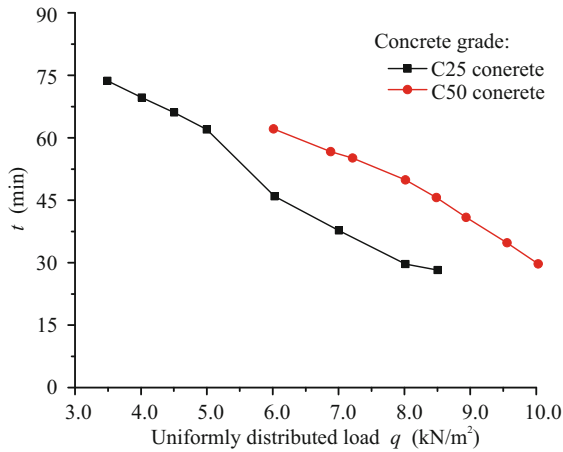


Fig. 9.5 Fire endurance of the composite slab with different concrete grades

determined by the applied load, the depth of the composite slab and the grade of concrete, which can be comprehensively expressed by the load ratio as

$$\eta_F = \frac{M_{\max}}{M_{RC}} \tag{9.1}$$

where M_{\max} is the maximum applied bending moment, M_{RC} is the bending moment capacity of the concrete slab given by

$$M_{RC} = W f_t \tag{9.2}$$

f_t is the tensile strength of the concrete at ambient temperature, as shown in Fig. 9.6.

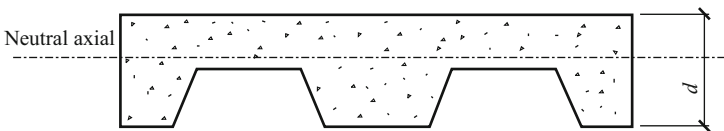


Fig. 9.6 Section of the concrete slab

Using regression method, the fire resistance of a composite slab is calculated^[3] by

$$t_{cr} = 114.06 - 26.8\eta_F \tag{9.3}$$

where t_{cr} is the fire endurance time of the composite slab in minutes.

The comparison of the fire endurance time predicated by Eq.(9.3) and numerical simulation is shown in Fig. 9.7. For the composite slab with a high concrete grade, the fire endurance time estimated by Eq.(9.3) is longer than that using numerical

analysis. The commonly used concrete grade in engineering practice for floor slabs is C30 and C50. In these circumstances, the fire endurance time predicated by Eq.(9.3) agrees well with the numerical result.

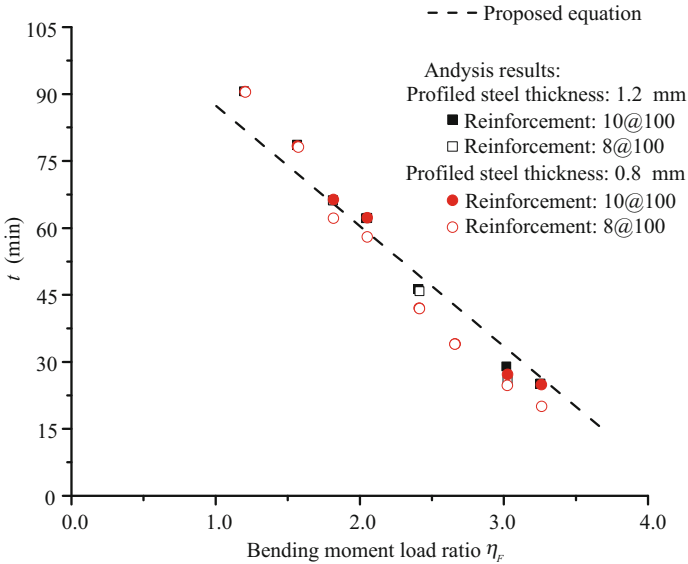


Fig. 9.7 Comparison of the fire endurance time predicated by Eq.(9.3) and numerical analysis

9.1.4 Verification by the Fire Resistance Test

A fire resistance test is carried out to verify the proposed design method for a composite slab^[3]. The profiled steel deck is shown in Fig. 9.8. Parameters of test specimens are listed in Table 9.4.

The test specimen was exposed to an ISO834 standard fire^[6]. The fire endurance times obtained by fire test and Eq.(9.3) are listed in Table 9.5. They agree with each other very well.

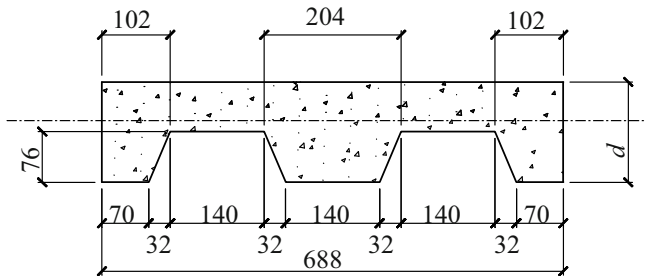
9.2 Fire Resistance Design Method for the Composite Slab Considering Membrane Action

9.2.1 Development of the Membrane Action of a Composite Slab in a Fire

It is found that very large deflection may be induced in the composite slabs^[1,2], and the deflection of the slab after the fire is shown in Fig. 9.9 and Fig. 9.10. Through

Table 9.4 Parameters of test specimens

	Test specimen 1	Test specimen 2
Span	4 m	4 m
Width	3 m	3 m
Depth of composite slab	140 mm	160 mm
Applied uniformly distributed load	3.62 kN/m ²	4.80 kN/m ²
Thickness of profiled steel deck	1.2 mm	1.2 mm
Reinforcement	φ4@150 (two direction)	φ4@150 (two direction)

**Fig. 9.8** The steel deck (mm)**Table 9.5** Comparison of the fire endurance time obtained by fire test and Eq.(9.3)

	Proposed method	Test results
Test specimen 1	22 min	19 min
Test specimen 2	28 min	26 min

investigations of real fire disasters and fire experiments, it is also noticed that the total bearing capacity of the floor slab in a fire may be much higher than that expected, based on the bending mechanism. This discrepancy was found to be due to the membrane action, which plays an important role in increasing the load bearing capacity of the floor slab in fire condition.

According to observations in experiments and real fires, a slab subjected to a fire is assumed to develop as Fig. 9.11. Before the membrane action occurs, the slab deformation is similar to that in classical yield line theory^[8], as shown in Fig. 9.11(a) to Fig. 9.11(f). At the early stage of a fire, when the temperature is not very high, the slab can bear the applied load in the bending mechanism. With an increase in temperature, the strength of steel and concrete in the slab reduce, and yield lines were



Fig. 9.9 Large deflection of the slab in a building after fire attack



Fig. 9.10 Large deflections of the slab in the Cardington fire test

formed in the slab. When the temperature of the slab increases further, the bending capacity of the slab is not enough, and the deflection of the slab will have to be further developed, which creates additional load-bearing capacity in the membrane mechanism to maintain the stability of the slab, as shown in Fig. 9.11(d). The tension force increases with the increase in slab deflection, see Fig. 9.11(e). Finally, most of the vertical load on the slab will be carried by the membrane action with the reinforcement acting as a net, the tension anchored by the peripheral concrete ring of compression, as shown in Fig. 9.11(f).

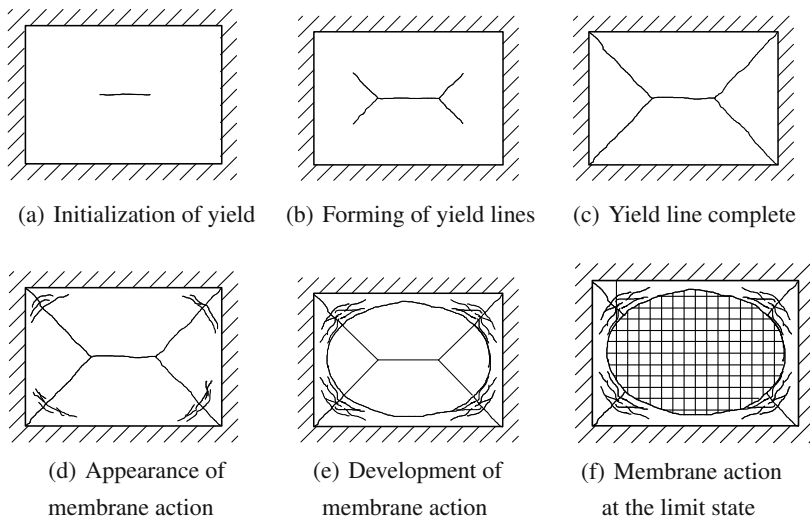


Fig. 9.11 Development of the membrane action in a floor slab

Although the membrane action in a floor slab at ambient temperature has been studied since the 1950's^[8], it was only recently noticed at elevated temperature in the Cardington experiments in the middle of the 1990s^[2,9]. Since then, a number of researchers studied this phenomenon. Among them, Wang^[9] used the membrane action to explain the increase in load bearing capacity of slabs in the Cardington fire tests. Usmani et al.^[10,11,12] analyzed the membrane action in floor slabs based on differential equations. Bailey et al.^[13,14,15,16] studied the mechanism of membrane action using yield-line theory. Huang et al.^[17,18] presented a nonlinear layered finite element procedure for predicting the membrane action of a composite slab in a fire. Li et al.^[19] proposed a practical design method for predicting the fire endurance time of a composite slab considering the membrane action in a fire.

In the analytical model presented by Usmani et al.^[10,11,12], it is assumed that most of the floor slab is elastic, so the deflection and the stress of the floor slab are governed by elastic equations. However, in real fire conditions the floor slab experiences large inelastic deformation^[1,2]. The elastic theory is not appropriate for analyzing the behavior of a floor slab with very large deflections. In the theory presented by Bailey et al.^[13,14,15,16], it is assumed that the floor slab deforms according to rigid plate deformation defined by the yield-line pattern. However, for a slab in real fire conditions, because the concrete may crack at the limit state, bending-resistance will play a small part in affecting slab behavior, and the reinforcement net may be more important. Therefore, the assumption of a yield-line pattern may not be appropriate for modeling the membrane action in floor slabs subjected to a fire.

The membrane action works apparently when the deflection of a slab is very large. In fire conditions, since the most important objective of designers is to avoid the collapse of the floor slab, large deflections are acceptable and it is desirable to

include the favorable effect of membrane action in the fire-resistant design of floor slabs.

9.2.2 Fire Test on the Composite Slab

The Cardington test^[2] showed that the performance of a composite slab with unprotected steel decks and beams in a fire condition was much better than the prediction without considering membrane action. The observation and analysis show that, during a fire, with the strength and stiffness of the steel deck decreasing, the capacity of the slab provided by the traditional bending mechanism will not be enough to bear the applied load. The membrane action will contribute to keeping the stability of the slab by forming a tensile reinforcement mesh in the center of the slab and a compressive concrete ring at the slab edges. The development of the membrane action is shown in Fig. 9.11.

From 1995 to 1996, six localized fire tests were conducted in Cardington^[2,9]. Test results showed that although the temperature of the unprotected beam was higher than 1000 °C, the slab maintained its load bearing capacity during all the tests owing to the membrane action.

In 1999, to prove the existence of the membrane action, Bailey^[13,14] performed a test on a 9.5 m×6.5 m composite floor slab at ambient temperature based on the data of the Cardington test^[20]. In order to validate the theoretical analysis, he performed some small scale tests on 15 reinforced concrete floor slabs. However, all the tests were under ambient temperature, which might not be appropriate for verifying the membrane theory^[8]. In 2008, CTICM^[21] launched a project FRACOF in which an 8.735 m×6.660 m composite floor slab was tested in an ISO standard fire. The test lasted for more than 120 min. Finally, the slab failed because of the fracture of the reinforcement bar. Therefore, this resulted in a limitation of the analysis of the limit state and failure of the slab^[9]. In 2008, Li and Zhang^[22,23] developed a new method to estimate the load bearing capacity of the composite floor slab under fire conditions with consideration of the membrane action. And four full-scale slab tests were performed at Tongji University in China with sponsorship from the National Natural Science Foundation of China to verify the proposed method.

9.2.2.1 Test Set-Up

The specimens were 5.232 m×3.72 m composite floor slabs with steel decks unprotected. The profiled steel deck was YX76-344-688 with a thickness of 1 mm and strength of 270 N/mm²^[22]. The decks were fixed on the primary beams and secondary beams (if they existed) by a shear connector with a diameter of 16 mm and a height of 125 mm. Total depth of the slabs was 146 mm and the thickness of the concrete on the top of the decks was 70 mm, with a concrete grade of C25. The reinforcement was double direction $\phi 8@150$ with a steel grade of Q235. The protective thickness of reinforcement was 21 mm for S-1 and 30 mm for S-2 to S-4. S-1 and S-2 had an unprotected secondary beam in the middle of the slab, while S-3 and S-4 had no secondary beam. The cross section of the secondary beam was I25b with a steel

grade of Q235. The slabs, the primary beams and secondary beams were designed in accordance with the Chinese Code GB50017-2003^[24] and YB9238-92^[25]. The test set-up is shown in Fig. 9.12 and Fig. 9.13. Parameters of tested slabs are listed in Table 9.6.

Table 9.6 The test slabs (mm)

Specimen No.	Arrangement of reinforcement	Fire protection thickness (mm)	Direction of the rib	Secondary beam
S-1	$\phi 8@150$	21	Along the	In the middle of the
S-2	$\phi 8@150$	30	long edge	long edge, unprotected
S-3	$\phi 8@150$	30	Along the	No secondary beam
S-4	$\phi 8@150$	30	short edge	

The slabs were loaded at 24 points to stimulate uniform load with a load ratio of 0.60 to 0.65, as shown in Fig. 9.14. The temperature time curve of the furnace used for the test followed an ISO834 standard fire. Displacements of the slab, temperatures at the surface and bottom of the slab, temperatures and strains of reinforcements in the slab, as well as the strain of the concrete were measured. The arrangement of measuring points is shown in Figs. 9.15–9.18.

9.2.2.2 Test Phenomena

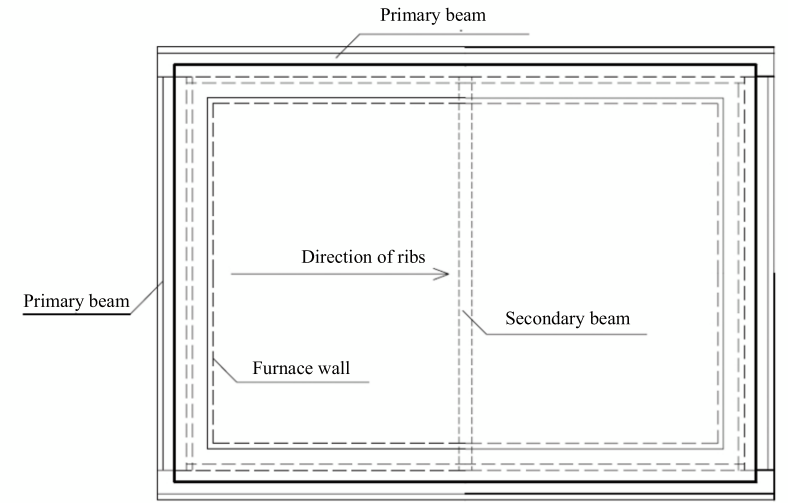
The applied load and test duration for the four tests are shown in Table 9.7.

Table 9.7 Test load and duration

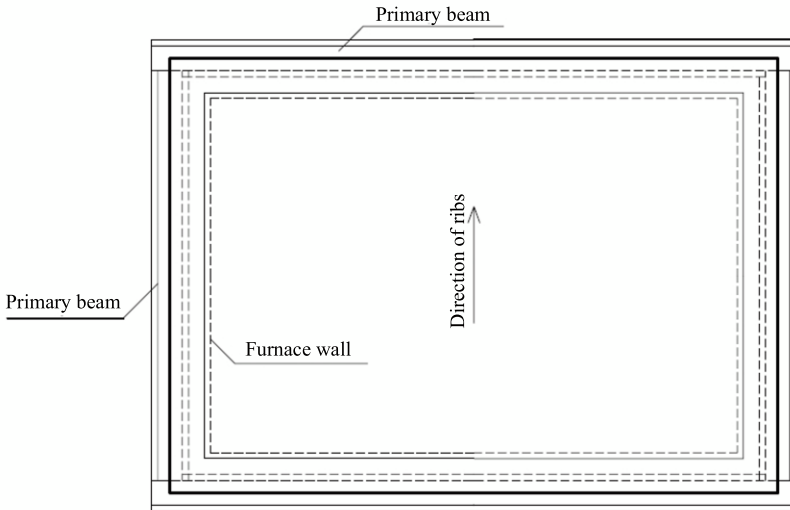
Specimen No.	load bearing capacity (kN/m ²)	Applied load (kN/m ²)	Load ratio	Test duration (min)
S-1	30.64	18.38	60	75
S-2	29.51	17.71	60	90
S-3*	14.57	8.75	60	100
S-4*	14.57	9.47	65	100

* Fire test stopped while the composite slab did not fail

In tests S-1 and S-2, cracks appeared beside the secondary beam firstly due to the negative moment caused by the decrease in the strength and stiffness of the slab. Then, significant cracks were found along the long edge of the slab because of the negative moment induced by the large deflection in the center of the slab. Cracks



(a) Specimens S-1 and S-2



(b) Specimens S-3 and S-4

Fig. 9.12 Test set-up

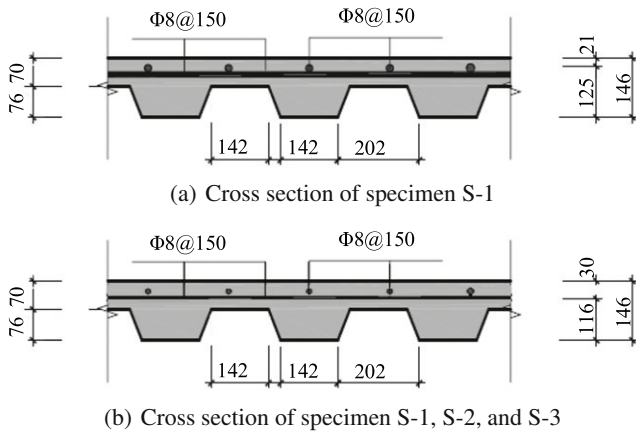


Fig. 9.13 Cross section of the specimen (mm)

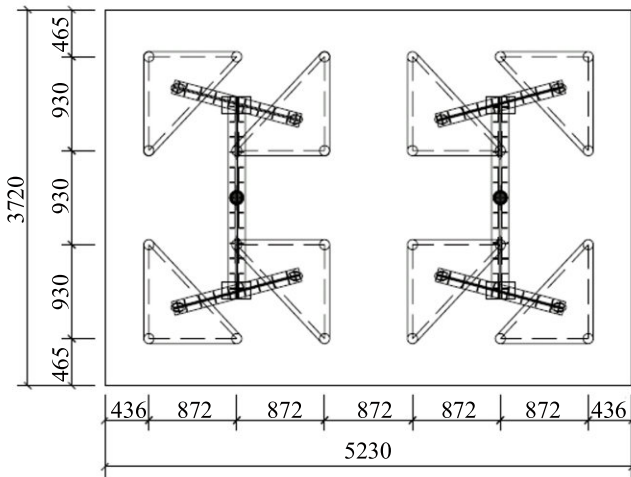


Fig. 9.14 Plan view of the loading system (mm)

were located at the weakest cross section of the slab, as shown in Fig. 9.19. Meanwhile, some cracks occurred along the short edge of the slab. Cracks developed not only on the surface of the slab, but also extended to the side face of the slab, as shown in Fig. 9.20. After the test, significant yield lines were founded at the slab corner. The concrete along the yield line was crushed, as shown in Fig. 9.21.

The deflection of the slab was very large. The deformation of the slabs was presented as elliptic parabolic after the test which was validation that the membrane action was developed to bear the applied load, as shown in Fig. 9.22.

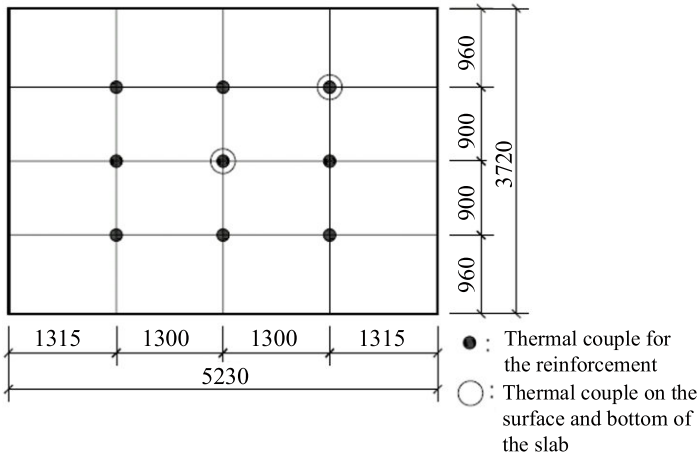


Fig. 9.15 Arrangement of thermal couples (mm)

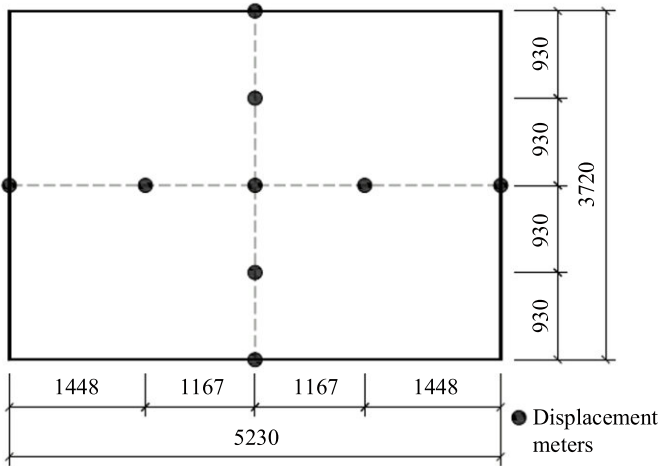


Fig. 9.16 Arrangement of displacement meters (mm)

Fig. 9.23 shows the distribution of cracks on S-2 after the test, where cracks caused by the membrane action can be found both at the center and at the corner of the slab. Fig. 9.24 shows the deflection of S-2. Although the deflection of the unprotected secondary beam was huge, no failure was found on the secondary beam. Fig. 9.25 shows the condition at the bottom of S-2. It was found that the profiled steel deck did not melt down, which helped the slab to integrate after 90 min in a standard fire. Water vapor exuded seriously during the test. Even after the test water vapor continued to exude.

The phenomena of tests S-3 and S-4 were similar to those of S-1 and S-2. Since there was no secondary beam, the concrete began to crack at the boundaries of the

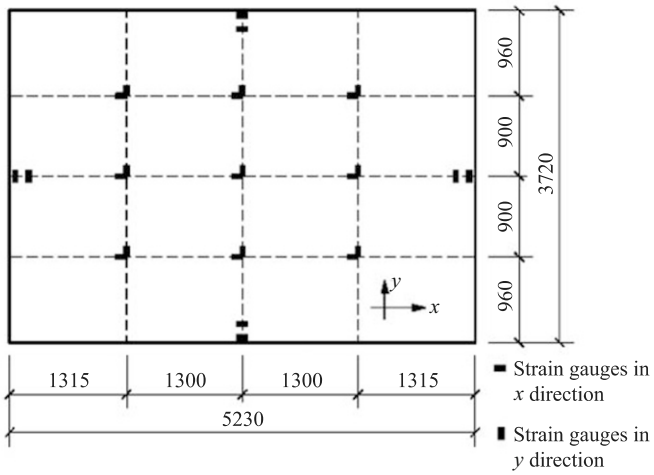


Fig. 9.17 Arrangement of strain gauges for the reinforcement (mm)

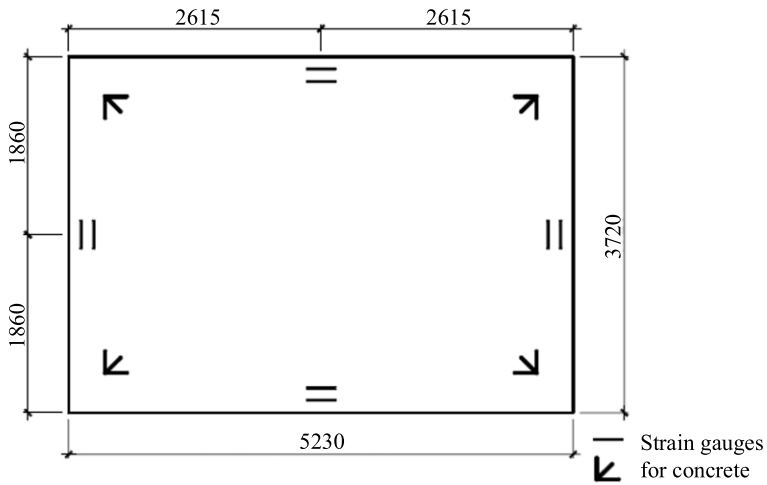


Fig. 9.18 Arrangement of strain gauges for the concrete (mm)



Fig. 9.19 Cracks along the long edge on S-1



Fig. 9.20 Cracks along the short side edge on S-1



Fig. 9.21 Yield lines at the corner on S-1



Fig. 9.22 Deformation of the slab after the test S-1



Fig. 9.23 Cracks on the S-2 after the test



Fig. 9.24 Deformation at the bottom of S-2 after the test

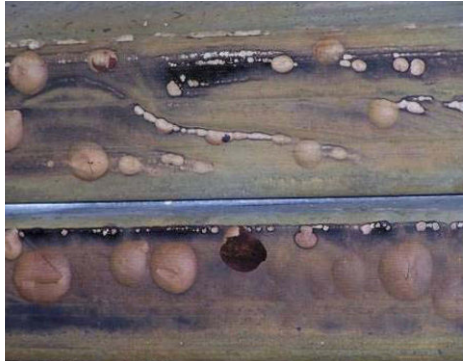


Fig. 9.25 Steel deck after the test

slab in test S-3 and S-4 instead of beside the secondary beam in tests S-1 and S-2. The distribution of cracks on S-3 and S-4 are shown in Fig. 9.26 and Fig. 9.27 respectively. Cracks in the center of S-3 and S-4 were not caused by the negative moment but by the membrane action. No collapse was found in these four tests, which shows that membrane action occurred so as to support the applied load on the slab and to maintain the stability of the floor system.



Fig. 9.26 Cracks on S-3 after the test



Fig. 9.27 Cracks on S-4 after the test

9.2.2.3 Test Results and Analysis

1) Temperature results

Fig. 9.28 shows the fire temperature indicating that the fire temperature coincided well with the ISO834 fire curve. Fig. 9.29 is the temperature in the middle of the slab bottom. After 75 min, the temperature can reach 700 °C or 800 °C. After 90 min to 100 min, the temperature at the slab bottom can be up to around 800 °C or 900 °C. Fig. 9.30 is the temperature in the middle of the slab surface. Fig. 9.31 is the average temperature of the reinforcement. During the whole test, the temperature at the slab surface is very low. After 90 min, the temperature is only around 100 °C.

The distance from the reinforcement to the slab bottom has a great impact to the temperature on the reinforcement.

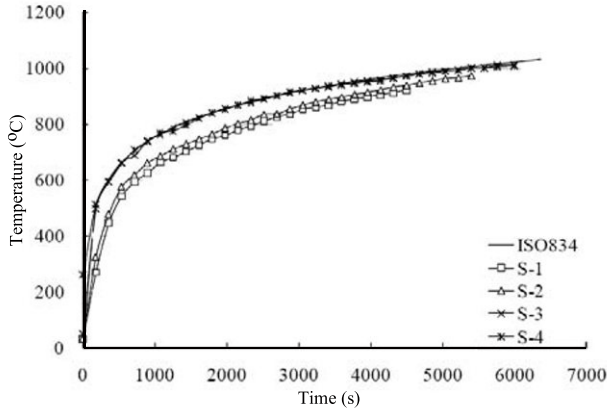


Fig. 9.28 Fire temperatures

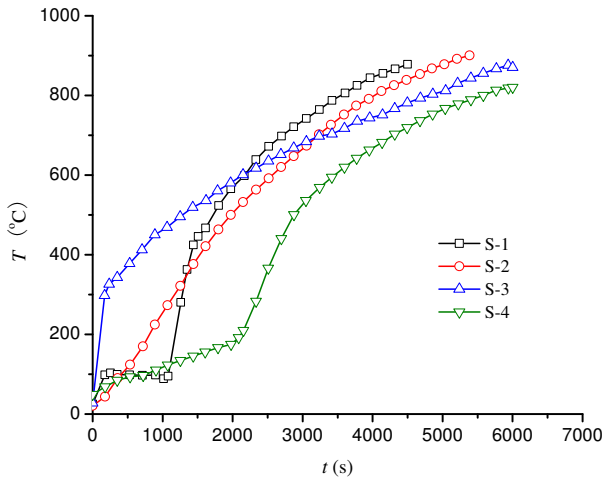


Fig. 9.29 Temperatures at the middle of the slab bottom

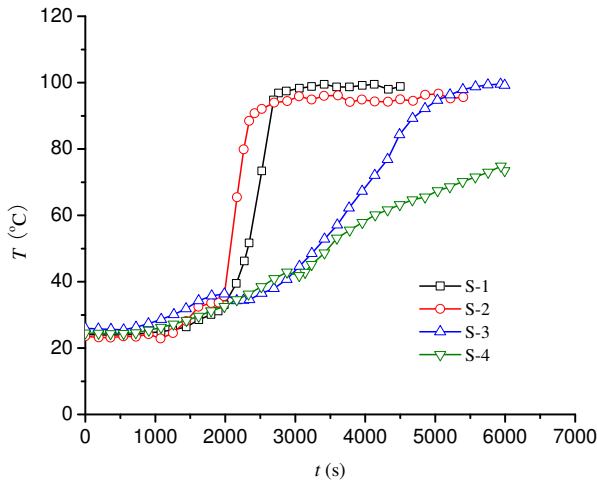


Fig. 9.30 Temperatures at the middle of the slab surface

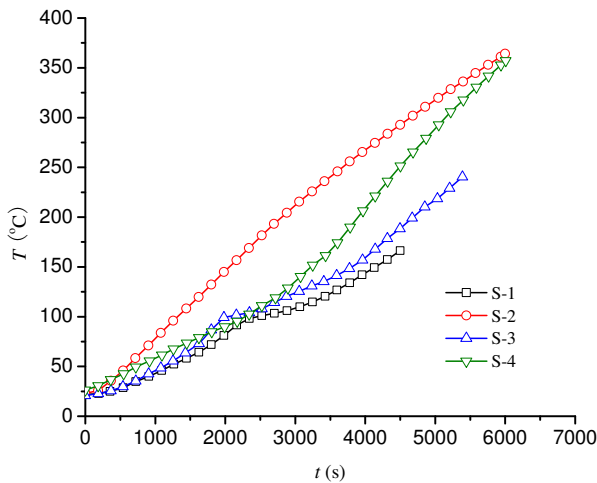


Fig. 9.31 Average temperatures of the reinforcement in test S-1 to S-4

2) Strains of the reinforcement and concrete

Fig. 9.32 and Fig. 9.33 show strains of the reinforcement along the short and long edge of the slab respectively. Since the effective working temperature of a strain gauge is less than 60 °C, the data when the temperature was higher than 60 °C was omitted in the figures. According to the yield line theory, the reinforcement in the slab was located at the compression zone of the slab. However, the data show that the reinforcement was under tension during most of the test period except for the beginning. This phenomenon proves the occurrence of tensile membrane action in the test.

Fig. 9.34 shows concrete strains at the edges of test S-4. In the middle of the edge the concrete was under compression that validates the existence of the concrete compressive ring. Based on the data taken by the strain gauges at the corner of the slab (see Fig. 9.18), compressive strains were found at the corner at an angle between 30° and 60° , which coincides with the failure phenomenon shown in Fig. 9.21.

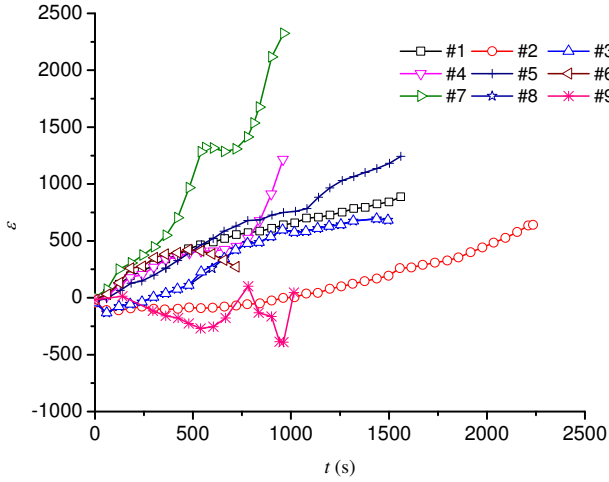


Fig. 9.32 Strains of the reinforcement along the short edge in test S-1

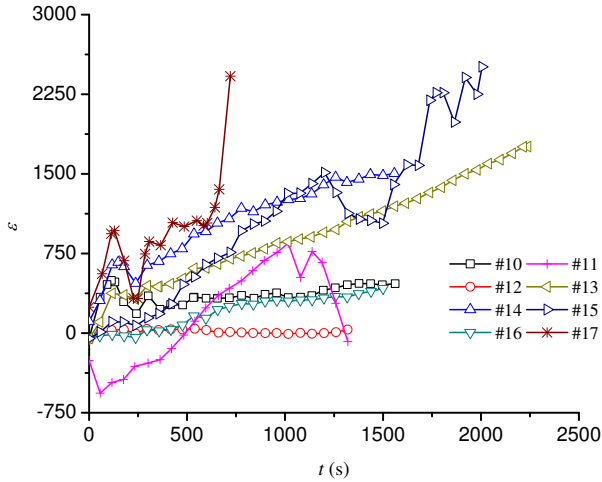


Fig. 9.33 Strains of the reinforcement along the long edge in test S-1

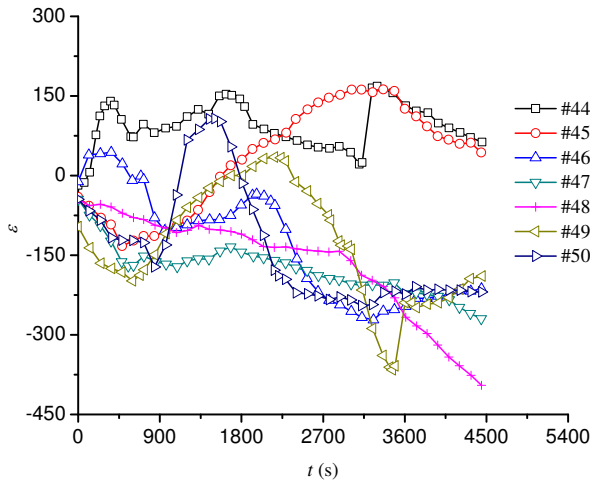


Fig. 9.34 Strains of the concrete at the boundary of test S-4

3) Deflection at the center of the slab

Fig. 9.35 and Fig. 9.36 show deflections at the center of the slab. It is found that the deflection can arrive at $l/25$ where l is the length of the slab short edge. It is reasonable to deduce that the load-bearing mechanism of the slab has been changed from the bending mechanism to the membrane action mechanism in such a large deflection.

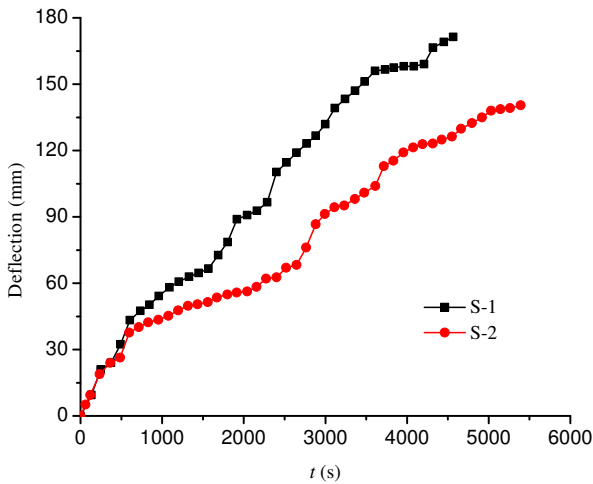


Fig. 9.35 Deflection of test S-1 and S-2

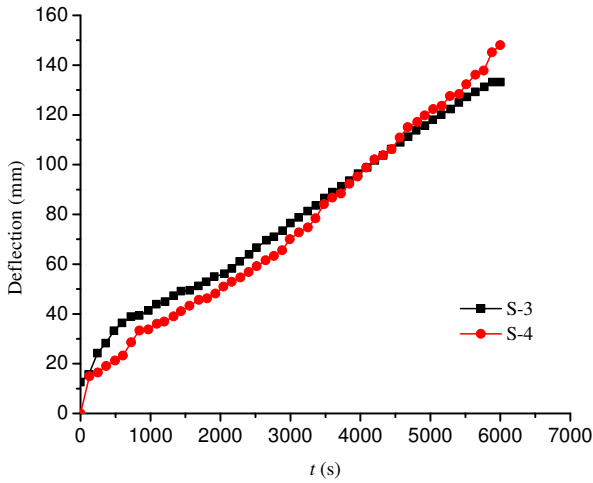


Fig. 9.36 Deflection of test S-3 and S-4

9.2.3 Analysis of the Composite Slab in Consideration of the Membrane Action in a Fire

9.2.3.1 Assumptions

The following assumptions are adopted for analyzing the composite slab when considering the membrane action in a fire

- the slab is a rectangular where the ratio between length and width should not be greater than 2;
- support-beams below the edges of the slab are protected and do not fail in a fire;
- boundaries of the slab are vertically restrained but there are no horizontal and rotational restraints;
- the reinforcement in the slab is continuous and arranged in two orthogonal directions without considering strain hardening;
- at the limit state, the slab deflects in the pattern shown in Fig. 9.11(f). The slab is divided into five parts as shown in Fig. 9.37, where (x_0, y_0) is the intersecting point of the bending yield line and the ellipse, α is the separation angle between the yield line and the long edge of the slab. Plates 1 through 4 shown in Fig. 9.11 are assumed to be rigid and only have a rigid rotational deformation. In the center of the slab, the concrete is cracked and the concrete slab is simplified as a reinforcement mesh. The profile of the reinforcement mesh is supposed to be an elliptic parabolic;
- at the limit state, the force distribution is as shown in Fig. 9.38, where C is the compression force between rigid plates, S is the shear force in the X - Y coordinate plane between rigid plates, T_{xh} and T_{yh} represent the in-plane components tension force of the reinforcement in X direction and Y direction respectively, \otimes and \boxtimes

represent the vertical component force of the reinforcement in X direction and Y direction respectively;

- at the limit state, the final deflection of the slab is as shown in Fig. 9.39, where θ_X , θ_Y are the rotation of the rigid plates about the X and Y axis respectively. The maximum deflection includes d_r and w , where d_r is the deflection caused by the rotation of rigid plates and w is the deflection of the elliptic part;
- the failure criterion of the slab is the fracture of the reinforcement mesh or the crushing of the concrete in the compressive ring.

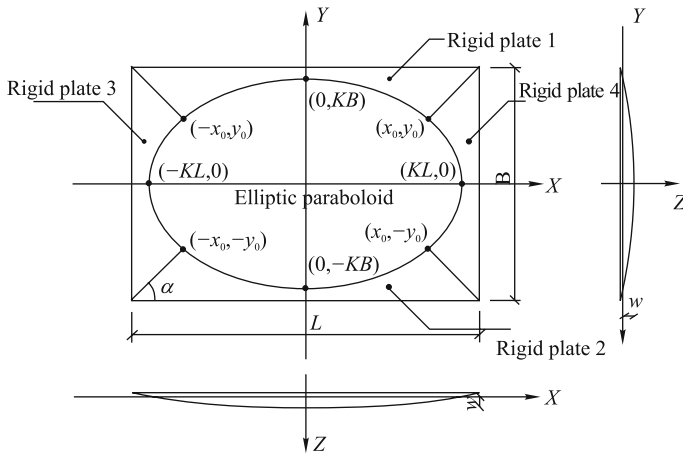


Fig. 9.37 Division and coordinate of the slab at the limit state

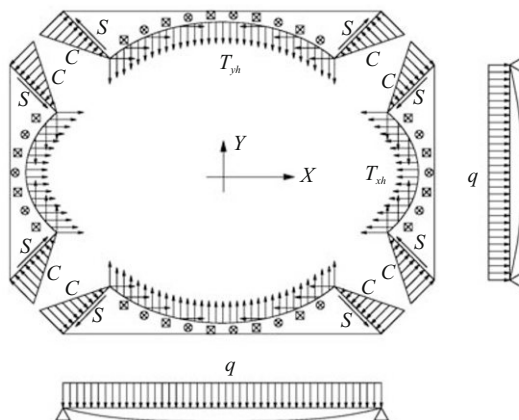


Fig. 9.38 Force distribution in the slab at the limit state

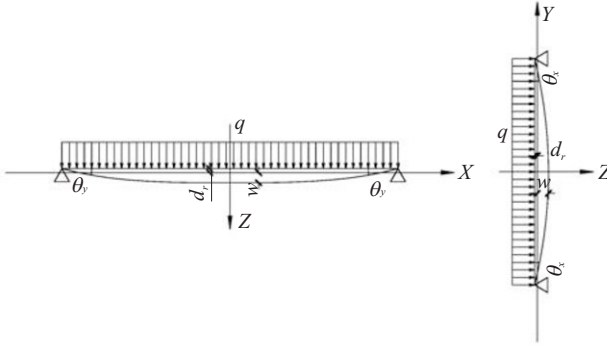


Fig. 9.39 Deflection of the slab at the limit state

9.2.3.2 Determination of Parameters

In the model proposed to simulate the membrane action in a slab, the main parameters include α , (x_0, y_0) , w , d_r , θ_x and θ_y , where α is the angle between the yield line and the long edge of the slab, (x_0, y_0) is the intersecting point of the yield line and the ellipse, w is the deflection of the elliptic part, d_r is the deflection caused by the rotation of the rigid plates, θ_x and θ_y are the rotations of the rigid plates. Determinations of these parameters are presented as follows.

1) Determination of α and (x_0, y_0)

The ultimate deflection of the slab at the limit state is developed from the yield line mechanism. Therefore, α can be determined by the traditional yield line theory^[8]. (x_0, y_0) is the intersecting point of the yield line and the ellipse, which is obtained by using an analytical geometry and given by

$$x_0 = -\frac{(B \tan \alpha - L \tan^2 \alpha)L^2}{2(B^2 + L^2 \tan^2 \alpha)} + \frac{BL\sqrt{-L^2 \tan^2 \alpha - B^2 + 2BL \tan \alpha + 4K^2 B^2 + 4K^2 L^2 \tan^2 \alpha}}{2(B^2 + L^2 \tan^2 \alpha)} \quad (9.4)$$

and

$$y_0 = \left(x_0 - \frac{1}{2}L\right) \tan \alpha + \frac{1}{2}B \quad (9.5)$$

2) Determination of w

It is assumed that the reinforced bar will reach its mechanical strain limit when the ultimate load is reached. The maximum deflection of the elliptic part should be determined by the limited elongation ratio of reinforced bars. At the same level of

deflection in the middle of the slab, the average strain in the reinforcement along the short span of the slab is larger than that along the long span. In this way, the maximum deflection of the slab is governed by the limited elongation of the reinforcement along the short span. According to the analysis by Kemp^[8], w is obtained by using the following equation as

$$w_{total} = w + d_r = KB\sqrt{\frac{3}{8}(\epsilon_{uk} + \alpha_s \Delta T)} + \left(\frac{1}{2}B - KB\right)\theta_x \tag{9.6}$$

where ϵ_{uk} is the characteristic limited elongation of reinforcement which is 2.5% when the diameter of the reinforcement is not greater than 12 mm or 5% when the diameter of the reinforcement is greater than 16 mm^[12], α_s is the average coefficient of thermal expansion of steel which is $1.4 \times 10^{-5}/^\circ\text{C}$, θ_x is the rotation between the rigid plates 1 and 2 and T is the temperature of the slab determined by^[13,14]

$$T = \left[\frac{0.6e^{-\frac{w_2}{w_4}} - 0.1}{h}d + 1 \right] \cdot \left[T_0 + \frac{1}{8}e^{\frac{0.05+0.135t/20-0.005(t/20)^2-d}{0.007+0.0145t/20-0.005(t/20)^3}} \right] \tag{9.7}$$

where t is the heating time, d is the distance between the reinforcement and the bottom of the slab, w_2 and w_4 are sizes of steel deck for the slab as shown in Fig. 9.40.

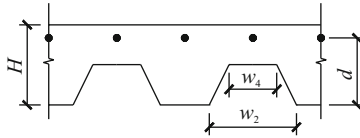


Fig. 9.40 Dimension of the composite slab

3) Determination of θ_x and θ_y

It is supposed that the rigid plate 1, 2 and the tangent of the elliptic compressive ring are continuous on the boundaries. Therefore θ_x is equal to the gradient of the elliptic compressive ring at point $(0, KB)$, and is obtained by the following equation as

$$\theta_x = \left. \frac{\partial z}{\partial y} \right|_{y=KB} = \frac{2w}{KB} \tag{9.8}$$

Based on the deformation compatibility condition of rigid plates 1, 2, 3 and 4 at the points of (x_0, y_0) , $(x_0, -y_0)$, $(-x_0, y_0)$, $(-x_0, -y_0)$, the rotation of plate 3 or plate 4 is determined by

$$\theta_y = \arctan \left(\frac{B/2 - y_0}{L/2 - x_0} \tan \theta_x \right) \tag{9.9}$$

9.2.3.3 Force Equilibrium in the Slab

1) Equivalent force of the reinforcement and concrete

With the temperature increase in the reinforcement and concrete after t minutes fire exposure obtained by Eq.(9.7), the strength of the reinforcement and concrete is obtained using the reduction formulas specified by Bailey et al.^[15]. Tensile forces per unit width in the reinforcement at temperature T in X and Y directions are determined by

$$\begin{aligned} T_{xu} &= f_y T_{,x} A_{sx} \\ T_{yu} &= f_y T_{,y} A_{sy} \end{aligned} \tag{9.10}$$

where A_{sx} and A_{sy} are the area of the reinforcement per unit slab length in X and Y direction respectively, calculated by

$$\begin{aligned} A_{sx} &= \frac{\pi d_x^2 / 4}{D_x} \\ A_{sy} &= \frac{\pi d_y^2 / 4}{D_y} \end{aligned} \tag{9.11}$$

where d_x and d_y are diameters of the reinforced bar in x and y direction respectively, D_x and D_y are the bar spacing in the x and y direction respectively.

2) Component force of the reinforcement

On the boundary of the elliptic-parabolic, the force exerted by the reinforcement is shown in Fig. 9.41.

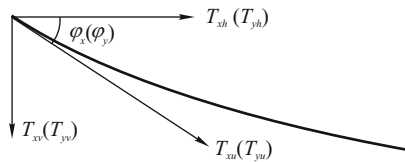


Fig. 9.41 Force component in the reinforced bar

In the y direction, $\tan \phi_y$ equals the gradient at the intersection of the elliptical part and the rigid plate obtained by the following equation as

$$\tan \phi_y = \left. \frac{\partial z}{\partial y} \right|_{z=0} = \frac{2w}{KB} \sqrt{1 - \left(\frac{x}{KL} \right)^2} \tag{9.12}$$

therefore,

$$\begin{aligned} \sin \phi_y &= \frac{2w\sqrt{1 - \left(\frac{x}{KL}\right)^2}}{\sqrt{(KB)^2 + 4w^2 \left[1 - \left(\frac{x}{KL}\right)^2\right]}} \\ \cos \phi_y &= \frac{KB}{\sqrt{(KB)^2 + 4w^2 \left[1 - \left(\frac{x}{KL}\right)^2\right]}} \end{aligned} \quad (9.13)$$

So the horizontal and vertical component forces in the reinforcement in the y direction are obtained by

$$\begin{aligned} T_{yh(x)} &= T_{yu} \frac{KB}{\sqrt{(KB)^2 + 4w^2 \left[1 - \left(\frac{x}{KL}\right)^2\right]}} \\ T_{yv(x)} &= T_{yu} \frac{2w\sqrt{1 - \left(\frac{x}{KL}\right)^2}}{\sqrt{(KB)^2 + 4w^2 \left[1 - \left(\frac{x}{KL}\right)^2\right]}} \end{aligned} \quad (9.14)$$

Similarly for the reinforcement in the x direction, the horizontal and vertical component forces in the reinforcement are given by

$$\begin{aligned} T_{xh(y)} &= T_{xu} \frac{KL}{\sqrt{(KL)^2 + 4w^2 \left[1 - \left(\frac{y}{KB}\right)^2\right]}} \\ T_{xv(y)} &= T_{xu} \frac{2w\sqrt{1 - \left(\frac{y}{KB}\right)^2}}{\sqrt{(KL)^2 + 4w^2 \left[1 - \left(\frac{y}{KB}\right)^2\right]}} \end{aligned} \quad (9.15)$$

3) Force equilibrium

At the limit state, the membrane force in each rigid plate is shown in Fig. 9.42. The force equilibrium in the x and y direction is expressed as

$$\begin{cases} C \cos \alpha + S \sin \alpha = \int_0^{x_0} T_{yh(x)} dx \\ C \sin \alpha - S \cos \alpha = \int_0^{y_0} T_{xh(y)} dy \end{cases} \quad (9.16)$$

which leads to

$$\begin{cases} S = \sin \alpha \int_0^{x_0} T_{yh(x)} dx - \cos \alpha \int_0^{y_0} T_{xh(y)} dy \\ C = \frac{\int_0^{x_0} T_{yh(x)} dx - 2S \sin \alpha}{\cos \alpha} \end{cases} \quad (9.17)$$

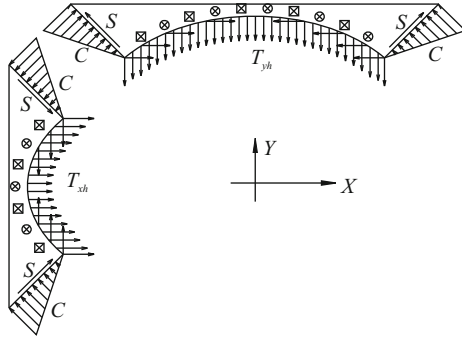


Fig. 9.42 Membrane forces in rigid plates 1 and 3

4) Bending moment equilibrium

At the limit state, the force diagram of each rigid plate is shown in Fig. 9.43, where q_{12} is the loading capacity of plate 1 and plate 2, and q_{34} is the loading capacity of plate 3 and plate 4. Bending moment equilibriums about axis O' and O are expressed as

$$\left\{ \begin{array}{l} M_{q_{12}} + M_{T_{vx}} + M_{T_{hx}} - 2C \cos \alpha \left[h_{0x} - \frac{1}{3} \left(\frac{1}{2}B - y_0 \right) \theta_x \right] \\ \quad - 2S \sin \alpha \left[h_{0x} - \frac{1}{2} \left(\frac{1}{2}B - y_0 \right) \theta_x \right] - M_{xu} = 0 \\ M_{q_{34}} + M_{T_{vy}} + M_{T_{hy}} - 2C \sin \alpha \left[h_{0y} - \frac{1}{3} \left(\frac{1}{2}L - x_0 \right) \theta_y \right] \\ \quad - 2S \cos \alpha \left[h_{0y} - \frac{1}{2} \left(\frac{1}{2}L - x_0 \right) \theta_y \right] - M_{yu} = 0 \end{array} \right. \quad (9.18)$$

Values of $M_{q_{12}}$, $M_{T_{hx}}$, $M_{T_{vx}}$, $M_{q_{34}}$, $M_{T_{hy}}$, $M_{T_{vy}}$, M_{ux} and M_{uy} are determined by

$$\left\{ \begin{array}{l} M_{q_{12}} = q_{12}A_{12}d_x \\ M_{T_{hx}} = 2 \int_0^{x_0} T_{yh} \left[h_{0x} - \left(\frac{1}{2}B - y_0 \right) \theta_x \right] dx \\ M_{T_{vx}} = 2 \int_0^{x_0} T_{yv} \left[\frac{1}{2}B - KB \sqrt{1 - \left(\frac{x}{KL} \right)^2} \right] dx \\ \quad + 2 \int_{y_0}^{KB} T_{xv} \left(\frac{1}{2}B - y \right) dy \\ M_{ux} = A_{sx}f_{yT,x} \left(h_{cx} - 0.59A_{sx} \frac{f_{yT,x}}{f_{cT}} \right) (L - 2x_0) \end{array} \right. \quad (9.19)$$

$$\begin{cases} M_{q_{34}} = q_{34}A_{34}d_y \\ M_{Thy} = 2 \int_0^{y_0} T_{xh} \left[h_{0y} - \left(\frac{1}{2}L - y_0 \right) \theta_y \right] dy \\ M_{T_{vy}} = 2 \int_0^{y_0} T_{xv} \left[\frac{1}{2}L - KL \sqrt{1 - \left(\frac{y}{KB} \right)^2} \right] dy \\ \quad + 2 \int_{x_0}^{KL} T_{yv} \left(\frac{1}{2}L - x \right) dx \\ M_{uy} = A_{sy} f_y T_{xy} \left(h_{cy} - 0.59 A_{sy} \frac{f_y T_{xy}}{f_c T} \right) (BL - 2y_0) \end{cases} \quad (9.20)$$

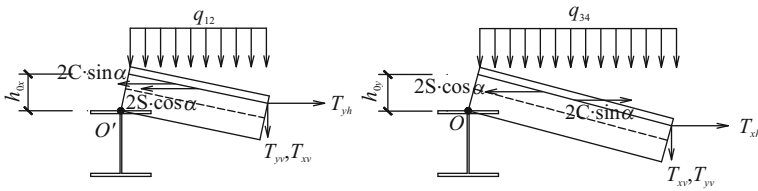


Fig. 9.43 Forces applied on rigid plate 1 and plate 3

9.2.3.4 Ultimate Load Capacity of the Composite Slab

The load bearing capacity of the elliptical part contributed by the vertical component force of the reinforcement in the elliptical compressive ring is obtained by

$$q_e = 4 \frac{\int_0^{KL} T_{yv(x)} dx + \int_0^{KB} T_{xv(y)} dy}{\pi(KL)(KB)} \quad (9.21)$$

By making the average load capacity of the four rigid plates equal the load capacity of the elliptical compressive ring, the following equation is obtained as

$$q_e = \frac{q_{12}A_{12} + q_{34}A_{34}}{A_{12} + A_{34}} \quad (9.22)$$

where q_{12} , q_{34} and K can be determined by solving the Eq.(9.18), Eq.(9.21) and Eq.(9.22). Through averaging the load capacities of the rigid plates and the elliptical part over the whole area of the slab, the ultimate load capacity of the composite slab is determined by

$$q = \frac{2q_{12}A_{12} + 2q_{34}A_{34} + 4 \int_0^{KL} T_{yv(x)} dx + \int_0^{KB} T_{xv(y)} dy}{LB} \quad (9.23)$$

9.2.3.5 Strength of the Concrete Compressive Ring

It is possible that the concrete compressive ring is crushed before the fracture of the reinforcement in the slab, exerting a membrane action to resist the fire. The strength of the concrete compressive ring should be checked to insure that the membrane action works. At the limit state, the stress in the concrete compressive ring at the section A-A or B-B will reach the ultimate compressive strength of the concrete as shown in Fig. 9.44. The force equilibrium in the concrete compressive ring is expressed as

$$\int_0^{K_y B} T_{T_{yh}(y)} dy = \left(\frac{1}{2} - K_x\right) B h_c f_{cT} \quad (9.24)$$

$$\int_0^{K_x L} T_{T_{yh}(x)} dx = \left(\frac{1}{2} - K_y\right) L h_c f_{cT}$$

K_x and K_y can be obtained by solving Eq.(9.24). If K_x or K_y is smaller than K , the concrete compressive ring will be crushed earlier than the reinforcement. Take the smaller of K_x and K_y to substitute K in Eq.(9.18), Eq.(9.21), Eq.(9.22) and Eq.(9.23). The ultimate load capacity of the slab in fire conditions is obtained.

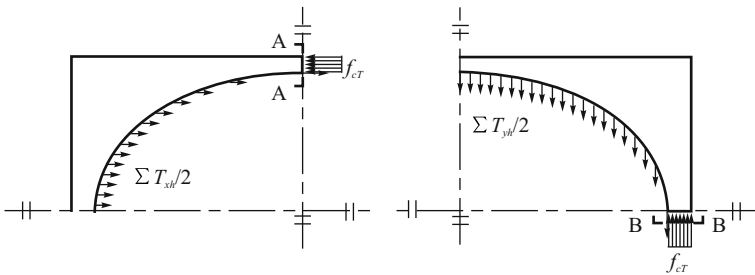


Fig. 9.44 Force distribution over the concrete compressive ring at the limit state

9.2.3.6 Verification

The method for modeling the membrane action for fire-resistance of a composite slab is verified by tests. The main data for the slabs tested are given in Table 9.8. Maximum deflections of the slab measured in the test and predicted by various methods are compared in Table 9.9. Applied ultimate loads and loads capacities predicted are compared in Table 9.10.

Tests 1–7 were performed at ambient temperature and Test 8 and Test 9 were performed at high temperatures. Because the limited elongation of the reinforcement at high temperature is larger than that at ambient temperature, the value of characteristic limited elongation of the reinforcement in tests 1–7 has been reduced by 30% based on statistical regression analysis.

Table 9.8 Parameters of test slabs

No.	Reinforce- ment	Slab size (m×m)	h_0 (mm)	f_y (N/mm ²)	w (mm)	q (kN/m ²)
1	φ3@30	1.6×1.1	26	263	127	45.13
2	φ3@60	2.0×1.0	26	263	76	17.14
3	φ4.8@76.2	1.829×1.829	43.6	376	81	42.9
4	φ4.8@63.5	1.829×1.829	37.3	376	98	39.03
5	φ4.8@122	1.829×1.829	69	376	84	38.13
6	φ6.36@120	2.745×1.829	68.2	450	106	45.5
7	φ6.35@120	1.829×1.829	67.8	450	100	75
8	φ6@200	9.98×7.57		460	390	5.48
9	φ4@150	3×2	76	300	130	10

h_0 is the effectiveness depth of the slab; f_y is the yield strength of the reinforcement at ambient temperature; w is the recorded maximum deflection in the fire test; and q is the applied load in the test

Table 9.9 Comparison of maximum deflections between measured and predicted

No.	w_{test} (mm)	w^* (mm)	w^{**} (mm)	w_{cal} (mm)	$\frac{w^*}{w_{test}}$	$\frac{w^{**}}{w_{test}}$	$\frac{w_{cal}}{w_{test}}$
1	127	25	43	58.6	0.356	0.339	0.461
2	76	31	36	55	0.187	0.474	0.724
3	81	33.5	72	95.9	0.435	0.889	1.184
4	98	33.5	72	92.8	0.409	0.735	0.947
5	84	33.5	72	103.8	0.372	0.857	1.236
6	106			95.1			0.897
7	100			93.6			0.936
8	390			450.2			1.154
9	90			127			1.4

* is the deflection predicted by Bailey et al. [15]; ** is the deflection predicted by Li et al. [4]

Table 9.10 Comparison of the applied load and predicted

No.	q_{test} (kN/m ²)	q^* (kN/m ²)	q^{**} (kN/m ²)	q_{cal} (kN/m ²)	$\frac{q^*}{q_{test}}$	$\frac{q^{**}}{q_{test}}$	$\frac{q_{cal}}{q_{test}}$
1	45.13	45.24	44.18	34.4	1.002	0.979	0.762
2	17.14	14.21	14.63	17.85	0.829	0.854	1.041
3	42.9	35.27	33.60	41.18	0.822	0.783	0.960
4	39.03	40.03	35.51	48.75	1.026	0.910	1.249
5	38.13	31.22	31.22	31.18	0.819	0.819	0.818
6	45.5			41.89			0.897
7	75			58.3			0.735
8	5.48			5.318			0.970
9	10			7.13			0.713

* is the load predicted by Bailey et al. ^[15]; ** is the load predicted by Li et al. ^[4]

According to the comparison, the method proposed gives a more reasonable prediction to the maximum deflection and load-bearing capacity of a composite slab exposed to a fire.

References

- [1] A. D. Weller. *Broadgate phase 8: Fire, 22 June 1990. Summary Report of Damage and Repair*. Building Research Establishment PD 21/92, 1992.
- [2] C. G. Bailey, T. Lennon, and D. B. Moore. The behaviour of full-scale steel framed buildings subjected to compartment fires. *The Structural Engineer*, 77(8):15–21, 1999.
- [3] S. C. Jiang. *Theory and Experimental Studies on Fire Resistance of Steel Concrete Composite Slabs*. PhD thesis, Tongji University, 2001.
- [4] S.C. Jiang, G. Q. Li, H. Y. Zhou, and Q. Wang. Experimental study of behavior of steel-concrete composite slabs subjected to fire. *Journals of Building Structures*, 25(3), 2004.
- [5] S. C. Jiang, G. Q. Li, G. B. Lou, and Y. J. Sun. Numerical approach of behavior of steel-concrete composite slabs subjected to fire. *Journals of Building Structures*, 25(3), 2004.
- [6] International Organization for Standardization. *Fire-Resistance Tests – Elements of Building Construction, Part 1: General Requirements*. International Organization for Standardization, 1999.
- [7] G. Q. Li, Y. Y. Zhi, and S. C. Jiang. Analysis of the temperature distribution in composite slabs subjected to fires. *Industrial Construction*, 29(12), 1999.
- [8] K. O. Kemp. Yield of a square reinforced concrete slab on simple supports, allowing for membrane forces. *The Structural Engineer*, 45(7):235–240, 1967.
- [9] Y. C. Wang. *Tensile membrane action and fire resistance of steel framed buildings*. Proceedings of the 5th international symposium on fire safety science, Melbourne, Australia, 1997.
- [10] A. S. Usmani, J. M. Rotter, S. Lamont, A. M. Sanad, and M. Gillie. Fundamental principles of structural behaviour under thermal effects. *Fire Safety Journal*, 36(8):721–744, 2001.
- [11] M. Gillie, A. S. Usmani, Rotter, J. M., and M. O'Connor. Modeling of heated composite floor slabs with reference to the cardington experiments. *Fire Safety Journal*, 36(8):745–767, 2001.
- [12] M. Gillie, A. S. Usmani, and J. M. Rotter. Bending and membrane action in concrete slabs. fire and materials. *Fire and Materials*, 28:139–157, 2004.
- [13] C. G. Bailey and D. B. Moore. The structural behaviour of steel frames with composite floor slabs subjected to fire, part 1: Theory. *The Structural Engineer*, 78(11):19–27, 2000.
- [14] C. G. Bailey and D. B. Moore. The structural behaviour of steel frames with composite floor slabs subjected to fire, part 1: Design. *The Structural Engineer*, 78(11):28–33, 2000.
- [15] C. G. Bailey, D. S. White, and D. B. Moore. The tensile membrane action of unrestrained composite slabs simulated under fire conditions. *Engineering Structures*, 22(12):585–595, 2000.
- [16] C. G. Bailey. Membrane action of unrestrained lightly reinforced concrete slabs at large displacements. *Engineering Structures*, 23(5):470–483, 2001.

- [17] Z. H. Huang, I. W. Burgess, and R. J. Plank. Modeling membrane action of concrete slabs in composite buildings in fire. i: Theoretical development. *Journal of Structural Engineering*, 129(8):1093–1102, 2003.
- [18] Z. H. Huang, I. W. Burgess, and R. J. Plank. Modeling membrane action of concrete slabs in composite buildings in fire. ii: Validations. *Journal of Structural Engineering*, 129(8):1103–1112, 2003.
- [19] G. Q. Li, S. X. Guo, and H. S. Zhou. Modeling of membrane action in floor slabs subjected to fire. *Engineering Structures*, 29(6):880–887, 2007.
- [20] R. H. Wood. *Plastic and Elastic Design of Slabs and Plates*. Thames and Hudson, London, 1961.
- [21] J.P. Boutin. *Pratique du calcul de la résistance au feu des structures en béton*. Eyrolles, 1983.
- [22] N. S. Zhang. *Analysis of Practical Fire Resistant Design for Floor Slabs*. Master thesis, Tongji University, 2008.
- [23] N. S. Zhang and G. Q. Li. Experimental study on membrane action effects of composite slab in fire. *China Civil Engineering Journal*, (3), 2010.
- [24] Ministry of Housing and Urban-Rural Development of China. *Code for Design of Steel Structures (GB50017-2003)*. China Plan Press, 2003.
- [25] Central Research Institute of Building and Ministry of Metallurgical Industry Construction. *Code for Design and Construction of Steel Concrete Composite Floor Slab*. Ministry of Metallurgical Industry, 1992.

Analysis of Steel Moment-Resistant Frames Subjected to a Fire

Because of the size limitation of a furnace, the fire resistant test is usually carried out on a member or substructure with simplified boundary conditions^[1]. Test results do not readily represent the fire resistance of a structure in a real fire. On the other hand, costs and technical restraints also make it unfeasible to carry out fire tests on the full scale complete structure. Establishing analytical approaches for predicating the behavior of a steel construction in a fire have been the effort of many researchers.

Owing to its ability to include various factors (e.g. material and geometrical non-linearity, non-uniform distribution of temperature) that affect the behavior of a structure in a fire, the finite element method is the most general and versatile approach. However in previous research the cross section of an element was divided into many segments with uniform temperature and homogeneous material properties. The elemental stiffness was then obtained by integrating the contribution of each segment at each temperature step^[2,3,4,5,6]. Theoretically, this approach can be applied to any steel construction with an arbitrary temperature distribution. Nevertheless, this approach is not convenient for engineering practice due to the considerable time required for input data preparation and computation. The more practical element needs to be developed.

The tangent stiffness matrix for an element at high temperature is developed introducing the generalized Clough model^[7]. The similarity between the form of the elemental stiffness matrix at elevated temperature and that at normal temperature brings much convenience to its application to practical designs. It is also consistent with design methods adopted by many fire-resistant codes^[8,9] for a single member, for the fire resistant design of a single member is based on the format of the design method at normal temperature. In the proposed approach, the temperature-dependent material nonlinearity as well as the geometrical nonlinearity on elemental stiffness is considered and the effect of thermal strain is converted to equivalent thermal loads acting on the structure. In order to investigate behavior of a steel frame subjected to a fire and validate the proposed approach, fire resistant tests on two single-storey two-bay steel frames were carried out at Tongji University. The main results are presented below.

10.1 Element for Analysis

The effective yield strength and Young's modulus of steel at elevated temperatures adopt the recommendation by ECCS^[10]. The creep of steel is considered implicitly in the material model. For convenience of analysis, the following hypotheses are employed

- the stress-strain relationship of steel at high temperature is bi-linear as shown in Fig. 10.1;
- the plastic deformation is concentrated at element nodes;
- the temperature varies linearly within the element cross section and the temperature profile is identical along the element length;
- only H-shaped and box-shaped cross sections are considered.

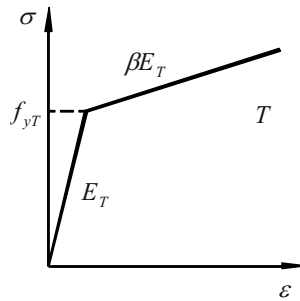


Fig. 10.1 Stress-strain relationship of the steel at high temperature

10.1.1 Properties of the Elemental Cross-Section

In a real fire the temperature distribution in a steel member is non-uniform, especially when part of it is in contact with heat sink material. The cross section of a structural member with non-uniform temperature profile is converted to an equivalent section with uniform temperature distribution, as shown in Fig. 10.2 and Fig. 10.3, on the basis of the same geometrical and physical properties. Noticing that the web of the H-shaped cross section (the side walls of the box-shaped cross section may be considered to be equivalent to the web of the H-shaped section) contributes very little to the inertia moment and the moment resistance of the section, it is in practice reasonable to assume that the width of the web in the equivalent section varies linearly. Then, the following formula is derived to calculate the geometrical and physical properties of the elemental cross-section.

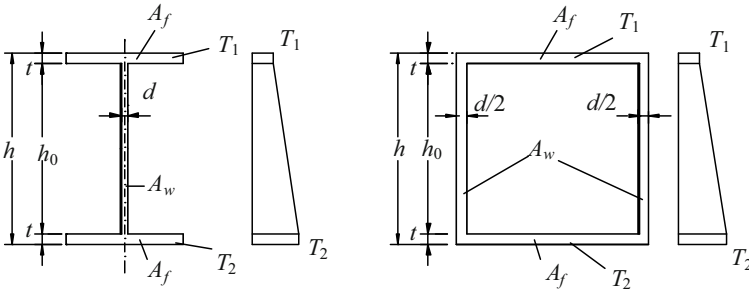


Fig. 10.2 Dimension and temperature profile of an elemental cross-section

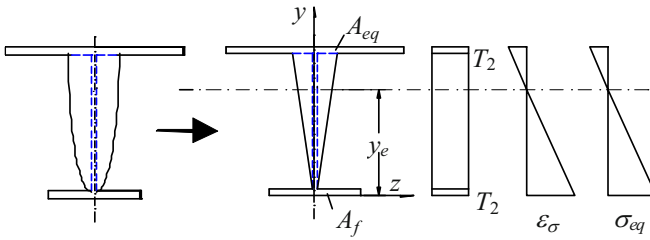


Fig. 10.3 Equivalent cross section in an elastic state

10.1.2 Location of the Neutral Axis in an Elastic State

The location of the neutral axis in elastic state is calculated by

$$y_e = \frac{u_e A_f h + (1 - u_e) A_f t / 2 + (1 + u_e) A_w t / 2 + (1 + 2u_e) A_w h_0 / 2}{(1 + u_e) (2A_f + A_w) / 2} \quad (10.1)$$

where

$$u_e = \frac{E_{T_1}}{E_{T_2}} \quad (10.2)$$

The symbols are shown in Fig. 10.3.

10.1.3 Equivalent Axial Stiffness

The equivalent axial stiffness is

$$(EA)_{eq} = E_{T_2} A_{eq} \quad (10.3)$$

where A_{eq} is the equivalent area of the cross-section obtained by

$$A_{eq} = (1 + u_e) (2A_f + A_w) / 2 \quad (10.4)$$

10.1.4 Equivalent Bending Stiffness in an Elastic State

The equivalent bending stiffness in an elastic state is

$$(EI)_{eq} = E T_2 I_{eq} \tag{10.5}$$

where I_{eq} is the equivalent moment of inertia calculated through

$$I_{eq} = \frac{1}{12} (1 + u_e) A_f t^2 + A_f (y_e - \frac{t}{2})^2 + A_f u_e (h - y_e - \frac{t}{2})^2 + \frac{(u_e^2 + 4u_e + 1) d h_0^3}{36(1 + u_e)} + \frac{1}{2} (1 + u_e) A_w (y_e - \frac{2u_e + 1}{3(1 + u_3)} h_0)^2 \tag{10.6}$$

10.1.5 Initial Yielding Moment

As shown in Fig. 10.4, the bending moment when the edge fiber reaching the yielding point is

$$M_s = \frac{f_y T_2 I_{eq}}{y_{max}} \tag{10.7}$$

and

$$y_{max} = \max\{y_e, h - y_e\} \tag{10.8}$$

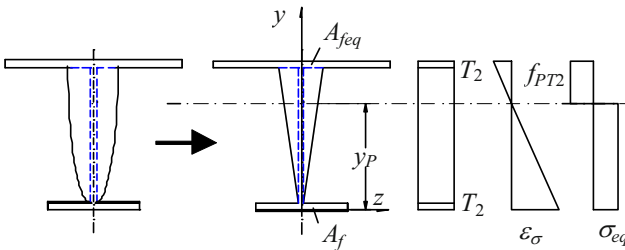


Fig. 10.4 Equivalent cross section in plastic state

10.1.6 Location of the Neutral Axis in Total Plastic State

According to Fig. 10.4, the location of the neutral axis in a total plastic state is calculated by

(1) for $u_p \neq 1$

$$y_p = \frac{1}{2\zeta} \left\{ 4(\zeta t - d)^2 - 4\zeta[(h_0 + 2t)(\zeta t - d) - (h_0^2 + 2t + 2h_0 t)/2 - (u_p - 1)A_f] \right\}^{1/2} + \frac{\zeta t - d}{\zeta} \tag{10.9}$$

and (2) for $u_p = 1$

$$y_p = \frac{h_0}{2} + t \tag{10.10}$$

where

$$u_p = \frac{f_y T_1}{f_y T_2}; \zeta = \frac{u_p - 1}{h_0} d$$

10.1.7 Plastic Moment

The plastic moment is obtained by

$$M_p = f_y T_2 [(y_p - t/2)A_f + (h - y_p - t/2)A_f u_p + (d_0 + 2d)(y_p - t)/6 + (d_0 + 2u_p d)(h - y_p - t)^2/6] \tag{10.11}$$

where

$$d_0 = \frac{(y_p - t)(u_p - 1)d + dh_0}{d_0} \tag{10.12}$$

10.1.8 Stiffness of Element

Fig. 10.5 shows the force $\{f\}$ and displacement $\{\delta\}$ of an element and Fig. 10.6 shows the nonlinear moment-curvature relationship of the elemental cross-section with strain hardening involved.

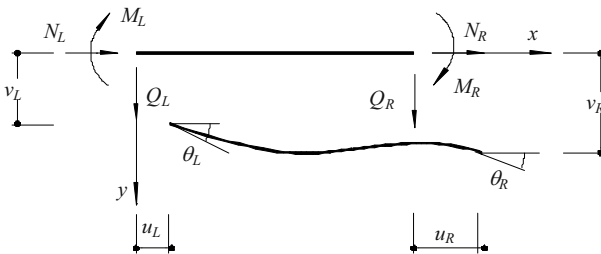


Fig. 10.5 Elemental forces and displacements

Based the philosophy of the generalized Clough model^{[10][11]}, an element is assumed to be composed of three sub-elements with different boundary conditions (see Fig. 10.7) and the incremental stiffness equation of the element is obtained by

$$\{df\} = [K_T][d\delta] \tag{10.13}$$

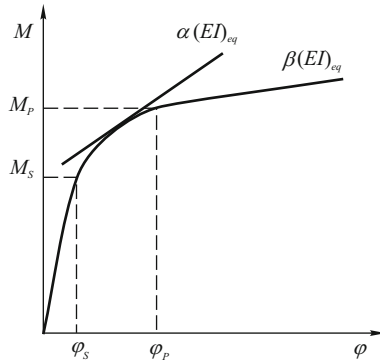


Fig. 10.6 Moment-curvature relation

and

$$[K_T] = \begin{cases} \alpha_R([K_0] + [K_{G0}]) + (\alpha_L - \alpha_R)([K_2] + [K_{G2}]) \\ \quad + (1 - \alpha_L)([K_3] + [K_{G3}]), & \alpha_L \geq \alpha_R \\ \alpha_L([K_0] + [K_{G0}]) + (\alpha_R - \alpha_L)([K_2] + [K_{G2}]) \\ \quad + (1 - \alpha_R)([K_3] + [K_{G3}]), & \alpha_L < \alpha_R \end{cases} \quad (10.14)$$

where $\{df\}$ and $\{d\delta\}$ are the incremental force vector and incremental displacement vector respectively, $[K_0]$, $[K_1]$, $[K_2]$ and $[K_3]$ are the elastic stiffness matrices of the element with both ends in an elastic state, the left end in an elastic state and the right end in elasto-plastic state, the left end in an elasto-plastic state and the right end in elastic state and both ends in an elasto-plastic state respectively, which are expressed in Appendix B and obtained by using the equivalent axial and bending stiffness determined by Eq.(10.3) and Eq.(10.5). $[K_{G0}]$, $[K_{G1}]$, $[K_{G2}]$ and $[K_{G3}]$ are the geometrical stiffness matrices of the element with corresponding end elasto-plastic conditions for $[K_0]$, $[K_1]$, $[K_2]$ and $[K_3]$ respectively, which are also expressed in Appendix B. α_R and α_L are the coefficients indicating the deformation state of the two ends of the element, which can be determined according to values of the bending moment at the elemental ends as

$$\alpha = \begin{cases} 1, & M \leq M_s \\ \frac{1}{1 + \left(\frac{M - M_s}{M_p - M_s}\right)^m \left(\frac{1}{\beta} - 1\right)}, & M_s < M \leq M_p \\ \beta, & M > M_p \end{cases} \quad (10.15)$$

where

$$m = 7.8 \left(1 - \frac{M_s}{M_p}\right) - 1$$

M_s and M_p are the initial yielding moment and plastic moment respectively (Fig. 10.6) determined by Eq.(10.7), Eq.(10.10) and Eq.(10.11). β is the strain hardening factor of steel.

10.2 Thermal Force of Element

When the thermal expansion of the element is restrained, there will be an additional axial load and bending moment (thermal forces) induced in the element. The thermal forces in an element transfer to those elements that constrain it. Thus, effects of thermal expansion in a structure are treated as thermal loads acting on the structure. Based on the generalized Clough model (see Fig. 10.7 and Fig. 10.8), the thermal loads induced by the elevation of temperature in an element are expressed as

$$\{P_T\} = \begin{Bmatrix} N_L \\ Q_L \\ M_L \\ N_R \\ Q_R \\ M_R \end{Bmatrix} \quad (10.16)$$

and

$$\begin{aligned} N_L &= -(EA)_{eq} \alpha \Delta T_2 \\ Q_L &= -3(\alpha_L - \alpha_R)(EI)_{eq} \frac{\alpha(\Delta T_1 - \Delta T_2)}{2hl} \\ M_L &= \begin{cases} -\frac{3\alpha_L - \alpha_R}{2h}(EI)_{eq} \alpha(\Delta T_2 - \Delta T_1), & \text{when } \alpha_L \geq \alpha_R \\ -\frac{\alpha_L}{2h}(EI)_{eq} \alpha(\Delta T_2 - \Delta T_1) & , \text{when } \alpha_L < \alpha_R \end{cases} \\ N_R &= (EA)_{eq} \alpha \Delta T_2 \\ Q_R &= 3(\alpha_L - \alpha_R)(EI)_{eq} \frac{\alpha(\Delta T_1 - \Delta T_2)}{2hl} \\ M_R &= \begin{cases} \frac{\alpha_R}{h}(EI)_{eq} \alpha(\Delta T_2 - \Delta T_1) & , \text{when } \alpha_L \geq \alpha_R \\ \frac{3\alpha_R - \alpha_L}{h}(EI)_{eq} \alpha(\Delta T_2 - \Delta T_1) & , \text{when } \alpha_L < \alpha_R \end{cases} \end{aligned} \quad (10.17)$$

where ΔT_1 is the temperature increment in the top flange and ΔT_2 is the temperature increment in the bottom flange.

10.3 Structural Analysis

When the temperature in the structure increases, the balance between internal and external forces will be broken due to the degradation in structural stiffness and thermal expansion. Further displacement of the structure will take place to equilibrate the unbalanced forces and a new balanced state will be established (Fig. 10.9).

Thus a step by step Newton-Raphson procedure is adopted to predicate the response of a structure subjected to elevated temperatures. This is briefly described as follows:

- (1) update the geometrical and physical properties of all elements when the temperature of the structure is increased from $\{T_{i-1}\}$ to $\{T_i\}$;

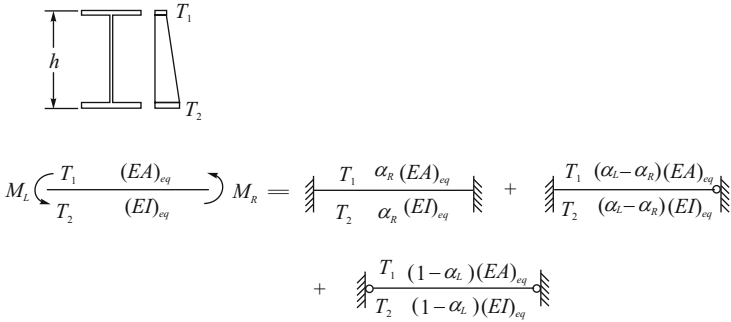


Fig. 10.7 Philosophy of the generalized Clough model ($\alpha_L \geq \alpha_R$)

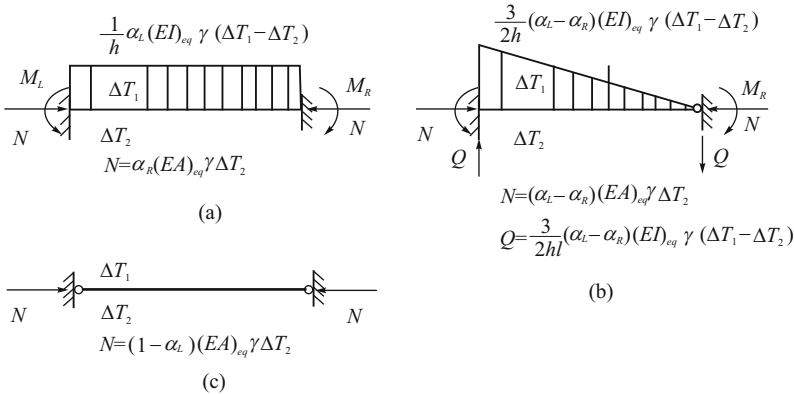


Fig. 10.8 Thermal forces induced in an element with different boundary conditions ($\alpha_L \geq \alpha_R$). (a) The element with fix-fix ends; (b) The element with fix-pin ends; (c) The element with pin-pin ends

- (2) calculate the thermal load vector of each element $\{P_{T_i}\}^e$ due to the temperature increment $\{\Delta T\} = \{T_i\} - \{T_{i-1}\}$, and thermal load vector of the structure at nodes $\{P_{T_i}\}$;
- (3) calculate the unbalanced nodal forces through

$$\{\Delta R\} = \{P\} - \{F_{i-1}\} + \{P_{T_i}\} \tag{10.18}$$

where $\{P\}$ is the nodal external load vector, $\{F_{i-1}\}$ is the resultant of the internal force $\{F_{i-1}\}^e$ at the temperature $\{T_i\}$ corresponding to the elastic displacement $\{\delta_{i-1}\}_e^e$ at temperature $\{T_{i-1}\}$, $\{F_{i-1}\}^e$ is the element force at temperature $\{T_i\}$ corresponding to the elastic displacements $\{\delta_{i-1}\}_e^e$ and

$$\{F_{i-1}\}^e = [K_{T_i}]_e^e \{\delta_{i-1}\}_e^e + \{F_G\}^e \tag{10.19}$$

$[K_{T_i}]_e^e$ is the elastic stiffness matrix of the both ends fixed element at temperature $\{T_i\}$, $\{\delta_{i-1}\}_e^e$ is the elastic displacement of the elements at temperature $\{T_{i-1}\}$,

- (5) calculate the increment in the elemental elastic displacement $\{\delta_i\}_e^e$ corresponding to the incremental elemental force $\{\Delta F_i\}_e^e$ by

$$\{\Delta\delta_i\}_e^e = \left\{ \begin{array}{l} \Delta u_L \\ \Delta v_L \\ \frac{1}{6i}(2\Delta M_L - \Delta M_R) - \frac{1}{l}(\Delta v_L - \Delta v_R) \\ \Delta u_L + \frac{1}{(EA)_{eq}}\Delta N_R \\ \Delta v_R \\ \frac{1}{6i}(2\Delta M_R - \Delta M_L) - \frac{1}{l}(\Delta v_L - \Delta v_R) \end{array} \right\} \quad (10.22)$$

where

$$i = \frac{(EI)_{eq}}{l} \quad (10.23)$$

- (6) calculate the displacement vector $\{\delta_i\}$ of the structure and the elemental elastic displacement $\{\delta_i\}_e^e$ at temperature $\{T_i\}$.

$$\{\delta_i\} = \{\delta_{i-1}\} + \{\Delta\delta_i\} \quad (10.24)$$

$$\{\delta_i\}_e^e = \{\delta_{i-1}\}_e^e + \{\Delta\delta_i\}_e^e \quad (10.25)$$

- (7) repeat (1) to (6) until $[K_T]$ becomes non-positive and then the limit state of the structure is determined.

10.4 Experimental and Theoretical Prediction

To investigate the structural behavior of a steel frame in a fire and validate the proposed approach, experimental research on two large-scale steel frame models was carried out at Tongji University. Both models were single-storey two-bay frames with the span of 1620 mm and a height of 1400 mm. All columns were protected from out-of-plane deformation and tensional displacement by lateral supporting elements. The model configuration and the location of restraints are shown in Fig. 10.10. Beams were made of rolled I-shape steel (I10) with a measured yielding strength of 294.9 MPa and modulus of elasticity of 2.03E+5 MPa at room temperature. Columns were made of square steel tubes of 100 mm×100 mm×4.2 mm with a measured yield strength and modulus of elasticity at room temperature of 334.2 MPa and 2.18E+5 MPa respectively. Seven vertical loads of 30.0 kN were applied to the model (see Fig. 10.10) and the load-bearing capacity of the model at room temperature was approximately $P=60.0$ kN.

A specially designed gas furnace was used to heat the frame. The load was kept constant during the heating. Thermocouple locations for measuring the steel temperature are shown in Fig. 10.11. The failure model of the frame is shown in Fig. 10.12(a) and Fig. 10.12(b) respectively. The temperatures of FRAME 1 and FRAME 2 are shown in Fig. 10.13 and Fig. 10.14 respectively.

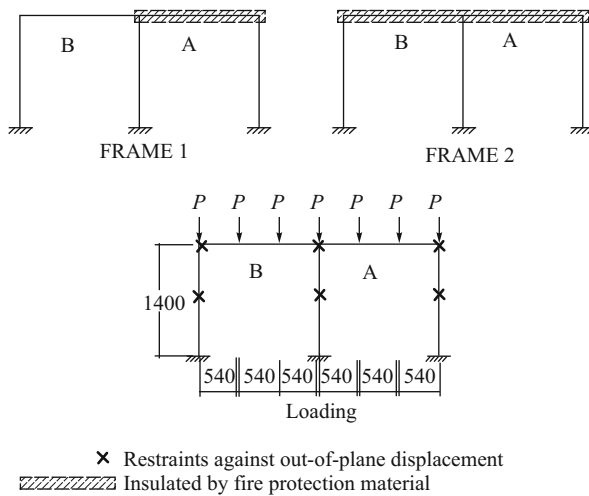


Fig. 10.10 Configuration of the model frame (mm)

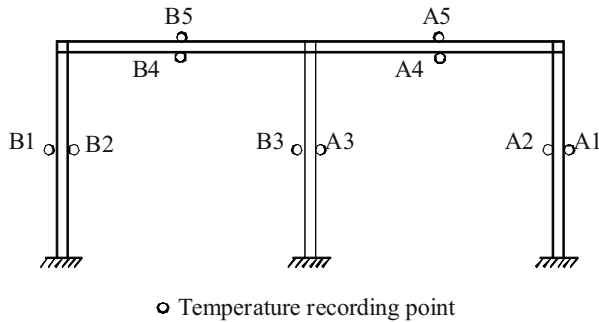
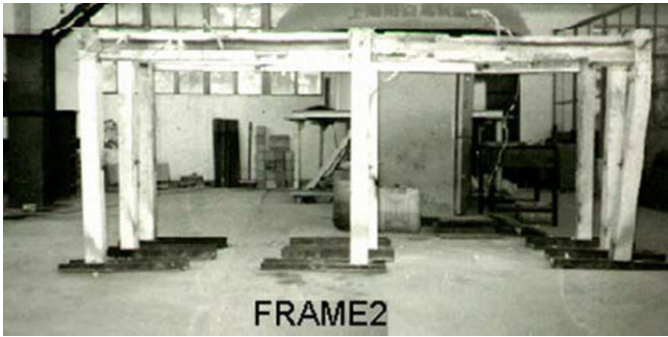


Fig. 10.11 Positions of thermocouples

Failure temperatures of the two model frames were evaluated using the proposed analytical approach. One element was used for each column and a beam was divided into four elements with the same length. Fig. 10.15 and Fig. 10.16 show comparisons between the measured deflection at mid-span of the beam with the predicted result using recorded temperatures as input data. Table 10.1 compares the fire resistance times of the two frames which shows reasonable agreement between predictions and test results.



(a) Failure of FRAME 1

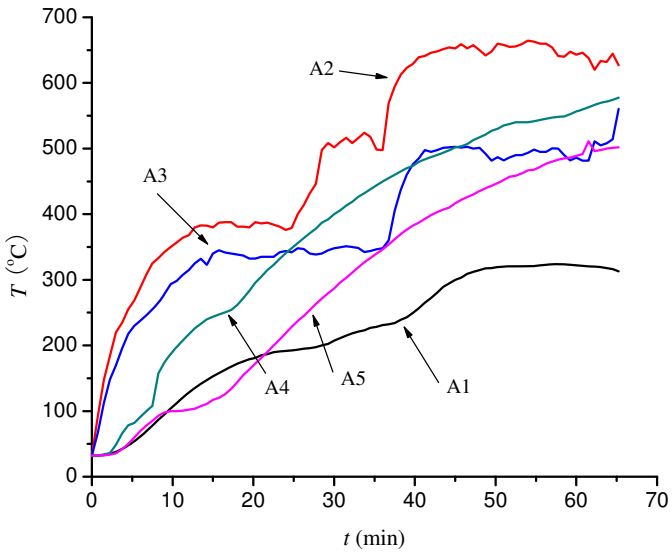


(b) Failure of FRAME 2

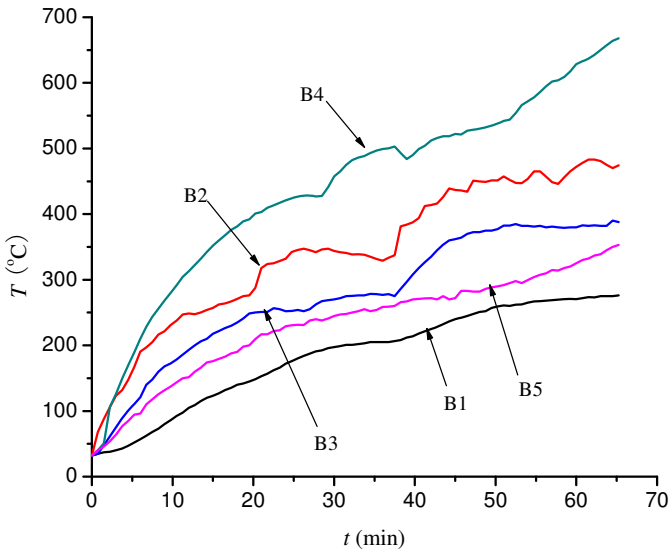
Fig. 10.12 Failure of the frames in the test

Table 10.1 Fire resistance of the models (min)

	FRAME 1	FRAME 2
Experimental	64	76
Calculated	58	74

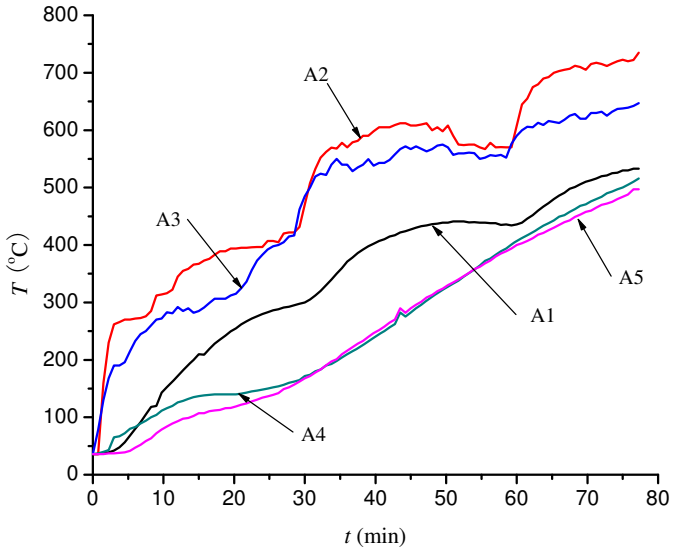


(a) Recorded temperatures in the fire protected part in FRAME 1

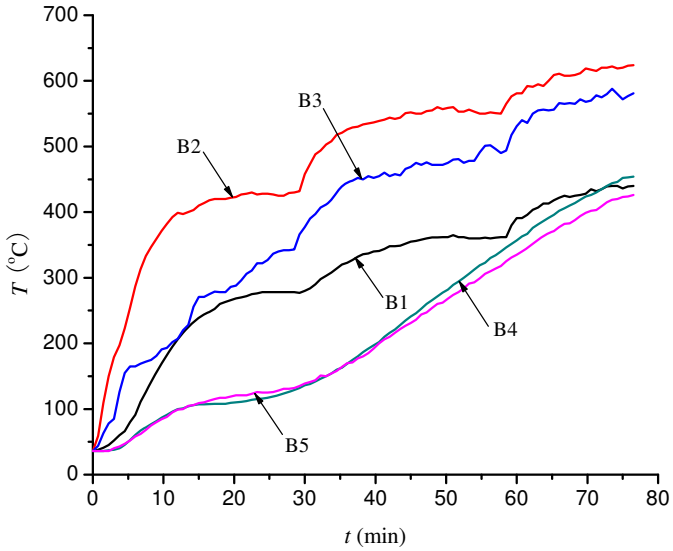


(b) Recorded temperatures in the unprotected part in FRAME 1

Fig. 10.13 Recorded temperatures of FRAME 1

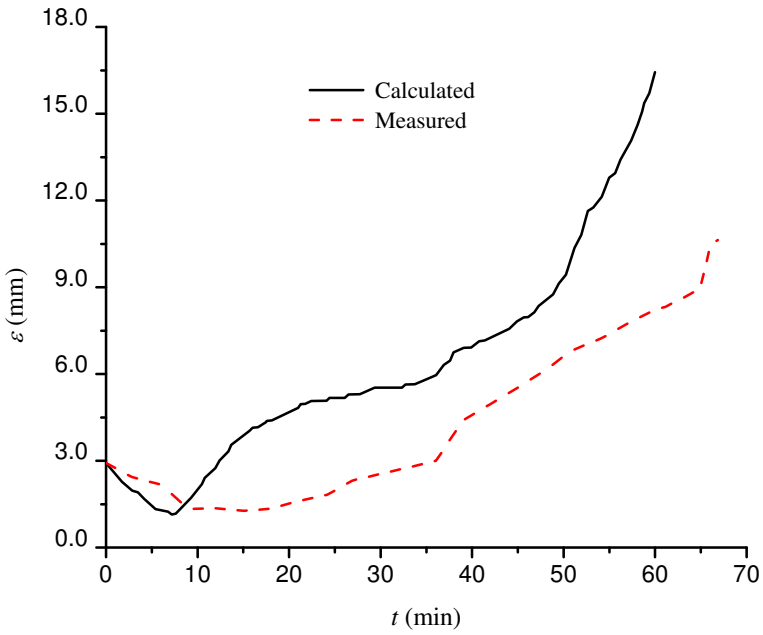


(a) Recorded temperatures in the fire protected part in FRAME 2

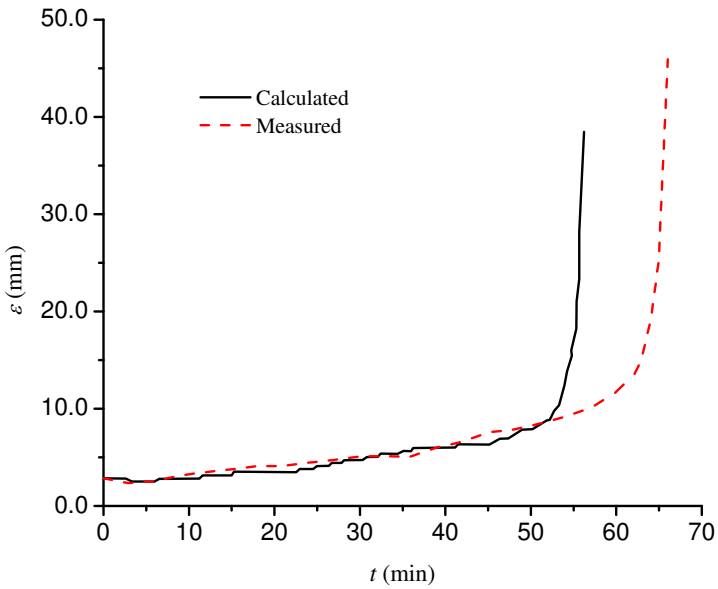


(b) Recorded temperatures in the unprotected part in FRAME 2

Fig. 10.14 Recorded temperatures of FRAME 2

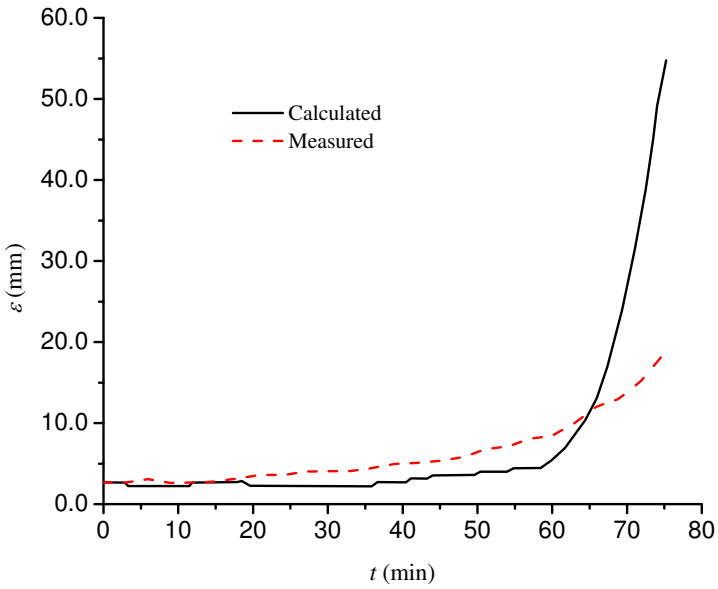


(a) Beam A

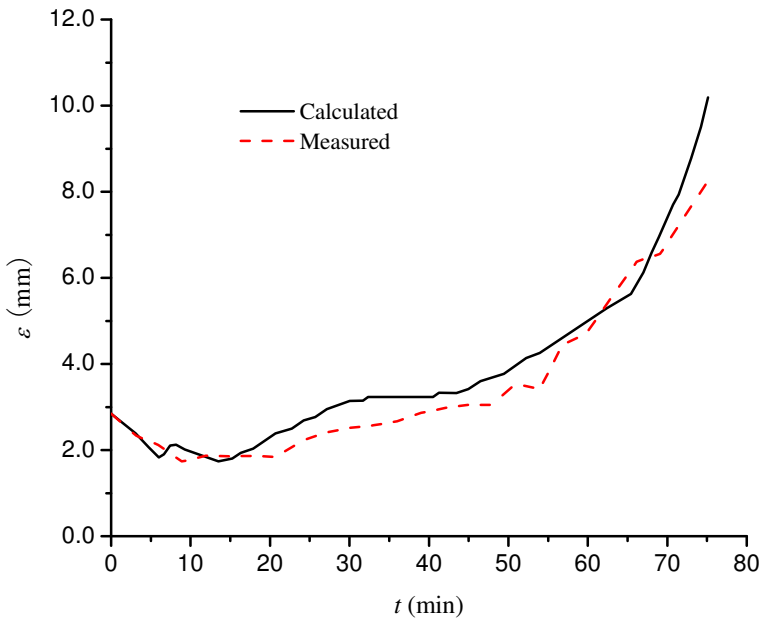


(b) Beam B

Fig. 10.15 Comparison between the calculated and measured deflections of FRAME 1



(a) Beam A



(b) Beam B

Fig. 10.16 Comparison between the calculated and measured deflection of FRAME 2

References

- [1] Y. C. Wang and D. B. Moore. Steel frames in fire: Analysis. *Engineering Structures*, 17(6), 1995.
- [2] W. C. Cheng. Theory and application on the behavior of steel structures at elevated temperatures. *Computers and Structures*, 16(1-4), 1983.
- [3] I. W. Burgess, J. A. El-Rimawi, and R. J. Plank. Analysis of beam with non-uniform temperature profile due to fire exposure. *Journal of Constructional Steel Research*, 16(3):169–192, 1990.
- [4] I. W. Burgess, J. El-Rimmawi, and R. J. Plank. Studies of behavior of steel beam in fire. *Journal of Constructional Steel Research*, 19(4):285–312, 1991.
- [5] A. Rubert and P. Schaumann. Critical temperatures of steel columns exposed to fire. *Fire Safety Journal*, 13(1):39–44, 1988.
- [6] H. A. Saab and D. A. Nethercot. Modelling steel frame behaviour under fire conditions. *Engineering Structures*, 13(4):371–382, 1991.
- [7] G. Q. Li and Z. Y. Shen. A practical approach for nonlinear analysis of steel frames. *Structure Engineers*, 4, 1994.
- [8] European Committee for Standardization. *EN1993-1-2. Eurocode 3: Design of Steel Structures, Part 1.2, General Rules, Structural Fire Design*. European Committee for Standardization, 2005.
- [9] British Standard Institution. *British Standard BS 5950, Part 8, Code of Practice for Fire Resistance Design*. British Standard Institution, 2000.
- [10] European Convention for Construction Steelwork. *Calculation for Fire Resistance of Composite Structures*. Technical Note No. 55, ECCS Technical Committee 3, 1989.
- [11] R. W. Clough and K. L. Benuska. Nonlinear earthquake behavior of tall buildings. *Journal of Engineering Mechanics, ASCE*, 93, 1967.

Analysis and Design of Large Space Steel Structure Buildings Subjected to a Fire

Large space steel structure buildings are widely used in industrial and commercial areas, as shown in Fig. 11.1. A catastrophe to this type of structure caused by a fire happens occasionally, as shown in Fig. 11.2. There are both scientific and engineering demand for proposing analysis and design methods for the fire safety of large space steel structure buildings.

11.1 Practical Analysis Approach for Steel Portal Frames in a Fire

Steel loses most of its strength when its temperature rises to 600 °C. Fire protection is a very important issue for steel structures. Conventionally, the thickness of fire protection of a steel structural member is determined through a standard fire test. This approach is not reasonable since there are lots of factors influencing the fire-resistance of a component that can not be reflected merely through tests. Analytical approaches for the fire safety design of steel members are proposed and employed in the codes of many countries for design of steel structures subjected to a fire^[1,2,3,4].

The fire safety design of a steel portal frame can be based on analysis of the behavior of the overall structure in a fire. Investigations are carried, through nonlinear FEM, on effects of structural parameters on the critical temperature of a steel portal frame. By only including the major parameters, a practical design approach is developed for the fire safety design of a steel portal frame^[5,6,7].

11.1.1 Finite Element Modeling and Assumptions

The 2D nonlinear beam element with tapered section is adopted for the analysis. The following assumptions are employed

- the perfect elastic-plastic stress-strain model is used for the steel at elevated temperatures;



Fig. 11.1 Application of the steel portal frame



Fig. 11.2 Damage to steel portal frames caused by a fire

- the yield strength and elastic modulus of the steel at elevated temperatures used for this investigation as

$$\begin{aligned} \frac{f_{yT}}{f_y} &= 1.0413 - 1.3 \times 10^{-3} T_s + 2.0 \times 10^{-6} T_s^2 - 3.0 \times 10^{-9} T_s^3 \\ \frac{E_T}{E} &= 1.0 - 1.0 \times 10^{-4} T_s + 7.0 \times 10^{-7} T_s^2 - 3.0 \times 10^{-9} T_s^3 \end{aligned} \quad (11.1)$$

- the local buckling in the web of a structural component is ignored;
- only vertical loads are taken into account.

The accuracy of the FEM approach proposed was verified by experimental results on steel portal frames^[6].

11.1.2 Parameters Influencing the Fire Resistance of a Steel Portal Frame

Steel portal frames are commonly fabricated with tapered H-section members. Three parameters affect the critical temperature of a steel portal frame subjected to a fire, as shown in Fig. 11.3:

- loads applied on the structure including their forms and values;
- geometrical parameters of the member section including section height h , flange width b , flange thickness t_f , web thickness t_w and wedge rate of tapered member α ; and
- geometrical parameters of the overall structure including column height H , frame span L and girder slope of the frame φ .

11.1.2.1 Effects of Load Ratio

Loads that govern the structural design of steel portal frames are mainly vertical loads for the relatively low height of this kind of building. To simplify the analysis, only the uniformly distributed vertical load on the steel portal frame is taken into account. Define the load ratio R as the ratio of the design vertical load applied on a structure in case of fire to the elastic ultimate limit load of the structure at room temperature.

Effects of R on the critical temperature of a steel portal frame were analyzed through studying the steel portal frame with non-tapered members. Other parameters of the frame are $h_0=500$ mm, $b=150$ mm, $t_f=12$ mm, $t_w=8$ mm, $H=4$ m, $L=24$ m and $\varphi=15^\circ$. The critical temperature of the frame varying with the load ratio is listed in Table 11.1. R has significant effects on the critical temperature of a steel portal frame.

11.1.2.2 Effects of Wedge Rate of a Tapered Member

The steel portal frame members usually use the H-shaped section with a varying height of web. The maximum and minimum section heights of the beam h_1 and h_2

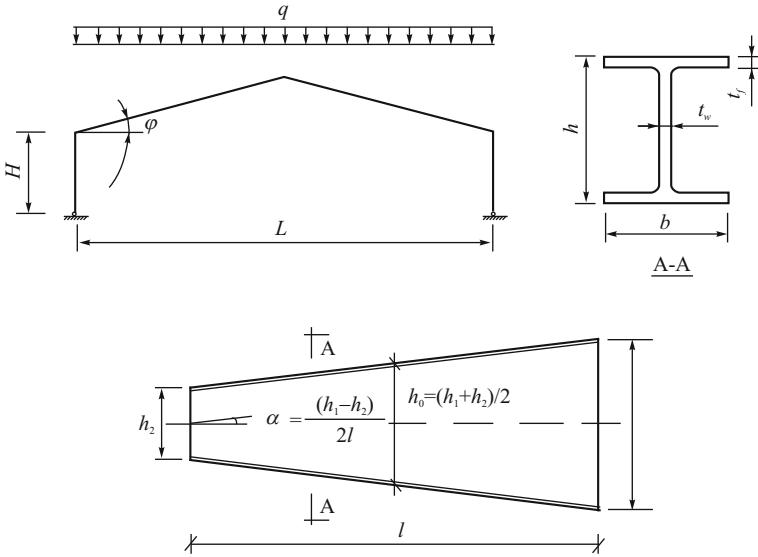


Fig. 11.3 Portal frame

Table 11.1 Critical temperature of a steel portal frame with different load ratios

R	0.2	0.3	0.4	0.5	0.6	0.7	0.8	0.9
Critical temperature ($^{\circ}\text{C}$)	760	710	675	630	610	580	545	505

are assumed to be equal to that of the column. Other parameters of the frame are $h_0=360$ mm, $b=170$ mm, $t_f=12.7$ mm, $t_w=8$ mm, $H=4$ m, $L=20$ m and $\varphi=15^{\circ}$. The critical temperature of the steel portal frame varying with the wedge rate is listed in Table 11.2.

Table 11.2 Effects of the wedge rate on the critical temperature of a steel portal frame ($^{\circ}\text{C}$)

R	Critical temperature			
	$\alpha=0^{\circ}$	0.5°	1.0°	1.5°
0.3	635	650	650	635
0.4	610	605	615	610
0.5	555	555	550	555
0.6	490	510	515	510
0.7	370	415	440	445

As listed in Table 11.2, the wedge rate of a tapered member has little effect on the critical temperature of the steel portal frame when the load ratio is less than 0.7, which is usual in practice.

11.1.2.3 Effects of Flange Width, Flange Thickness and Web Thickness of the Member Section

To investigate effects of the flange width, the flange and web thickness of a member on the critical temperature of a steel portal frame, a set of steel portal frames with uniform members are selected for analysis. All the members in the studied frame are assumed to have the same section as shown in Fig. 11.4. Other parameters of the frame are $h_0=450$ mm, $H=4$ m, $L=20$ m and $\phi=15^\circ$. Critical temperatures of frames with different flange width, flange thickness and web thickness of a member are listed in Table 11.3.

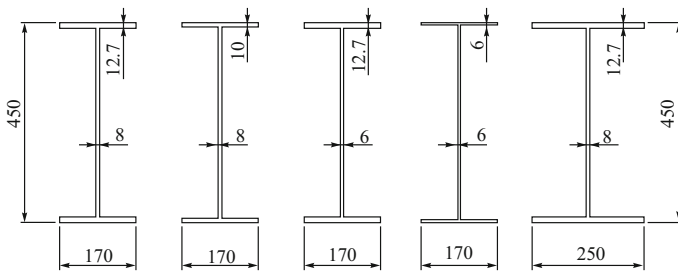


Fig. 11.4 Frame member sections (mm)

Table 11.3 Effects of the flange width, the flange and web thickness of a member on the critical temperature of a steel portal frame ($^\circ\text{C}$)

R	Critical temperature				
	A*	B	C	D	E
0.4	685	690	675	685	685
0.6	615	615	615	615	615
0.8	550	565	550	555	550
1.0	465	460	460	470	465

*A-E: Sections

The flange width, the flange thickness and the web thickness of a member have little effect on the critical temperature of a steel portal frame.

11.1.2.4 Effect of Section Height

Change the section height to identify its effect on the critical temperature. Other parameters of the frame are $t_f=12$ mm, $t_w=8$ mm, $H=4$ m, $L=24$ m and $\phi=15^\circ$. Three

different section heights, 900, 600 and 400 mm, are considered, and the corresponding flange widths are 300, 200 and 100 mm respectively. Critical temperatures of studied frames with different section height are listed in Table 11.4.

Table 11.4 Effect of the section height on the critical temperature of a steel portal frame (°C)

h_0	Critical temperature								
	$R=0.2$	0.3	0.4	0.5	0.6	0.7	0.8	0.9	1.0
400	720	680	650	605	575	520	480	415	350
600	780	710	680	645	615	595	575	535	505
900	780	715	685	655	625	600	575	550	525

The section height of a member has significant effect on the critical temperature of a steel portal frame. The critical temperature increases as the section height of a member increases.

11.1.2.5 Effect of Girder Slope

Two different girder slopes φ , 5° and 15° are considered. Other structural parameters of the steel portal are $h_0=600$ mm, $b=200$ mm, $t_f=12$ mm, $t_w=8$ mm, $H=4$ m and $L=24$ m. The critical temperature of the studied frame with different girder slopes are listed in Table 11.5. The girder slope has little effect on the critical temperature of a steel portal frame.

Table 11.5 Effect of the girder slope on the critical temperature of a steel portal frame (°C)

φ	Critical temperature								
	$R=0.2$	0.3	0.4	0.5	0.6	0.7	0.8	0.9	1.0
5°	770	710	685	630	615	595	565	530	490
15°	780	710	680	645	615	595	575	535	505

11.1.2.6 Effect of Frame Span

Four different frame spans, 40 m, 32 m, 24 m and 16 m are considered for investigating their effect on the critical temperature. The other parameters of the steel portal frames with uniform members are $h_0=500$ mm, $b=150$ mm, $t_f=12$ mm, $t_w=8$ mm, $H=4$ m and $\varphi=15^\circ$. Critical temperatures of these frames with various beam spans are listed in Table 11.6. The frame span has a significant effect on the critical temperature. The critical temperature decreases as the frame span increases.

Table 11.6 Effect of the frame span on the critical temperature of a steel portal frame (°C)

L	Critical temperature								
	$R=0.2$	0.3	0.4	0.5	0.6	0.7	0.8	0.9	1.0
16	775	710	685	650	620	605	575	535	515
24	760	710	675	630	610	580	545	505	460
32	730	690	650	605	575	535	480	420	335
40	710	670	610	585	540	490	435	360	260

11.1.2.7 Effect of Column Height

Three different column heights, 10 m, 7 m and 4 m are considered. Other parameters of the steel portal frames are $h_0=600$ mm, $b=200$ mm, $t_f=12$ mm, $t_w=8$ mm, $L=24$ m and $\phi=15^\circ$. Critical temperature of the studied frames with various column heights are listed in Table 11.7. The critical temperature of the frames decreases as the column height increases.

Table 11.7 Effect of the column height on the critical temperature of a steel portal frame (°C)

H	Critical temperature								
	$R=0.2$	0.3	0.4	0.5	0.6	0.7	0.8	0.9	1.0
4	780	710	680	645	615	595	575	535	505
7	730	705	660	620	595	565	525	480	415
10	710	675	620	600	555	500	450	365	285

11.1.3 Estimation of the Critical Temperature of a Steel Portal Frame

Through previous systematic investigations on effects of various parameters on the critical temperature of a steel portal frame subjected to a fire, it has been found that major parameters are the load ratio, the frame span L , the column height H and the member section height h . Other parameters, such as the wedge rate of tapered members, the flange width, the flange thickness and the web thickness of a member and the girder slope have insignificant effects on the critical temperature of a steel portal frame.

In order to build a simplified design equation for fire-resistance of a portal frame structure, a parametric study was performed. Studied parameters are

- seven different member section heights as listed in Table 11.8 in Appendix F;

- seventeen different load ratio as $R=0.2, 0.25, 0.3, 0.35, 0.4, 0.45, 0.5, 0.55, 0.6, 0.65, 0.7, 0.75, 0.8, 0.85, 0.9, 0.95$ and 1.0 ;
- six frame spans as $L=52$ m, 40 m, 32 m, 16 m and 12 m; and
- three column heights as $H=4$ m, 7 m and 10 m.

In total, 126 steel portal frames with member section heights varying from 300 mm to 900 mm, frame spans varying from 12 m to 54 m and column heights varying from 4 m to 10 m are analyzed.

Table 11.8 Member section (mm)

Section No.	1	2	3	4	5	6	7
h	900	800	700	600	500	400	300
b	300	250	200	200	150	100	100
t_w	8	8	8	8	8	8	8
t_f	12	12	12	12	12	12	12

The critical temperature of steel portal frames decreases as the span increases if $L > 2H$, while the critical temperature increases as the span increases if $L \leq 2H$. It is regarded that the critical temperature is governed by the frame span L if $L > 2H$, while it is governed by column height H if $L \leq 2H$. It is further found that the critical temperature is in proportion to the frame span and in inverse proportion to the member section height.

Define the parameter K as

$$K = \frac{L}{h^c}$$

where c is a constant to be determined. The value of c is obtained in such a way that the critical temperature of a steel portal frame with the same K and H but different L and h should equal each other. In this way it is obtained that $c=1.5$ when $H=4$ m, $c=1.8$ when $H=7$ m and $c = 4.5 - 3h_0$ when $H=10$ m. Thus, the critical temperature of a steel portal frame can be finally determined in the form of Tables 11.9–11.11.

Through comparing the critical temperature obtained by FEM and listed in Tables 11.9–11.11, it is found that when $R \leq 0.6$, the biggest difference in critical temperatures is 15 °C and normally less than 10 °C. When $0.6 < R \leq 0.8$ the biggest difference in critical temperatures is 20 °C and normally less than 10 °C. When $R > 0.8$, the biggest difference in critical temperatures is 25 °C and normally less than 15 °C. Therefore the table approach presented for estimating the critical temperature of a steel portal frame is effective.

The following points must be pointed out for estimating the critical temperature of a steel portal frame in Tables 11.9–11.11:

- Tables 11.9–11.11 are applicable for the steel portal frame with either tapered members or uniform members. However, the frame span should be less than 52

Table 11.9 Critical temperature of a steel portal frame with $H=4$ m ($^{\circ}\text{C}$)

R	Critical temperature						R	Critical temperature					
	$K=40$	60	80	100	120	140		$K=40$	60	80	100	120	140
0.20	780	760	740	720	710	700	0.65	610	600	560	540	510	480
0.25	740	720	710	700	690	680	0.70	600	580	540	510	470	440
0.30	710	710	700	690	660	650	0.75	580	570	520	490	450	420
0.35	700	690	680	660	630	620	0.80	570	560	500	470	420	390
0.40	680	680	650	640	610	610	0.85	560	530	480	440	380	360
0.45	670	660	630	620	590	580	0.90	540	510	450	400	360	340
0.50	650	630	620	610	570	570	0.95	530	490	420	360	320	290
0.55	640	620	600	580	550	530	1.00	510	460	380	310	290	260
0.60	620	610	580	560	530	500							

Note: $K = L/h^{1.5}$

Table 11.10 Critical temperature of a steel portal frame with $H=7$ m ($^{\circ}\text{C}$)

R	Critical temperature						R	Critical temperature					
	$K=40$	60	80	100	120	140		$K=40$	60	80	100	120	140
0.20	750	730	720	710	700	690	0.65	590	570	550	530	490	470
0.25	720	710	700	690	680	670	0.70	570	560	530	500	460	440
0.30	710	700	680	670	660	650	0.75	560	540	500	470	430	420
0.35	700	680	650	650	630	620	0.80	540	520	480	440	400	380
0.40	670	660	630	620	610	600	0.85	520	500	450	410	360	340
0.45	650	640	620	610	600	580	0.90	500	470	410	380	330	310
0.50	630	620	610	590	570	560	0.95	480	430	370	340	300	270
0.55	610	610	590	580	550	520	1.00	460	400	330	300	260	230
0.60	600	600	570	550	530	500							

Note: $K = L/h^{1.8}$

m and the column height should be less than 10 m to meet the condition $L > 2H$.

The section height of the frame members h can vary from 300 to 900 mm;

- when $K < 40$, it can be safely assumed that $K=40$. However, when K is beyond the upper limit in Tables 11.9–11.11, the tables can not be used;
- if the column height is between 4 m and 7 m or between 7 m and 10 m, the interpolation method is employed for determining the critical temperature of a steel portal frame;
- if the column height of a steel portal frame is less than 4 m, but $L > 2H$, it can be safely assumed that $H=4$ m. If the span of a steel portal frame is less than 12 m and $L > 2H$, it can be safely assumed that $L=12$ m.

Table 11.11 Critical temperature of a steel portal frame with $H=10\text{m}$ ($^{\circ}\text{C}$)

R	Critical temperature						R	Critical temperature					
	$K=40$	60	80	100	120	140		$K=40$	60	80	100	120	140
0.20	740	710	710	710	710	710	0.65	590	560	540	530	520	480
0.25	710	700	700	700	690	680	0.70	570	540	510	490	480	460
0.30	700	690	680	670	660	660	0.75	550	510	490	470	460	430
0.35	690	670	650	640	640	630	0.80	530	490	460	450	420	390
0.40	670	630	630	620	620	610	0.85	520	450	420	400	380	340
0.45	640	620	610	610	600	590	0.90	500	420	390	370	350	320
0.50	620	610	600	590	590	580	0.95	480	380	340	330	320	290
0.55	610	590	580	570	570	550	1.00	450	350	320	290	280	250
0.60	600	580	560	550	540	520							

Note: $K = L/h^{4.5-3h_0}$

11.1.4 Example

Geometric parameters of the studied steel portal frame are $H=5\text{ m}$, $L=20\text{ m}$, $\varphi=15^{\circ}$, $h_1=540\text{ mm}$, $h_2=180\text{ mm}$, $b=170\text{ mm}$, $t_f=12.7\text{ mm}$ and $t_w=8\text{ mm}$. The frame is made of Q345 steel and subjected to a uniform vertical load with $q=8\text{ kN/m}$ in case of a fire.

Design procedure:

(a) The average section height of the frame is

$$h_0 = \frac{h_1 + h_2}{2} = 360\text{ mm}$$

(b) The elastic limit vertical load of the steel portal frame with equivalent uniform section height of 360 mm is

$$q_{\max} = 10.92\text{ kN/m}$$

and the load parameter is

$$R = \frac{q}{q_{\max}} = \frac{8}{10.92} = 0.73$$

(c) Estimate the critical temperature of the corresponding frame by Table 11.9 and Table 11.10 for $H=4\text{ m}$ and $H=7\text{ m}$ respectively. For $H=4\text{ m}$, $K=20/0.351.5=93$. The critical temperature of the frame is estimated in Table 11.9 as $T_4=500\text{ }^{\circ}\text{C}$. For $H=7\text{ m}$, $K=20/0.351.8=126$. The critical temperature of the frame is estimated in Table 11.10 as $T_7=500\text{ }^{\circ}\text{C}$.

(d) The critical temperature of the example frame is obtained by linear interpolation of T_4 and T_7 gives $T_{cr}=477\text{ }^{\circ}\text{C}$.

(e) The critical temperature of the frame with tapered members predicated by FEM is 520 °C, and that of the frame with equivalent uniform members is 480 °C.

It is obvious that the critical temperature of a steel portal frame with uniform members estimated in the tables presented agree with the FEM results very well, while the critical temperature of the steel portal frame with tapered members is slightly higher than that of the corresponding steel portal frames with uniform members.

11.1.5 Fire Protection

The thickness of fire protection of the steel portal frame required to resist ISO834 standard fire^[8] is calculated^[9,10] as

$$d = \lambda \frac{F}{V} \left[2 \times 10^5 \left(\frac{T - 20}{t} + 0.2 \right)^2 - 880 \right]^{-1} \quad (11.2)$$

where T is the critical temperature, t is the fire-resistance duration requirement of the frame considered in seconds.

11.2 Critical Temperature of a Square Pyramid Grid Structure in a Fire

A square pyramid grid is the most common used grid structure form in China^[11]. Parametric studies on the square pyramid grid in a fire are performed using the finite element software ANSYS^[12,13,14]. And a practical design method is presented based on the analytical results^[15].

11.2.1 Parameters of Grid Structures

The size of the grid is 3 m×3 m with the long side of the grid structure from 24 m to 36 m and short side of the structure from 24 m to 36 m.

11.2.1.1 Member Sizes and Material Properties

The structural member is made of Q235 steel with a yield strength of 215 N/mm² and an elastic modulus of 2.05×10^5 N/mm² at ambient temperature. Details of structural members are listed in Table 11.12.

11.2.1.2 Boundary Conditions

In order to release the thermal expansion, the grid structure is usually pin supported.

Table 11.12 Details of the structural member

No.	Section size ($\phi \times t$)	Sectional area A (cm ²)	Moment of inertia I (mm ⁴)	Slenderness λ	Stability factor ϕ (at ambient)
1	60×3.5	6.21	24.88	150	0.339
2	76×3.75	9.05	58.81	118	0.507
3	89×4	10.68	96.68	100	0.638
4	108×6	19.22	250.78	83	0.763
5	127×8	29.91	531.53	71	0.834
6	159×10	46.81	1304.22	57	0.894
7	159×14	63.74	1690.84	58	0.890
8	168×18	108	2229.85	54	0.904

ϕ is the outer diameter of the component; t is the thickness of the pipe; λ is calculated assuming the component with length of 3 m

11.2.2 Definition of Parameters

11.2.2.1 Stability Stress Ratio

The stability stress ratio is defined as

$$R_{\sigma} = \frac{\sigma_0}{\phi f} \quad (11.3)$$

where σ_0 is the stress of a structural member at ambient temperature.

11.2.2.2 Structural Load Ratio

The structural load ratio is defined as^[15]

$$R = \frac{F^T}{F_{cr}} \quad (11.4)$$

where F_{cr} is the applied load on the structure when the member stability stress ratio $R_{\sigma}=1$ and F^T is the applied load on the structure in a fire situation. R is usually between 0.3 to 0.8.

11.2.2.3 Characteristic of the Grid Structure

The analysis of a grid structure usually uses the pseudo plate theory^[16]. The stiffness of a square pyramid grid structure in the x - and y -direction are

$$D_x = \frac{A_{ax}A_{bx}}{A_{ax} + A_{bx}} \frac{Eh^2}{s} \tag{11.5}$$

$$D_y = \frac{A_{ay}A_{by}}{A_{ay} + A_{by}} \frac{Eh^2}{s}$$

where s is the dimension of the grid, as shown in Fig. 11.5.

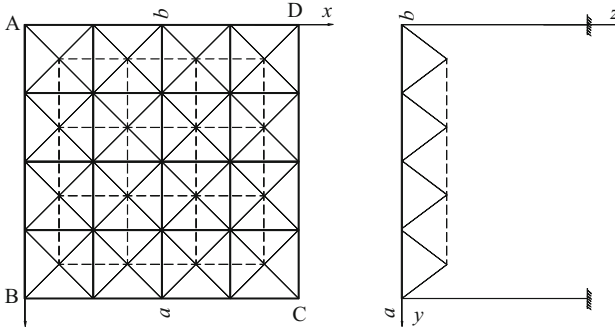


Fig. 11.5 Square pyramid grid structure

The overall bending stiffness of the grid structure is

$$D = \sqrt{D_x D_y} \tag{11.6}$$

The shear stiffness of the square pyramid structure in the x - and y -direction is the same and is calculated by

$$C = C_x = C_y = \frac{\sqrt{2EA_c \sin^2 \beta \cos \beta}}{s} \tag{11.7}$$

11.2.2.4 Controlling Structural Component and Non-controlling Structural Component

The structural component with the maximum stability stress ratio is the controlling structural component in the design. And the others are non-controlling structural components. The relation between the structural load ratio and the stability stress ratio of the structural component is

$$R = \max\{R_\sigma\} \tag{11.8}$$

11.2.2.5 Critical Temperature of the Steel Grid Structure

The temperature at which the first structural component reaches its ultimate limit state is called the critical temperature of the structural component (T_{cr0}) and the temperature at which the whole structure reaches its ultimate state is called the critical

temperature of the whole structure (T_{cr1}). Usually, T_{cr1} will be higher than T_{cr0} . For very important buildings, it should be designed according to T_{cr0} . If the large deformation of a structure is allowed, it can be designed according to T_{cr1} .

11.2.3 Critical Temperature of the Structural Component

The steel grid structure is analyzed using finite element software ANSYS^[15]. The stress development of the structural controlling component is shown in Fig. 11.6. With the elevation of temperature, the stability stress degrades. The critical temperature is reached when the stability stress equals the stress of the structural controlling component at ambient temperature.

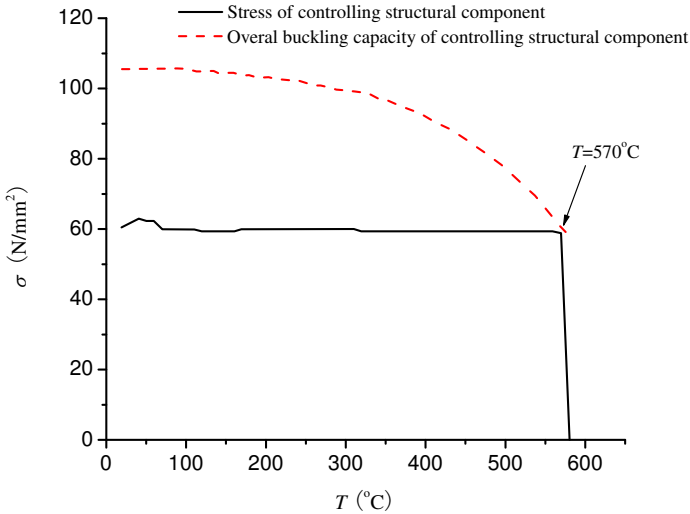


Fig. 11.6 Critical temperature of the structural controlling component

11.2.4 Critical Temperature of the Grid Structure in Uniform Temperature Field

Grid structures with different load ratio, dimension and value of C/D are analyzed using ANSYS. Critical temperatures of structural components and the overall structure in uniform temperature field are listed in Table 11.13.

The dimension and the ratio C/D have a very limited effect on the critical temperature of a grid structure, as shown in Table 11.13. Critical temperatures of structural components and those of the overall structure are close to each other. Hence, the critical temperatures of a grid structure in a uniform temperature field are further simplified, as listed in Table 11.14.

Table 11.13 Critical temperatures of the grid structure in a uniform temperature field (°C)

C/D	Dimension $L_{AB} \times L_{AD}$ (m)	T_{cr0}						T_{cr1}					
		R=0.8	0.7	0.6	0.5	0.4	0.3	R=0.8	0.7	0.6	0.5	0.4	0.3
0.238	24×24	480	530	560	580	620	650	490	540	570	600	630	660
0.222	24×27	430	520	550	580	620	650	440	530	560	600	630	660
0.21	24×30	480	520	560	600	630	660	490	530	570	610	640	670
0.208	27×27	470	530	540	580	620	650	480	540	550	590	630	660
0.205	24×33	440	520	560	580	620	650	450	530	570	600	630	660
0.189	24×24	450	530	550	600	630	660	460	540	570	610	640	670
0.187	30×30	460	540	560	600	630	650	480	550	580	610	640	670
0.168	33×33	490	530	560	600	630	650	500	540	580	610	640	670
0.164	24×24	500	530	570	600	630	650	510	540	580	610	640	670
0.154	27×27	490	540	570	600	630	650	500	550	580	610	640	670
0.139	36×36	440	480	560	590	620	650	450	490	570	600	630	660
0.131	30×30	480	530	550	590	620	650	490	540	560	600	630	660
0.121	33×33	480	530	570	600	620	650	500	540	580	610	630	660
0.11	27×27	490	530	570	600	630	660	500	550	580	610	640	670
0.109	36×36	460	520	560	590	630	660	470	530	570	600	640	670
0.101	24×24	500	540	570	600	630	660	510	550	580	610	640	670
0.096	33×33	500	540	570	600	620	660	510	550	580	610	630	670
0.089	27×27	510	540	580	600	630	660	520	550	590	610	640	670
0.088	30×30	490	540	570	600	630	660	500	550	580	610	640	670
0.077	30×30	520	560	580	610	640	670	530	570	590	620	650	680
0.063	33×33	490	550	580	610	630	650	500	560	590	620	640	660
0.06	36×36	500	530	570	590	630	660	510	540	580	600	640	670
0.056	36×36	510	540	570	600	630	660	520	550	580	610	640	670

Table 11.14 Critical temperatures of the grid structure in a uniform temperature field (°C)

R	0.8	0.7	0.6	0.5	0.4	0.3
T_{cr}	480	550	580	600	640	670

11.2.5 Critical Temperatures of the Grid Structure in a Non-Uniform Temperature Field

The smoke temperature in a large space building fire usually is non-uniformly distributed. The smoke temperature at the fire center is the highest, and the temperature decreases further away from the fire center one goes. Thermal stresses are generated in a grid structure in a non-uniformly distributed temperature field.

11.2.5.1 Non-uniformly Distributed Temperature Field

The temperature field is determined by

$$f(x) = \eta + (1 - \eta)e^{-\frac{x - b}{\mu}} \tag{11.9}$$

where η and μ are parameters as listed in Table 11.15 and x is the distance to the fire center.

Table 11.15 Values of parameter η and μ

η	μ	η	μ
	0.5		0.5
0.85	1	0.75	1
	3		2
	8		5
0.8	0.5		0.8
	1	0.7	1
	2		3
	6		

11.2.5.2 Critical Temperature of the Structural Component

Analysis results showed that the critical temperature of a structural component depends on the load ratio and the parameter η . The critical temperature of structural components with a different load ratio and temperature distribution type is listed in Table 11.16.

For convenience in engineering applications, the critical temperature of a structural component is also expressed by

$$T_{cr0} = \begin{cases} 290 + 930\eta^2 - (200 + 700\eta)R, & 0.2 \leq \eta < 0.6 \\ 840 - \frac{120}{\eta^2} - 410R^2, & 0.6 \leq \eta < 0.8 \end{cases} \tag{11.10}$$

Table 11.16 Critical temperature of the structural component (°C)

η	Critical temperature					
	$R=0.8$	0.7	0.6	0.5	0.4	0.3
0.8	401	467	516	556	593	630
0.7	340	409	463	503	539	572
0.6	253	320	367	407	448	487
0.5	210	263	300	335	368	402
0.4	189	227	258	287	316	347
0.3	163	197	222	247	273	301
0.2	144	164	193	216	237	257

11.2.5.3 Critical Temperature of the Overall Structure

The critical temperature of the overall structural component depends on the structural load ratio and the temperature distribution of the fire. The critical temperature of the overall structure is listed in Table 11.17. The stiffness ratio C/D has very little effect on the critical temperature.

Table 11.17 Critical temperature of the overall structure (°C)

η	Critical temperature					
	$R=0.8$	0.7	0.6	0.5	0.4	0.3
0.8	441	510	567	610	650	691
0.7	397	495	577	647	708	764
0.6	319	429	494	582	667	730
0.5	275	378	457	562	662	732
0.4	247	349	421	540	629	710
0.3	226	321	386	514	603	726
0.2	196	253	346	477	587	715

The critical temperature of the overall structure is also expressed by

$$T_{cr} = T_{cr0} + \Delta T \tag{11.11}$$

where ΔT is the difference between the critical temperature of the overall structure and the structural component and given by

$$\Delta T = \begin{cases} 720 - 985\eta^2 - (870 - 1395\eta^2)R, & 0.2 \leq \eta < 0.6 \\ 365 + 84\frac{\eta}{\ln \eta} - (468 + 119\frac{\eta}{\ln \eta})R^2, & 0.6 \leq \eta < 0.8 \end{cases} \tag{11.12}$$

11.2.6 Conditions for a Grid Structure with no Need of Fire Protection

If the temperature of a grid structure in a fire is lower than the critical temperature of a structural component, the structure does not need fire protection. Configuration factors of structural components in a grid structure are usually very high. For simplicity, the temperature of a structural component be the same temperature as the smoke. In a large space building fire, the smoke temperature depends on the fire power. Table F-1 gives the maximum fire power at which the grid structure does not need fire protection, including the floor area A , the load ratio R , the height of the structure above the floor and the non-uniformly distributed temperature parameter η .

11.3 Continuous Approach for Cable-Net Structural Analysis in a Fire

The saddle-backed cable net structure is constructed by concave cables which are the load bearing components and convex cables which behave as the stabilizing cable. The commonly used cable net structure is shown in Fig. 11.7.

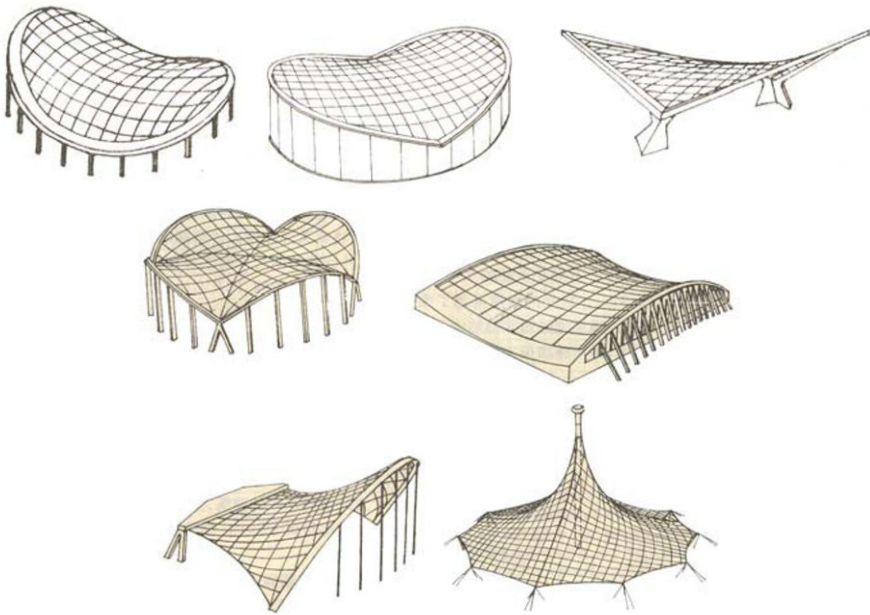


Fig. 11.7 Commonly used saddle-backed cable net structures

Cable net structures are commonly used in large space buildings, such as stadiums and multiple storey houses. The shape and load bearing mechanism of a cable net structure is formed through the tensile force in the cable. However, the elastic modulus and strength of the high strength cable degrades quickly at high temperature. For example, at a temperature of 700 °C, the tensile strength is only 10% of that at ambient temperature and the elastic modulus is only 3% of that at ambient temperature^[17]. On the other hand, the thermal strain will cause loss of tensile force in the cable which may cause a shape change or large displacement of the structure.

A continuous progress is developed to predict the fire resistance of a cable net structure. It is assumed that only the cable is under tension only.

11.3.1 Behavior of a Single Cable in a Fire

11.3.1.1 Formulation and Solution of a Single Cable at Ambient Temperature

The cable satisfies the equilibrium equation as^[18,19,20]

$$z_0 = \frac{M_0(x)}{H_0} + \frac{c}{l}x \tag{11.13}$$

where z_0 is the deflection of the cable, q_0 is the applied uniformly distributed load on the cable, l is the span of the cable, $M_0(x)$ is the moment at the position x induced by the applied load, H_0 is the tensile force in the cable and c is the vertical displacement of the support, as shown in Fig. 11.8.

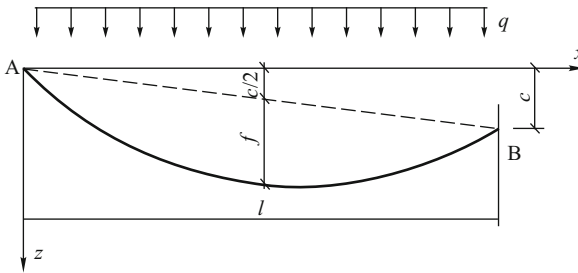


Fig. 11.8 Simplified model of a single cable under uniformly distributed load

If the load q_0 is increased by Δq , the new equilibrium equation and deformation condition should satisfy

$$H - H_0 = \frac{EA}{2l} \int_0^l \left[\left(\frac{dz}{dx} \right)^2 - \left(\frac{dz_0}{dx} \right)^2 \right] dx + EA \frac{u_r - u_l}{l} - EA\alpha\Delta T \tag{11.14}$$

$$z = \frac{M(x)}{H} + \frac{c}{l}x \tag{11.15}$$

where u_r and u_l are the displacement of the support.

Eq.(11.14) can be rewritten as

$$\begin{aligned}
 H - H_0 &= \frac{EA}{2l} \int_0^l \left[\left(\frac{V}{H} \right)^2 + \frac{2Vc}{Hl} + \left(\frac{c}{l} \right)^2 \right. \\
 &\quad \left. - \left(\frac{V_0}{H_0} \right)^2 - \frac{2V_0c_0}{H_0l} - \left(\frac{c_0}{l_0} \right)^2 \right] dx \\
 &\quad + EA \frac{u_r - u_l}{l} - EA\alpha\Delta T \\
 &= EA \frac{c^2 - c_0^2}{2l^2} + \frac{EA}{2l} \int_0^l \left(\frac{V^2}{H^2} - \frac{V_0^2}{H_0^2} \right) dx \\
 &\quad + EA \frac{u_r - u_l}{l} - EA\alpha\Delta T
 \end{aligned} \tag{11.16}$$

where $V_0(x)$ and $V_0(y)$ are the vertical force at position x ^[17].

Assume that

$$\int_0^l V^2 dx = D; \int_0^l V_0^2 dx = D_0 \tag{11.17}$$

and Eq.(11.16) can be rewritten as

$$H - H_0 = \frac{EA}{2l} \left(\frac{D^2}{H^2} - \frac{D_0^2}{H_0^2} \right) + EA \frac{c^2 - c_0^2}{2l^2} + EA \frac{u_r - u_l}{l} - EA\alpha\Delta T \tag{11.18}$$

The tensile force H in the cable is solved by Eq.(11.18). Then the deflection z of the cable is solved by Eq.(11.15).

11.3.1.2 Formulation and Solution of a Single Cable at High Temperature

1) Assumptions

For simplifying the formulation of a single cable in a fire, it is assumed that

- the stress-strain relationship of high strength cable is bilinear, as shown in Figs. 11.9 and 11.10; and
- the cable is in tension only.

2) Behavior of a single cable in a fire

The behavior of a cable in a fire is different to that at ambient temperature from three aspects

- the thermal expansion of steel will cause a loss in the pre-tension force in the cable;
- the elastic modulus of the steel will degrade with the elevation in temperature;
- the stress-strain relationship of steel is non-linear at high temperature.

The structural analysis of the cable structure is both geometrically nonlinear and materially nonlinear.

The stress development route of a high strength cable at elevated temperature is shown in Figs. 11.9 and 11.10. When the temperature increases from t_i to t_{i+1} , there are four possible stress development routes shown as

- **route 1 (plastic loading)**
The steel changes from a plastic state at the current temperature to a plastic state at the next temperature.
- **route 2 (plastic unloading)**
The steel changes from a plastic state at the current temperature to an elastic state at the next temperature.
- **route 3 (elastic loading)**
The steel changes from an elastic state at the current temperature to a plastic state at the next temperature.
- **route 4 (elastic unloading)**
The steel changes from an elastic state at the current temperature to an elastic state at the next temperature.

If the temperature step is small enough, the stress-strain relationship used is that at $(t_{i+1} + t_i)/2$ for simplicity, as shown in Fig. 11.10.

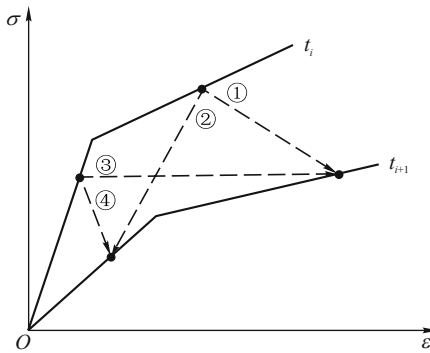


Fig. 11.9 Stress development routes of high strength cable at changing temperatures

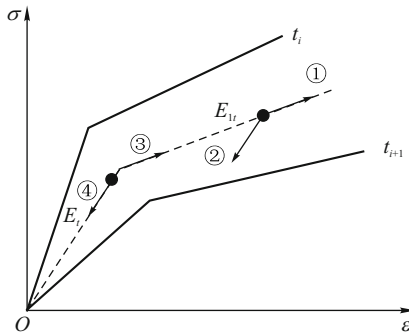


Fig. 11.10 Simplified stress development routes of high strength cable at changing temperatures

As shown in Fig. 11.11, for a temperature increase from T_i to T_{i+1} , the increase in the cable length is

$$\Delta S = \frac{D}{2H^2} - \frac{D_0}{2H_0^2} \quad (11.19)$$

where D and D_0 are calculated according to Eq.(11.17), H and H_0 show the horizontal tensile force in the cable at elevated and ambient temperatures respectively.

The strain increment is

$$\Delta \varepsilon = \Delta \varepsilon^{th} + \Delta \varepsilon^N \quad (11.20)$$

where $\Delta \varepsilon^N$ is the increase in mechanical strain and $\Delta \varepsilon^{th}$ is the increase in thermal strain calculated by

$$\Delta \varepsilon^{th} = \alpha \Delta T \quad (11.21)$$

The change in mechanical strain $\Delta \varepsilon^N$ is different for different stress development routes, as shown in Fig. 11.10:

- for route 1, the change in mechanical strain is

$$\Delta \varepsilon^N = \frac{\Delta F}{E_{1t}A} \quad (11.22)$$

where E_{1t} is the tangent modulus of steel at temperature T_{i+1} and ΔF is the change in the tensile force in the cable;

- for stress route 2, the change in the mechanical strain is

$$\Delta \varepsilon^N = \frac{\Delta F}{E_t A} \quad (11.23)$$

where E_t is the elastic modulus of steel at temperature t_i ;

- for stress route 3, the change in the mechanical strain is

$$\Delta \varepsilon^N = \frac{\sigma_s}{E_t} + \frac{H}{E_{1t}A} - \frac{\sigma_s}{E_{1t}} - \frac{H_0}{E_t A} \quad (11.24)$$

where σ_s is the stress in the cable at temperature t_i ;

- for stress route 4, the change in the mechanical strain is

$$\Delta \varepsilon^N = \frac{\Delta F}{E_t A} \quad (11.25)$$

In summary, the change in length of the cable can be determined as

- if the stress develops following route 2 or route 4, the change in the cable length is

$$\begin{aligned}
 \Delta &= \int_{S_0} \left(\frac{\Delta F}{E_t A} + \alpha \Delta t \right) dS_0 \\
 &= \int_{S_0} \left(\frac{\Delta H}{E_t A} \frac{dx}{dS_0} + \alpha \Delta t \right) \frac{dS_0}{dx} dx \\
 &= \frac{\Delta H}{E_t A} \int_l \left[1 + \left(\frac{dz_0}{dx} \right)^2 \right] dx + \alpha \Delta t \int_l \sqrt{1 + \left(\frac{dz_0}{dx} \right)^2} dx
 \end{aligned}
 \tag{11.26}$$

Combining Eq.(11.19) and Eq.(11.26), gives the deformation compatibility equation as

$$\frac{D}{2H^2} - \frac{D_0}{2H_0^2} = \frac{(H - H_0)\xi l}{E_t A} + \alpha \Delta t \eta l
 \tag{11.27}$$

where l is the length of the cable, ξ and η are obtained by

$$\xi = \frac{1}{l} \int_l \left[1 + \left(\frac{dz_0}{dx} \right)^2 \right] dx
 \tag{11.28}$$

$$\eta = \frac{1}{l} \int_l \left[1 + \frac{1}{2} \left(\frac{dz_0}{dx} \right)^2 \right] dx$$

- if the stress develops following route 1, the deformation compatibility equation is

$$\frac{D}{2H^2} - \frac{D_0}{2H_0^2} - \frac{(H - H_0)\xi l}{E_{1t} A} - \alpha \eta l \Delta t = 0
 \tag{11.29}$$

- if the stress develops following route 3, the deformation compatibility equation is

$$\frac{D}{2H^2} - \frac{D_0}{2H_0^2} - \left(\frac{\sigma_s}{E_t} + \frac{H}{E_{1t} A} - \frac{\sigma_s}{E_{1t}} - \frac{H_0}{E_{1t} A} + \alpha \Delta t \right) \eta l = 0
 \tag{11.30}$$

The behavior of the single cable is obtained by solving Eq.(11.27), Eq.(11.29) and Eq.(11.30).

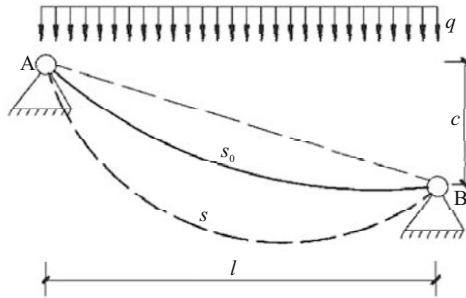


Fig. 11.11 Shape change of the cable at increasing temperature

11.3.1.3 Verification

A single cable structure loaded by a concentrated force $P=0.5$ kN is studied, as shown in Fig. 11.12. The cross section area of the cable $A=0.674$ cm², the elastic modulus 2.0×10^{11} N/m², the span $l=26$ m and the initial tensile force in the cable is 11.7 kN. The comparison of the tensile force obtained by the proposed method and the finite element method is listed in Table 11.18 and Fig. 11.13. The two methods agree very well.

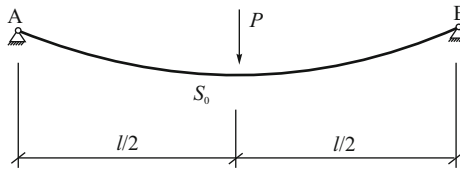


Fig. 11.12 Single cable under concentrated load

Table 11.18 Comparison of tensile forces in a cable at elevated temperatures (N)

Temperature t ($^{\circ}\text{C}$)	Tensile forces	
	FEM results	Proposed method
20	11930	11099
50	8737	8233
100	5883	5673
150	4533	4450
200	3789	3751
250	3312	3293
300	2975	2966
350	2723	2718
400	2524	2523
450	2363	2364
500	2229	2231
550	2106	2119

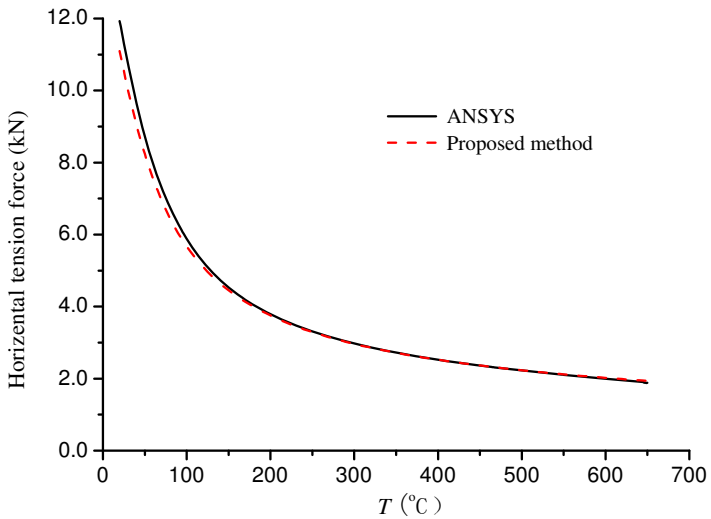


Fig. 11.13 Tensile forces of a single cable

11.3.2 Behavior of the Cable-Net Structure in a Fire

11.3.2.1 Behavior of the Cable Net Structure at Ambient Temperature

The level view of the studied saddle back cable net structure is shown in Fig. 11.14, in which MN and PQ stand for the main cable and the stable cable, respectively. Assume that both the main cable and the stable cable can only resist the tensile force.

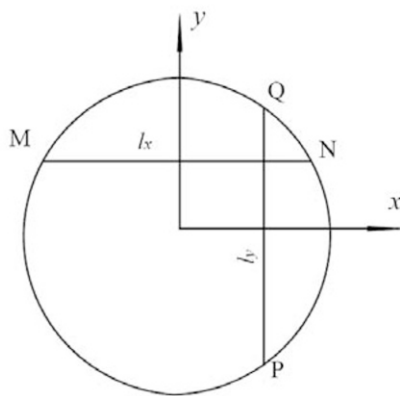


Fig. 11.14 Plan view of the cable net structure

For the cable net structure, the equilibrium equation in incremental form is

$$H_{x0} \frac{\partial^2 w}{\partial x^2} + H_{y0} \frac{\partial^2 w}{\partial y^2} + \Delta H_x \left(\frac{\partial^2 z_0}{\partial x^2} + \frac{\partial^2 w}{\partial x^2} \right) + \Delta H_y \left(\frac{\partial^2 z_0}{\partial y^2} + \frac{\partial^2 w}{\partial y^2} \right) + \Delta q = 0 \quad (11.31)$$

where H_{x0} and H_{y0} show the initial tensile force in the cable respectively, ΔH_{x0} and ΔH_{y0} are the increments in the tensile force, Δq_0 is the increment in the applied load, z_0 is the initial deflection and w is the increment in the vertical deflection.

The deformation compatibility equation for the main cable is

$$\Delta S = u_N - u_M + \int_M^N \left[\frac{\partial z_0}{\partial x} \frac{\partial w}{\partial x} + \frac{1}{2} \left(\frac{\partial w}{\partial x} \right)^2 \right] dx \quad (11.32)$$

where ΔS is the length increment of the main cable. The deformation compatibility equation for the stable cable can be obtained by changing x to y .

11.3.2.2 Behavior of the Cable Net Structures at Elevated Temperatures

With the elevation of temperature, both the main cable and stable cable are elastically unloaded. The mechanical strain is calculated by

$$\Delta \epsilon^N = \frac{\Delta H}{E_t A} \quad (11.33)$$

and the length increment in the main cable is

$$\Delta S = \Delta H_x \frac{l_x \xi}{E_t A_x} + \alpha \Delta t l_x \quad (11.34)$$

By combining Eq.(11.32) and Eq.(11.32), the deformation compatibility of the main cable is obtained as

$$\Delta H_x \frac{l_x}{E_t A_x} \xi = u_N - u_M + \int_M^N \left[\frac{\partial z_0}{\partial x} \frac{\partial w}{\partial x} + \frac{1}{2} \left(\frac{\partial w}{\partial x} \right)^2 \right] dx - \alpha \Delta t l_x \quad (11.35)$$

Similarly, the deformation compatibility of the stable cable is

$$\Delta H_y \frac{l_y}{E_t A_y} \xi = u_Q - u_P + \int_P^Q \left[\frac{\partial z_0}{\partial y} \frac{\partial w}{\partial y} + \frac{1}{2} \left(\frac{\partial w}{\partial y} \right)^2 \right] dy - \alpha \Delta t l_y \quad (11.36)$$

Eq.(11.31), Eq.(11.35) and Eq.(11.36) can be solved by the weighted residual approach. The analysis presented above is used for analysis of a diamond cable net structure.

As a demonstration, the approach is surmised to be as follows.

(1) The initial formation of the cable net structure is assumed to be

$$z_0 = f \left(-\frac{x^2}{a^2} + \frac{y^2}{b^2} \right) \quad (11.37)$$

(2) At the temperature step T_i , the vertical deflection of the cable net structure is

$$w_i = w_{0i} \left(1 - \frac{x}{a} - \frac{y}{b}\right) \left(1 + \frac{x}{a} + \frac{y}{b}\right) \left(1 - \frac{x}{a} + \frac{y}{b}\right) \left(1 + \frac{x}{a} - \frac{y}{b}\right) \quad (11.38)$$

where w_{0i} is the maximum deflection of the cable net structure for the temperature step T_i .

(3) The final deformation of the cable net structure at temperature T_i is

$$z = z_0 + \sum_{i=1}^{n-1} w_i = z_o + w_g \quad (11.39)$$

where n is the step number.

(4) Substituting Eq.(11.39) into Eq.(11.39) and Eq.(11.39) gives

$$\Delta H_{xi} = u_i(8b^4 + 24b^3y + 76b^2y^2 + 24by^3 + 8y^4)(-b + y)^2 + v_i(b^2 + y^2 + 3by)(-b + y)^2 - \alpha\Delta tEA_x \quad (11.40)$$

$$\Delta H_{yi} = r_i(8a^4 + 24a^3x + 76a^2x^2 + 24ax^3 + 8x^4)(-a + x)^2 - 7a^2s_i(a^2 + 3ax + x^2)(-a + x)^2 - \alpha\Delta tEA_y \quad (11.41)$$

where

$$u_i = \frac{16w_{0i}EA_xw_g}{105a^2b^6}, \quad v_i = \frac{16w_{0i}EA_xfb^2}{105a^2b^6} \quad (11.42)$$

$$r_i = \frac{16w_{0i}EA_yw_g}{105a^26b^2}, \quad s_i = \frac{16w_{0i}EA_y}{105a^6b^2}$$

Hence, the tensile force in a cable is

$$\begin{aligned} H_{x0i} &= H_{x0i-1} + \Delta H_{xi} \\ H_{y0i} &= H_{y0i-1} + \Delta H_{yi} \end{aligned} \quad (11.43)$$

In summary, the tensile force in the cable is rewritten as

$$\begin{aligned} H_{xi} &= U(8b^4 + 24b^3y + 76b^2y^2 + 24by^3 + 8y^4)(-b + y)^2 \\ &\quad + V(b^2 + y^2 + 3by)(-b + y)^2 + m \\ H_{yi} &= R(8a^4 + 24a^3x + 76a^2x^2 + 24ax^3 + 8x^4)(-a + x)^2 \\ &\quad - 7a^2S(b^2 + y^2 + 3by)(-a + x)^2 + p \end{aligned} \quad (11.44)$$

where

$$\begin{aligned} U &= \sum_{i=1}^{n-1} u_i; V = \sum_{i=1}^{n-1} v_i; R = \sum_{i=1}^{n-1} r_i; S = \sum_{i=1}^{n-1} s_i \\ m &= H_{x0} - \sum_{i=1}^{n-1} (\alpha\Delta tEA_x)_i \\ p &= H_{y0} - \sum_{i=1}^{n-1} (\alpha\Delta tEA_y)_i \end{aligned} \quad (11.45)$$

Through substituting Eq.(11.43) and Eq.(11.44) into Eq.(11.31), the residual of the equilibrium equation $R_{00}^{[1]}$ is obtained. Further substituting R_{00} into a Galerkin variation equation gives

$$\iint_{\Omega} R_{00} \left(1 - \frac{x}{a} - \frac{y}{b}\right) \left(1 + \frac{x}{a} + \frac{y}{b}\right) \left(1 - \frac{x}{a} + \frac{y}{b}\right) \left(1 + \frac{x}{a} - \frac{y}{b}\right) dxdu = 0 \quad (11.46)$$

that is a high order function of w_{0i} .

Considering that the vertical displacement and the temperature step are small, Eq.(11.46) is simplified as

$$Aw_{0i} + B = 0 \quad (11.47)$$

where

$$\begin{aligned} A = & (-2.844a^2b^4m - 2.844a^4b^2p - 2.496a^2b^8V + 5.325EA_yfa^4w_g \\ & - 5.325EA_xfb^4w_g + 2.844EA_ya^4b^2\alpha\Delta t - 1.765EA_yf^2a^4 \\ & - 1.765EA_xf^2b^4 + 2.844EA_xa^2b^4\alpha\Delta t + 17.472fa^{10}b^2S \\ & - 4.263EA_xb^4w_g^2 - 28.681a^2b^{10}U - 27.974a^{10}b^2R \\ & - 4.263EA_ya^4w_g^2)/a^3b^3 \end{aligned}$$

and

$$\begin{aligned} B = & (2.844EA_ya^4b^2\alpha\Delta tw_g + 2.844EA_xa^4b^4\alpha\Delta tw_g \\ & + 1.778EA_xfa^2b^4\alpha\Delta t - 1.778EA_yfa^4b^2\alpha\Delta t)/a^3b^3 \end{aligned}$$

The maximum deflection w_{0i} of the structure at the temperature T_i is obtained by solving Eq.(11.47). The complete deformation history is obtained by solving Eq.(11.47) incrementally.

11.3.2.3 Verification

A diamond cable net structure is shown in Fig. 11.15. The two spans of the structure are $a=36.6$ m and $b=24.4$ m. The distances between the main cable and the stable cable are $\Delta a=\Delta b=9.15$ m. The initial stiffness of the cable is $EA_x=EA_y=293590$ kN, the applied load $q=60$ N/m². The initial configuration of the structure is

$$z = 3.66 \left(-\frac{x^2}{a^2} + \frac{y^2}{b^2} \right) \quad (11.48)$$

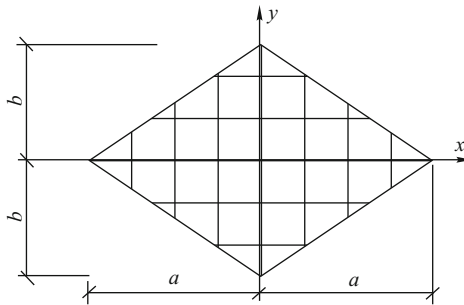


Fig. 11.15 Plan view of a cable net structure

When the temperature increases from 20 °C to 100 °C the comparison of the maximum vertical deflection of the structure predicated by the proposed method and that by FEM analysis is listed in Table 11.19. It can be seen that the two results agree very well.

Table 11.19 Comparison of the maximum vertical deflection (m)

	Vertical displacement (m)
FEM results	0.06
Proposed method	0.067

11.3.3 Simplified Method for the Critical Temperature of a Cable-Net Structure

11.3.3.1 Parameters that Affect the Critical Temperature of a Cable-Net Structure

For the commonly used cable net structure, the load ratio is in the range of 0.3–0.8 and the pre-stress ratio is less than 0.6.

The load ratio is defined as

$$R = \frac{q}{q_{\max}} \tag{11.49}$$

where q is the applied load and q_{\max} is the load bearing capacity of the cable net structure at ambient temperature.

1) Maximum applied load in an elliptical cable net structure

The maximum applied load is calculated by

$$q_{\max} = \frac{10}{9} (B_0 w_{0\max}^3 + B_1 w_{0\max}^2) \tag{11.50}$$

and

$$B_0 = \left(\frac{EA_x}{a^4} + \frac{EA_y}{b^4} \right) \tag{11.51}$$

$$B_1 = 3 \left(\frac{EA_x f_1}{a^4} - \frac{EA_y f_2}{b^4} \right)$$

where q_{\max} is the maximum applied load, a and b are the length of the major and minus radius of the ellipse, EA_x and EA_y are the stiffness of the main cable and the stable cable respectively, $w_{0\max}$ is the maximum deflection given by

$$w_{0\max} = -f_1 + \sqrt{f_1^2 + \frac{3a^2 \Delta H_{x\max}}{4EA_x}} \tag{11.52}$$

where f_1 is the initial deflection of the cable, $\Delta H_{x\max}$ is the increase in the tensile force in the main cable per unit width given by

$$\Delta H_{x\max} = A_x \sigma_{\max} - H_{x0} \quad (11.53)$$

$\sigma_{x\max}$ is the maximum stress in the main cable and A_x is the cross-sectional area of the main cable per unit width.

2) Maximum applied load in a diamond cable net structure

The load bearing capacity of a diamond cable net structure is estimated by

$$q_{\max} = \frac{w_{0\max}}{0.222} \left[0.711 \left(\frac{H_{x0}}{a^2} + \frac{H_{y0}}{b^2} \right) + 0.441 \left(\frac{EA_x}{a^4} + \frac{EA_y}{b^4} \right) \right] \quad (11.54)$$

and

$$w_{0\max} = \frac{15a^2 \Delta H_{x\max}}{16EA_x f} \quad (11.55)$$

where f is the initial deflection of the cable.

3) Load bearing capacity of a parabolic cable net structure

The load bearing capacity of a parabolic cable net structure is determined by

$$q_{\max} = -\frac{1}{1.219ab} (Aw_{0\max} + Bw_{0\max}^2 + Dw_{0\max}^3) \quad (11.56)$$

and

$$w_{0\max} = -f + \sqrt{f^2 + \frac{3a^2 \Delta H_{x\max}}{2EA_x}} \quad (11.57)$$

$$A = -2.438 \frac{b}{a} m_0 - 0.271 \frac{b}{a} m_1 - 3.251 \frac{a}{b} n_0 - 0.606 \frac{a}{b} n_1 - 2.627 \frac{bf^2}{a^3} EA_x + \frac{a}{b^3} (-2.404h^2 + 6.256hf - 4.129f^2) EA_y \quad (11.58)$$

$$B = 3.940 \frac{bf}{a^3} EA_x + \frac{a}{b^3} (-4.691h + 6.194f) EA_y$$

$$D = -1.313 \frac{b}{a^3} EA_x - 2.064 \frac{a}{b^3} EA_y$$

where m_0 , m_1 , n_0 and n_1 are determined by the initial state and load distribution.

The horizontal tensile force in the cable is determined through

$$\begin{aligned} H_{x0} &= m_0 + m_1 \frac{y^2}{b^2} \\ H_{y0} &= n_0 + n_1 \frac{x^2}{a^2} \end{aligned} \quad (11.59)$$

where x and y are shown in Fig.11.15.

4) Load bearing capacity of a cable net structure determined when a stable cable stops working

The ultimate limit state is determined by the stable cable when it is in compression or the tensile force in it reduces to zero. And the load bearing capacity is

$$q_{\max} = \frac{H_{\max}}{\delta_b} \sqrt{\frac{q_0^2}{H_0^2} + \frac{24(H_{\max} - H_0)}{EA l^2}} \quad (11.60)$$

where δ_b is the distance between main cables, H_0 is the initial tensile force in the main cable and H_{\max} is the maximum tensile force in the main cable given by

$$H_{\max} = A_x \sigma_{\max} \quad (11.61)$$

11.3.4 Critical Temperature of a Cable-Net Structure with Elliptical or Diamond Plan View

The curvature of every cable is constant along its length in a elliptical or diamond cable net structure. If the dimension, the load ratio, and the pre-stressed stress ratio between that in the main cable and that in the stable cable are given, the curvature of the cable is determined.

Using the method proposed, the critical temperature of a cable net structure with elliptical or diamond plan view is listed in Table 11.20.

Table 11.20 Critical temperature of the cable net structure with elliptical or diamond plan view (°C)

Load ratio	Critical temperature			
	$R_{\text{pre-stress}}=0.3$	0.4	0.5	0.6
0.3	564	566	572	588
0.4	530	530	544	558
0.5	494	506	512	528
0.6	472	474	484	502
0.7	440	442	452	474
0.8	408	412	422	452
0.9	374	378	394	426

$R_{\text{pre-stress}}$: Pre-stressed stress ratio between that in the main cable and that in the stable cable

11.3.5 Critical Temperature of the Cable-Net Structure with Parabolic Plan View

The curvature of a cable is different at different positions in a parabolic plan view cable net structure. And the pre-stressed stress ratio between that in the main cable

and that in the stable cable is changing too. The critical temperature of a cable net structure with three pre-stress ratios (0.5, 0.75, and 1.0) are listed in Tables 11.21–11.23.

Table 11.21 Critical temperatures of the cable net structure with a ratio of 0.5 between the pre-stressed stress in the main cable and that in the stable cable ($^{\circ}\text{C}$)

Load ratio	Critical temperature			
	$R_{\text{pre-stress}}=0.3$	0.4	0.5	0.6
0.3	548	552	560	564
0.4	512	516	520	528
0.5	476	480	488	492
0.6	440	448	452	464
0.7	404	412	420	432
0.8	356	368	384	400
0.9	312	328	344	356

$R_{\text{pre-stress}}$: Pre-stressed stress ratio between that in the main cable and that in the stable cable

Table 11.22 Critical temperatures of the cable net structure with ratio of 0.75 between the pre-stressed stress in the main cable and that in the stable cable ($^{\circ}\text{C}$)

Load ratio	Critical temperature			
	$R_{\text{pre-stress}}=0.3$	0.4	0.5	0.6
0.3	552	556	564	572
0.4	512	520	528	540
0.5	476	484	492	508
0.6	444	448	460	480
0.7	408	416	428	452
0.8	360	376	396	420
0.9	328	328	352	384

$R_{\text{pre-stress}}$: Pre-stressed stress ratio between that in the main cable and that in the stable cable

Table 11.23 Critical temperatures of the cable net structure with ratio of 1.0 between the pre-stressed stress in the main cable and that in the stable cable (°C)

Load ratio	Critical temperature			
	$R_{\text{pre-stress}}=0.3$	0.4	0.5	0.6
0.3	556	560	572	584
0.4	520	520	536	556
0.5	484	484	504	528
0.6	448	452	472	500
0.7	412	416	444	476
0.8	372	376	412	448
0.9	328	332	376	420

$R_{\text{pre-stress}}$: Pre-stressed stress ratio between that in the main cable and that in the stable cable

References

- [1] China Association for Engineering Construction Standardization. *Technical Code for Fire Safety of Steel Structures in Buildings (CECS200-2006)*. China Plan Press, 2006.
- [2] European Convention for Construction Steelwork. *Calculation for Fire Resistance of Composite Structures*. Technical Note No. 55, ECCS Technical Committee 3, 1989.
- [3] European Committee for Standardization. *EN1993-1-2. Eurocode 3: Design of Steel Structures, Part 1.2, General Rules, Structural Fire Design*. European Committee for Standardization, 2005.
- [4] British Standard Institution. *British Standard BS 5950, Part 8, Code of Practice for Fire Resistance Design*. British Standard Institution, 2000.
- [5] K. C. and G. Q. Li. Fire-resistant design of steel portal frames. *Structure Engineer*, supplementary issue, 1999.
- [6] K. Chen. *Fire-Resistant Analysis and Practical Design Method of Steel Portal Frames*. Msc dissertation, Tongji University, 2000.
- [7] J. Q. Huang, G. Q. Li, P. Q. Bao, and K. Liu. A practical approach for fire-resistant design of steel portal frames. *Progress in Steel Building Structures*, 9(6), 2007.
- [8] International Organization for Standardization. *Fire-Resistance Tests, Elements of Building Construction, Part 1: General Requirements*. International Organization for Standardization, 1999.
- [9] G. Q. Li, L. H. Han, G. B. Lou, and S. C. Jiang. *Steel and Steel-Concrete Composite Structures Fire Resistance Design*. China Architecture & Building Press, 2006.
- [10] J. Q. Huang and G. Q. Li. The critical conditions on eliminating fire protection cover for steel portal frames. *Fire Science and Technology*, 26(4), 2007.

- [11] S. Z. Shen. Theoretical study and engineering practice of long-span spatial structures. *Engineering Science*, 3(3), 2001.
- [12] Y. Du and G. Q. Li. Critical temperature of regular pyramidal space truss in non-uniform fire temperature field. *Journal of Nanjing University of Technology(Natural Science Edition)*, 30(6), 2008.
- [13] Y. Du and G. Q. Li. Critical temperature of regular half-octahedra grid structure in uniform fire temperature field. *Progress in Steel Building Structures*, 10(6), 2008.
- [14] Y. Du and G. Q. Li. Fire-resistant performance of grid structures under bearing restraint. *Journal of Natural Disasters*, 17(5), 2008.
- [15] Y. Du. *A Practical Approach for Fire Resistance Design of Large Space Building Grid Structures*. PhD thesis, Tongji University, 2007.
- [16] Z. Y. Shen and Y. J. Chen. *Space Grid structures and Shell Structures*. Tongji University Press, 1999.
- [17] H. T. Zhou. *Fire resistance of cable net structures*. PhD thesis, Tongji University, 2006.
- [18] S. Z. Shen. *Design of Cable Net Structure*. China Building & Architecture Press, 2006.
- [19] D. P. Greenberg. Inelastic analysis of suspension roof structures. *Journal of Structural Division, ASCE*, 5:905–930, 1996.
- [20] P. Krishna. *Cable Suspended Roofs*. MC Graw Hill, 1978.

Appendix A: Parameters for Calculating the Smoke Temperature in Large Space Building Fire

Table A-1 Parameters for calculating the smoke temperature in large space building fire with small power fire

Floor area A (m ²)	Building height h (m)	Height above Z (m)	Small power fire						
			T_Z	η	μ	β			
						Slow	Medium	Fast	Ultra fast
500	4	4	180	0.6	6	0.002	0.003	0.004	0.005
		3	145	0.85	0.5				
		2	140	0.7	0.8				
	6	6	170	0.6	5	0.002	0.003	0.004	0.005
		5	140	0.8	1				
		4	130	0.8	1				
		3	130	0.8	1				
	9	9	160	0.65	5	0.002	0.003	0.004	0.005
		8	130	0.8	1				
		7	120	0.85	1				
		6	120	0.85	1				
	12	12	140	0.7	3	0.002	0.003	0.004	0.005
11		120	0.8	2					
10		120	0.8	2					
9		120	0.8	1					
15	15	120	0.8	2	0.001	0.002	0.003	0.004	
	14	110	0.8	2					
	13	110	0.8	2					
	12	110	0.8	2					
20	20	90	0.85	8	0.0005	0.001	0.002	0.003	
	19	90	0.85	8					
	18	90	0.85	8					
	17	90	0.85	8					
1000	4	4	180	0.4	5	0.002	0.003	0.004	0.005
		3	130	0.6	1				

(To be continued)

(Table A-1)

Floor area A (m^2)	Building height h (m)	Height above Z (m)	Small power fire						
			Tz	η	μ	β			
						Slow	Medium	Fast	Ultra fast
		2	110	0.55	1				
	6	6	130	0.5	0.35	0.002	0.003	0.004	0.005
		5	100	0.65	1				
		4	100	0.6	0.8				
		3	100	0.6	0.8				
	9	9	110	0.55	4.5	0.002	0.003	0.004	0.005
		8	90	0.7	1				
		7	90	0.7	1				
		6	90	0.7	1				
	12	12	100	0.6	5	0.002	0.003	0.004	0.005
		11	85	0.7	1				
		10	80	0.7	1				
		9	80	0.65	1				
	15	15	90	0.7	5	0.001	0.002	0.003	0.004
		14	80	0.75	2				
		13	80	0.75	1				
		12	80	0.75	1				
	20	20	80	0.7	4	0.0005	0.001	0.002	0.003
		19	70	0.8	1				
		18	70	0.8	1				
		17	70	0.8	1				
3000	4	4	150	0.3	6	0.002	0.003	0.004	0.005
		3	110	0.4	2				
		2	90	0.35	1				
	6	6	110	0.4	3	0.002	0.003	0.004	0.005
		5	100	0.4	1				
		4	100	0.35	1				
		3	100	0.35	1				
	9	9	90	0.45	4	0.001	0.002	0.003	0.004
		8	80	0.45	1				
		7	80	0.45	1				
		6	80	0.45	1				
	12	12	80	0.45	3	0.001	0.002	0.003	0.004
		11	70	0.55	2				
		10	60	0.55	2				
		9	60	0.55	2				
	15	15	70	0.55	2	0.001	0.002	0.003	0.004
		14	65	0.55	2				
		13	60	0.55	2				
		12	60	0.55	2				
	20	20	60	0.6	3	0.0005	0.001	0.0015	0.002
		19	55	0.55	1				
		18	55	0.55	1				

(To be continued)

(Table A-1)

Floor area A (m ²)	Building height h (m)	Height above Z (m)	Small power fire						
			T_z	η	μ	β			
						Slow	Medium	Fast	Ultra fast
		17	55	0.55	1				
6000	4	4	140	0.15	7	0.002	0.003	0.004	0.005
		3	100	0.25	2				
		2	100	0.25	2				
	6	6	100	0.2	6	0.002	0.003	0.004	0.005
		5	90	0.25	6				
		4	90	0.2	0.9				
		3	90	0.2	0.9				
	9	9	80	0.4	7	0.002	0.003	0.004	0.005
		8	70	0.3	3				
		7	70	0.3	3				
		6	70	0.3	3				
	12	12	70	0.3	5	0.001	0.002	0.003	0.004
		11	60	0.35	4				
		10	60	0.35	4				
		9	60	0.35	4				
15	15	60	0.4	3	0.001	0.002	0.003	0.004	
	14	50	0.45	1.5					
	13	50	0.45	1.5					
	12	50	0.45	1.5					
20	20	50	0.4	6	0.0005	0.001	0.002	0.003	
	19	45	0.4	4					
	18	40	0.4	4					
	17	40	0.4	4					

Table A-2 Parameters for calculating the smoke temperature in large space building fire with medium power fire

Floor area A (m ²)	Building height h (m)	Height above Z (m)	Medium power fire						
			T_z	η	μ	β			
						Slow	Medium	Fast	Ultra fast
500	4	4	330	0.75	4	0.001	0.002	0.003	0.004
		3	280	0.75	0.5				
		2	230	0.75	0.5				
	6	6	300	0.6	4	0.001	0.002	0.003	0.004
		5	280	0.7	1				
		4	240	0.75	1				
		3	240	0.7	1				
	9	9	300	0.75	2	0.001	0.002	0.003	0.004
		8	260	0.75	1				
		7	240	0.75	1				

(To be continued)

(Table A-2)

Floor area A (m ²)	Building height h (m)	Height above Z (m)	Medium power fire							
			T _Z	η	μ	β				
						Slow	Medium	Fast	Ultra fast	
	12	6	240	0.75	1					
		12	300	0.75	2	0.001	0.002	0.003	0.004	
		11	260	0.75	1					
		10	240	0.75	1					
		9	240	0.75	1					
	15	15	280	0.7	1	0.001	0.002	0.003	0.004	
		14	230	0.75	1					
		13	230	0.7	1					
		12	230	0.7	1					
	20	20	190	0.75	2	0.001	0.002	0.003	0.004	
		19	170	0.85	1					
		18	170	0.8	1					
		17	170	0.8	1					
	1000	4	4	230	0.6	10	0.001	0.002	0.003	0.004
			3	190	0.8	2				
			2	150	0.8	1				
6		6	230	0.7	8	0.001	0.002	0.003	0.004	
		5	200	0.75	5					
		4	140	0.95	1					
		3	110	1	1					
9		9	230	0.6	8	0.001	0.002	0.003	0.004	
		8	190	0.8	2					
		7	160	0.85	2					
		6	140	0.9	2					
12		12	210	0.65	7	0.001	0.002	0.003	0.004	
		11	180	0.8	1					
		10	170	0.8	1					
		9	170	0.8	1					
15		15	170	0.75	3	0.001	0.002	0.003	0.004	
		14	160	0.75	1					
		13	150	0.8	0.5					
		12	140	0.8	2					
20		20	150	0.7	3	0.0005	0.001	0.002	0.003	
	19	140	0.8	1						
	18	130	0.8	1						
	17	130	0.8	1						
3000	4	4	230	0.3	7	0.0005	0.001	0.002	0.003	
		3	140	0.5	2.5					
		2	110	0.4	1					
	6	6	180	0.45	5	0.001	0.002	0.003	0.004	
		5	140	0.55	3					
		4	110	0.6	0.8					
		3	100	0.55	1					
	9	9	140	0.6	6	0.001	0.002	0.003	0.004	

(To be continued)

(Table A-2)

Floor area A (m ²)	Building height h (m)	Height above Z (m)	Medium power fire						
			T_z	η	μ	β			
						Slow	Medium	Fast	Ultra fast
		8	130	0.6	3				
		7	110	0.7	1				
		6	110	0.7	1				
	12	12	140	0.6	4	0.0005	0.001	0.002	0.003
		11	130	0.6	3				
		10	110	0.65	1				
		9	110	0.65	1				
	15	15	130	0.55	3	0.0005	0.001	0.002	0.003
		14	110	0.65	1				
		13	100	0.65	1				
		12	100	0.65	1				
	20	20	120	0.6	4	0.0002	0.0005	0.001	0.002
		19	110	0.6	3				
		18	110	0.65	2				
		17	110	0.65	2				
	6000	4	4	160	0.2	14	0.001	0.002	0.003
3			120	0.45	7				
2			100	0.35	1.5				
6		6	140	0.3	8	0.001	0.002	0.003	0.004
		5	110	0.4	5				
		4	90	0.4	1				
9		3	70	0.5	1				
		9	120	0.4	6	0.001	0.002	0.003	0.004
		8	100	0.5	3				
		7	90	0.5	1				
12		6	80	0.5	1				
		12	110	0.4	8	0.001	0.002	0.003	0.004
		11	100	0.5	3				
		10	90	0.5	1				
15		9	90	0.5	1				
		15	100	0.45	8	0.001	0.002	0.003	0.004
		14	90	0.5	4				
		13	80	0.55	1.5				
20		12	80	0.55	1.5				
		20	80	0.55	6	0.0005	0.001	0.002	0.003
		19	70	0.6	4				
		18	70	0.55	2				
			17	70	0.55	2			

Table A-3 Parameters for calculating the smoke temperature in large space building fire with Large power fire

Floor area A (m ²)	Building height h (m)	Height above Z (m)	Large power fire						
			T_z	η	μ	β			
						Slow	Medium	Fast	Ultra fast
500	4	4	880	0.6	6	0.0004	0.0008	0.0018	0.002
		3	830	0.8	0.5				
		2	700	0.8	0.5				
	6	6	790	0.8	6	0.0004	0.0008	0.0018	0.002
		5	750	0.85	3				
		4	680	0.8	2				
		3	500	1	1				
	9	9	780	0.55	6	0.0004	0.0008	0.0018	0.002
		8	720	0.7	1				
		7	620	0.75	1				
		6	580	0.8	1				
	12	12	780	0.6	6	0.0004	0.0008	0.0018	0.002
		11	730	0.8	1				
		10	680	0.8	1				
		9	660	0.8	0.5				
	15	15	780	0.7	6	0.0004	0.0008	0.0018	0.002
		14	740	0.75	0.5				
		13	700	0.75	1				
		12	680	0.75	1				
	20	20	640	0.7	6	0.0004	0.0008	0.0018	0.002
19		550	0.8	2					
18		510	0.85	2					
17		500	0.85	2					
1000	4	4	830	0.4	8	0.0004	0.0008	0.0018	0.002
		3	730	0.6	1				
		2	580	0.6	2				
	6	6	700	0.5	7	0.0004	0.0008	0.0018	0.002
		5	620	0.7	2				
		4	500	0.8	1				
		3	400	0.85	2				
	9	9	660	0.6	8	0.0004	0.0008	0.0018	0.002
		8	580	0.7	4				
		7	500	0.8	2				
		6	440	0.85	2				
	12	12	630	0.6	8	0.0004	0.0008	0.0018	0.002
		11	550	0.7	2				
		10	480	0.8	1				
		9	460	0.8	1				
	15	15	610	0.6	6	0.0004	0.0008	0.0018	0.002
		14	550	0.7	2				
		13	480	0.8	1				

(To be continued)

(Table A-3)

Floor area A (m ²)	Building height h (m)	Height above Z (m)	Large power fire							
			T_Z	η	μ	β				
						Slow	Medium	Fast	Ultra fast	
		12	480	0.8	1					
	20	20	580	0.6	6	0.0003	0.0005	0.0015	0.0018	
		19	510	0.7	2					
		18	480	0.75	1					
		17	480	0.75	1					
3000	4	4	660	0.3	8	0.0004	0.0008	0.0018	0.002	
		3	510	0.4	6					
		2	430	0.4	2					
	6	6	630	0.35	6	0.0004	0.0008	0.0018	0.002	
		5	580	0.4	2.5					
		4	400	0.5	1					
		3	300	0.55	2					
		9	9	530	0.5	4	0.0004	0.0008	0.0018	0.002
	12	8	450	0.55	3					
		7	380	0.6	1.5					
		6	330	0.65	2					
		12	12	480	0.5	6	0.0004	0.0008	0.0018	0.002
	15	11	460	0.55	2					
		10	380	0.6	1.5					
		9	380	0.6	1.5					
		15	15	450	0.55	4	0.0004	0.0008	0.0018	0.002
		14	400	0.6	2.5					
		13	360	0.6	2					
		12	360	0.6	2					
	20	20	350	0.65	6	0.0003	0.0005	0.0015	0.0018	
19		320	0.7	2						
18		280	0.75	2						
17		280	0.75	2						
6000		4	4	560	0.2	10	0.0004	0.0008	0.0018	0.002
6	3	490	0.25	6						
	2	400	0.3	2						
	6	540	0.26	7	0.0004	0.0008	0.0018	0.002		
	5	490	0.28	4						
	4	360	0.35	1						
9	3	260	0.4	2						
	9	480	0.3	7	0.0004	0.0008	0.0018	0.002		
	8	400	0.36	6						
	7	310	0.45	1						
12	6	280	0.5	0.8						
	12	410	0.4	7.8	0.0004	0.0008	0.0018	0.002		
	11	350	0.45	5						
	10	310	0.5	1						
	9	280	0.55	2						
15	15	380	0.4	7	0.0004	0.0008	0.0018	0.002		

(To be continued)

(Table A-3)

Floor area A (m ²)	Building height h (m)	Height above Z (m)	Large power fire						
			T_z	η	μ	β			
						Slow	Medium	Fast	Ultra fast
		14	330	0.5	2				
		13	280	0.55	1				
		12	280	0.55	1				
	20	20	340	0.45	6	0.0003	0.0005	0.0015	0.0018
		19	310	0.45	3				
		18	280	0.5	2				
		17	280	0.5	2				

$$[K_3] = \begin{bmatrix} \frac{(EA)_{eq}}{l} & & & & & & \\ 0 & 0 & & & & & \\ 0 & 0 & 0 & & & & \\ \frac{(EA)_{eq}}{l} & 0 & 0 & \frac{(EA)_{eq}}{l} & & & \\ 0 & 0 & 0 & 0 & 0 & & \\ 0 & 0 & 0 & 0 & 0 & 0 & \end{bmatrix} \quad (\text{B-4})$$

$$[K_{G0}] = \begin{bmatrix} 0 & & & & & & \\ 0 & \frac{6}{5l} & & & & & \\ 0 & \frac{1}{10} & \frac{2l}{15} & & & & \\ 0 & 0 & 0 & 0 & & & \\ 0 & -\frac{6}{5l} & -\frac{1}{10} & 0 & \frac{6}{5l} & & \\ 0 & \frac{1}{10} & -\frac{l}{30} & 0 & -\frac{1}{10} & \frac{2l}{15} & \end{bmatrix} \quad (\text{B-5})$$

$$[K_{G1}] = \begin{bmatrix} 0 & & & & & & \\ 0 & \frac{6}{5l} & & & & & \\ 0 & \frac{1}{10} & \frac{2l}{15} & & & & \\ 0 & 0 & 0 & 0 & & & \\ 0 & -\frac{6}{5l} & -\frac{1}{10} & 0 & \frac{6}{5l} & & \\ 0 & \frac{1}{5} & 0 & 0 & -\frac{1}{5} & \frac{l}{5} & \end{bmatrix} \quad (\text{B-6})$$

$$[K_{G2}] = \begin{bmatrix} 0 & & & & & & \\ 0 & \frac{6}{5l} & & & & & \\ 0 & \frac{1}{5} & \frac{l}{5} & & & & \\ 0 & 0 & 0 & 0 & & & \\ 0 & -\frac{6}{5l} & -\frac{1}{5} & 0 & \frac{6}{5l} & & \\ 0 & 0 & 0 & 0 & 0 & 0 & \end{bmatrix} \quad (\text{B-7})$$

$$[K_{G2}] = \begin{bmatrix} 0 & & & & & & \\ 0 & \frac{1}{l} & & & & & \\ 0 & 0 & 0 & & & & \\ 0 & 0 & 0 & 0 & & & \\ 0 & -\frac{1}{l} & 0 & 0 & \frac{1}{l} & & \\ 0 & 0 & 0 & 0 & 0 & 0 & \end{bmatrix} \quad (\text{B-8})$$

Appendix C: Height of the Flame

Table C-1 Height of the flame

F_s/V (m^{-1})	ξ	Height (m)							
		$T_g=100$	200	300	400	500	600	700	800
10	0.7	0.35	0.35	0.35	0.4	0.4	0.4	0.5	0.6
	0.6	0.4	0.4	0.45	0.45	0.45	0.5	0.6	0.7
	0.5	0.5	0.5	0.5	0.5	0.5	0.6	0.7	0.8
	0.4	0.6	0.6	0.6	0.6	0.7	0.7	0.8	0.9
	0.3	0.8	0.8	0.9	-	-	-	-	-
20	0.7	0.2	0.2	0.2	0.25	0.3	0.4	0.4	0.5
	0.6	0.2	0.25	0.3	0.3	0.4	0.4	0.5	0.6
	0.5	0.3	0.3	0.4	0.4	0.4	0.5	0.6	0.7
	0.4	0.4	0.4	0.4	0.5	0.6	0.7	0.8	0.9
	0.3	0.5	0.5	0.6	0.7	0.8	0.9	0.9	0.9
	0.25	0.5	0.5	0.6	0.7	0.9	-	-	-
	0.2	0.6	0.7	0.8	0.9	-	-	-	-
30	0.7	0.15	0.2	0.2	0.25	0.3	0.35	0.4	0.4
	0.6	0.2	0.2	0.25	0.25	0.4	0.4	0.5	0.5
	0.5	0.2	0.2	0.3	0.4	0.4	0.5	0.6	0.6
	0.4	0.3	0.3	0.4	0.4	0.5	0.6	0.7	0.8
	0.3	0.4	0.4	0.5	0.6	0.7	0.8	0.9	-
	0.25	0.5	0.5	0.6	0.7	0.9	-	-	-
	0.2	0.6	0.7	0.8	0.9	-	-	-	-
	0.15	0.8	0.9	-	-	-	-	-	-
40	0.7	0.15	0.15	0.2	0.25	0.3	0.35	0.35	0.4
	0.6	0.2	0.2	0.25	0.3	0.35	0.4	0.4	0.5
	0.5	0.2	0.2	0.3	0.3	0.4	0.5	0.5	0.6
	0.4	0.3	0.4	0.5	0.5	0.6	0.7	0.8	0.9
	0.3	0.4	0.5	0.6	0.7	0.8	0.9	-	-
	0.25	0.5	0.6	0.8	0.9	-	-	-	-
	0.2	0.7	0.8	0.9	-	-	-	-	-
50	0.7	0.15	0.15	0.2	0.25	0.3	0.3	0.35	0.4
	0.6	0.15	0.2	0.25	0.3	0.35	0.4	0.4	0.5

(To be continued)

(Table C-1)

F_s/V (m^{-1})	ξ	Height (m)							
		$T_g=100$	200	300	400	500	600	700	800
	0.5	0.2	0.2	0.3	0.3	0.4	0.4	0.5	0.6
	0.4	0.2	0.3	0.4	0.4	0.5	0.6	0.6	0.7
	0.3	0.3	0.4	0.5	0.6	0.7	0.8	0.8	0.9
	0.25	0.4	0.5	0.6	0.7	0.8	0.9	-	-
	0.2	0.5	0.6	0.8	0.9	-	-	-	-
100	0.7	0.15	0.15	0.2	0.25	0.25	0.3	0.4	0.7
	0.6	0.15	0.2	0.25	0.25	0.3	0.35	0.5	0.7
	0.5	0.2	0.2	0.3	0.3	0.3	0.4	0.6	0.9
	0.4	0.2	0.3	0.3	0.4	0.4	0.5	0.7	0.9
	0.3	0.3	0.4	0.5	0.5	0.6	0.7	0.9	-
	0.25	0.4	0.5	0.6	0.6	0.7	0.9	-	-
	0.2	0.5	0.6	0.7	0.8	0.9	-	-	-
	0.15	0.7	0.8	0.9	-	-	-	-	-
150	0.7	0.15	0.15	0.2	0.25	0.3	0.4	0.6	0.9
	0.6	0.15	0.2	0.25	0.25	0.35	0.45	0.75	0.9
	0.5	0.2	0.2	0.2	0.3	0.4	0.5	0.9	-
	0.4	0.2	0.3	0.3	0.4	0.5	0.7	0.9	-
	0.3	0.3	0.4	0.4	0.5	0.7	0.9	-	-
	0.25	0.4	0.5	0.5	0.6	0.8	0.9	-	-
	0.2	0.5	0.6	0.7	0.8	0.9	-	-	-
	0.15	0.7	0.8	0.9	-	-	-	-	-
200	0.7	0.15	0.15	0.2	0.25	0.3	0.5	0.8	0.9
	0.6	0.15	0.2	0.2	0.3	0.4	0.6	0.9	-
	0.5	0.2	0.2	0.2	0.3	0.4	0.7	0.9	-
	0.4	0.2	0.3	0.3	0.4	0.6	0.9	-	-
	0.3	0.3	0.4	0.4	0.6	0.8	0.9	-	-
	0.25	0.4	0.5	0.5	0.7	0.9	-	-	-
	0.2	0.5	0.6	0.7	0.9	-	-	-	-
	0.15	0.8	0.9	-	-	-	-	-	-
300	0.7	0.15	0.15	0.25	0.3	0.4	0.6	0.9	-
	0.6	0.15	0.2	0.25	0.3	0.4	0.7	0.9	-
	0.5	0.2	0.2	0.3	0.4	0.5	0.8	0.9	-
	0.4	0.2	0.3	0.4	0.5	0.7	0.9	-	-
	0.3	0.3	0.4	0.5	0.6	0.9	-	-	-
	0.25	0.4	0.5	0.6	0.8	0.9	-	-	-
	0.2	0.5	0.6	0.7	0.9	-	-	-	-
	0.15	0.7	0.8	0.9	-	-	-	-	-

Note: The '-' in the table means that (a) the effect of flame radiation need not be considered if $C > 0$; and (b) the ISO834 standard fire is used for calculating the temperature of a structural component if $C \leq 0$. T_g : Smoke temperature ($^{\circ}C$)

Appendix D: Critical Temperatures of Composite Beams

Table D-1 Critical temperatures of simply-supported composite beams (°C)

Fire duration (min)	Load level	Critical temperatures (°C)		
		<i>D</i> =50	70	100
60	0.3	690	696	702
	0.35	654	672	679
	0.4	620	649	656
	0.45	591	628	636
	0.5	559	606	615
	0.55	528	582	591
	0.6	497	559	569
	0.65	463	531	549
	0.7	422	497	524
	0.75	367	459	501
0.8	-	417	472	
90	0.3	628	688	700
	0.35	597	656	677
	0.4	566	620	654
	0.45	535	585	631
	0.5	501	553	609
	0.55	455	520	588
	0.6	393	485	566
	0.65	-	441	542
	0.7	-	393	516
	0.75	-	-	489
0.8	-	-	459	
120	0.3	606	641	698
	0.35	576	606	672
	0.4	539	573	649
	0.45	497	539	626
	0.5	441	505	603

(To be continued)

(Table D-1)

Fire duration (min)	Load level	Critical temperatures (°C)		
		<i>D</i> =50	70	100
	0.55	339	463	579
	0.6	-	413	556
	0.65	-	-	528
	0.7	-	-	501
	0.75	-	-	472
	0.8	-	-	427

D: Slab depth (mm)

Table D-2 Critical temperatures of fix-ended composite beams (°C)

Fire duration (min)	Load level	Critical temperatures (°C)		
		<i>D</i> =50	70	100
30	0.3	649	652	657
	0.35	626	629	634
	0.4	604	607	612
	0.45	580	583	589
	0.5	554	557	567
	0.55	526	533	540
	0.6	496	504	515
	0.65	460	476	484
	0.7	421	439	452
60	0.75	365	389	412
	0.8	-	-	355
	0.3	629	644	657
	0.35	604	621	634
	0.4	580	595	610
	0.45	551	570	586
	0.5	522	540	561
	0.55	492	511	537
	0.6	456	476	508
90	0.65	417	439	476
	0.7	355	389	443
	0.75	-	-	398
	0.8	-	-	314
	0.3	612	626	652
	0.35	586	598	629
	0.4	557	570	604
	0.45	530	544	580
	0.5	496	511	554
0.55	452	476	526	
0.6	394	439	496	
0.65	-	389	460	

(To be continued)

(Table D-2)

Fire duration (min)	Load level	Critical temperatures (°C)		
		<i>D</i> =50	70	100
	0.7	-	-	417
	0.75	-	-	350
	0.8	-	-	427
120	0.3	604	610	647
	0.35	577	583	623
	0.4	547	557	598
	0.45	511	526	567
	0.5	468	492	537
	0.55	412	452	508
	0.6	-	394	468
	0.65	-	-	430
	0.7	-	-	370
	0.75	-	-	350
	0.8	-	-	427

D: Slab depth (mm)

Appendix E: Critical Temperatures of a Steel Column Subjected to Combined Axial Force and Bending Moment

Table E-1 Critical temperature of a steel component subjected to the combined axial force and bending moment fails by buckling T_{dx} or T_{dy} (°C)

$\lambda \sqrt{\frac{f_y}{235}}$	e_{x2} (e_{y2})	e_{x1} (e_{y1})	Load ratio R_x (R_y)													
			0.30	0.35	0.40	0.45	0.50	0.55	0.60	0.65	0.70	0.75	0.80	0.85	0.90	
≤ 50	-	-	670	649	630	612	595	577	560	542	524	506	487	467	446	
100	≤ 0.1	≤ 0.1	667	647	630	614	599	582	565	547	528	508	487	463	438	
		0.3	662	642	625	609	594	577	559	541	522	502	481	458	433	
		1.0	660	640	623	607	590	573	555	537	519	499	479	457	433	
		3.0	665	644	626	609	592	575	557	539	521	502	483	462	440	
		≥ 10	671	650	631	613	596	578	561	543	525	507	488	468	446	
	≤ 0.3	≤ 0.1	669	649	631	615	600	583	566	549	530	510	489	466	441	
		0.3	665	645	628	612	596	579	562	544	525	505	484	462	437	
		1.0	663	643	625	608	592	575	557	539	521	501	481	459	435	
		3.0	666	645	627	610	593	575	558	540	522	503	484	463	440	
		≥ 10	671	650	631	613	596	578	561	543	525	507	488	468	446	
	1	-	668	647	629	612	596	579	561	544	525	506	486	464	441	
		≥ 3	671	651	632	615	598	581	563	545	527	508	489	468	446	
	150	≤ 0.1	≤ 0.1	663	643	628	613	600	584	567	550	529	508	484	457	426
			0.3	657	638	622	608	593	576	559	541	521	499	476	449	420
1.0			656	637	620	605	589	572	554	536	516	496	474	450	423	
3.0			662	642	624	607	591	574	556	538	520	501	480	459	435	
≥ 10			670	649	630	612	595	578	560	543	524	506	487	467	445	
0.3		≤ 0.1	666	646	630	616	602	586	569	552	532	511	488	462	432	
		0.3	661	642	626	611	597	580	563	545	525	504	481	455	427	
		1.0	659	639	622	607	591	574	557	539	519	499	477	454	427	
		3.0	663	643	625	608	592	575	557	539	521	502	481	460	436	
		1	≥ 10	670	649	630	613	595	578	560	543	525	506	487	467	445
≤ 0.1		670	650	633	618	604	588	571	554	535	514	492	467	439		
		0.3	668	648	631	615	601	585	568	551	531	511	489	464	437	

(To be continued)

(Table E-1)

$\lambda \sqrt{\frac{f_y}{235}}$	e_{x2} (e_{y2})	e_{x1} (e_{y1})	Load ratio R_x (R_y)												
			0.30	0.35	0.40	0.45	0.50	0.55	0.60	0.65	0.70	0.75	0.80	0.85	0.90
		1.0	665	645	628	612	597	580	563	545	526	506	484	461	435
		3.0	666	645	628	611	595	578	560	543	524	505	484	463	439
		≥ 10	670	650	631	613	596	579	561	544	525	507	488	467	445
	3	-	670	650	632	616	602	585	568	550	531	512	490	467	441
		≥ 10	-	672	652	634	618	602	586	569	551	532	513	492	469
	200	≤ 0.1	≤ 0.1	661	642	627	613	600	584	567	550	530	507	482	452
0.3			655	637	621	607	593	576	559	541	520	498	473	444	412
1.0			654	635	619	604	588	571	554	535	515	495	472	446	419
3.0			661	641	623	607	591	573	556	538	519	500	479	457	433
≥ 10			669	649	630	612	595	578	560	542	524	506	486	466	444
0.3			≤ 0.1	664	645	630	616	603	588	571	554	534	512	488	458
		0.3	659	640	625	611	597	581	564	546	526	504	480	451	418
		1.0	657	638	622	607	592	575	557	539	519	498	476	450	422
		3.0	662	642	624	608	592	575	558	540	521	501	481	458	434
		≥ 10	669	649	630	612	595	578	560	543	525	506	487	466	444
		1.0	≤ 0.1	668	648	633	619	606	592	576	559	540	518	493	464
0.3			665	646	630	616	603	588	572	554	535	513	489	461	426
1.0			663	643	627	612	599	582	565	547	528	507	484	458	427
3.0			664	644	627	611	596	579	562	544	525	505	484	461	435
≥ 10			670	649	631	613	597	579	562	544	526	507	487	467	444
≥ 3.0			≤ 0.1	667	648	631	615	601	585	568	550	531	511	489	464
		0.3	668	649	633	619	606	593	577	559	540	519	494	466	428
		1.0	668	648	632	617	604	589	573	555	536	515	492	464	430
		3.0	669	650	634	620	607	594	578	561	542	520	496	467	428
		≥ 10	670	650	632	615	599	582	565	547	528	509	489	467	443

'-' indicates that the item can take any value

Appendix F: Maximum Fire Power at Which a Grid Structure Does not Need Fire Protection

Table F-1 Maximum fire power that a grid structure does not need fire protection (MW)

A (m ²)	R	H (m)	Maximum fire power						
			$\eta=0.8$	0.7	0.6	0.5	0.4	0.3	0.2
500	0.8	4	7.6	5.4	3.5	2.6	2.2	1.7	1.3
		6	9.1	6.6	3.9	2.9	2.4	1.8	1.4
		9	9.2	6.7	4.0	3.1	2.6	2.1	1.7
		12	9.2	6.7	4.1	3.3	2.9	2.4	2.1
		15	9.8	7.4	4.5	3.7	3.3	2.8	2.5
		20	14.4	11.7	7.8	5.9	5.0	4.2	3.6
	0.7	4	10.0	7.9	4.8	3.7	2.9	2.3	1.7
		6	11.8	9.5	5.8	4.2	3.3	2.6	1.9
		9	12.0	9.5	5.8	4.2	3.4	2.8	2.1
		12	12.0	9.5	5.8	4.3	3.6	3.1	2.5
		15	12.5	10.2	6.6	4.7	4.0	3.4	2.8
		20	17.3	14.7	10.8	8.2	6.6	5.3	4.2
	0.6	4	11.8	9.8	6.4	4.4	3.6	2.8	2.3
		6	13.8	11.7	7.7	5.0	4.0	3.2	2.5
		9	14.0	11.8	7.8	5.0	4.1	3.3	2.7
		12	14.0	11.8	7.8	5.0	4.2	3.5	3.0
		15	14.4	12.3	8.5	5.8	4.6	3.9	3.4
		20	19.5	17.1	12.9	9.9	8.0	6.4	5.1
	0.5	4	13.2	11.3	7.8	5.2	4.1	3.3	2.7
		6	15.5	13.3	9.4	6.4	4.7	3.8	3.1
		9	15.7	13.5	9.5	6.5	4.7	3.9	3.2
		12	15.7	13.5	9.5	6.5	4.8	4.0	3.4
		15	16.0	13.9	10.1	7.2	5.1	4.4	3.8
		20	21.3	18.9	14.6	11.4	9.3	7.5	6.2
0.4	4	14.6	12.6	9.3	6.4	4.7	3.9	3.1	
	6	17.0	14.8	11.0	7.8	5.7	4.3	3.6	
	9	17.2	15.0	11.2	7.8	5.7	4.4	3.7	

(To be continued)

(Table F-1)

A (m ²)	R	H (m)	Maximum fire power							
			$\eta=0.8$	0.7	0.6	0.5	0.4	0.3	0.2	
		12	17.2	15.0	11.2	7.8	5.7	4.5	3.8	
		15	17.5	15.4	11.7	8.5	6.4	4.9	4.2	
		20	22.9	20.5	16.5	12.9	10.6	8.7	7.1	
	0.3	4	15.9	13.8	10.7	7.6	5.6	4.4	3.5	
		6	18.5	16.1	12.6	9.2	6.9	5.0	4.0	
		9	18.8	16.3	12.8	9.3	7.0	5.0	4.1	
		12	18.8	16.3	12.8	9.3	7.0	5.0	4.2	
		15	19.0	16.7	13.3	9.9	7.7	5.8	4.6	
		20	24.6	22.0	18.2	14.4	12.0	9.9	8.0	
	1000	0.8	4	10.7	8.7	5.8	3.8	2.5	1.0	*
			6	12.3	9.7	6.0	4.4	3.8	3.0	2.4
			9	13.0	10.1	6.1	4.5	4.0	3.3	2.9
			12	14.1	11.2	7.1	5.0	4.4	3.7	3.2
			15	15.5	12.7	8.8	6.8	5.9	4.7	4.0
20			16.7	13.8	9.8	7.8	6.8	5.6	4.7	
0.7		4	12.9	11.0	8.0	7.0	6.1	3.0	1.0	
		6	15.1	12.6	8.8	6.4	4.9	4.0	3.0	
		9	16.0	13.3	9.2	6.5	4.9	4.2	3.4	
		12	17.2	14.5	10.2	7.5	5.8	4.7	3.8	
		15	18.5	15.9	11.8	9.2	7.6	6.2	4.8	
		20	19.7	17.1	12.9	10.3	8.6	7.2	5.7	
0.6		4	14.5	12.8	9.6	9.2	7.3	4.5	2.8	
		6	17.2	14.9	10.8	8.0	6.2	4.8	3.9	
		9	18.3	15.8	11.4	8.3	6.3	4.8	4.1	
		12	19.6	17.1	12.5	9.3	7.3	5.6	4.5	
		15	20.7	18.3	14.0	10.9	9.0	7.4	6.1	
		20	22.0	19.6	15.1	12.0	10.0	8.4	7.0	
0.5		4	15.9	14.1	10.9	11.3	8.5	5.6	4.5	
		6	18.9	16.6	12.5	9.5	7.4	5.7	4.6	
		9	20.1	17.7	13.2	9.9	7.7	5.8	4.7	
		12	21.5	19.0	14.4	11.0	8.7	6.8	5.3	
		15	22.6	20.1	15.8	12.5	10.3	8.5	7.1	
		20	23.9	21.4	17.0	13.6	11.4	9.5	8.1	
0.4		4	17.1	15.3	12.3	13.3	9.6	6.4	5.2	
		6	20.5	18.2	14.3	10.9	8.7	6.8	5.3	
		9	21.9	19.4	15.1	11.4	9.0	7.0	5.3	
		12	23.2	20.7	16.3	12.5	10.1	8.0	6.3	
	15	24.2	21.8	17.6	14.0	11.6	9.7	8.1		
	20	-	23.1	18.9	15.1	12.7	10.7	9.1		
0.3	4	18.3	16.4	13.6	15.3	10.7	7.4	5.9		
	6	22.0	19.6	15.9	12.3	10.0	8.0	6.2		
	9	23.6	21.0	17.0	13.0	10.4	8.3	6.3		
	12	25.0	22.2	18.2	14.1	11.5	9.3	7.2		
	15	-	23.3	19.4	15.6	13.1	11.0	9.0		

(To be continued)

(Table F-1)

A (m ²)	R	H (m)	Maximum fire power						
			$\eta=0.8$	0.7	0.6	0.5	0.4	0.3	0.2
3000	0.8	20	-	24.6	20.7	16.7	14.2	12.0	10.0
		4	13.0	10.1	6.1	4.3	3.5	2.5	1.8
		6	14.8	12.1	8.2	6.3	5.4	4.3	3.5
		9	18.4	15.3	10.8	8.6	7.5	6.2	5.2
		12	20.4	16.8	11.7	9.1	7.9	6.4	5.2
		15	21.9	18.1	12.7	10.0	8.7	7.1	5.9
	0.7	20	-	24.1	16.6	12.8	11.0	8.7	7.1
		4	16.0	13.3	9.2	6.5	4.9	3.8	2.5
		6	17.8	15.2	11.2	8.7	7.1	5.8	4.3
		9	21.8	18.8	14.2	11.3	9.5	7.9	6.2
		12	24.2	20.8	15.6	12.2	10.1	8.4	6.4
		15	-	22.4	16.9	13.3	11.1	9.2	7.1
	0.6	20	-	-	22.4	17.4	14.3	11.7	8.8
		4	18.3	15.0	11.4	8.3	6.3	4.7	3.6
		6	19.9	17.6	13.3	10.3	8.5	6.9	5.6
		9	24.3	21.6	16.6	13.2	11.1	9.2	7.7
		12	-	24.0	18.4	14.4	11.9	9.8	8.1
		15	-	-	19.8	15.6	13.0	10.8	8.9
	0.5	20	-	-	-	20.7	17.0	13.9	11.4
		4	20.2	17.7	13.2	9.9	7.7	5.8	4.4
		6	21.7	19.4	15.1	11.9	9.8	8.0	6.6
		9	-	23.6	18.7	15.0	12.5	10.5	8.9
		12	-	-	20.7	16.5	13.7	11.3	9.5
		15	-	-	22.3	17.8	14.8	12.3	10.4
0.4	20	-	-	-	23.7	19.5	16.0	13.4	
	4	21.9	19.4	15.1	11.4	9.0	7.0	5.3	
	6	23.4	21.0	16.9	13.4	11.0	9.1	7.5	
	9	-	-	20.8	16.7	14.0	11.8	10.0	
	12	-	-	23.1	18.4	15.4	12.8	10.7	
	15	-	-	24.9	19.9	16.6	13.9	11.7	
0.3	20	-	-	-	-	22.0	18.3	15.2	
	4	23.6	20.9	17.0	13.0	10.4	8.3	6.3	
	6	25.0	22.4	18.6	14.9	12.4	10.4	8.4	
	9	-	-	22.8	18.4	15.6	13.3	11.0	
	12	-	-	-	20.4	17.2	14.5	11.9	
	15	-	-	-	22.0	18.6	15.7	12.9	
6000	0.8	20	-	-	-	-	24.7	20.7	16.9
		4	17.1	14.0	9.7	7.5	6.5	5.2	2.6
		6	18.1	15.0	10.7	8.5	7.5	6.2	5.2
		9	20.6	17.2	12.4	10.0	8.8	7.4	6.3
		12	24.4	20.3	14.5	11.7	10.3	8.5	7.3
		15	-	22.1	15.9	12.9	11.4	9.5	8.1
	0.7	20	-	25.0	18.3	15.0	13.4	11.4	9.9
		4	20.4	17.45	13.0	10.2	8.4	6.9	5.2
		6	21.4	18.5	14.0	11.2	9.4	7.9	6.2

(To be continued)

(Table F-1)

A (m ²)	R	H (m)	Maximum fire power						
			$\eta=0.8$	0.7	0.6	0.5	0.4	0.3	0.2
		9	24.3	21.1	16.1	12.9	10.9	9.3	7.4
		12	-	24.9	19.0	15.2	12.8	10.8	8.6
		15	-	-	20.7	16.6	14.1	11.9	9.6
		20	-	-	23.5	19.1	16.3	14.0	11.5
0.6		4	22.8	20.2	15.4	12	9.9	8.1	6.7
		6	23.8	21.2	16.4	13.0	10.9	9.1	7.65
		9	-	24.1	18.7	15.0	12.7	10.7	9.1
		12	-	-	22.1	17.7	14.9	12.5	10.5
		15	-	-	24.1	19.3	16.3	13.7	11.6
		20	-	-	-	21.9	18.7	15.9	13.7
0.5		4	24.8	22.2	17.4	13.8	11.4	9.4	7.8
		6	-	23.2	18.4	14.8	12.4	10.4	8.8
		9	-	-	20.9	16.9	14.3	12.1	10.3
		12	-	-	24.8	20.0	16.8	14.1	12.1
		15	-	-	-	21.8	18.4	15.5	13.3
		20	-	-	-	24.6	20.9	17.8	15.5
0.4		4	-	24.0	19.4	15.4	12.8	10.7	8.9
		6	-	25.0	20.4	16.4	13.8	11.7	9.9
		9	-	-	23.2	18.8	15.9	13.5	11.5
		12	-	-	-	22.2	18.7	15.9	13.5
		15	-	-	-	24.1	20.4	17.4	14.8
		20	-	-	-	-	23.2	19.8	17.1
0.3		4	-	-	21.4	17.1	14.4	12.4	9.9
		6	-	-	22.4	18.1	15.47	13.1	10.9
		9	-	-	-	20.7	17.6	15.1	12.6
		12	-	-	-	24.5	20.8	17.7	14.8
		15	-	-	-	-	22.6	19.4	16.2
		20	-	-	-	-	-	22.0	18.6

'-' stands for the fire power can be any value; * stands for the structure need fire protection

Index

A

ABAQUS 202, 204
ANSYS 156
Axial load 116, 121, 190
Axial restraint 189, 192
Axial restraint stiffness 139, 153, 154
Axially restrained steel column 244
Analytical 6, 7
Approach 5, 6, 7
Arc length of the buckled lower flange 176

B

Bending moment 98
Bending moment capacity 93, 94
Buckling temperature 189, 198
Broadgate Street 1
Building 1, 2
BRE Blackness factor 86

C

Cardington 99, 113
Cardington fire test 189
Catenary action 131, 139, 142
Column buckling curve 117
Configuration factor 88
Convective heat transfer 67
Critical temperature 2, 38
Critical element 311
Critical stress 115, 117
Creep strain 41
Compartment fire 13, 15
Comprehensive heat transfer 71, 73

Coefficient 54, 57, 59
Cooling phase 20, 32
Combined axial load and bending moment 205, 222
Concrete compressive ring 276
Continuous approach 316, 317
Cable net structure 65, 316

D

Damage of fire protection 245
Design temperature 6
Deflection reversal 150, 151

E

Effective length of column 199
Effective width of the concrete slab 102, 103, 105
Effects of non-uniform temperature distribution 216
Emissivity 69
Enclosure fire equivalent 14
Exposure time 31, 32
Experimental approach 6
Empirical rating 12
Effective axial stiffness 145
Equivalent axial stiffness 283
Equivalent bending stiffness 284

F

Finite element method 79, 91
Fire engineering 185
Fire load density 33

- Fire protection 5, 8
- Fire protection thickness 107, 234
- Fire resistance 2, 5
- Fire resistant steel 37
- Fire test 9, 132
- Flashover 14, 15
- Fire power 32
- Fracture of the beam-to-column connection 1, 3
- Fuel controlled fire 14, 16
- Field model 17, 18
- Fire duration 21, 89
- Failure temperature 189, 198
- Failure criteria 206, 237

- G**
- Global collapse 1
- Grid Structure 35, 91

- H**
- Heat transfer 231
- Hogging bending moment 179
- Hydrocarbon fire curve 69
- Heating models 7
- Heat release rate 12, 15, 16
- High strength steel 37, 48
- Heavy weight fire protection 69, 70
- Heavy section

- I**
- Integrated configuration factor 88
- Interaction equations 214, 219
- Isolated beam 139, 143

- L**
- Large deflection 145, 146
- Lateral torsional buckling 93, 94
- Light weight fire protection 72
- Limit state 113, 186
- Local buckling 1, 3
- Load ratio 95, 97
- Localized fire 256
- Limit state function 5
- Large space building fire 13, 314
- Load eccentricity 240

- M**
- Membrane action 245, 252
- Mass of equivalent wood 11

- Modified factor of the overall stability factor 118

- N**
- Nature fire
- Non-uniformly distributed temperature 314, 316

- O**
- Overall buckling 312
- Overall stability factor 94, 95

- P**
- Parametric fire 21
- Partial fire protection 113, 159
- Portal frames 299, 300
- Post buckling 130, 189
- Post flash over 17
- Prescriptive approach 6
- Proof stress 41, 48, 49

- R**
- Radiation 67, 68
- Restrained steel beam 131, 132, 133
- Restrained steel column 189, 190
- Restrained slab 256
- Restrained steel-concrete composite beams 159, 169
- Restraint stiffness 174, 178
- Required fire 96, 97
- Resistance time 97, 121
- Rotational 146, 147
- Restraint 147, 150
- Residual deflection 199, 200

- S**
- Sagging bending moment 179
- Section factor 69, 71
- Simplified method 78, 131
- Stainless steel 37, 54
- Standard fire test 99, 131
- Steady state 28, 34, 40
- Stress-strain curve 48, 49, 60
- Structural models 7
- Swedish curves 20, 21
- Specific heat 24, 37
- Slenderness ratio 118, 119
- Stability stress ratio 310

Structural load ratio 311, 315

T

Temperature distribution 13, 27

Thermal bowing 202

Thermal expansion 40, 54

Thermal conductivity 37, 38, 39

Taipei Oriental Science District Building 1, 3

Transient state 40, 41

Thermal Force of Element 287

Tapered member 301, 303

U

Unprotected structural component 70, 71

Ultimate limit state 2

V

Ventilation controlled fire 16

View factor 69, 81

W

World trade center 1

Y

Yielding load 238

Z

Zone model 17, 18, 23